AALBORG UNIVERSITY

DENMARK

Error Modeling and Design Optimization of Parallel Manipulators

Wu, Guanglei

Error Modeling and Design Optimization of Parallel Manipulators

Ph.D. Thesis

by

Guanglei Wu

Department of Mechanical and Manufacturing Engineering, Aalborg Univesity
Fibigerstræde 16, DK-9220 Aalborg, Denmark
E-mail: gwu@m-tech.aau.dk

Preface

The thesis is submitted as partial fulfillment of the requirements for the Doctor of Philosophy at the Faculty of Engineering and Science, Aalborg University (AAU). The work has been carried out during the period from March 2010 to February 2013 at the Department of Mechanical and Manufacturing Engineering (M-Tech), AAU. This work is supervised by Associate Professor Jørgen Kepler, AAU and co-supervised by Associate Professor Shaoping Bai, AAU.

I would like to express my gratitude to my supervisor, Prof. Jørgen Kepler and Prof. Shaoping Bai, for their splendid supervision and support during the past three years. I would like to thank Prof. Kepler and Prof. Bai for their help in solving theoretical problems encountered during the research and for always sharing their experience to my project. I also appreciate their assistance in writing reports which have revolutionized my academic-writing skills.

I would like to acknowledge Dr. Stéphane Caro at Institut de Recherche en Communications et Cybernétique de Nantes (IRCCyN), France, for his great help in my research and during my exchange study in IRCCyN. I would like to thank Dr. Caro for taking time out from his busy schedule to revise my papers and discuss the technical problems.

Special thanks are also due to all the colleagues in M-Tech for their help and friendship as well as for their contributions to creating the most pleasing working atmosphere that I ever enjoyed.

Last, but not least, I would like to thank my parents, who are at the root of every effort embedded in my whole life. The warmth from them encouraged me all these years.

Guanglei Wu
Aalborg, October 2013

Abstrakt

Robotmanipulatorer, som er baseret på parallel-mekanismer, kan ofte være fordelagtige i forhold til seriel-mekanismer når der måles på præcision, stivhed, arbejdshastighed og nyttelast. De finder derfor stigende anvendelse i flere industrielle anvendelsesområder.

Parallel-mekanismer er imidlertid typisk stærkt kinematisk og dynamisk ulineære, hvilket stiller særlige udfordringer i relation til design og anvendelse. Derfor er parameter- og ydelsesanalyse, i relation til stivhed og præcision, af særlig vigtighed. I forhold til et kompleks af almene kvalitetskriterier, så som lav vægt, fysisk størrelse, præcision og energiforbrug, kan optimeringsmetodik med fordel anvendes.

Der er p.t. ingen anerkendt fællesmetodisk tilgang til design af parallel-manipulatorer. Nærværende studium søger blandt andet at opstille en systematisk analysetilgang som kan benyttes i den tidlige designfase, idet der holdes særligt fokus på præcision. Fremgangsmåden eksemplificeres gennem studier af særlige typer plane og sfæriske parallel-manipulatorer. I gennemgangen af disse behandles ligeledes kinematisk og dynamisk analyse, kinetostatisk modellering samt stivhedsanalyse.

Indledningsvis gennemføres undersøgelse af den kinematiske sammenhæng for plane og sfæriske parallel-manipulatorer, baseret på den specifikke mekaniske konfiguration. Videre undersøgelse omfatter opstilling af kinematiske ligninger, udledning af kinematisk Jacobi-matrice, dynamisk modellering etc.

Herefter opstilles differentialligninger af de kinematiske bindingsligninger, med henblik på fejlmodelleringen. Fejlmodellerne tager højde for aktuatorfejl (positionspræcision, slør) samt tolerance ved fremstilling og montage af de passive kinematiske par (drejeled, linearføringer). Fejlmodelleringen illustreres som fejlområder for givne nominelle konfigurationer. For den plane parallel-mekanisme sammenholdes den modellerede fejl med tilsvarende eksperimentelt fundne data.

Sfæriske parallel-manipulatorer behandles ydermere gennem anvendelse af skrue-teori og opstilling af virtuel fjedring. Dette sammenholdes med finite-element modellering af systemet. Modellen danner grundlag for samlet stivhedsmodellering af en særlig type sfærisk parallel-manipulator, og stivheden illustreres via isokonturer. Undersøgelsen

demonstrerer at den elastiske deformation i almindelighed må medtages i en kinematisk analyse. Stivheden, og implicit positioneringspræcisionen, vurderes for forskellige elementgeometrier.

På baggrund af de etablerede modeller opstilles optimeringsproblemet med henblik på at optimere de strukturelle og geometriske parametre for en sfærisk parallel-manipulator. Fremgangsmåden eksemplificeres gennem en specifik optimering (minimering af systemmasse og optimering af kinematisk og dynamisk ydelse). Metodikken tillader arbitrært valg af objektfunktion.

Abstract

Parallel mechanism based robotic manipulators feature higher performance in terms of accuracy, rigidity, speed and payload over the serial manipulators and they have found the industrial applications in many fields.

Nevertheless, the design and application of parallel manipulators face many challenges due to their highly nonlinear behaviors, thus, the parameter and performance analysis, especially the accuracy and stiffness, are particularly important. Toward the requirements of robotic technology such as light weight, compactness, high accuracy and low energy consumption, utilizing optimization technique in the design procedure is a suitable approach to handle these complex tasks.

As there is no unified design guideline for the parallel manipulators, the study described in this thesis aims to provide a systematic analysis for this type of mechanisms in the early design stage, focusing on accuracy analysis and design optimization. The proposed approach is illustrated with the planar and spherical parallel manipulators. The geometric design, kinematic and dynamic analysis, kinetostatic modeling and stiffness analysis are also presented.

Firstly, the study on the geometric architecture and kinematic problem of the planar and spherical parallel manipulators is carried out. The kinematic problem is the basis for further study of mechanisms, which includes the development of the kinematic closure equation, derivation of the kinematic Jacobian matrix, input-output expression of velocity and accelerations, dynamic modeling etc.

Next, the first-order differential equation of the kinematic closure equation of planar parallel manipulator is obtained to develop its error model both in Polar and Cartesian coordinate systems. The established error model contains the error sources of actuation error/backlash, manufacturing and assembly errors and joint clearances. From the error prediction model, the distributions of the pose errors due to joint clearances are mapped within its constant-orientation workspace and the correctness of the developed model is validated experimentally.

Additionally, using the screw theory and virtual spring approach, a general kinetostatic model of the spherical parallel manipulators is developed and validated with Finite Element approach. This model is applied to the stiffness analysis of a special spherical parallel manipulator with unlimited rolling motion and the obtained stiffness isocontours show an overall image of the stiffness. The elastic deformation of the center of rotation or center shift for spherical parallel manipulators cannot be neglected. Moreover, the positioning accuracies of the spherical parallel manipulators with different structures were compared. The comparison reveals the influence of link structures on the orientation accuracy.

Finally, with the previously developed kinematic, kinetostatic and dynamic models, a multiobjective optimization problem is formulated to optimize the structural and geometric parameters of the spherical parallel manipulator. The proposed approach is illustrated with the design optimization of the proposed spherical parallel manipulator that aims to minimize the mechanism mass and to maximize the global conditioning index to enhance both kinematic and dynamic performances. Behind the implemented study case, the proposed method offers a great flexibility to select any criterion as an objective function based on requirements, as different kinds of performances ranging from kinematics, statics to dynamics are employed to formulate this systematic approach for design optimization.

Publications

Parts of the work has been published or submitted to peer-reviewed scientific journals and international conferences.

Journal Papers

1. G. Wu, S. Caro, S. Bai, J.A. Kepler, 2014. Mobile platform center shift in spherical parallel manipulators with flexible limbs, *Mechanism and Machine Theory*, 75: 12-26, DOI:10.1016/j.mechmachtheory.2014.01.001.

2. G. Wu, S. Caro, S. Bai, J.A. Kepler, 2014. Dynamic modeling and design optimization of a 3-DOF spherical parallel manipulator, *Robotics and Autonomous Systems*, DOI: 10.1016/j.robot.2014.06.006.

3. G. Wu, 2012. Multiobjective Optimum Design of a 3-RRR Spherical Parallel Manipulator with Kinematic and Dynamic Dexterities, *Modeling, Identification and Control*, 33(3): 111–122, DOI: 10.4173/mic.2012.3.3.

4. G. Wu, S. Bai, J.A. Kepler, S. Caro, 2012. Error Modelling and Experimental Validation of a Planar 3-PPR Parallel Manipulator with Joint Clearances, *ASME Journal of Mechanisms and Robotics*, 4(4): 041008(1–12), DOI: 10.1115/1.4007487.

Conference Papers

1. G. Wu, S. Bai, J.A. Kepler, 2012. Stiffness Analysis and Comparison of 3-PPR Planar Parallel Manipulators with Actuation Compliance. *Proc. of ASME 2012 11th Biennial Conference on Engineering Systems Design and Analysis (ESDA2012)*, 3:255–264, July 2-4, 2012, Nantes, France.

2. G. Wu, S. Bai, J.A. Kepler, 2011. Error Modelling and Experimental Validation for a Planar 3-PPR Parallel Manipulator. *IEEE The 15th International Conference on Advanced Robotics*, Tallinn, Estonia, 259–264, DOI: 10.1109/ICAR.2011.6088573.

Contents

Abbreviations

CAD   **C**omputer-**A**ided **D**esign

CCT   **C**onservative **C**ongruence **T**ransformation

DOF   **D**egree-**O**f-**F**reedom

EE   **E**nd-**E**ffector

FEA   **F**inite **E**lement **A**nalysis

GA   **G**enetic **A**lgorithm

GCI   **G**lobal **C**onditioning **I**ndex

MOEA   **M**ulti**O**bjective **E**volutionary **A**lgorithm

MP   **M**obile(**M**oving) **P**latform

NSGA   **N**on-dominated **S**orting **G**enetic **A**lgorithm

PKM   **P**arallel **K**inematic **M**achine

PM   **P**arallel **M**anipulator(**M**echanism)

PPM   **P**lanar **P**arallel **M**anipulator

SPM   **S**pherical **P**arallel **M**anipulator

VJM   **V**irtual **J**oint **M**ethod

Nomenclature

For Chapters 1–3. Where a specific nomenclature is used in the scientific papers, this is provided in the paper in question.

$\mathbf{K}_C$	Cartesian stiffness matrix
$\mathbf{K}_J$	stiffness matrix in joint space
$\mathbf{p}$	position vector of the end-effector
$\mathcal{F}_b$	reference coordinate system
$\mathcal{F}_p$	local coordinate system
$\mathbf{E}$	right angle rotation matrix
$\mathbf{A}$, $\mathbf{B}$	forward and inverse kinematic Jacobian matrix
$\mathbf{J}$	kinematic Jacobian matrix
$\mathbf{Q}$	rotation matrix
$\mathbf{t}$	twist of a rigid body
$\hat{\$}$, $\hat{\$}_r$	unit screw and its reciprocal screw
p	pitch in a screw
$\boldsymbol{\omega}$	angular velocity of the mobile-platform in the reference frame
$\boldsymbol{\omega}'$	angular velocity of the mobile-platform in the local frame
$\dot{\boldsymbol{\varphi}}$	angle rates
$\boldsymbol{\Phi}$	transformation matrix between the angular velocity $\boldsymbol{\omega}$ and angle rates
$\boldsymbol{\Phi}'$	transformation matrix between the angular velocity $\boldsymbol{\omega}'$ and angle rates
$\boldsymbol{\omega}_i$	angular velocity of the ith link in the reference frame

$\bar{x}$ mass center position of a curved link

L Lagrangian of the mechanical system

T kinetic energy

V potential energy

$\mathbf{q}$ dependent Lagrangian coordiantes

$\mathbf{Q}_{ex}$ vector of the generalized external forces

$\mathbf{\Phi_q}$, $\mathbf{C_q}$ constraint Jacobian matrix

$\boldsymbol{\lambda}$ Lagrange multipliers

$\mathbf{I}_p$ matrix of the mass moment of inertia of the mobile platform

$\mathbf{M(q)}$ mass matrix of the spherical parallel manipulator

$\mathbf{1}_3$ Identity matrix

$[\cdot]_\times$ skew-symmetric matrix of vector $(\cdot)$

1

Introduction

The presented research work in this thesis aims to provide a systematic analysis for the design and applications of parallel manipulators, focusing on error and kinetostatic analysis and their applications in the optimal design of parallel mechanisms. A new and valid error prediction model was proposed for the planar manipulators and a new stiffness model was established for the spherical manipulators. In the design procedure, a systematic optimization method was formulated for the parallel manipulators. Some results can be extended to serial and other parallel mechanisms as well.

1.1 Parallel Manipulators

Parallel Manipulators or Mechanisms (PMs), also sometimes called parallel robots or Parallel Kinematic Machines (PKMs), is a class of multi-loop mechanisms contrary to the conventional serial-chains based mechanisms, see Figure 1.1.

A parallel mechanism (PM) is generally composed of two platforms, one fixed platform and one mobile platform, which are connected by at least two independent serial kinematic chains [3]. Their unique structures allow the parallel manipulators to perform better over the serial manipulators:

- The actuators of a parallel manipulator are usually arranged on or close to its fixed platform that enables the manipulator perform higher performances such as low mass in motion, high speed and better dynamic behaviors.

- The non-accumulated errors of the manipulator end-effector provide high accuracy and repeatability.

- The closed-loop kinematic chains simplify the manipulator structure and achieve high specific structural stiffness and payload ratio.

(a)

(b)
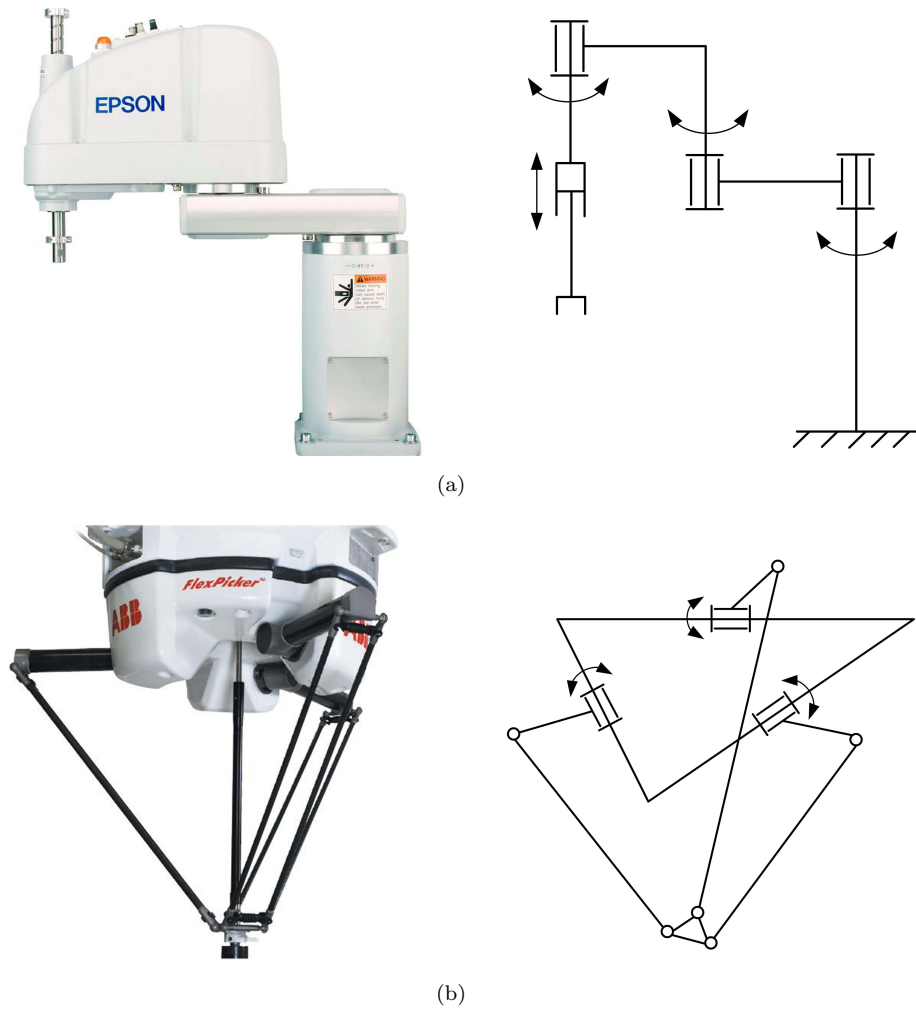
Figure 1.1: Serial and parallel manipulators: (a) Epson SCARA G10 [1], (b) ABB FlexPicker [2].

- The symmetric structure of a parallel manipulator ensures better kinematic isotropy, i.e., approximately equivalent performance in all directions.

- PMs can readily achieve real-time control due to their simple inverse kinematics.

Parallel manipulators were originally proposed to cope with the previous problems encountered with their serial counterparts [3, 4]. The milestone of the development of parallel manipulators is the appearance of the known "Gough-Stewart" platform (see Figure 1.2) introduced by Gough as a tire testing machine [5] and then by Stewart as an aircraft simulator [6]. After that, parallel mechanisms have been extensively studied, focusing on different aspects, i.e., mechanism theory, mobility analysis, dimensional synthesis, kinematic and dynamic modeling, static/elastostatic analysis, and design optimization.
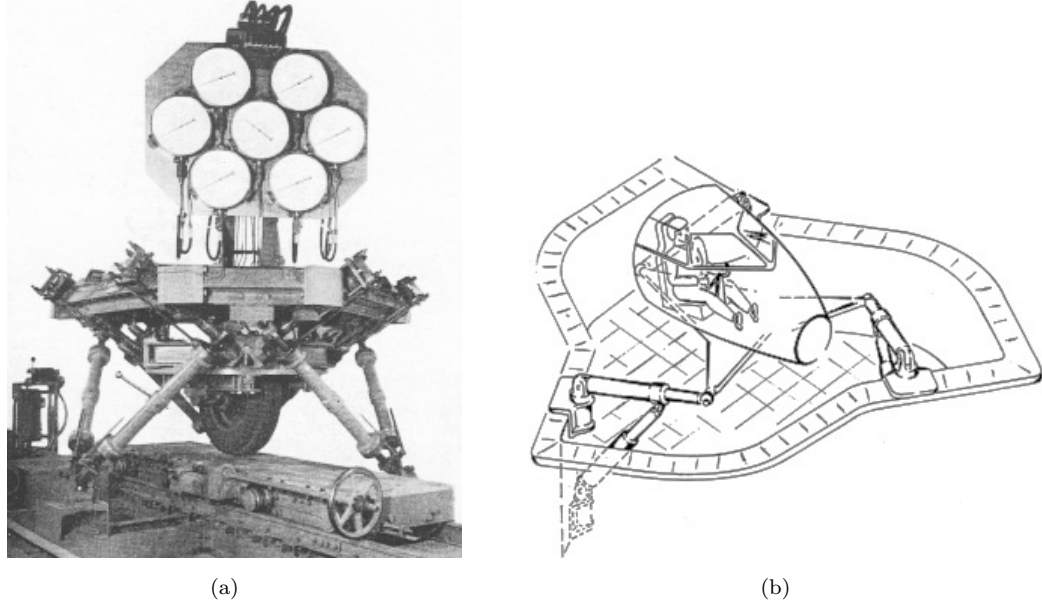
Figure 1.2: Gough-Stewart platform: (a) Gough platform as a tire testing device (1956) [5], (b) schematic of Stewart platform (1965) [6].
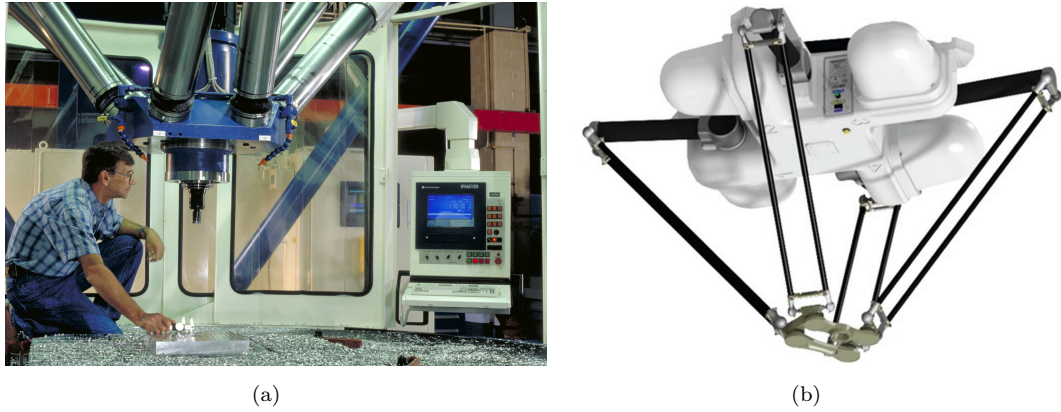
Figure 1.3: Successful applications of parallel manipulators: (a) Octahedral Hexapod machine tool of Ingersoll (photo by Kathie Koenig Simon/NIST, National Institute of Standards and Technology), (b) Adept Quattro robot [53].

Nowadays, parallel manipulators can find their applications in many fields, i.e., aircraft and vehicle simulators [7–15], medical devices [16–25], adjustable articulated trusses [26–30], force/torque sensor [31–38], and micro-robot [39–46]. One of their successful applications is that they have been used in the high precision machine tools by many companies such as Giddings & Lewis, Ingersoll, Hexel, Geodetic and Toyoda, and the Hexapod machine tool (Figure 1.3(a)) [47–51]. Besides, PMs are widely used in the food and assembly industry, i.e., ABB Delta robot [2, 52] and Adept Quattro robot (Figure 1.3(b)) [53, 54]. Parallel manipulators have become an indispensable part of general robotic manipulators both in industry and in academia and their research and development have been a key technology of robot applications in engineering.

1.2   Background

Of the different types of PMs, three degrees-of-freedom (DOF) parallel mechanisms based manipulators have high potential and good prospect of practical implementation in industry, such as ABB Tricept [55] and FlexPicker [2], see Figure 1.4. 3-DOF parallel manipulators include translation, orientation, planar and spatial mixed-DOF manipulators [3], which can be used as robotic manipulators [56–58], double parallel robotic arm [59], shoulder or wrist joint [60–62] and micro-positioning devices [63], see Figure 1.5. The translation (ABB Tricept [55] and FlexPicker [2]; Orthoglide robot [58]) and spatial mixed-DOF (CaPaMan robot [64]; Micro robot MIPS [65]; Hunt's mechanism [66] in the *Dockwelder* project [67]) manipulators have achieved success in many applications, while for the planar and orientation (spherical) ones, their research and development were received relatively less attention. The research work in this thesis will focus on these two types of manipulators.

The planar and spherical manipulators have fewer mobility degrees than the Stewart platform [6], thus, one advantage is that they are easy to be built. Moreover, they are able to alleviate the shortcoming of the limited workspace by changing the structure or layout of their kinematic chains without largely increased mechanism space. However, toward the increasing requirements of robotic technology such as light weight, high accuracy and rigidity, and low energy consumption, their design and application face many challenges due to their highly nonlinear behaviors. The following sections present some problems encountered in the design and application of the parallel manipulators that will be investigated in this thesis.

1.2.1   Planar Parallel Manipulator

Planar parallel manipulators (PPMs) are parallel manipulators that have two translations in the plane and one rotation whose revolute axis is perpendicular to the plane. In the design and application of parallel manipulators, the accuracy is one of the most important performance criteria, which can be evaluated by conducting error analysis. Sources of errors for parallel mechanisms are diverse. The most significant ones are related to manufacturing/assembly errors and compliance in the mechanical architecture, actuation errors/backlash in the control loop, and clearances in the joints. As indicated in [68–73], the influence of most sources of errors is predictable and can be compensated through calibration and model-based control except joint clearance due to its poor repeatability.

(a) (b)
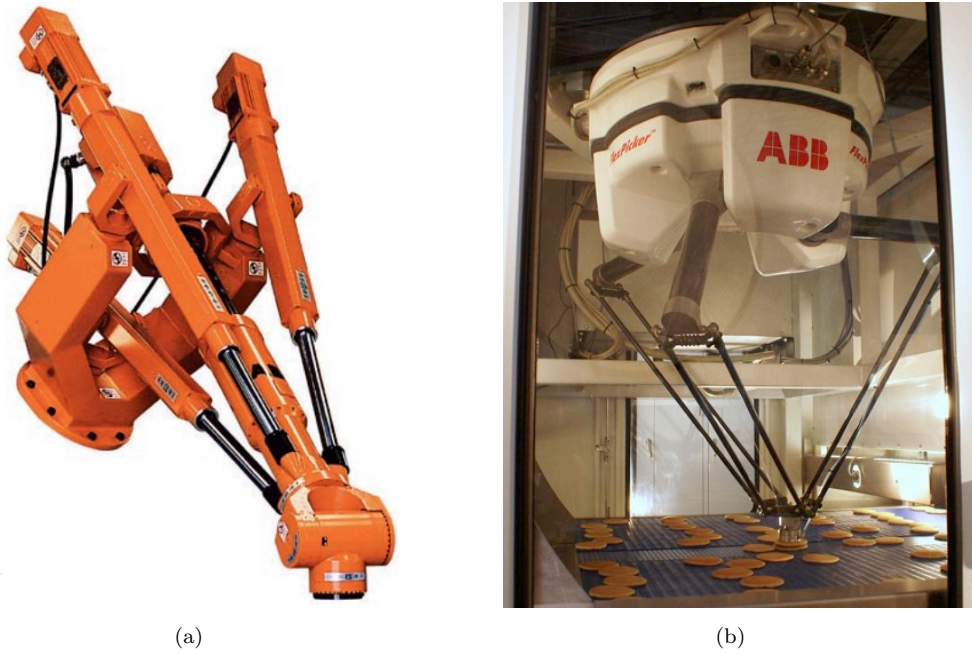
Figure 1.4: ABB Tricept [55] (left) and FlexPicker [2] (right) robots.

(a) (b)

(c) (d) (e)
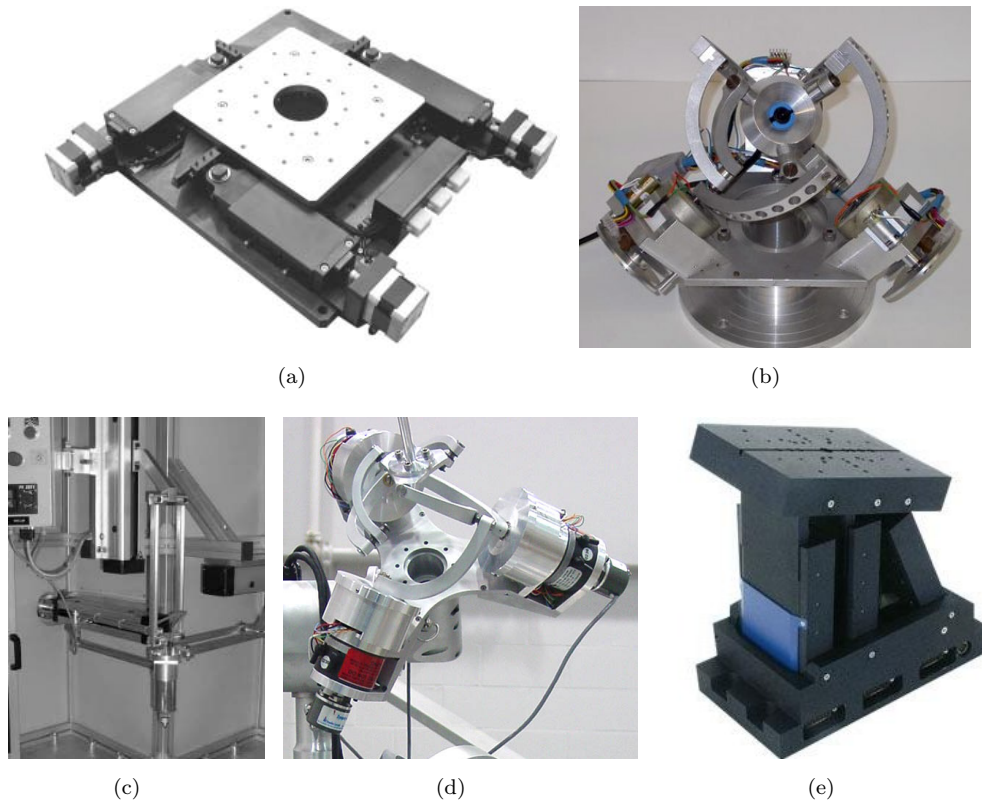
Figure 1.5: Applications of 3-DOF parallel manipulators: (a) precision planar robot [56], (b) Agile Eye for orientating camera [57], (c) Orthoglide robot [58], (d) Agile wrist [61], (e) Goniometer Micro-Positioner from PI, US [63].

(a)

(b)
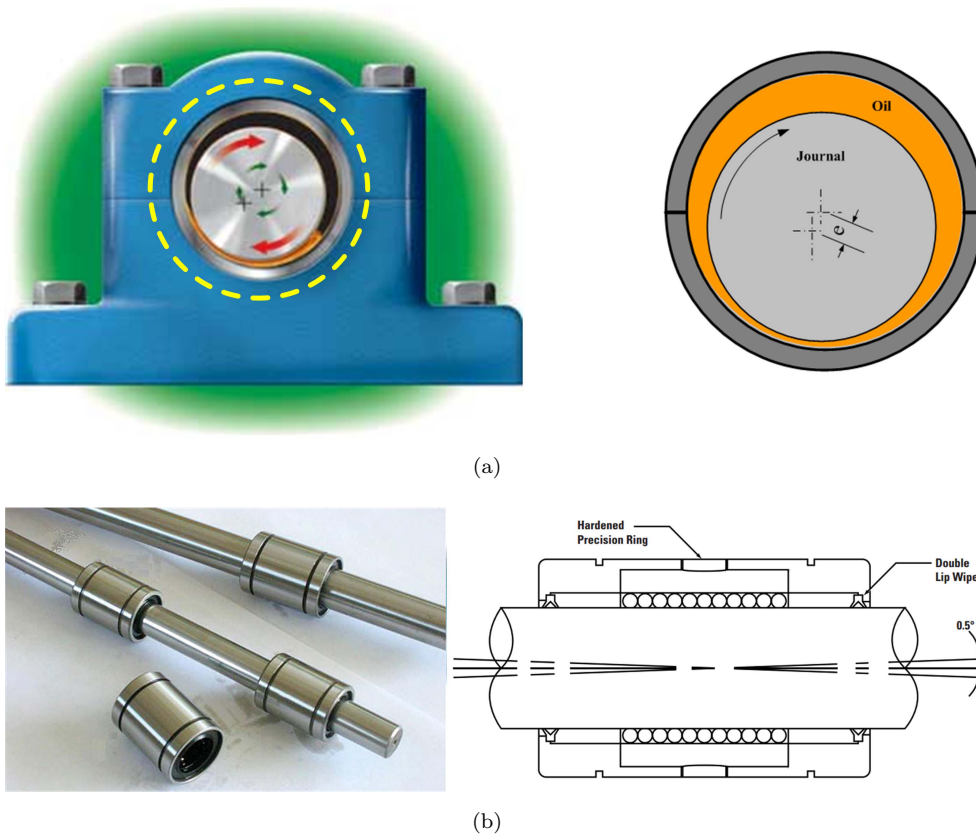
Figure 1.6: Existence of clearance in some common used transmission components: (a) journal bearing [74], (b) linear bearing [75].
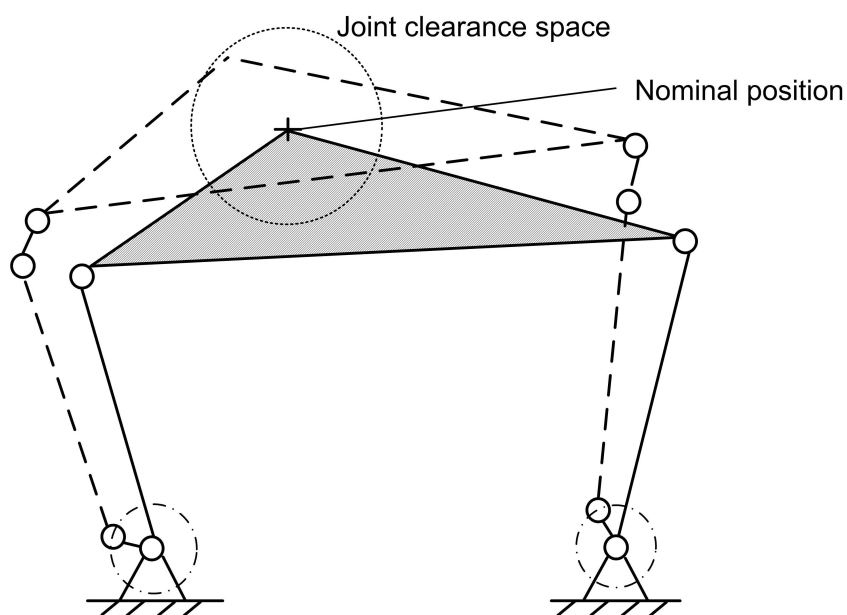
Figure 1.7: Joint clearance-affected mechanism: joint clearance introduce extra mobility degrees that is equivalent to kinematic joints.

Despite the fact that joint clearance can ease assembly/manufacturing and is sometimes inevitable (see Figure 1.6), the existence of the joint clearance will lead to poor performances of the mechanism as it introduces extra DOF of displacements between the pairing elements of a joint. As shown in Figure 1.7, the existing joint clearances may lead to an uncertain location of the manipulator end-effector that is unexpected. Besides, it results in impact of the pairing elements and thus quicker wears of the mechanism elements. Thus, the error modelling and analysis with respect to joint clearances are of importance for both design and control in order to utilize the PMs potential of high accuracy in applications.

1.2.2   Spherical Parallel Manipulator

Spherical Parallel Manipulators (SPMs) are a class of parallel mechanisms for which all points on the mobile bodies are located on concentric spheres, which is a relatively new research area in robotics, with a history of around two decades. A representative example for this type of mechanism is the Agile Eye [57], see Figure 1.5(b).

The motivation of the research on SPMs is to meet the increasing demands of actuating technology providing 3-DOF rotations. The traditional approach to achieve pure rotations is through serial-chains based wrist mechanism, see Figure 1.8. Such kinds of mechanisms normally have a relatively low payload ratio and complicated structure. Moreover, it increases the energy consumption with unevenly distributed power requirements among the actuators. To overcome these drawbacks, wrists based-on SPMs can be utilized. With advantages inherent from the parallel structure, wrists made of SPMs are able to rotate accurately with high transmission torque. In order to improve the performance of such kind of spherical actuated joints, the wrist mechanisms have to be compact, lightweight, stiff and energy efficient. This can be accomplished with optimization method which is able to take multiple design criteria into account simultaneously.

The subject of this study in particular is to develop modeling method and formulation of design guidelines used for parallel manipulators, focusing on error and stiffness analysis and design optimization. It is envisaged that the error model should be simple, readily identifiable from principal error sources and valid for its application of the error compensation. Besides, the kinetostatic model can be used for the optimum design to formulate systematic design guidelines. Eventually, the developed models are expected to improve characterization of the PMs.

| (a) | (b) |
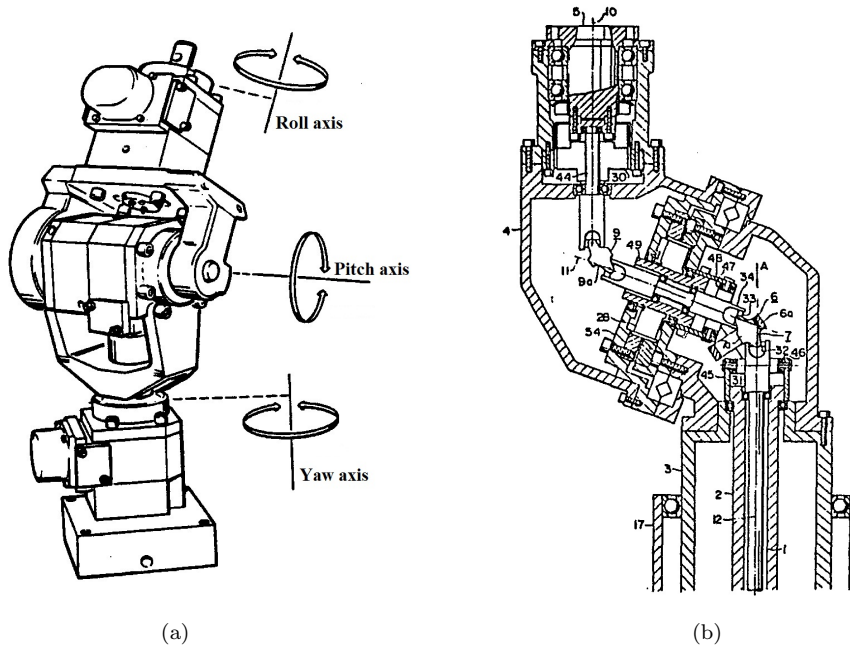
Figure 1.8: Serial-chains based wrist mechanisms: (a) overview [76], (b) assembly details of a patented wrist mechanism [77].

1.3 State-of-the-Art

To highlight the significance of the project study, this section presents a brief review on the applied and developed methodologies for the research and development of the parallel manipulators, with particular emphasis on the topics directly related to the presented work in this thesis.

1.3.1 Error Analysis of Parallel Manipulators with Joint Clearances

There are many sources of pose (position and orientation, see Figure 1.9) error, such as manufacturing tolerance, joint clearances and link flexibility. Among these sources of errors, joint clearance requires a special consideration due to its random nature and low repeatability.

A substantial body of research has been devoted to the study of joint clearance and its effect on the position accuracy of mechanisms. From the geometrical/kinematic consideration, the clearance problem of the mechanisms is usually dealt with through two approaches: (1) to predict the most probable final position/orientation of the end-effector; (2) to evaluate the maximum pose errors. For the former problem, the probabilistic technique is widely used to determine the pose error of clearance-affected joints and the manipulator end-effector. Most of these analysis models are on the basis of the statistical
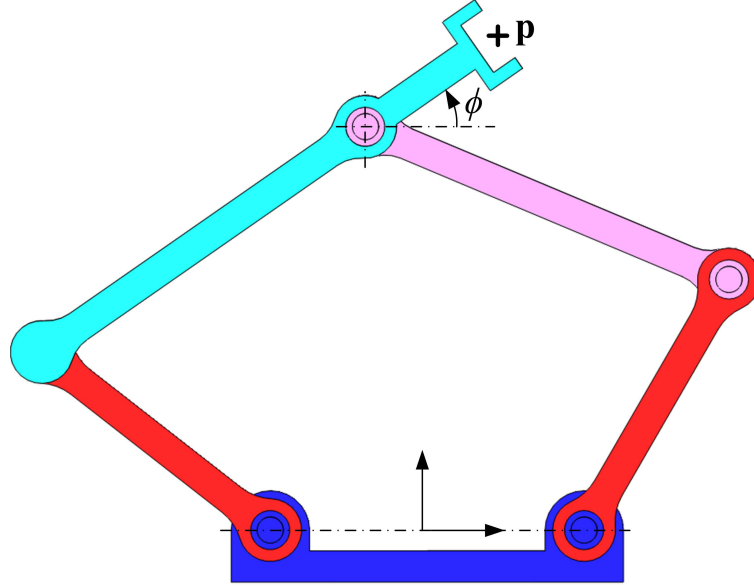
Figure 1.9: Position and orientation of the manipulator end-effector.

method [78–85], in which the mean, variance and probability are used to characterize the performance variation of the mechanism.

Due to the fact that the robot Jacobian relates velocities to approximate the clearances and tolerances of mechanisms, the first-order derivatives of the loop closure equation can be used in the clearance problem, which is called the Jacobian method. Hartenberg and Denavit [86] utilized the derivatives of a four-bar mechanism to get a first order approximation to the output error. Fogarasy and Smith [87] utilized the first-order derivatives of the closure equations combined with statistical analysis to predict the error of spatial manipulators.

The error analysis of parallel manipulators, focused on the influence of joint clearances, has been reported in a number of publications. Most of the works adopt an efficient approach, i.e., to predict the maximum errors. On the evaluation of the influence of joint clearances to the mechanism pose errors, one basic problem lies in the modeling of clearance in kinematic pairs, mainly the lower pairs, such as the prismatic (P) and revolute (R) joints as shown in Figure 1.10. This has been well documented by Venanzi and Castelli [73, 88, 89].

To predict precisely the end-effector's displacement error for the planar 3-RRR[1], the Gough-Stewart and the Hexa manipulators with joint clearance, Voglewede and Up-hoff [72] assumed all the passive joints to be equivalent revolute/spherical ones to ease

---

[1]Kinematic joints used in PMs include: revolute (R), prismatic (P), cylindrical (C), spherical (S), universal (U). Actuated joints are underlined.
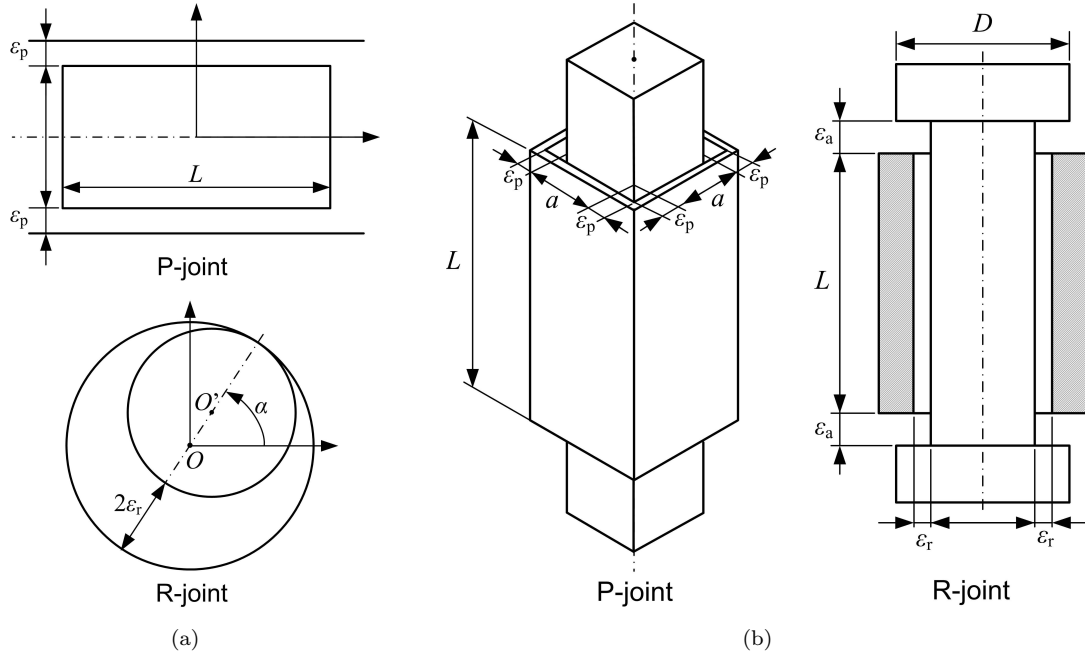
Figure 1.10: Prismatic and revolute joints with clearances: (a) planar mechanisms, (b) spatial mechanisms. The subscripted ϵ stands for the clearance magnitude, which makes one element of the kinematic pair floating with respect to the other.

the clearance problem. Whereas, the computation expense of their precise method becomes infeasible for general spatial mechanisms.

Bamberger et al. [90] proposed an analytical approach to find the minimal value of joint clearance to avoid the worst case of uncertain direct kinematic solutions due to joint clearances for the 3-DOF micro planar parallel manipulators, in which the direct kinematics are solved by a six DOF polynomial equation to found the clearance space.

Meng et al. [91] proposed an error prediction model as a standard convex optimization problem to predict the maximal pose errors within a prescribed workspace, of which the constraints are formed through a set of inequalities on the basis of the joint clearance model [73]. It is found that part of the joint displacement errors for the overconstrained parallel mechanisms depends on the remaining ones, which is different from the non-overconstrained PMs whose joint displacement errors are subject to the joint geometry and magnitudes of the clearance.

Binaud et al. [92] developed a general error prediction model applicable for both serial and parallel manipulators by means of differential screw theory. In their approach, two nonconvex quadratically constrained quadratic programs, one for finding the maximum position error and the other for orientation error subject to given joint clearances, were formulated. Later on, this model was used to analyze the kinematic sensitivity of a

3-PPR planar parallel manipulator to joint clearances and to map the error contours over its constant-orientation workspaces [93].

Chaker et al. [94] investigated the pose error of the platform affected by the clearances and manufacturing errors for a 3-RCC spherical parallel manipulators by means of screw theory, in which these error sources are assumed to be infinitesimal displacements. In this approach, these errors were calculated in many combinations of different orientations and values of manufacturing errors and clearances and the results showed the pose errors and joint clearances are configuration dependent.

Besides the above mentioned kinematic clearance problem, i.e., free movement, two other types of motion between joint parts exist: impact and continuous contact. Lim et al. [95] analyzed the dynamic error of a parallel mechanism by considering the elasticity of links and they evaluated the effects of deformations and clearances separately. Aginaga et al. [96] illustrated a screw theory based deterministic method with a planar five-bar mechanism, in which the influences of the joint clearances and link deformation to the pose errors are approximated by making use of the velocity equation.

Due to the random nature of joint clearance, a common approach to eliminate these sources of errors is to preload the joint. For instance, Wei and Simaan [97] proposed an optimization algorithm from static force ellipsoids to determine the preload force on the joints based on Karush-Kuhn-Tucker (KKT) condition in order to design planar parallel robots with prescribed backlash-free workspace. Another approach to improve the manipulator accuracy is by adding redundant actuation [98].

From the foregoing literatures, it is known that the error analysis of parallel manipulators with joint clearances has been extensively studied, however, the validations for the established error models are lacked. Due to the uncertainty and low repeatability of the pose errors caused by the joint clearances, in order to ease this problem, the maximum errors of a 3-PPR planar parallel manipulator are evaluated to validate the established error model. In addition, without losing generality, each kinematic leg of such a manipulator includes both prismatic and revolute joints.

1.3.2 Stiffness Analysis of Parallel Manipulators

The stiffness of a parallel manipulator is a measure of the ability of its end-effector to resist deformation due to an external wrench (forces and moments). For the PMs, a matrix called stiffness matrix maps the translational/rotational displacement variations to the external wrench in Cartesian space, which can characterize the stiffness of the

manipulator at a given workspace point. The stiffness matrix of a mechanism is generally defined as the transformation which relates the generalized wrench applied to the end-effector and the resulted linear and angular displacements [99]. The conventional mapping of the stiffness between the Cartesian and joint space is formulated as,

$$\mathbf{K}_C = \mathbf{J}^T \mathbf{K}_J \mathbf{J} \tag{1.1}$$

where $\mathbf{K}_C$ is the Cartesian stiffness matrix, $\mathbf{K}_J$ is the stiffness matrix in joint space and $\mathbf{J}$ is the Jacobian matrix. This formulation was first derived by Salisbury [100] and has been accepted in many publications.

As frequently documented, the stiffness matrix of a parallel mechanism usually depends on its configuration and is related to the stiffness of active joints and linkages, whereas, a full analysis is difficult. Among the methods of stiffness modeling, the Virtual Joint Method (VJM), which is often called the lumped modeling [100–109], has been widely used to establish the mechanism stiffness model as it provides acceptable accuracy in short computational time. This approach is based on the expansion of the traditional rigid model by adding virtual joints (localized springs) to describe compliance of the manipulator components (links, joints and actuators) [109]. The Cartesian stiffness matrix relies on the calculation of both the parallel mechanism's Jacobian matrix and the stiffness matrix in joint space.

With the VJM based stiffness matrix, El-Khasawneh and Ferreira [102] addressed on the minimum and maximum stiffnesses and their directions for a mechanism at a given posture, namely, the eigenvalue problem. Furthermore, they used the Finite Element Analysis (FEA) model to validate their model. In general, using FEA approach to validate the analytical model has been a necessary procedure in the stiffness analysis of mechanisms especially for the structure-complex mechanisms. However, the identification of eigenvalues and eigenvectors from the stiffness matrix does not make sense for an inhomogeneous matrix due to the different physical meanings of dimensionally inconsistent entries. Angeles [110] investigated the eigenvalue problem of the 6×6 Cartesian stiffness matrix in its generalized form based on the screw theory, where the eigenforce is proposed to indicate the direction that the manipulator is stiffer or weak. Kövecses and Angeles [107] discussed the other properties of the Cartesian stiffness matrix, i.e., be necessarily symmetric, be positive- or semi- definite. This work focuses on stiffness modeling and analysis while the nature (physical property) of the Cartesian stiffness matrix will not be discussed.

Gosselin [101] applied the model of Equation (1.1) to parallel manipulator, in which only the actuation compliance described by one-dimensional linear springs were considered (the links were assumed to be rigid, and the passive joints to be perfect). In

Gosselin's works, the diagonal elements of the stiffness matrix were used as the stiffness to formulate the stiffness distribution mappings. These elements represent the pure stiffness in each direction clearly and directly. Later, Chen and Kao [103] verified that this equation is only valid when robotic manipulators are at their unloaded equilibrium configuration. They proposed the Conservative Congruence Transformation (CCT) to analyze the effect of robot geometry change due to external force, i.e., the Hessian matrix. By considering the changes in the Jacobian, Alici and Shirinzadeh [105] validated the conservative stiffness formulation under external loading via the implementation of experiments to a serial robotic manipulator. Quennouelle and Gosselin [108] also investigated the conservative property of the stiffness matrix with the consideration of the external loads and the differentiation of the kinematic Jacobian matrix, the novelty of which is that the influence of the passive joints is firstly taken into account.

In the previous reports [103, 105, 108], the stiffness models of the manipulators are formulated under external payloads, which is also called "large displacement" case. In some applications of the stiffness matrix, such as design optimization, stiffness matrix in the form of Equation (1.1) is needed. In this approach, the derivation of the stiffness is on the basis of the assumption that the manipulator is at an unloaded equilibrium configuration.

Generally, the link flexibilities have been taken into account during the development of the VJM approach. Gosselin and Zhang [111, 112] replaced the flexible links by rigid beams mounted on revolute joints plus torsional spring located at the existing joints, see Figure 1.11(a). This flexible-link lumped parameter model was also used by Majou et al. [106] to characterize the stiffness of the Orthoglide robots. Particularly, different simplified VJMs were applied to the CaPaMan robot [104], Gough-Stewart platform based micro-positioning mechanisms [113], Tripod-based PKM prototype [114], a class of manipulators with US/UPS legs [115] and among others. The differences among these existing variations of the VJM approaches focus on modeling assumptions and numerical techniques.

Combing the advantages of the previously mentioned approaches, Pashkevich et al. [109] proposed a stiffness modeling method named as virtual spring approach, which has been widely adopted for the requirement of high computation accuracy in the analysis and optimum design. Here, this approach will be adopted to model and analyze the stiffness of the spherical parallel manipulator. In this approach, the link flexibility is replaced by localizing a n-dofs virtual spring associated with the mobility freedoms describing both the translational and rotational deflections and the coupling between them, where the spring compliance is evaluated based on the concept of FEA approach to ensure higher accuracy. This kinetostatic model considers the influence of the passive
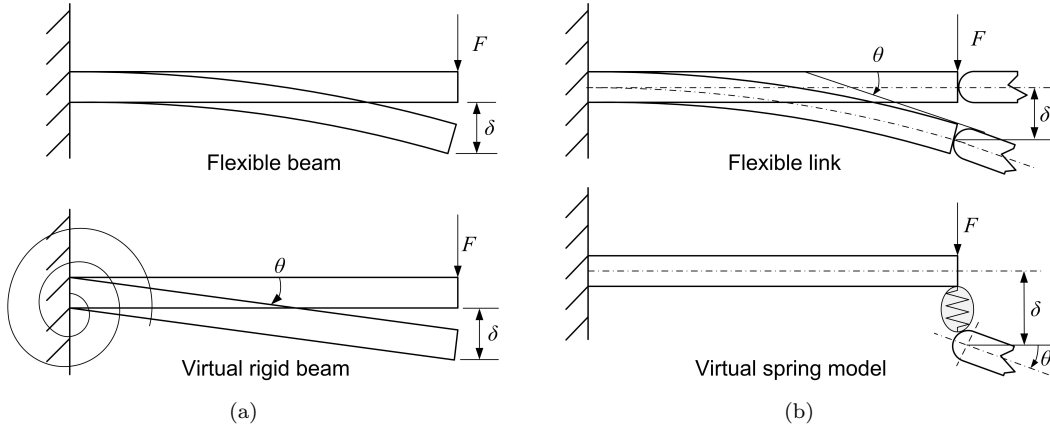
Figure 1.11: Two flexible-link lumped-parameter models: (a) Zhang's model [106, 111, 116], (b) virtual spring model [109].

joints and it can predict the stiffness for the manipulators at non-singular and singular configurations. This approach gives almost the same accuracy as FEA but with less computational consumption. The difference between the widely used flexible-link model by Zhang [106, 111, 116] and the virtual spring model is illustrated with the planar case displayed in Figure 3.6. Both of these two models provide acceptable accuracy, while the virtual spring approach performs more accurate parameter transformation from the current link to the following one, which ensures high computation accuracy.

Due to these advantages, the virtual spring approach is adopted in this work for both stiffness characterization and design optimization. The Jacobian of such a VJM approach is derived based on the (differential) homogeneous transformation matrix, which can be applied to variations of parallel mechanisms. For some special cases like the spherical parallel manipulators, since their links are curved beams and inverse geometry problem is complicated that bring computational burden, simple and fast approach is needed to solve this kinematic problem. An approach could be through the screw theory [117], which is a useful tool in the synthesis of parallel mechanisms [118]. In this thesis, a screw theory based virtual spring approach will be proposed for stiffness modeling.

1.3.3 Design Optimization of Parallel Manipulators

Parallel manipulators possess a number of advantages over the traditional serial manipulators. Nevertheless, their design is a challengeable task due to their highly nonlinear and nonintuitive behaviors. An efficient and systematic way to deal with this problem is to use optimization technique in the design process. Depending on the particular application, certain performance criteria may be of more importance than others. In

other words, the mutual dependency among all kinds of performances is related to manipulator applications. In the optimization procedure, some of the performance criteria will be specified as objectives, while some others as constraints.

Table 1.1 lists major evaluation criteria that were used in design optimization. These evaluation criteria can be roughly classified into two groups: one relates to the kinematic performance while the other relates to the kinetostatic/dynamic performance. In general, the design process simultaneously deals with these two aspects [119], both of which include a number of performance measures that essentially vary throughout the workspace but remain within the prescribed bounds. Kinematic aspects are relatively less complex compared to the kinetostatic/dynamic aspects, as the latter work with a detailed description of the mechanism structure and their evaluation is usually time consuming. In the kinematic considerations, the quality of the workspace that reflects the shape, size and presence of singularities is of primary importance in the PMs design. Another utmost important concern is the dexterity, which is usually evaluated through the conditioning number of the kinematic Jacobian matrix. For the kinetostatic aspect, stiffness is particularly important in the context of PMs [120] among the properties of mechanical systems. Indeed, one of the major design issues in kinetostatic design is the computation of the stiffness matrix [121]. Moreover, minimizing the mass in motion (linear and angular momentum) of the mechanism is an important task toward the requirement of light weight since the mass strongly influences the dynamic behaviors.

With the multiple evaluation criteria for optimum design, an efficient approach is to solve a multiobjective optimization problem, which can take all or most of the evaluation criteria into account. As the objective functions are usually conflicting, no single solution can be achieved in this process. The solutions of such a problem are non-dominated solutions, also called Pareto-optimal solutions or Pareto-front (frontier). To solve this problem, non-gradient optimization methods are widely used as they are robust in achieving the global optimality.

Of the existing optimization methods, the Genetic Algorithm (GA) based multiobjective optimization methods are widely used. A non-dominated sorting-based MOEA (Multiobjective Evolutionary Algorithms), called NSGA-II (Non-dominated Sorting Genetic Algorithm II) [150] is a computationally fast and elitist algorithm, which is adopted in this work thanks to its advantages, i.e., to guarantee relatively better spread of solutions and better convergence in the obtained non-dominated front than some other genetic algorithms.

Table 1.1: Overview of the evaluation criteria for PMs optimum design.

Geometry	• Architecture geometry, shape; mechanical collision [122–124] • Compactness: overall size; footprint ratio, i.e., ratio between workspace and mechanism size
Geometric kinematics	• Workspace shape and size: Regular workspace; (constant-) orientation volume; minimal guaranteed prescribed workspace; maximal workspace [119, 125–131] • Motion range for the active and passive joints [132] • Error: dimension error; maximal positioning errors of the end-effector [133] • Singularities within the workspace: serial and parallel singularities, self-motions [134] • Dexterity: conditioning of the kinematic Jacobian; isotropy of the performances, i.e., global conditioning index (GCI) [120, 127, 135–140]
Differential kinematics	• Maximal velocities of the actuators and end-effector • Minimal guaranteed velocity of the moving platform over a given workspace • Manipulability, velocity transmission [141]
Statics	• Wrench capability: maximal forces or torques on the links and platform [142] • Stiffness/compliance: maximal stiffness; minimal elastic deformation; stiffness range and response of the stiffness change [143–145]
Dynamics	• Mass property: usually used as an objective for the light-weight requirement [119, 146] • Maximal accelerations of the actuators and platform • Minimal guaranteed acceleration for the end-effector over a given workspace subject to limited joint acceleration and velocity • Minimal energy consumption of the actuators/system [147] • Maximal output torque; minimal input torque [148, 149]

1.4   Objectives and Scope of the Work

The objective of this thesis is to provide a systematic analysis for characterizing the properties of parallel mechanisms and PMs design, of which the main tasks are:

1. to develop an error prediction model including the sources of dimensional errors, actuation errors/backlash, joint clearances;

2. to develop a kinetostatic model for spherical parallel manipulators that can be generalized to other types of parallel manipulators;

3. to develop a method for optimum design of spherical parallel manipulators and to formulate the design guideline that can be applied to other types of parallel manipulators.

To achieve these goals, this project will deal with the following research problems:

1. *Geometric and kinematic modeling of planar and spherical parallel manipulators.* Revisit the basic kinematic problem of the manipulators and find all the inverse kinematic solutions and assembly modes. Find the workspace and singular configurations. Use Solidworks$^{\text{TM}}$ to establish their CAD models. All possible configurations will be investigated.

2. *Error modeling and experimental validation of the planar parallel manipulator.* Develop the first-order derivatives of the loop closure equation and formulate the error model to predict the maximum pose errors. Design an experiment and measure the representative workspace points to validate the error model.

3. *Stiffness formulation of beam element as employed in the specific SPM.* Found the analytical stiffness matrix of the curved beam with Euler-Bernoulli model and validate it by means of Ansys$^{\text{TM}}$.

4. *Dynamic modeling of spherical parallel manipulator.* With Lagrangian dynamics equation, develop the dynamic model of spherical parallel manipulator and use Matlab$^{\text{TM}}$/simulink to realize the simulation. Compare the analytical model with independent simulation by Adams$^{\text{TM}}$.

5. *Design optimization of spherical parallel manipulator.* Using the kinetostatic and dynamic models developed in the previous steps, optimize the kinematic and dynamic performances of the spherical parallel manipulator with the implementation of *genetic algorithm* in Matlab$^{\text{TM}}$.

The expectation of this thesis therefore become obvious: develop simple and valid error model, build the kinetostatic model, optimize the geometric architecture of spherical parallel manipulator. The results of the work can provide a framework for further study of parallel mechanisms such as error compensation and control programming.

1.5 Outline of the Thesis

Chapters 2 and 3 introduce the geometric architecture of the planar and spherical parallel manipulators. The kinematic and dynamic modeling are described in detail for the further study.

Chapters 4-7 are the selected and representative publications through which the thesis subjects are treated specifically.

Chapter 4 presents the error modeling for a 3-PPR planar parallel manipulator and the experimental validation for this robot with joint clearances. The maximal pose errors subject to the clearances are predicted from an optimization algorithm and are mapped within the constant-orientation workspace. A vision system is built to measure the maximal pose errors at its uniformly distributed workspace points to validate the error model.

Chapter 5 details the lumped-flexibility model for joints and the curved links of the spherical parallel manipulator and the stiffness modeling for this class of mechanisms. The developed model is illustrated with an unlimited rolling 3-DOF spherical parallel mechanisms. Furthermore, the stiffness model is validated with Ansys$^{\text{TM}}$/workbench.

Chapters 6 and 7 describe the design optimization of a spherical parallel manipulator. Two optimization problems considering kinematic, elastostatic and dynamic performances are formulated for different performances improvement. The proposed approaches are numerically conducted with a genetic algorithm embedded in Matlab$^{\text{TM}}$. The Pareto-fronts for the proposed optimization problems are obtained as well as the scatter matrices for both objective functions and variables.

Chapter 8 concludes this thesis, with a summary of observations from the project study and contributions. The future work is also suggested.

Kinematic Modeling of Planar Parallel Manipulator

This chapter revisits the kinematic problem, including the position, workspace and singularity analysis, to characterize the planar parallel manipulator studied.

The planar parallel manipulators (PPMs) can present with the sequence of the three joints in each kinematic chain: RRR, RPR, RRP, RPP, PRR, PPR, PRP, PPP, see Figure 2.1. Their kinematic problem has been studied in detail [151, 152]. Most of these PPMs adopt a symmetric topology, which implies that all three legs are equally spaced. The design with a symmetric topology can achieve kinematic isotropy. However, a symmetrical design may not be optimal in terms of some kinematic performance, such as workspace; it will be demonstrated that a nonsymmetric structure can admit a large workspace compared to the symmetric counterparts [153].
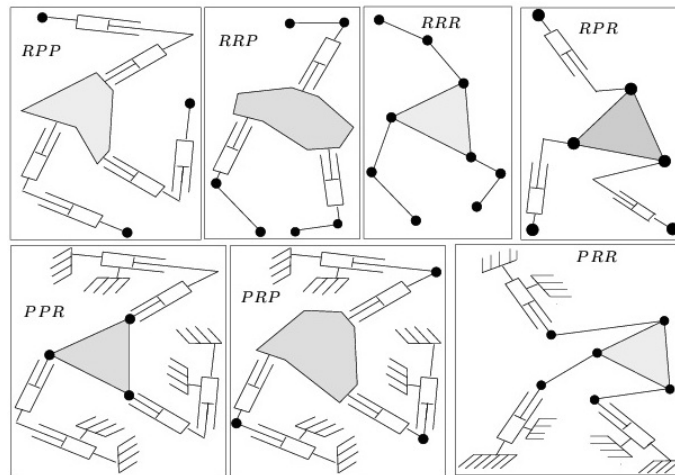
Figure 2.1: The 3-DOF PPMs with identical kinematic chains, taken from [3].

(a)   (b)
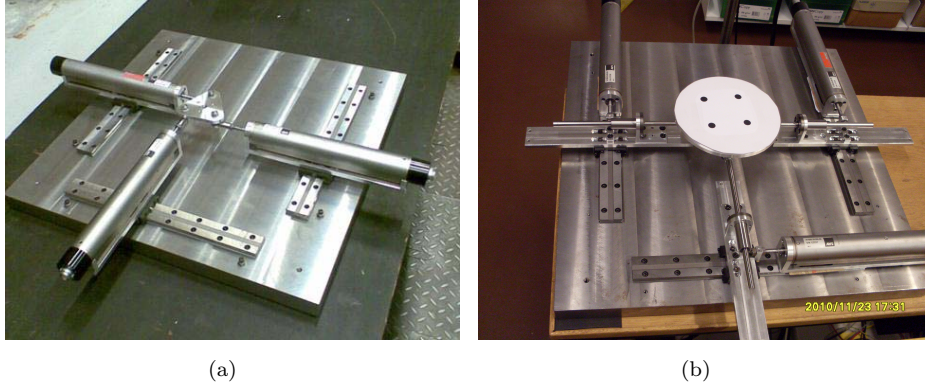
Figure 2.2: 3-DOF PPM prototype: (a) P$\underline{P}$R [153], (b) $\underline{P}$PR [154].
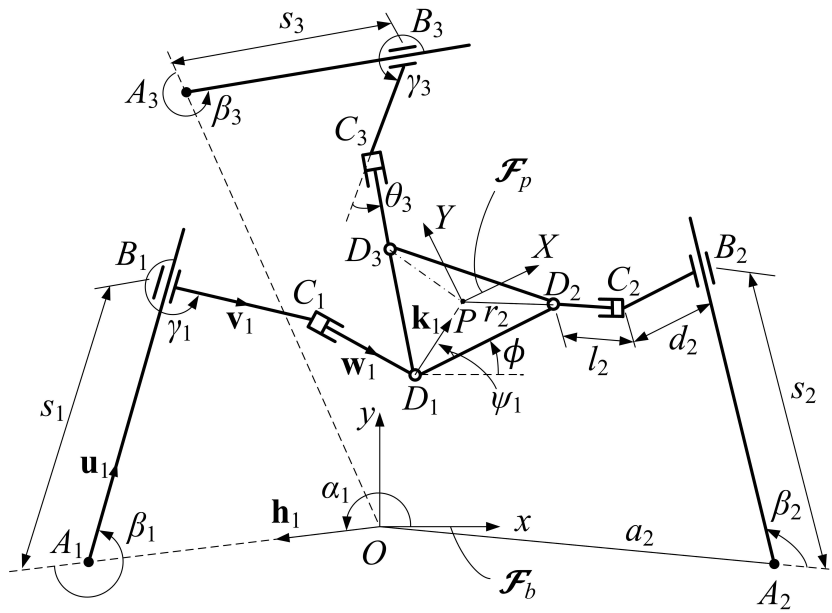
Figure 2.3: Parameterization of the 3-PPR PPM.

2.1 Manipulator Under Study

Figure 2.2 presents the prototype of the 3-PPR PPM with different mobile platforms (MPs), i.e., disk- and triangle-shaped. In each leg, one prismatic joint can be chosen as active joint while the other one is a passive joint.

The parameterization of the manipulator is illustrated in Figure 2.3. The x-axis of the reference coordinate system $\mathcal{F}_b$ is parallel to the segment A_1A_2, where A_i, $i = 1, 2, 3$, are fixed points on the base. The origin P of the coordinate system $\mathcal{F}_p$ is located at the geometric center of the mobile platform. The X-axis is parallel to the segment D_1D_2, where D_i are the centers of the revolute joints. The location and orientation of the MP are denoted by $\mathbf{p}$ and ϕ, where $\mathbf{p} = [x, y]$ is the position vector of point P in $\mathcal{F}_b$.

2.2 Kinematics of the PPM

This section deals with the kinematic analysis of the 3-PPR PPM, including the position, singularity and workspace. This analysis can also be applied to the other PPMs.

2.2.1 Displacement Analysis

For each kinematic chain O-A_i-B_i-C_i-D_i-P shown in Figure 2.3, the position vector of point P can be expressed in $\mathcal{F}_b$ as follows,

$$\mathbf{p} = a_i\mathbf{h}_i + s_i\mathbf{u}_i + d_i\mathbf{v}_i + l_i\mathbf{w}_i + r_i\mathbf{k}_i, \ i = 1, \ 2, \ 3 \tag{2.1}$$

with

$$\mathbf{h}_i = \begin{bmatrix} \cos\alpha_i \\ \sin\alpha_i \end{bmatrix}, \ \mathbf{u}_i = \begin{bmatrix} \cos\beta_i' \\ \sin\beta_i' \end{bmatrix}, \ \mathbf{v}_i = \begin{bmatrix} \cos\gamma_i' \\ \sin\gamma_i' \end{bmatrix}, \ \mathbf{w}_i = \begin{bmatrix} \cos\theta_i' \\ \sin\theta_i' \end{bmatrix}, \ \mathbf{k}_i = \begin{bmatrix} \cos(\phi + \psi_i) \\ \sin(\phi + \psi_i) \end{bmatrix} \tag{2.2}$$

where

$$\beta_i' = \alpha_i + \beta_i, \ \gamma_i' = \alpha_i + \beta_i + \gamma_i, \ \theta_i' = \alpha_i + \beta_i + \gamma_i + \theta_i \tag{2.3}$$

The inverse kinematics of the manipulator can be derived from Eqn. (2.1),

$$s_i = (\mathbf{w}_i^T\mathbf{E}\mathbf{u}_i)^{-1}\mathbf{w}_i^T\mathbf{E}\,(\mathbf{p} - a_i\mathbf{h}_i - d_i\mathbf{v}_i - r_i\mathbf{k}_i) \tag{2.4a}$$

$$l_i = (\mathbf{u}_i^T\mathbf{E}\mathbf{w}_i)^{-1}\mathbf{u}_i^T\mathbf{E}\,(\mathbf{p} - a_i\mathbf{h}_i - d_i\mathbf{v}_i - r_i\mathbf{k}_i) \tag{2.4b}$$

where $\mathbf{E}$ is the right angle rotation matrix defined as

$$\mathbf{E} = \begin{bmatrix} 0 & -1 \\ 1 & 0 \end{bmatrix} \tag{2.5}$$

Equation (2.1) establishes a system of six equations. The forward displacements can be solved by virtue of analytical method.

2.2.2 Kinematic Jacobian Matrix

Differentiating Eqn. (2.1) with respect to time yields

$$\dot{\mathbf{p}} = \dot{s}_i\mathbf{u}_i + \dot{l}_i\mathbf{w}_i + \dot{\phi}r_i\mathbf{E}\mathbf{k}_i, \ i = 1, \ 2, \ 3 \tag{2.6}$$

After elimination of the idle term $\dot{l}_i$ and then by multiplying both sides of Eqn. (2.6) with $\mathbf{w}_i^T\mathbf{E}^T$ and the subsequent matrix manipulation, the velocity expression of the

manipulator is deduced as below:

$$\mathbf{A} \begin{bmatrix} \dot{\mathbf{p}} \\ \dot{\phi} \end{bmatrix} = \mathbf{B}\dot{\mathbf{s}} \tag{2.7}$$

with

$$\mathbf{A} = \begin{bmatrix} \mathbf{w}_1^T \mathbf{E}^T & -r_1 \mathbf{w}_1^T \mathbf{k}_1 \\ \mathbf{w}_2^T \mathbf{E}^T & -r_2 \mathbf{w}_2^T \mathbf{k}_2 \\ \mathbf{w}_3^T \mathbf{E}^T & -r_3 \mathbf{w}_3^T \mathbf{k}_3 \end{bmatrix} \tag{2.8a}$$

$$\mathbf{B} = \mathrm{diag} \begin{bmatrix} \mathbf{w}_1^T \mathbf{E}^T \mathbf{u}_1 & \mathbf{w}_2^T \mathbf{E}^T \mathbf{u}_2 & \mathbf{w}_3^T \mathbf{E}^T \mathbf{u}_3 \end{bmatrix} \tag{2.8b}$$

$$\dot{\mathbf{s}} = \begin{bmatrix} \dot{s}_1 & \dot{s}_2 & \dot{s}_3 \end{bmatrix}^T \tag{2.8c}$$

where $\mathbf{A}$ and $\mathbf{B}$ are named as the direct and inverse kinematic Jacobian matrices of the manipulator, respectively. If $\mathbf{A}$ is nonsingular, the kinematic Jacobian matrix $\mathbf{J}$ of the manipulator takes the form:

$$\mathbf{J} = \mathbf{A}^{-1}\mathbf{B} \tag{2.9}$$

2.2.3 Singularity Analysis

It is known that the parallel mechanisms can have three types of singularity, which can be identified by virtue of the Jacobian matrices $\mathbf{A}$ and $\mathbf{B}$ derived in Sec. 2.2.2: (1) Type I (serial) singularity when $det(\mathbf{B}) = 0$, usually occurs at the workspace boundary; (2) Type II (parallel) singularity when $det(\mathbf{A}) = 0$; (3) Type III singularity when both $det(\mathbf{A}) = 0$ and $det(\mathbf{B}) = 0$. These types of singularities are graphically illustrated with a five-bar (5R) mechanism as shown in Figure 2.4.

Accordingly, the studied manipulator in Figure 2.2(b) reaches a parallel singularity, namely, matrix $\mathbf{A}$ is singular when $\phi = \pm\pi/2$, see Figure 2.5. While matrix $\mathbf{B}$ is never singular, which means that the manipulator is free of serial singularity.
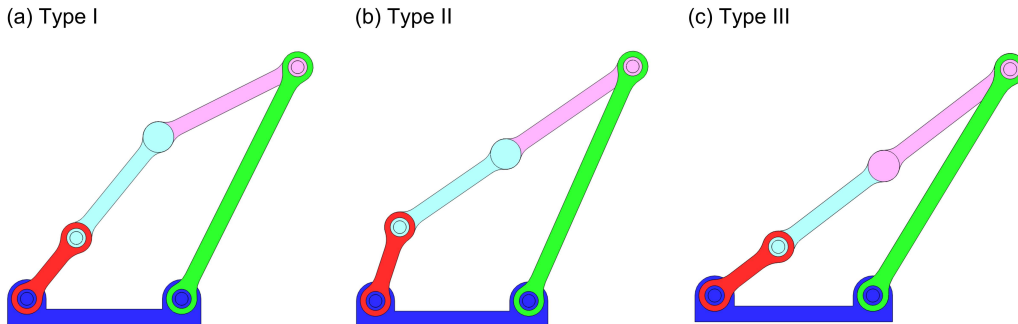
Figure 2.4: Singularities of a five-bar mechanism.
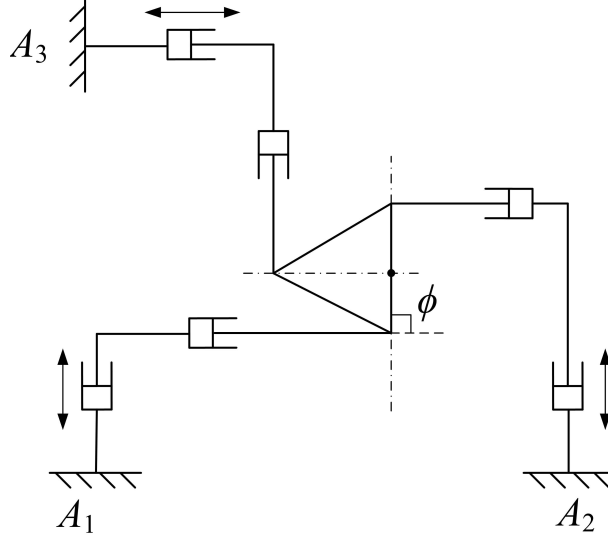
Figure 2.5: Parallel singularity of the 3-PPR PPM when $\phi = \pi/2$.

2.2.4 Constant-Orientation Workspace

The reachable area of the mobile platform will be investigated by the constant-orientation workspace. To obtain the reachable area geometrically, the inverse kinematic model subject to prescribed joint motion ranges are used to find the boundaries of the end-effector displacements, which is usually called the searching method. Eqns. (2.4a) and (2.4b) establish a system of 12 inequalities, namely,

$$s_{imin} \leq s_i \leq s_{imax}, \, l_{imin} \leq l_i \leq l_{imax}, \, i = 1, 2, 3 \tag{2.10}$$

where the bounds are found as

$$s_{imin} = 52 \, \text{mm}, \, s_{imax} = 102 \, \text{mm}; \, l_{imin} = 20 \, \text{mm}, \, l_{imax} = 165 \, \text{mm}$$

With the parameters shown in Table 2.1 and $r_i = r = 30 \, \text{mm}$, $a_i = 192.34 \, \text{mm}$, $i = 1, 2, 3$, three constant-orientation Cartesian workspaces are presented in Figure 2.6.

Figure 2.7 shows the comparison of the constant-orientation workspace size between the symmetrical and unsymmetrical PPMs, which reveals that the unsymmetrical structure can admit a larger workspace.

Table 2.1: The Design Parameters of the 3-<u>P</u>PR PPM

i	α_i[rad]	β_i'[rad]	γ_i', θ_i'[rad]	ψ_i[rad]	d_i[mm]
1	-2.781	$\pi/2$	0	$\pi/6$	114
2	-0.360	$\pi/2$	π	$5\pi/6$	27
3	1.751	0	$-\pi/2$	$3\pi/2$	42

Figure 2.6: Constant-orientation workspaces for the manipulator under study.

$\phi = 0°$ $\phi = 30°$

(a)

$\phi = 0°$ $\phi = 30°$

(b)
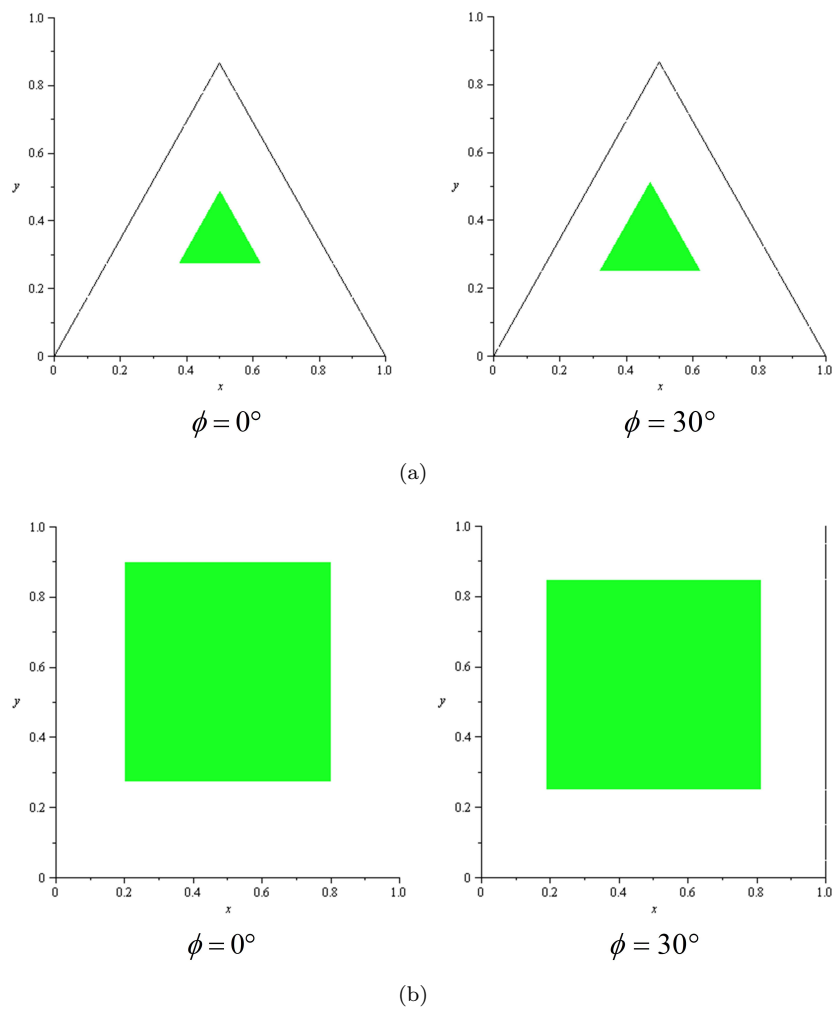
Figure 2.7: Comparison of the constant-orientation workspace size: (a) symmetric PPM, (b) unsymmetrical PPM, taken from [153].

<div align="right">**3**</div>

Kinematics and Dynamics of Spherical Parallel Manipulator

This chapter describes the geometric architecture of the spherical parallel manipulator and its kinematic and dynamic modeling. A numerical example is carried out to illustrate the motion of the spherical manipulator, in which the dynamics is also investigated.

3.1 Background Theory

This section gives a brief review of the background theory used in the kinematic and dynamic modeling of the spherical parallel manipulator. The screw theory will focus on the kinematic aspect and the dynamic model is derived on the basis of the Lagrangian multipliers approach.

3.1.1 Azimuth-Tilt-Torsion Angles

Apart from the orientation representations such as Euler angles, the *Tilt-and-Torsion (T&T) angles* take full advantage of a mechanism's symmetry [155]. This description can better characterize the orientation workspace of a mechanism, which will be adopted in this work.

The T&T angles are defined in two stages with three angles: ϕ, θ, σ. In the first stage, illustrated in Figure 3.1(a), the body frame is tilted about a horizontal axis, a, at an angle θ, referred to as the *tilt*. The direction of axis a is defined by an angle ϕ, called the *azimuth*, which is the angle between the projection of the body z'-axis onto the fixed xy
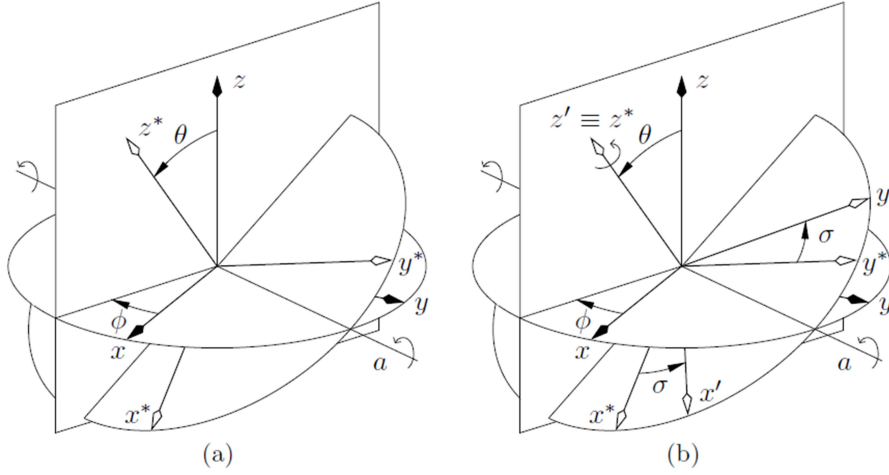
Figure 3.1: The successive rotations of the T&T angles: (a) tilt, (b) torsion [155].

plane and the fixed x-axis. In the second stage, illustrated in Figure 3.1(b), the body frame is rotated about the body z'-axis at an angle σ, called the *torsion*.

The derivation process is well documented by Bonev [156] and the resulting rotation matrix $\mathbf{Q}$ is kinematically equivalent to the Euler convention *Z-Y-Z*, namely,

$$\mathbf{Q} = \mathbf{R}_z(\phi)\mathbf{R}_y(\theta)\mathbf{R}_z(-\phi)\mathbf{R}_z(\sigma) = \mathbf{R}_z(\phi)\mathbf{R}_y(\theta)\mathbf{R}_z(\sigma - \phi) \tag{3.1}$$

thus,

$$\mathbf{Q} = \begin{bmatrix} c\phi c\theta c(\phi - \sigma) + s\phi s(\phi - \sigma) & c\phi c\theta s(\phi - \sigma) - s\phi c(\phi - \sigma) & c\phi s\theta \\ s\phi c\theta c(\phi - \sigma) - c\phi s(\phi - \sigma) & s\phi c\theta s(\phi - \sigma) + c\phi c(\phi - \sigma) & s\phi s\theta \\ -s\theta c(\phi - \sigma) & -s\theta s(\phi - \sigma) & c\theta \end{bmatrix} \tag{3.2}$$

where $\phi \in (-\pi, \pi]$, $\theta \in [0, \pi)$, $\sigma \in (-\pi, \pi]$, and s, c stand for *sine* and *cosine* functions, respectively.

3.1.2 Screw Theory

Screw theory underlies the foundation of both instantaneous kinematics and statics. A spatial displacement of a rigid body can be defined by a rotation about a line and a translation along the same line, called a *screw displacement*, in which the line is called *screw axis*. The rotation and translation is further coupled by a scalar quantity called a *pitch*. The screw in kinematics therefore called a twist is formed by a pair of three dimensional vectors, namely, angular and linear velocity, written as

$$\mathbf{t} = \begin{bmatrix} \omega\mathbf{e} \\ \mathbf{r} \times \omega\mathbf{e} + v\mathbf{e} \end{bmatrix} \tag{3.3}$$
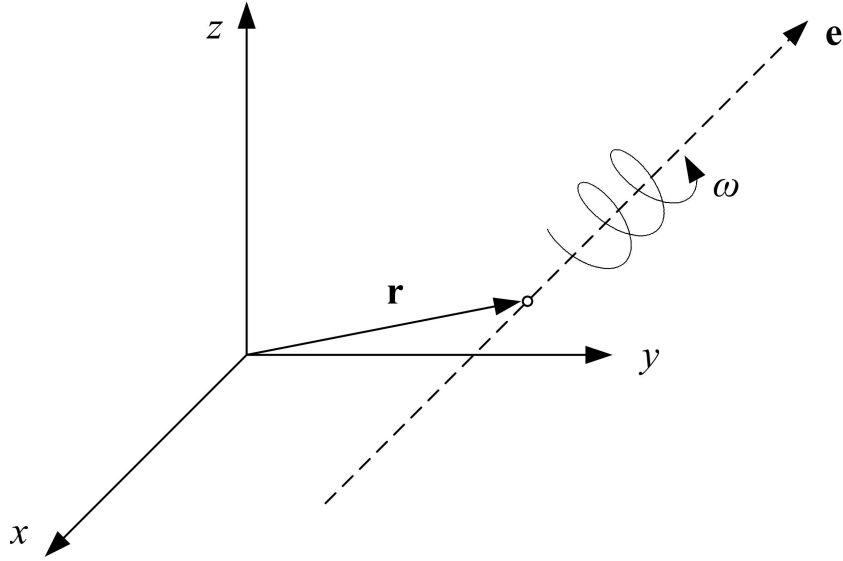
Figure 3.2: A general motion defined by a general twist.

where vectors $\mathbf{e}$ and $\mathbf{r}$ denote the direction of and a point on the screw axis $\mathbf{e}$, respectively, scalars ω and v are the magnitude of angular velocity and linear velocity along the axis, see Figure 3.2. The pitch is defined as the ratio of the linear velocity to angular velocity, i.e., $p = v/\omega$. From Eqn. (3.3), a unit screw is defined as

$$\hat{\$} = \begin{bmatrix} \mathbf{e} \\ \mathbf{r} \times \mathbf{e} + p\mathbf{e} \end{bmatrix} = \begin{bmatrix} s_1 & s_2 & s_3 & s_4 & s_5 & s_6 \end{bmatrix}^T \tag{3.4}$$

On the other hand, this screw is called a *wrench* if it represents a system of forces and couples acting on a rigid body.

For special cases of a pure rotation and a pure translation in space are represented by a zero-pitch and infinite-pitch twist, respectively, expressed as

$$p = 0: \quad \mathbf{t} = \begin{bmatrix} \omega\mathbf{e} \\ \mathbf{r} \times \omega\mathbf{e} \end{bmatrix}, \hat{\$} = \begin{bmatrix} \mathbf{e} \\ \mathbf{r} \times \mathbf{e} \end{bmatrix} \tag{3.5}$$

$$p = \infty: \quad \mathbf{t} = \begin{bmatrix} \mathbf{0} \\ v\mathbf{e} \end{bmatrix}, \hat{\$} = \begin{bmatrix} \mathbf{0} \\ \mathbf{e} \end{bmatrix} \tag{3.6}$$

Two screws, $\hat{\$}$ and $\hat{\$}_r$, are said to be reciprocal if they satisfy the following condition by applying the orthogonal product ($\circ$) [157]:

$$\hat{\$}_r \circ \hat{\$} = s_{r4}s_1 + s_{r5}s_2 + s_{r6}s_3 + s_{r1}s_4 + s_{r2}s_5 + s_{r3}s_6 \tag{3.7}$$

with

$$\hat{\$}_r = \begin{bmatrix} s_{r1} & s_{r2} & s_{r3} & s_{r4} & s_{r5} & s_{r6} \end{bmatrix}^T \tag{3.8}$$

3.1.3 Equations of Motion–Method of the Lagrange Multipliers

The SPMs are mostly used in applications involving high-speed motion, therefore, the dynamics has a very important effect on the required actuator torques. With the consideration of the kinematics and dynamics, such a SPM is a multibody dynamic system. In order to determine the motion of the entire system, it is necessary to establish the dynamic equilibrium condition that leads to a system of second order differential equations generally called the *equations of motion* [158]. Due to the highly nonlinear behaviors and the complicated kinematic problem, the *equations of motion* for the SPM can be formulated in dependent coordinates, where the method of the Lagrange Multipliers can achieve this aim.

In the method of the Lagrange Multipliers, let the vector $\mathbf{q}$ represents a set of n unknown dependent coordinates, m is the total number of independent kinematically constraint equations, the constraint conditions are written in the following general form:

$$\boldsymbol{\Phi}(\mathbf{q},\, t) = \mathbf{0} \tag{3.9}$$

The Lagrange's equations of a system is expressed as:

$$\frac{\mathrm{d}}{\mathrm{d}t}\left(\frac{\partial L}{\partial \dot{\mathbf{q}}}\right) - \frac{\partial L}{\partial \mathbf{q}} + \boldsymbol{\Phi}_{\mathbf{q}}^{T}\boldsymbol{\lambda} = \mathbf{Q}_{ex} \tag{3.10}$$

where $L = T - V$ is the *Lagrangian* function. $T = T(\mathbf{q},\, \dot{\mathbf{q}})$ is the kinetic energy of the system and $V = V(\mathbf{q})$ is the potential energy. The matrix $\boldsymbol{\Phi}_{\mathbf{q}}$ is the Jacobian matrix of the nonlinear constraint equations 3.9 and the vector $\boldsymbol{\lambda}$ represents the Lagrange multipliers. $\mathbf{Q}_{ex}$ is the vector of generalized external forces acting along the dependent coordinates $\mathbf{q}$ of a constrained mechanical system.

The kinetic energy of a multibody system can be written as follows:

$$T = \frac{1}{2}\dot{\mathbf{q}}^{T}\mathbf{M}(\mathbf{q})\dot{\mathbf{q}} \tag{3.11}$$

where $\mathbf{M}(\mathbf{q}) = \mathbf{M}$ is the mass matrix of the system. The first and second terms in Eqn. (3.10) can be expressed as below:

$$\frac{\mathrm{d}}{\mathrm{d}t}\left(\frac{\partial L}{\partial \dot{\mathbf{q}}}\right) = \mathbf{M}\ddot{\mathbf{q}} + \dot{\mathbf{M}}\dot{\mathbf{q}},\ \frac{\partial L}{\partial \mathbf{q}} = L_{\mathbf{q}} = T_{\mathbf{q}} - V_{\mathbf{q}} \tag{3.12}$$

For the general case in which the kinetic energy depends on $\mathbf{q}$, Eqn. (3.10) becomes

$$\mathbf{M}\ddot{\mathbf{q}} + \boldsymbol{\Phi}_{\mathbf{q}}^{T}\boldsymbol{\lambda} = \mathbf{Q}_{ex} + L_{\mathbf{q}} - \dot{\mathbf{M}}\dot{\mathbf{q}} = \boldsymbol{\tau} \tag{3.13}$$

On the other hand, differentiating the constraint equations (3.9) twice with respect to time yields

$$\boldsymbol{\Phi_q \ddot{q}} = -\dot{\boldsymbol{\Phi}}_t - \dot{\boldsymbol{\Phi}}_q \dot{\boldsymbol{q}} \equiv \mathbf{c} \tag{3.14}$$

By writing Eqns. (3.13) and (3.14) jointly leads to:

$$\begin{bmatrix} \mathbf{M} & \boldsymbol{\Phi}_q^T \\ \boldsymbol{\Phi}_q & \mathbf{0} \end{bmatrix} \begin{bmatrix} \ddot{\mathbf{q}} \\ \boldsymbol{\lambda} \end{bmatrix} = \begin{bmatrix} \boldsymbol{\tau} \\ \mathbf{c} \end{bmatrix} \tag{3.15}$$

The system of equations (3.15) can be used for the simultaneous solution of the dynamic problem of the mechanical system.

3.2 Manipulator Architecture

A general spherical parallel manipulator is shown in Figure 3.3(a) with its parameterized ith leg in Figure 3.3(b), $i = 1, 2, 3$. Each leg is composed of three revolute joints, the axes of which intersect at a common center, namely, center of rotation. The origin O of the reference coordinate system xyz is located at the center of rotation. The unit vectors of joint axes are denoted by $\mathbf{u}_i$, $\mathbf{w}_i$ and $\mathbf{v}_i$, $i = 1, 2, 3$. The arc angles of the three proximal curved links are the same and equal to α_1. Likewise, the arc angles of the three distal curved links are the same and equal to α_2. Geometric angles γ and β define the geometry of the two pyramidal base and mobile platforms.

(a)   (b)
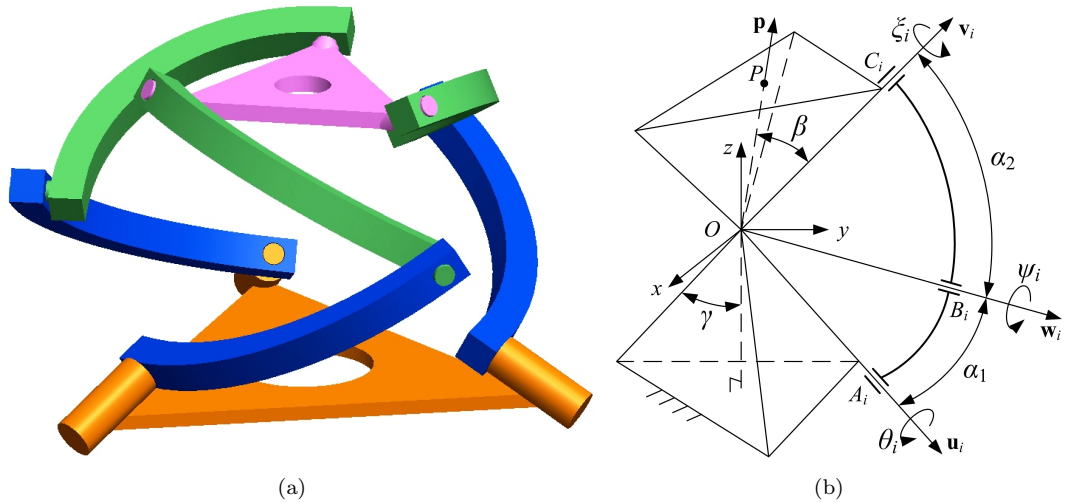
Figure 3.3: Architecture of a general SPM: (a) overview, (b) parameterization of the ith leg.

3.3 Kinematic Modeling of a 3-RRR SPM

The kinematics of the SPMs has been well documented [135], therefore, the details will not be repeated. The orientation of the mobile platform is described with the orientation representation of *azimuth-tilt-torsion* (ϕ-θ-σ), for which the rotation matrix $\mathbf{Q}$ is defined by Eqn. (3.2) in Sec. 3.1.1.

Under the coordinate system xyz, unit vector $\mathbf{u}_i$ is expressed as:

$$\mathbf{u}_i = \begin{bmatrix} -\sin\eta_i\sin\gamma & \cos\eta_i\sin\gamma & -\cos\gamma \end{bmatrix}^T \tag{3.16}$$

where $\eta_i = 2(i-1)\pi/3$, $i = 1, 2, 3$.

Unit vector $\mathbf{w}_i$ in the coordinate system xyz is expressed as:

$$\mathbf{w}_i = \begin{bmatrix} -s\eta_i s\gamma c\alpha_1 + (c\eta_i s\theta_i - s\eta_i c\gamma c\theta_i)s\alpha_1 \\ c\eta_i s\gamma c\alpha_1 + (s\eta_i s\theta_i + c\eta_i c\gamma c\theta_i)s\alpha_1 \\ -c\gamma c\alpha_1 + s\gamma c\theta_i s\alpha_1 \end{bmatrix} \tag{3.17}$$

Unit vector $\mathbf{v}_i$ is a function of the mobile-platform orientation, namely,

$$\mathbf{v}_i = \begin{bmatrix} v_{ix} & v_{iy} & v_{iz} \end{bmatrix}^T = \mathbf{Q}\mathbf{v}_i^* \tag{3.18}$$

where $\mathbf{v}_i^*$ is the unit vector of the top revolute joint axis when the mobile platform is at its home configuration:

$$\mathbf{v}_i^* = \begin{bmatrix} -\sin\eta_i\sin\beta & \cos\eta_i\sin\beta & \cos\beta \end{bmatrix}^T \tag{3.19}$$

The inverse kinematics of SPMs is solved by making use of the following equation:

$$\mathbf{w}_i \cdot \mathbf{v}_i = \cos\alpha_2, \ i = 1, 2, 3 \tag{3.20}$$

3.3.1 Kinematic Jacobian Matrix

Let $\boldsymbol{\omega} = [\omega_x \ \omega_y \ \omega_z]^T$ denote the angular velocity of the mobile-platform, the screws velocity equation via the ith leg can be stated as

$$\$_\omega = \begin{bmatrix} \boldsymbol{\omega} \\ \mathbf{0} \end{bmatrix} = \dot\theta_i\hat\$_A^i + \dot\psi_i\hat\$_B^i + \dot\xi_i\hat\$_C^i \tag{3.21}$$

with the screws for the revolute joints at points A_i, B_i and C_i expressed as

$$\hat{\$}^i_A = \begin{bmatrix} \mathbf{u}_i \\ \mathbf{0} \end{bmatrix}, \hat{\$}^i_B = \begin{bmatrix} \mathbf{w}_i \\ \mathbf{0} \end{bmatrix}, \hat{\$}^i_C = \begin{bmatrix} \mathbf{v}_i \\ \mathbf{0} \end{bmatrix} \tag{3.22}$$

Since the axes of the two passive revolute joints in each leg lie in the plane B_iOC_i, the following screw is reciprocal to all the revolute joint screws of the ith leg and does not lie in its constraint wrench system:

$$\hat{\$}^i_r = \begin{bmatrix} \mathbf{0} \\ \mathbf{w}_i \times \mathbf{v}_i \end{bmatrix} \tag{3.23}$$

Applying the orthogonal product ($\circ$) to both sides of Eqn. (3.21) yields

$$\hat{\$}^i_r \circ \$_\omega = (\mathbf{w}_i \times \mathbf{v}_i)^T \boldsymbol{\omega} = \dot{\theta}_i \mathbf{u}_i \cdot (\mathbf{w}_i \times \mathbf{v}_i) = (\mathbf{u}_i \times \mathbf{w}_i) \cdot \mathbf{v}_i \dot{\theta}_i \tag{3.24}$$

As a consequence, the expression mapping from the mobile platform twist to the input angular velocities is stated as:

$$\mathbf{A}\boldsymbol{\omega} = \mathbf{B}\dot{\boldsymbol{\theta}} \tag{3.25}$$

with

$$\mathbf{A} = \begin{bmatrix} \mathbf{w}_1 \times \mathbf{v}_1 & \mathbf{w}_2 \times \mathbf{v}_2 & \mathbf{w}_3 \times \mathbf{v}_3 \end{bmatrix}^T \tag{3.26a}$$

$$\mathbf{B} = \text{diag}\begin{bmatrix} (\mathbf{u}_1 \times \mathbf{w}_1) \cdot \mathbf{v}_1 & (\mathbf{u}_2 \times \mathbf{w}_2) \cdot \mathbf{v}_2 & (\mathbf{u}_3 \times \mathbf{w}_3) \cdot \mathbf{v}_3 \end{bmatrix} \tag{3.26b}$$

where $\dot{\boldsymbol{\theta}} = \begin{bmatrix} \dot{\theta}_1 & \dot{\theta}_2 & \dot{\theta}_3 \end{bmatrix}^T$. Matrices $\mathbf{A}$ and $\mathbf{B}$ are named as the forward and inverse Jacobian matrices of the manipulator, respectively. If $\mathbf{B}$ is nonsigular, the kinematic Jacobian matrix $\mathbf{J}$ is obtained as:

$$\mathbf{J} = \mathbf{B}^{-1}\mathbf{A} = \begin{bmatrix} \mathbf{j}_1 & \mathbf{j}_2 & \mathbf{j}_3 \end{bmatrix}^T \tag{3.27}$$

with

$$\mathbf{j}_i = \frac{\mathbf{w}_i \times \mathbf{v}_i}{(\mathbf{u}_i \times \mathbf{w}_i) \cdot \mathbf{v}_i}, \, i = 1, 2, 3 \tag{3.28}$$

3.3.2 Velocity and Acceleration Analysis

Figure 3.4 demonstrates the movements of the proximal and distal links and mobile platform. $\boldsymbol{\omega} = [\omega_x \, \omega_y \, \omega_z]^T$ stands for the angular velocity of the mobile platform in the reference coordinate frame xyz.
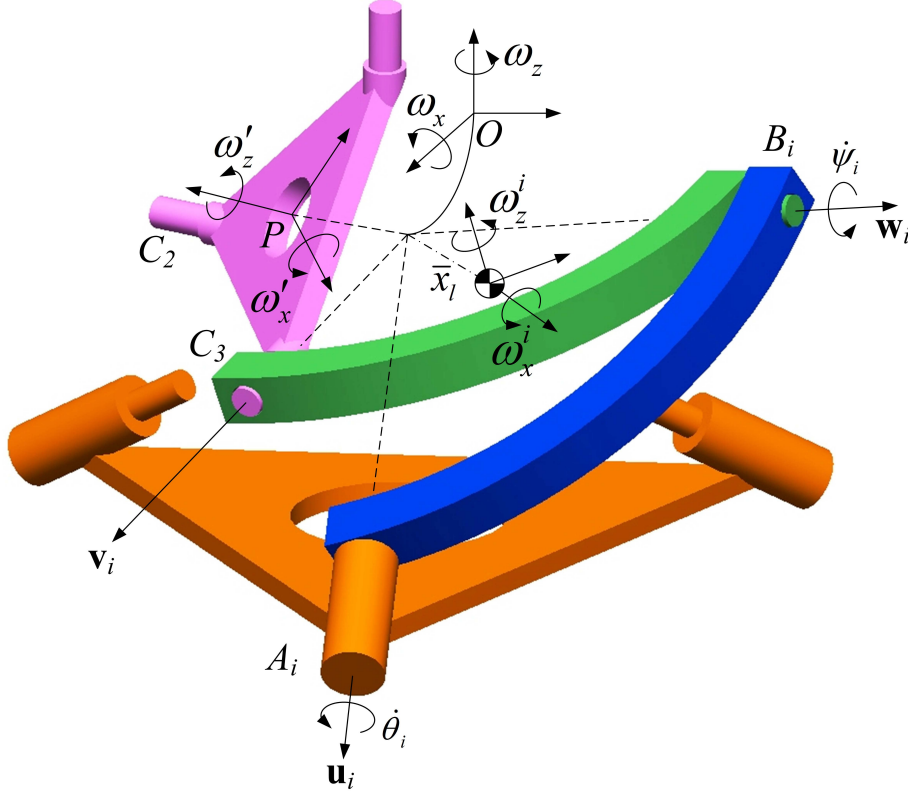
Figure 3.4: The movements of the mobile platform and links.

The previously defined rotation matrix (3.2) is kinematically equivalent to the Euler convention Z-Y-Z of $\mathbf{R}_z(\phi)\mathbf{R}_y(\theta)\mathbf{R}_z(\sigma - \phi)$, thus, the relationship between the angle rates $\dot{\boldsymbol{\varphi}} = \begin{bmatrix} \dot{\phi} & \dot{\theta} & \dot{\sigma} \end{bmatrix}^T$ and the angular velocity $\boldsymbol{\omega}$ is found as [159]:

$$\begin{bmatrix} \omega_x \\ \omega_y \\ \omega_z \end{bmatrix} = \begin{bmatrix} -\mathrm{s}\theta\mathrm{c}\phi & -\mathrm{s}\phi & \mathrm{s}\theta\mathrm{c}\phi \\ -\mathrm{s}\theta\mathrm{s}\phi & \mathrm{c}\phi & \mathrm{s}\theta\mathrm{s}\phi \\ 1 - \mathrm{c}\theta & 0 & \mathrm{c}\theta \end{bmatrix} \begin{bmatrix} \dot{\phi} \\ \dot{\theta} \\ \dot{\sigma} \end{bmatrix} \rightarrow \boldsymbol{\omega} = \boldsymbol{\Phi}\dot{\boldsymbol{\varphi}} \tag{3.29}$$

Differentiating Eqn. (3.29) with respect to time yields

$$\dot{\boldsymbol{\omega}} = \boldsymbol{\Phi}\ddot{\boldsymbol{\varphi}} + \dot{\boldsymbol{\Phi}}\dot{\boldsymbol{\varphi}} = \boldsymbol{\Phi}\ddot{\boldsymbol{\varphi}} + \left(\frac{\partial \boldsymbol{\Phi}}{\partial \phi}\dot{\phi} + \frac{\partial \boldsymbol{\Phi}}{\partial \theta}\dot{\theta} + \frac{\partial \boldsymbol{\Phi}}{\partial \sigma}\dot{\sigma} \right)\dot{\boldsymbol{\varphi}} \tag{3.30}$$

with

$$\frac{\partial \boldsymbol{\Phi}}{\partial \phi} = \begin{bmatrix} \mathrm{s}\theta\mathrm{s}\phi & -\mathrm{c}\phi & -\mathrm{s}\theta\mathrm{s}\phi \\ -\mathrm{s}\theta\mathrm{c}\phi & -\mathrm{s}\phi & \mathrm{s}\theta\mathrm{c}\phi \\ 0 & 0 & 0 \end{bmatrix}, \frac{\partial \boldsymbol{\Phi}}{\partial \theta} = \begin{bmatrix} -\mathrm{c}\theta\mathrm{c}\phi & 0 & \mathrm{c}\theta\mathrm{c}\phi \\ -\mathrm{c}\theta\mathrm{s}\phi & 0 & \mathrm{c}\theta\mathrm{s}\phi \\ \mathrm{s}\theta & 0 & -\mathrm{s}\theta \end{bmatrix}, \frac{\partial \boldsymbol{\Phi}}{\partial \sigma} = \mathbf{0}_3 \tag{3.31}$$

Movements of mobile platform

The velocities of the mobile platform is expressed as $\mathbf{v}_p = \boldsymbol{\omega} \times R\cos\beta\mathbf{p}$ and the angular velocities in its local frame is found as

$$\begin{bmatrix} \omega'_x \\ \omega'_y \\ \omega'_z \end{bmatrix} = \begin{bmatrix} -\mathrm{s}\theta\mathrm{c}(\sigma - \phi) & \mathrm{s}(\sigma - \phi) & 0 \\ \mathrm{s}\theta\mathrm{s}(\sigma - \phi) & \mathrm{c}(\sigma - \phi) & 0 \\ \mathrm{c}\theta - 1 & 0 & 1 \end{bmatrix} \begin{bmatrix} \dot{\phi} \\ \dot{\theta} \\ \dot{\sigma} \end{bmatrix} \rightarrow \boldsymbol{\omega}' = \boldsymbol{\Phi}'\dot{\boldsymbol{\varphi}} \qquad (3.32)$$

Similarly, the angular accelerations is expressed as

$$\dot{\boldsymbol{\omega}}' = \boldsymbol{\Phi}'\ddot{\boldsymbol{\varphi}} + \dot{\boldsymbol{\Phi}}'\dot{\boldsymbol{\varphi}} = \boldsymbol{\Phi}'\ddot{\boldsymbol{\varphi}} + \left(\frac{\partial\boldsymbol{\Phi}'}{\partial\phi}\dot{\phi} + \frac{\partial\boldsymbol{\Phi}'}{\partial\theta}\dot{\theta} + \frac{\partial\boldsymbol{\Phi}'}{\partial\sigma}\dot{\sigma} \right)\dot{\boldsymbol{\varphi}} \qquad (3.33)$$

with

$$\frac{\partial\boldsymbol{\Phi}'}{\partial\phi} = \begin{bmatrix} -\mathrm{s}\theta\mathrm{s}(\sigma - \phi) & -\mathrm{c}(\sigma - \phi) & 0 \\ -\mathrm{s}\theta\mathrm{c}(\sigma - \phi) & \mathrm{s}(\sigma - \phi) & 0 \\ 0 & 0 & 0 \end{bmatrix}, \; \frac{\partial\boldsymbol{\Phi}'}{\partial\theta} = \begin{bmatrix} -\mathrm{c}\theta\mathrm{c}(\sigma - \phi) & 0 & 0 \\ \mathrm{c}\theta\mathrm{s}(\sigma - \phi) & 0 & 0 \\ -\mathrm{s}\theta - 1 & 0 & 0 \end{bmatrix}$$

$$\frac{\partial\boldsymbol{\Phi}'}{\partial\sigma} = \begin{bmatrix} \mathrm{s}\theta\mathrm{s}(\sigma - \phi) & -\mathrm{c}(\sigma - \phi) & 0 \\ \mathrm{s}\theta\mathrm{c}(\sigma - \phi) & -\mathrm{s}(\sigma - \phi) & 0 \\ 0 & 0 & 0 \end{bmatrix} \qquad (3.34)$$

Movements of the distal links

The angular velocities of the intermediate passive joints $\dot{\boldsymbol{\psi}} = \begin{bmatrix} \dot{\psi}_1 & \dot{\psi}_2 & \dot{\psi}_3 \end{bmatrix}^T$ are obtained by referring to the computation of the active velocity $\boldsymbol{\theta}$, expressed as:

$$\dot{\boldsymbol{\psi}} = [\mathbf{j}_{\psi 1} \quad \mathbf{j}_{\psi 2} \quad \mathbf{j}_{\psi 3}]^T \boldsymbol{\omega} = \mathbf{J}_\psi\boldsymbol{\omega}, \quad \mathbf{j}_{\psi i} = \frac{\mathbf{u}_i \times \mathbf{v}_i}{(\mathbf{u}_i \times \mathbf{v}_i) \cdot \mathbf{w}_i} \qquad (3.35)$$

Therefore, the angular velocities of the ith distal link in the reference coordinate system xyz is expressed as:

$$\boldsymbol{\omega}_{li} = \dot{\theta}_i\mathbf{u}_i + \dot{\psi}_i\mathbf{w}_i \qquad (3.36)$$

Let $\boldsymbol{\omega}_i = \begin{bmatrix} \omega_x^i & \omega_y^i & \omega_z^i \end{bmatrix}^T$ denotes the angular velocities of the ith link in its inertial frame, then we have:

$$\omega_x^i\mathbf{e}_{ix} + \omega_y^i\mathbf{e}_{iy} + \omega_z^i\mathbf{e}_{iz} = \mathbf{E}_i\boldsymbol{\omega}_i = \boldsymbol{\omega}_{li} \qquad (3.37)$$

with

$$\mathbf{e}_{ix} = \frac{\mathbf{x}_i}{\|\mathbf{x}_i\|} = \frac{\mathbf{w}_i + \mathbf{v}_i}{\|\mathbf{w}_i + \mathbf{v}_i\|}, \; \mathbf{e}_{iy} = \frac{\mathbf{y}_i}{\|\mathbf{y}_i\|} = \frac{\mathbf{v}_i - \mathbf{w}_i}{\|\mathbf{v}_i - \mathbf{w}_i\|}, \; \mathbf{e}_{iz} = \frac{\mathbf{z}_i}{\|\mathbf{z}_i\|} = \frac{\mathbf{w}_i \times \mathbf{v}_i}{\|\mathbf{w}_i \times \mathbf{v}_i\|} \qquad (3.38)$$

Since $\mathbf{E}_i$ is an orthogonal matrix, the angular velocities of the ith link in its inertial frame is found as

$$\boldsymbol{\omega}_i = \mathbf{E}_i^T \boldsymbol{\omega}_{li} \tag{3.39}$$

The velocity of the mass center of the ith link is obtained by virtue of the velocity of the middle point of line segment B_iC_i:

$$\mathbf{v}_{BC}^i = \frac{1}{2}\left(\boldsymbol{\omega} \times \mathbf{v}_i + \dot{\theta}_i \mathbf{u}_i \times \mathbf{w}_i\right) R = R\cos\frac{\alpha_2}{2}\boldsymbol{\omega}_{BC}^i \times \mathbf{e}_{ix} \tag{3.40}$$

Thus, the velocity of the ith link is expressed as:

$$\mathbf{v}_{li} = \boldsymbol{\omega}_{BC}^i \times \mathbf{e}_{ix}\bar{x}_{l2} = \frac{1}{2}\csc\frac{\alpha_2}{2}\bar{x}_{l2}\left(\boldsymbol{\omega} \times \mathbf{v}_i + \dot{\theta}_i \mathbf{u}_i \times \mathbf{w}_i\right) \tag{3.41}$$

where $\bar{x}_{l2}$ denotes the position of the gravity center of a curved link can be found in Appendix A together with other details.

3.4 Dynamic Modeling of a 3-RRR SPM

The dynamics of the SPM can be solved by applying the Lagrange equation below

$$\frac{\mathrm{d}}{\mathrm{d}t}\left(\frac{\partial L}{\partial \dot{\mathbf{q}}}\right) - \frac{\partial L}{\partial \mathbf{q}} + \mathbf{C_q}^T\boldsymbol{\lambda} = \boldsymbol{\tau} \tag{3.42}$$

where $L \equiv T - V$ is the Lagrangian of the system and $\mathbf{q} = \begin{bmatrix} \theta_1 & \theta_2 & \theta_3 & \phi & \theta & \sigma \end{bmatrix}^T$. $\mathbf{C_q} = \begin{bmatrix} \mathbf{B} & -\mathbf{A}\boldsymbol{\Phi} \end{bmatrix}$ is the constraint Jacobian where $\mathbf{A}$ and $\mathbf{B}$ are defined in Eqn. (3.25) and $\boldsymbol{\lambda} = \begin{bmatrix} \lambda_1 & \lambda_2 & \lambda_3 \end{bmatrix}^T$ is a vector of Lagrange multipliers. $\boldsymbol{\tau} = \begin{bmatrix} \boldsymbol{\tau}_\theta^T & \mathbf{0}_{1\times3} \end{bmatrix}^T$ is the vector of torques in the Lagrangian coordinates, where $\boldsymbol{\tau}_\theta = \begin{bmatrix} \tau_1 & \tau_2 & \tau_3 \end{bmatrix}^T$ characterizes the actuator torques.

The **kinetic energy** T of the system includes:

- The kinetic energy T_{l1} of the proximal links is expressed as:

$$T_{l1} = \frac{1}{2}\left(m_{l1}\bar{x}_{l1}^2\sin^2\frac{\alpha_1}{2} + I_{l1}\right)\dot{\boldsymbol{\theta}}^T\dot{\boldsymbol{\theta}} \tag{3.43}$$

where m_{l1} is the mass of the lower link and $\bar{x}_{l1}$ denotes its mass center. I_{l1} is the mass moment of inertia about $\mathbf{u}_i$ given in Appendix A with α_1.

- The kinetic energy T_{l2} of the distal links is given by:

$$T_{l2} = \frac{1}{2}\sum_{i=1}^{3}\left(\boldsymbol{\omega}_i^T\mathbf{I}_l\boldsymbol{\omega}_i + m_{l2}\mathbf{v}_{li}^T\mathbf{v}_{li}\right) \tag{3.44}$$

where m_{l2} is the mass of the curved link and $\mathbf{I}_l = \text{diag}\begin{bmatrix} L_{xx} & L_{yy} & L_{zz} \end{bmatrix}$ describes its mass moment of inertia in its local frame. $\boldsymbol{\omega}_i$ and $\mathbf{v}_{li}$ are expressed in Eqns. (3.39) and (3.41), respectively.

- The kinetic energy T_p of the mobile platform is:

$$T_p = \frac{1}{2}m_p\mathbf{v}_p^T\mathbf{v}_p + \frac{1}{2}\boldsymbol{\omega}'^T\mathbf{I}_p\boldsymbol{\omega}' \tag{3.45}$$

where m_p is the mass of the mobile-platform and $\mathbf{I}_p = \text{diag}\begin{bmatrix} I_{xx} & I_{yy} & I_{zz} \end{bmatrix}$ denotes the mass moments of inertia in its local frame.

Thus, the kinetic energy T can be written in the following form:

$$T = T_{l1} + T_{l2} + T_p = \frac{1}{2}\dot{\mathbf{q}}^T\mathbf{M}(\mathbf{q})\dot{\mathbf{q}} = \frac{1}{2}\dot{\mathbf{q}}^T\begin{bmatrix} \mathbf{M}_1 & \mathbf{0}_{3\times3} \\ \mathbf{0}_{3\times3} & \boldsymbol{\Phi}'^T\mathbf{I}_p\boldsymbol{\Phi}' + \boldsymbol{\Phi}^T\mathbf{M}_2\boldsymbol{\Phi} \end{bmatrix}\dot{\mathbf{q}} \tag{3.46}$$

with

$$\mathbf{M}_1 = \left(m_{l1}\bar{x}_{l1}^2\sin^2\frac{\alpha_1}{2} + I_{l1}\right)\mathbf{1}_3 + \text{diag}\begin{bmatrix} L_{\theta1} & L_{\theta2} & L_{\theta3} \end{bmatrix} \tag{3.47a}$$

$$\mathbf{M}_2 = m_pR^2\cos^2\beta[\mathbf{p}]_\times^T[\mathbf{p}]_\times + \sum_{i=1}^{3}\left(\frac{1}{4}\csc^2\frac{\alpha_2}{2}m_{l2}\bar{x}_{l2}^2\mathbf{L}_{li} + \mathbf{R}_{li}\right) \tag{3.47b}$$

and

$$L_{\theta i} = \frac{1}{4}\csc^2\frac{\alpha_2}{2}m_{l2}\bar{x}_{l2}^2\mathbf{n}_i^T\mathbf{n}_i + \mathbf{u}_i^T\mathbf{I}_{li}\mathbf{u}_i \tag{3.48a}$$

$$\mathbf{L}_{li} = [\mathbf{v}_i]_\times^T[\mathbf{v}_i]_\times + [\mathbf{v}_i]_\times\mathbf{n}_i\mathbf{j}_i^T + \mathbf{j}_i\mathbf{n}_i^T[\mathbf{v}_i]_\times^T \tag{3.48b}$$

$$\mathbf{R}_{li} = \mathbf{j}_i\mathbf{u}_i^T\mathbf{I}_{li}\mathbf{w}_i\mathbf{j}_{\psi i}^T + \mathbf{j}_{\psi i}\mathbf{w}_i^T\mathbf{I}_{li}\mathbf{u}_i\mathbf{j}_i^T + \mathbf{j}_{\psi i}\mathbf{w}_i^T\mathbf{I}_{li}\mathbf{w}_i\mathbf{j}_{\psi i}^T \tag{3.48c}$$

where $\mathbf{n}_i = \mathbf{u}_i \times \mathbf{w}_i$ and $\mathbf{I}_{li} = \mathbf{E}_i\mathbf{I}_l\mathbf{E}_i^T$. $[\cdot]_\times$ stands for the skew-symmetric matrix whose elements are from the corresponding vector and $\mathbf{1}_3$ is the Identity matrix.

The **potential energy** V of the system is obtained as:

$$V = m_pgR\cos\beta\mathbf{k}^T\mathbf{p} + m_{l1}g\bar{x}_{l1}\sum_{i=1}^{3}\mathbf{k}^T\mathbf{l}_{1i} + m_{l2}g\bar{x}_{l2}\sum_{i=1}^{3}\mathbf{k}^T\mathbf{e}_{ix} \tag{3.49}$$

where $\mathbf{k}$ is the unit vector of z-axis and $\mathbf{l}_{1i} = \mathbf{h}_i/\|\mathbf{h}_i\|$, $\mathbf{h}_i = \mathbf{u}_i + \mathbf{w}_i$.

The **first term** in Eqn. (3.42) is obtained as below:

$$\frac{\mathrm{d}}{\mathrm{d}t}\left(\frac{\partial L}{\partial \dot{\mathbf{q}}}\right) = \mathbf{M}(\mathbf{q})\ddot{\mathbf{q}} + \dot{\mathbf{M}}(\mathbf{q})\dot{\mathbf{q}} = \mathbf{M}(\mathbf{q})\ddot{\mathbf{q}} + \begin{bmatrix} \dot{\mathbf{M}}_1(\mathbf{q}) & \mathbf{0} \\ \mathbf{0} & \dot{\mathbf{M}}_2(\mathbf{q}) \end{bmatrix}\dot{\mathbf{q}} \tag{3.50}$$

with

$$\dot{\mathbf{M}}_1(\mathbf{q}) = \mathrm{diag}\begin{bmatrix} \dot{L}_{\theta 1} & \dot{L}_{\theta 2} & \dot{L}_{\theta 3} \end{bmatrix} \tag{3.51a}$$

$$\dot{\mathbf{M}}_2(\mathbf{q}) = \dot{\mathbf{\Phi}}'^{T}\mathbf{I}_p\mathbf{\Phi}' + \mathbf{\Phi}'^{T}\mathbf{I}_p\dot{\mathbf{\Phi}}' + \dot{\mathbf{\Phi}}^{T}\mathbf{M}_2\mathbf{\Phi} + \mathbf{\Phi}^{T}\dot{\mathbf{M}}_2\mathbf{\Phi} + \mathbf{\Phi}^{T}\mathbf{M}_2\dot{\mathbf{\Phi}} \tag{3.51b}$$

These time-derived terms are given in Appendix B.

The **second term** in Eqn. (3.42) is given by:

$$\frac{\partial L}{\partial \mathbf{q}} = \frac{\partial T}{\partial \mathbf{q}} - \frac{\partial V}{\partial \mathbf{q}} = T_{\mathbf{q}} - V_{\mathbf{q}} \tag{3.52}$$

with

$$T_{\mathbf{q}} = \begin{bmatrix} T_{\theta 1} & T_{\theta 2} & T_{\theta 3} & T_\phi & T_\theta & T_\sigma \end{bmatrix}^{T} \tag{3.53a}$$

$$V_{\mathbf{q}} = \begin{bmatrix} V_{\theta 1} & V_{\theta 2} & V_{\theta 3} & V_\phi & -m_p g R \cos\beta \sin\theta + V_\theta & V_\sigma \end{bmatrix}^{T} \tag{3.53b}$$

and

$$T_{\theta i} = \frac{1}{2}\dot{\theta}_i^2 \frac{\partial L_{\theta i}}{\partial \theta_i} + \frac{1}{2}\boldsymbol{\omega}^{T}\left(\frac{1}{4}\csc^2\frac{\alpha_2}{2}m_{l2}\bar{x}_{l2}^2\frac{\partial \mathbf{L}_{li}}{\partial \theta_i} + \frac{\partial \mathbf{R}_{li}}{\partial \theta_i}\right)\boldsymbol{\omega}, \; i = 1, 2, 3 \tag{3.54a}$$

$$T_\mu = \frac{1}{2}\sum_{i=1}^{3}\dot{\theta}_i\mathbf{u}_i^{T}\frac{\partial \mathbf{I}_{li}}{\partial \mu}\mathbf{u}_i + \frac{1}{2}\dot{\boldsymbol{\varphi}}^{T}\frac{\partial \mathbf{M}(\mathbf{q})}{\partial \mu}\dot{\boldsymbol{\varphi}}, \; \mu \in \{\phi, \theta, \sigma\} \tag{3.54b}$$

$$V_{\theta i} = m_{l1}g\bar{x}_{l1}\mathbf{k}^{T}\frac{\frac{\partial \mathbf{w}_i}{\partial \theta_i}}{\|\mathbf{h}_i\|} + m_{l2}g\bar{x}_{l2}\mathbf{k}^{T}\frac{\frac{\partial \mathbf{w}_i}{\partial \theta_i}}{\|\mathbf{x}_i\|} \tag{3.54c}$$

$$V_\mu = m_{l2}g\bar{x}_{l2}\sum_{i=1}^{3}\mathbf{k}^{T}\frac{\frac{\partial \mathbf{v}_i}{\partial \mu}}{\|\mathbf{x}_i\|} \tag{3.54d}$$

where

$$\frac{\partial L_{\theta i}}{\partial \theta_i} = \frac{1}{2}\csc^2\frac{\alpha_2}{2}m_{l2}\bar{x}_{l2}^2\mathbf{n}_i^{T}\frac{\partial \mathbf{n}_i}{\partial \theta_i} + \mathbf{u}_i^{T}\frac{\partial \mathbf{I}_{li}}{\partial \theta_i}\mathbf{u}_i \tag{3.55a}$$

$$\frac{\partial \mathbf{M}(\mathbf{q})}{\partial \mu} = \frac{\partial \mathbf{\Phi}'^{T}}{\partial \mu}\mathbf{I}_p\mathbf{\Phi}' + \mathbf{\Phi}'^{T}\mathbf{I}_p\frac{\partial \mathbf{\Phi}'}{\partial \mu} + \frac{\partial \mathbf{\Phi}^{T}}{\partial \mu}\mathbf{M}_2\mathbf{\Phi} + \mathbf{\Phi}^{T}\mathbf{M}_2\frac{\partial \mathbf{\Phi}}{\partial \mu} + \mathbf{\Phi}^{T}\frac{\partial \mathbf{M}_2}{\partial \mu}\mathbf{\Phi} \tag{3.55b}$$

These variable-derived terms are given in Appendix B.

Moreover, differentiating Eqn. (3.25) with respect to time yields

$$\mathbf{C}_{\mathbf{q}}\ddot{\mathbf{q}} = -\dot{\mathbf{C}}_{\mathbf{q}}\dot{\mathbf{q}} \tag{3.56}$$
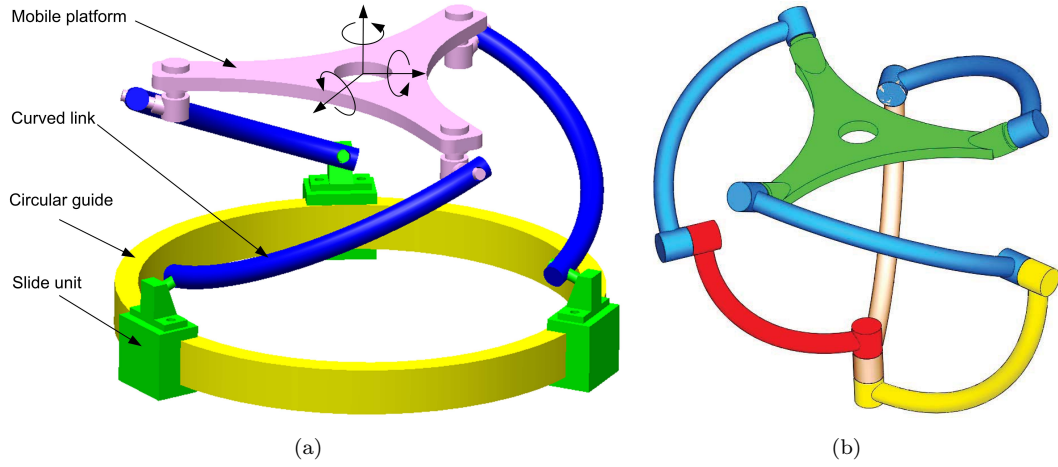
(a) (b)

Figure 3.5: Kinematic structure of unlimited rolling motion spherical parallel manipulator: (a) SPM under study, (b) an alternative structure.

with

$$\mathbf{C_q\ddot{q}} = \mathbf{C_q} \begin{bmatrix} \ddot{\boldsymbol{\theta}}^T & \ddot{\boldsymbol{\phi}}^T \end{bmatrix}^T, \quad -\dot{\mathbf{C}}_\mathbf{q}\dot{\mathbf{q}} = - \begin{bmatrix} \dot{\mathbf{B}} & -\dot{\mathbf{A}}\boldsymbol{\Phi} - \mathbf{A}\dot{\boldsymbol{\Phi}} \end{bmatrix} \dot{\mathbf{q}} \tag{3.57}$$

and

$$\dot{\mathbf{A}} = \begin{bmatrix} \dot{\mathbf{j}}_{A1} & \dot{\mathbf{j}}_{A2} & \dot{\mathbf{j}}_{A3} \end{bmatrix}^T, \quad \dot{\mathbf{j}}_{Ai} = \dot{\theta}_i \dot{\mathbf{w}}_i \times \mathbf{v}_i + \mathbf{w}_i \times \dot{\mathbf{v}}_i \tag{3.58a}$$

$$\dot{\mathbf{B}} = \text{diag} \begin{bmatrix} \dot{\mathbf{j}}_{B1} & \dot{\mathbf{j}}_{B2} & \dot{\mathbf{j}}_{B3} \end{bmatrix}, \quad \dot{\mathbf{j}}_{Bi} = \dot{\theta}_i (\mathbf{u}_i \times \dot{\mathbf{w}}_i) \cdot \mathbf{v}_i + (\mathbf{u}_i \times \mathbf{w}_i) \cdot \dot{\mathbf{v}}_i \tag{3.58b}$$

where $\dot{\mathbf{w}}_i = \dot{\theta}_i \mathbf{u}_i \times \mathbf{w}_i$ and $\dot{\mathbf{v}}_i = \boldsymbol{\omega} \times \mathbf{v}_i$.

Writing Eqns. (3.42) and (3.56) jointly [158] leads to

$$\begin{bmatrix} \mathbf{M}(\mathbf{q}) & \mathbf{C}_\mathbf{q}^T \\ \mathbf{C_q} & \mathbf{0} \end{bmatrix} \begin{bmatrix} \ddot{\mathbf{q}} \\ \boldsymbol{\lambda} \end{bmatrix} = \begin{bmatrix} \boldsymbol{\tau}_\theta - \dot{\mathbf{M}}(\mathbf{q})\dot{\mathbf{q}} + T_\mathbf{q} - V_\mathbf{q} \\ -\dot{\mathbf{C}}_\mathbf{q}\dot{\mathbf{q}} \end{bmatrix} \tag{3.59}$$

With an external moments $\mathbf{m}$, the actuator torques are found:

$$\boldsymbol{\tau}_a = \boldsymbol{\tau}_\theta - \mathbf{J}^{-T}\mathbf{m} \tag{3.60}$$

3.5 Numerical Simulation

The proposed spherical parallel manipulator is a special case with $\gamma = 0$, as shown in Figure 3.5(a), which consists of a mobile platform, a circular guide, three sliding units and three curved links. This SPM has an alternative structure as shown in Figure 3.5(b).

Based on the kinematics and dynamics, a simplified numerical example is given to illustrate the motion of the spherical parallel manipulator with Matlab$^{\text{TM}}$/simulink [160] as

shown in 3.6(a). Besides, an independent simulation model by Adams$^{\text{TM}}$ displayed in Figure 3.6(b) is created for comparison.

In these two models, the proximal links are replaced with the sliding units of mass m_s described in Figure 3.5(a). The parameters of the spherical parallel manipulator are given by Table 3.1, where a is the side length of the squared cross-section of the curved link and R is the midcurve. The initial conditions are listed in Table 3.2 with two payload cases. The mass and inertia properties are given in Table 3.3.

The simulation results are shown in Figure 3.7, from which it is seen that these two models generates quite close results.

Table 3.1: The design variables of the SPM simulation model.

α_1 [deg]	α_2 [deg]	β [deg]	a [m]	R [m]
60	80	75	0.010	0.100

Table 3.2: The initial conditions of the numerical simulation.

$[\phi,\,\theta,\,\sigma]$ [rad]	$[\dot{\theta}_1,\,\dot{\theta}_2,\,\dot{\theta}_3]$ [rad/s]	Case 1: $\mathbf{m}$ [Nm]	Case 2: $\mathbf{m}$ [Nm]
$[0,\,\pi/6,\,0]$	$[-8,\,-7,\,-9]$	$\mathbf{0}$	$[0.1,\,0.1,\,0.1]$

Table 3.3: Mass and inertia properties of the SPM model.

Mobile platform		Curved link		Sliding unit
m_p [kg]	$\mathbf{I}_p\,[10^{-4}\,\text{kg m}^2]$	m_l [kg]	$\mathbf{I}_l\,[10^{-4}\,\text{kg m}^2]$	m_s [kg]
0.332	[3.855 3.855 7.688]	0.114	[1.852 0.089 1.921]	0.123
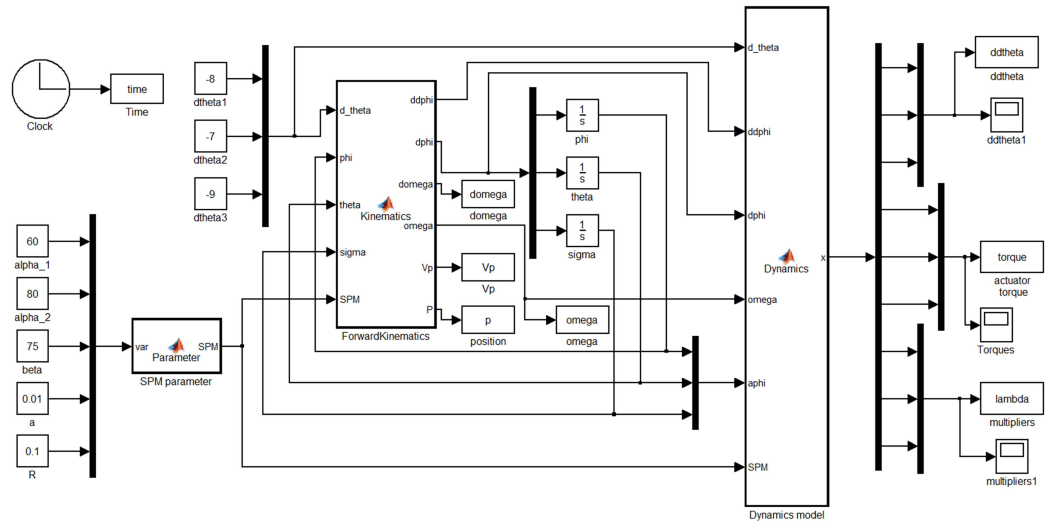
(a)
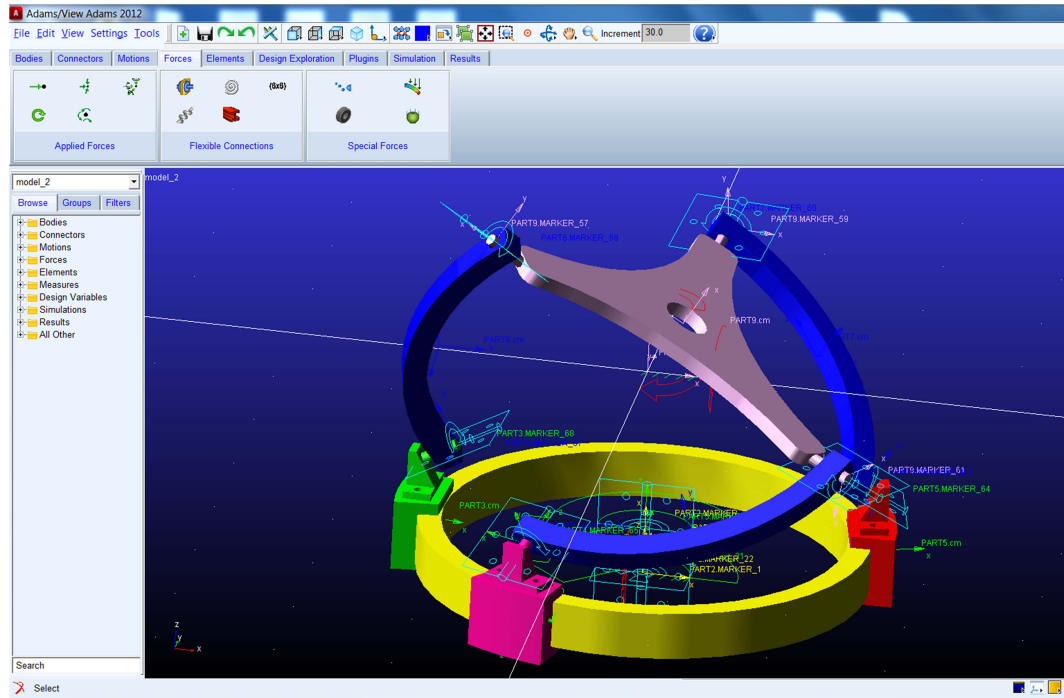
(b)

Figure 3.6: Simulation models: (a) Matlab$^{\text{TM}}$/simulink, (b) Adams$^{\text{TM}}$.
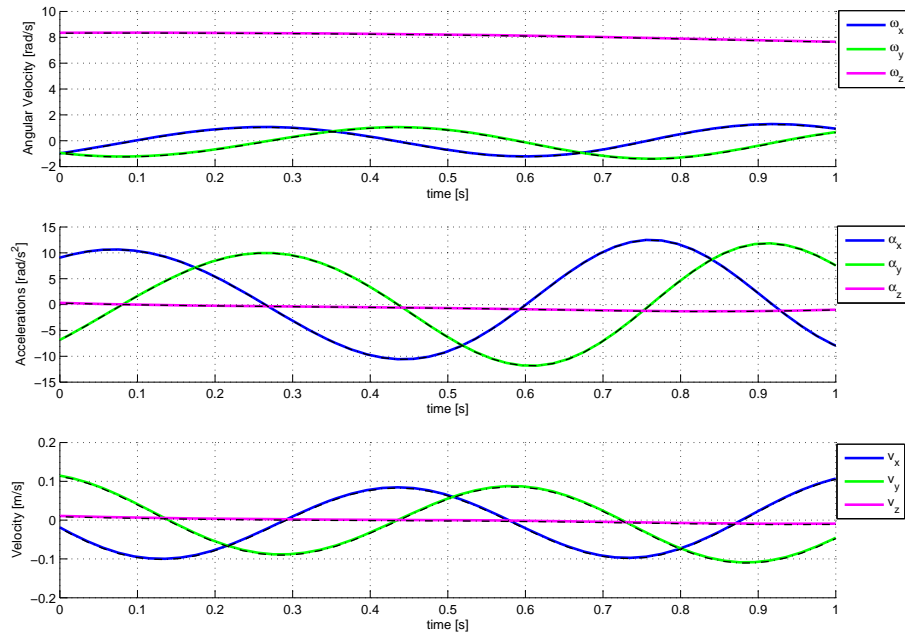
(a)
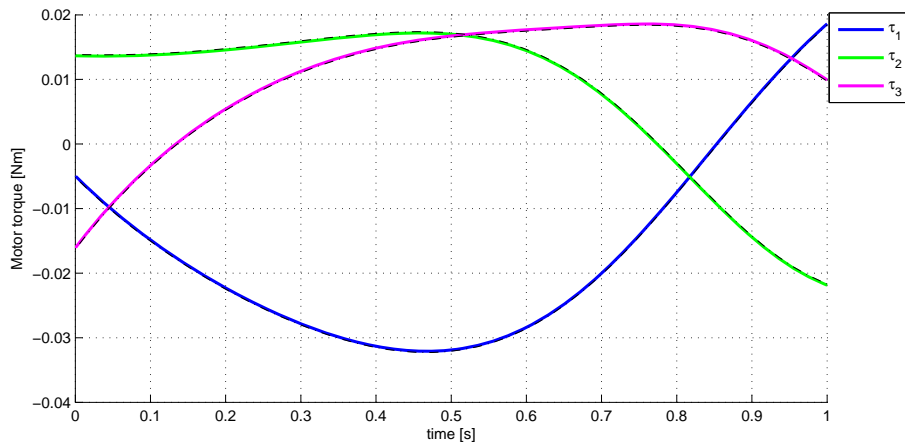
(b)
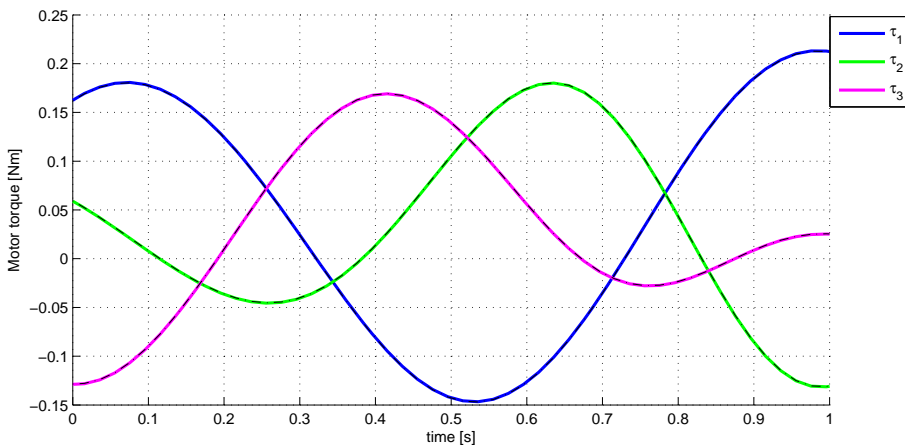
(c)

Figure 3.7: Simulation results (solid line stands for Matlab$^{\text{TM}}$ solver, dot-line for Adams$^{\text{TM}}$): (a) Velocity and acceleration of the mobile platform, (b) active joint torques of Case 1, (c) active joint torques of Case 2.

4

Paper I

G. Wu, S. Bai, J.A. Kepler, S. Caro, 2012. Error Modelling and Experimental Validation of a Planar 3-PPR Parallel Manipulator with Joint Clearances. *ASME Journal of Mechanisms and Robotics*, 4(4): 041008(1-12), DOI: 10.1115/1.4007487.

Guanglei Wu[1]
e-mail: gwu@m-tech.aau.dk

Shaoping Bai
e-mail: shb@m-tech.aau.dk

Jørgen A. Kepler
e-mail: jk@m-tech.aau.dk

Department of Mechanical and Manufacturing
Engineering, Aalborg University,
Fibigerstræde 16,
DK-9220 Aalborg East, Denmark

Stéphane Caro
Institut de Recherche en Communications et
Cybernétique de Nantes, France
e-mail: stephane.caro@irccyn.ec-nantes.fr

Error Modeling and Experimental Validation of a Planar 3-PPR Parallel Manipulator With Joint Clearances

This paper deals with the error modeling and analysis of a 3-PPR planar manipulator with joint clearances. The kinematics and the Cartesian workspace of the manipulator are analyzed. An error model is established with considerations of both configuration errors and joint clearances. Using this model, the upper bounds and distributions of the pose errors for this manipulator are established. The results are compared with experimental measurements and show the effectiveness of the error prediction model. [DOI: 10.1115/1.4007487]

1 Introduction

The planar parallel manipulators (PPMs) with three identical kinematic chains are special parallel manipulators (PMs), whose motion is confined in a plane. For this type of PM, the error modeling and analysis are important for both design and control in order to utilize the PMs potential of high accuracy in applications.

A number of works on accuracy analysis of parallel mechanisms can be found in the literature. Ryu and Cha derived a volumetric error model and a total error transformation matrix from a differential inverse kinematic equation, which includes possible kinematic error sources [1]. Liu et al. reported an approach of geometric error modeling for lower mobility manipulators by explicitly separating the compensatable and uncompensatable error sources affecting the pose accuracy [2]. Yu et al. reported a simple geometric approach to computing the exact local maximum position and orientation error by illustrating several different types of 3-dof planar parallel robots [3]. Briot and Bonev proposed a method based on geometric approach for detailed error analysis of a fully parallel robot with three translations and one rotation that brings valuable understanding of the error amplification problem [4].

Research focusing on the influence of joint clearances has been reported too. Lin and Chen proposed a homogeneous error transformation matrix to assess the effects of joint clearances on pose errors [5]. Ting et al. presented a simple method to identify the worst position and direction errors due to the joint clearance of linkages and manipulators, which offers a geometrical model to warranty the precision of a mechanism [6]. Fogarasy and Smith utilized the derivatives of the closure equations to obtain a first order approximation of the output error, which is called the Jacobian method [7]. Regarding the errors of universal and spherical joints due to clearances as a part of link errors, Lim et al. [8] analyzed the dynamic error of a cubic parallel mechanism by using its forward kinematics. Castelli and Venanzi applied the virtual work principle to determine the position of the end-effector when a given external load is applied [9,10]. Meng et al. proposed an error model of PMs subject to joint clearances by formulating the error prediction model as a standard convex optimization problem [11], of which the constraints are formed through a set of inequalities about the joint clearances. A general error prediction model considering joint clearances was established for serial and parallel

manipulators by means of differential screw theory in Ref. [12]. It was used to analyze the kinematic sensitivity of a 3-PPR parallel manipulator to joint clearances in Ref. [13]. Wei and Simaan proposed an approach for designing inexpensive planar parallel robots with prescribed backlash-free workspace by using preloaded flexible joints to replace the passive joints [14]. Among the sources of errors, the influence of assembly and manufacturing errors and actuation errors can be eliminated as indicated in Refs. [5,15–17] by calibration, except joint clearances due to its low repeatability. It means that the pose errors due to joint clearances require a special consideration. Simple and valid methods of error modeling for PPMs are needed for accuracy analysis.

In this paper, the error analysis of PPMs is studied with consideration of both configuration errors and joint clearances. An error model is established, upon which the maximal error problem was transformed into an optimization problem. The distributions of global maximal pose errors in the prescribed workspace can be formulated effectively. Moreover, the error model based on the joint clearances was validated experimentally. The work was conducted for a novel 3-PPR PPM with a nonsymmetrical base [18], which has a larger workspace and the same level of motion accuracy compared to the traditional symmetrical PPMs.

This paper is organized as follows. The architecture of the manipulator under study is presented in Sec. 2. The kinematics and Cartesian workspace are analyzed in Sec. 3. The error prediction model is established in Sec. 4. Sections 5 and 6 present the experimental validation, in which measured results are compared with the simulations. The work is concluded in Sec. 7.

2 Manipulator Under Study

Figure 1 presents the Computer-Aided Design (CAD) model of the planar 3-PPR parallel manipulator with a rigid equilateral triangle-shape moving platform (MP). Here and throughout this paper, P and R stand for prismatic and revolute joints, respectively. An underlined letter indicates an actuated joint. Each leg is driven by a *CAL* 35 actuator, a high resolution linear motor built with an encoder of 5 μm accuracy from SMAC company [19]. A THK linear guide of model HRW17 is used as the active prismatic joint P. A linear bearing mounted on the slider of the linear guide is used as the passive prismatic joint in each leg. The ball joints in Fig. 1 are preloaded, of which joint clearance does not exist. For the built physical prototype, the end-effector can also be replaced by a disk-shape MP with ordinary revolute joints to couple the three legs, but this introduces more error sources due to the clearances between the pin and the hole of the revolute joint.
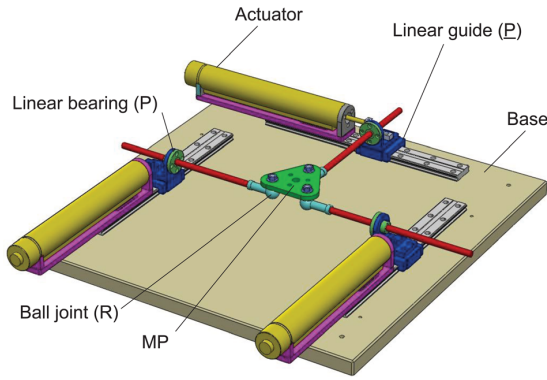

Fig. 1   CAD model of a 3-PPR PPM

The parameterization of the 3-PPR PPM is illustrated in Fig. 2, where A_i, $i = 1, 2, 3$, are fixed points on the base. The *x*-axis of the coordinate system $\mathcal{F}_b$ is parallel to the segment A_1A_2. The origin *P* of the coordinate system $\mathcal{F}_p$ is located at the geometric center of the triangle $\Delta D_1D_2D_3$ on the moving platform and the *X*-axis is parallel to the segment D_1D_2, where D_i, $i = 1, 2, 3$, are the centers of the revolute joints. The translational and orientational displacements of the MP are denoted by **p** and ϕ, where $\mathbf{p} = [x, y]$, *x* and *y* being the Cartesian coordinates of point *P* in $\mathcal{F}_b$.

3   Kinematic Modeling of the 3-PPR PPM

The kinematic modeling of the manipulator is described in this section. The workspace and singularities of the manipulator are also analyzed based on its closure equations.

From the closed-loop kinematic chains $O - A_i - B_i - C_i - D_i - P - O$ shown in Fig. 2, the position vector of point *P* can be expressed in $\mathcal{F}_b$ as follows:

$$\mathbf{p} = a_i\mathbf{h}_i + s_i\mathbf{u}_i + d_i\mathbf{v}_i + l_i\mathbf{w}_i + r_i\mathbf{k}_i, \ i = 1, 2, 3 \qquad (1)$$

with

$$\mathbf{h}_i = \begin{bmatrix} \cos\alpha_i \\ \sin\alpha_i \end{bmatrix}, \quad \mathbf{u}_i = \begin{bmatrix} \cos\beta_i' \\ \sin\beta_i' \end{bmatrix}, \quad \mathbf{v}_i = \begin{bmatrix} \cos\gamma_i' \\ \sin\gamma_i' \end{bmatrix},$$

$$\mathbf{w}_i = \begin{bmatrix} \cos\theta_i' \\ \sin\theta_i' \end{bmatrix}, \quad \mathbf{k}_i = \begin{bmatrix} \cos(\phi + \psi_i) \\ \sin(\phi + \psi_i) \end{bmatrix}$$
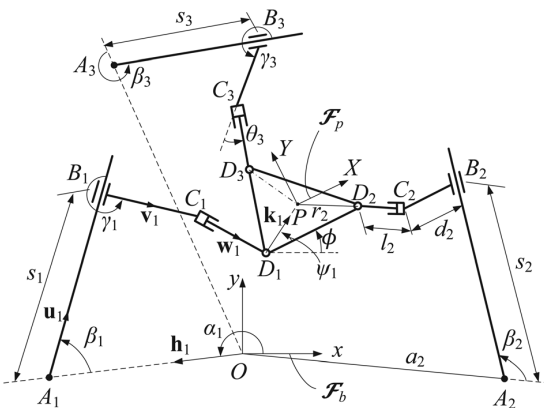

Fig. 2   Parameterization of the 3-PPR PPM

and

$$\beta_i' = \alpha_i + \beta_i, \gamma_i' = \alpha_i + \beta_i + \gamma_i, \theta_i' = \alpha_i + \beta_i + \gamma_i + \theta_i$$

The inverse kinematics of the manipulator can be derived from Eq. (1)

$$s_i = (\mathbf{w}_i^T \mathbf{E}\mathbf{u}_i)^{-1}\mathbf{w}_i^T \mathbf{E}(\mathbf{p} - a_i\mathbf{h}_i - d_i\mathbf{v}_i - r_i\mathbf{k}_i) \qquad (2a)$$

$$l_i = (\mathbf{u}_i^T \mathbf{E}\mathbf{w}_i)^{-1}\mathbf{u}_i^T \mathbf{E}(\mathbf{p} - a_i\mathbf{h}_i - d_i\mathbf{v}_i - r_i\mathbf{k}_i) \qquad (2b)$$

matrix **E** is the right angle rotation matrix defined as

$$\mathbf{E} = \begin{bmatrix} 0 & -1 \\ 1 & 0 \end{bmatrix}$$

Equation (1) establishes a system of six equations. The forward displacements can be solved by virtue of analytical method. The velocity expression of the manipulator can be derived from Eq. (1) as below

$$\mathbf{A}\begin{bmatrix} \dot{\mathbf{p}} \\ \dot{\phi} \end{bmatrix} = \mathbf{B}\dot{\mathbf{s}} \qquad (3)$$

with

$$\mathbf{A} = \begin{bmatrix} \mathbf{w}_1^T\mathbf{E}^T & -r_1\mathbf{w}_1^T\mathbf{k}_1 \\ \mathbf{w}_2^T\mathbf{E}^T & -r_2\mathbf{w}_2^T\mathbf{k}_2 \\ \mathbf{w}_3^T\mathbf{E}^T & -r_3\mathbf{w}_3^T\mathbf{k}_3 \end{bmatrix} \qquad (4a)$$

$$\mathbf{B} = \mathrm{diag}\begin{bmatrix} \mathbf{w}_1^T\mathbf{E}^T\mathbf{u}_1 & \mathbf{w}_2^T\mathbf{E}^T\mathbf{u}_2 & \mathbf{w}_3^T\mathbf{E}^T\mathbf{u}_3 \end{bmatrix} \qquad (4b)$$

$$\dot{\mathbf{s}} = \begin{bmatrix} \dot{s}_1 & \dot{s}_2 & \dot{s}_3 \end{bmatrix}^T \qquad (4c)$$

where **A** and **B** are the forward and backward Jacobians of the manipulator, respectively. The kinematic Jacobian matrix **J** of the manipulator takes the form

$$\mathbf{J} = \mathbf{A}^{-1}\mathbf{B} \qquad (5)$$

Matrix **A** is singular, i.e., the manipulator reaches a parallel singularity, when $\phi = \pm\pi/2$. Matrix **B** is never singular, namely, the manipulator is free of serial singularity.

The reachable area of the moving platform with a constant orientation can be obtained geometrically by means of searching method [13,18], where the inverse kinematics model, namely, Eqs. (2a) and (2b), establish a system of 12 inequations by virtue of the joint motion limits to formulate the motion constraints of the MP. With the parameters shown in Table 1 and $r_i = r = 30$ mm, $a_i = 192.34$ mm, $i = 1, 2, 3$, constant-orientation Cartesian workspaces for three orientations of the MP are illustrated in Fig. 3.

4   Error Modeling of a 3-PPR PPM

Here, a methodology introduced in Ref. [20] was used to derive the error model of the MP pose with regard to variations in the actuated and passive joints as well as in the Cartesian coordinates of points A_i, B_i, C_i, and D_i, $i = 1, 2, 3$.

Table 1   The design parameters of the 3-PPR PPM

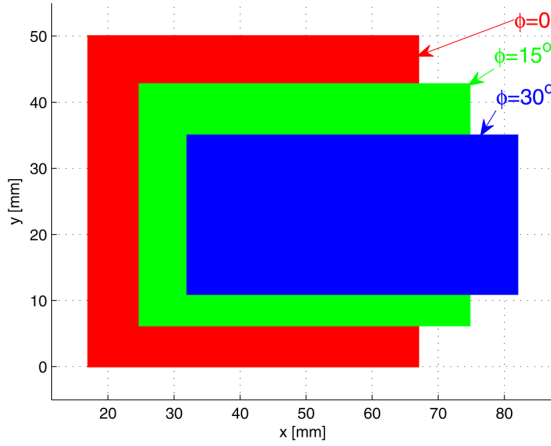| i	α_i(rad)	$\beta\prime_i$(rad)	γ_i', θ_i'(rad)	ψ_i(rad)	d_i(mm)
1	-2.781	$\pi/2$	0	$\pi/6$	114
2	-0.360	$\pi/2$	π	$5\pi/6$	27
3	1.751	0	$-\pi/2$	$3\pi/2$	42

Fig. 3 Constant-orientation workspaces

4.1 Error Prediction Model. The clearance in the revolute joint between the ith leg and the moving platform is characterized by the small displacement between points D_i and point D_i' as shown in Fig. 4. Upon differentiation of Eq. (1), we obtain the positioning error of point P with respect to each leg

$$\delta\mathbf{p} = \delta a_i\mathbf{h}_i + a_i\delta\alpha_i\mathbf{E}\mathbf{h}_i + \delta s_i\mathbf{u}_i + s_i\delta\beta_i'\mathbf{E}\mathbf{u}_i + \delta d_i\mathbf{v}_i$$
$$+ d_i\delta\gamma_i'\mathbf{E}\mathbf{v}_i + \delta l_i\mathbf{w}_i + l_i\delta\theta_i'\mathbf{E}\mathbf{w}_i + \delta\rho_i\mathbf{n}_i \quad (6)$$
$$+ \delta r_i\mathbf{k}_i + r_i(\delta\phi + \delta\psi_i)\mathbf{E}\mathbf{k}_i, i = 1, 2, 3$$

where

$$\delta\beta_i' = \delta\alpha_i + \delta\beta_i$$
$$\delta\gamma_i' = \delta\alpha_i + \delta\beta_i + \delta\gamma_i \quad (7)$$
$$\delta\theta_i' = \delta\alpha_i + \delta\beta_i + \delta\gamma_i + \delta\theta_i$$

where $\delta\mathbf{p}$ and $\delta\phi$ are the positioning and orientation errors of the moving platform expressed in $\mathcal{F}_b$, respectively. Moreover, $\delta a_i, \delta\alpha_i, \delta s_i, \delta\beta_i, \delta d_i, \delta\gamma_i, \delta l_i, \delta\theta_i, \delta r_i,$ and $\delta\psi_i$ denote variations in the geometric parameters illustrated in Fig. 4. In addition, $\delta\rho_i$ is a small displacement between point D_i and point $D\iota_i$ due to the clearance in the ith revolute joint and $\mathbf{n}_i = [\cos\varphi_i, \sin\varphi_i]^T$, as illustrated in Fig. 5(b). Substituting Eqs. (7) into (6) and eliminating the idle variation δl_i lead to
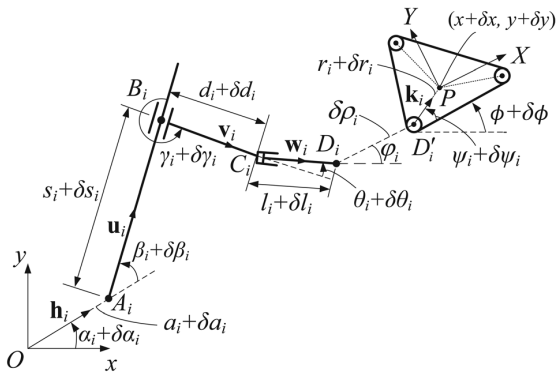

Fig. 4 Parameterization of the ith leg

$$\mathbf{w}_i^T\mathbf{E}^T\delta\mathbf{p} = \delta a_i\mathbf{w}_i^T\mathbf{E}^T\mathbf{h}_i + \delta\alpha_i\left[\mathbf{w}_i^T(a_i\mathbf{h}_i + s_i\mathbf{u}_i + d_i\mathbf{v}_i) + l_i\right]$$
$$+ \delta s_i\mathbf{w}_i^T\mathbf{E}^T\mathbf{u}_i + \delta\beta_i\left[\mathbf{w}_i^T(s_i\mathbf{u}_i + d_i\mathbf{v}_i) + l_i\right]$$
$$+ \delta d_i\mathbf{w}_i^T\mathbf{E}^T\mathbf{v}_i + \delta\gamma_i(d_i\mathbf{w}_i^T\mathbf{v}_i + l_i) + l_i\delta\theta_i \quad (8)$$
$$+ \delta\rho_i\mathbf{w}_i^T\mathbf{E}^T\mathbf{n}_i + \delta r_i\mathbf{w}_i^T\mathbf{E}^T\mathbf{k}_i + r_i(\delta\phi + \delta\psi_i)\mathbf{w}_i^T\mathbf{k}_i$$

Equation (8) can be cast in vector form

$$\mathbf{A}\begin{bmatrix}\delta x\\\delta y\\\delta\phi\end{bmatrix} = \mathbf{H}_a\begin{bmatrix}\delta a_1\\\delta a_2\\\delta a_3\end{bmatrix} + \mathbf{H}_\alpha\begin{bmatrix}\delta\alpha_1\\\delta\alpha_2\\\delta\alpha_3\end{bmatrix} + \mathbf{B}\begin{bmatrix}\delta s_1\\\delta s_2\\\delta s_3\end{bmatrix}$$
$$+ \mathbf{H}_\beta\begin{bmatrix}\delta\beta_1\\\delta\beta_2\\\delta\beta_3\end{bmatrix} + \mathbf{H}_d\begin{bmatrix}\delta d_1\\\delta d_2\\\delta d_3\end{bmatrix} + \mathbf{H}_\gamma\begin{bmatrix}\delta\gamma_1\\\delta\gamma_2\\\delta\gamma_3\end{bmatrix}$$
$$+ \mathbf{H}_\theta\begin{bmatrix}\delta\theta_1\\\delta\theta_2\\\delta\theta_3\end{bmatrix} + \mathbf{H}_\rho\begin{bmatrix}\delta\rho_1\\\delta\rho_2\\\delta\rho_3\end{bmatrix} \quad (9)$$
$$+ \mathbf{H}_r\begin{bmatrix}\delta r_1\\\delta r_2\\\delta r_3\end{bmatrix} + \mathbf{H}_\psi\begin{bmatrix}\delta\psi_1\\\delta\psi_2\\\delta\psi_3\end{bmatrix}$$

where all $\mathbf{H}_q, q \in \{a, \alpha, \beta, d, \gamma, \theta, \rho, r, \psi\}$, are 3×3 matrices as given in Appendix A. Moreover, assuming that $\mathbf{A}$ is nonsingular, the multiplication of both sides of Eq. (9) by $\mathbf{A}^{-1}$ leads to

$$\begin{bmatrix}\delta x\\\delta y\\\delta\phi\end{bmatrix} = \mathbf{J}_a\begin{bmatrix}\delta a_1\\\delta a_2\\\delta a_3\end{bmatrix} + \mathbf{J}_\alpha\begin{bmatrix}\delta\alpha_1\\\delta\alpha_2\\\delta\alpha_3\end{bmatrix} + \mathbf{J}\begin{bmatrix}\delta s_1\\\delta s_2\\\delta s_3\end{bmatrix} + \mathbf{J}_\beta\begin{bmatrix}\delta\beta_1\\\delta\beta_2\\\delta\beta_3\end{bmatrix}$$
$$+ \mathbf{J}_d\begin{bmatrix}\delta d_1\\\delta d_2\\\delta d_3\end{bmatrix} + \mathbf{J}_\gamma\begin{bmatrix}\delta\gamma_1\\\delta\gamma_2\\\delta\gamma_3\end{bmatrix} + \mathbf{J}_\theta\begin{bmatrix}\delta\theta_1\\\delta\theta_2\\\delta\theta_3\end{bmatrix} \quad (10)$$
$$+ \mathbf{J}_\rho\begin{bmatrix}\delta\rho_1\\\delta\rho_2\\\delta\rho_3\end{bmatrix} + \mathbf{J}_r\begin{bmatrix}\delta r_1\\\delta r_2\\\delta r_3\end{bmatrix} + \mathbf{J}_\psi\begin{bmatrix}\delta\psi_1\\\delta\psi_2\\\delta\psi_3\end{bmatrix}$$

with

$$\mathbf{J}_q = \mathbf{A}^{-1}\mathbf{H}_q, q \in \{a, \alpha, \beta, d, \gamma, \theta, \rho, r, \psi\} \quad (11)$$

where $\mathbf{J}$ and $\mathbf{J}_q$ are the sensitivity coefficients of the MP pose of the manipulator to variations in terms of coordinates of each link [20]. It will be more useful to find the sensitivity coefficients in the coordinates of all joint positions, namely, points A_i, B_i, C_i, and D_i. By making use of

$$\begin{bmatrix}\delta a_{ix}\\\delta a_{iy}\end{bmatrix} = \begin{bmatrix}\cos\alpha_i & -a_i\sin\alpha_i\\\sin\alpha_i & a_i\cos\alpha_i\end{bmatrix}\begin{bmatrix}\delta a_i\\\delta\alpha_i\end{bmatrix} \quad (12a)$$

$$\begin{bmatrix}\delta b_{ix}\\\delta b_{iy}\end{bmatrix} = \begin{bmatrix}\cos\beta_i & -s_i\sin\beta_i\\\sin\beta_i & s_i\cos\beta_i\end{bmatrix}\begin{bmatrix}0\\\delta\beta_i\end{bmatrix} \quad (12b)$$

$$\begin{bmatrix}\delta c_{ix}\\\delta c_{iy}\end{bmatrix} = \begin{bmatrix}\cos\gamma_i & -d_i\sin\gamma_i\\\sin\gamma_i & d_i\cos\gamma_i\end{bmatrix}\begin{bmatrix}\delta d_i\\\delta\gamma_i\end{bmatrix} \quad (12c)$$

$$\begin{bmatrix}\delta d_{ix}\\\delta d_{iy}\end{bmatrix} = \begin{bmatrix}\cos\psi_i & -r_i\sin\psi_i\\\sin\psi_i & r_i\cos\psi_i\end{bmatrix}\begin{bmatrix}\delta r_i\\\delta\psi_i\end{bmatrix} \quad (12d)$$

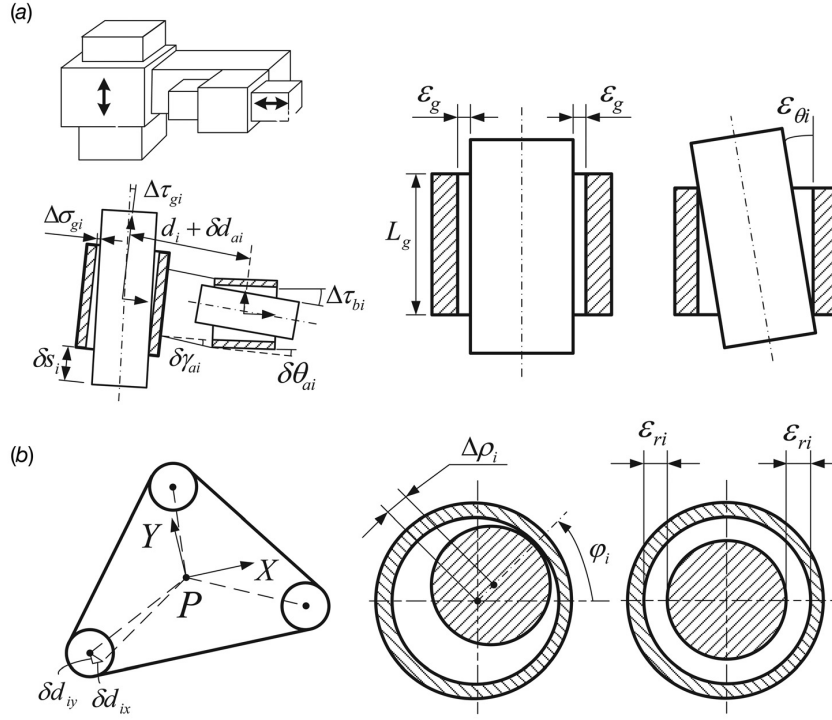**Fig. 5 Geometric errors and joint clearances related to the *i*th leg: (*a*) prismatic joint and (*b*) revolute joint**

Equation (10) is transformed as

$$
\begin{bmatrix} \delta\mathbf{p} \\ \delta\phi \end{bmatrix} = \mathbf{J} \begin{bmatrix} \delta s_1 \\ \delta s_2 \\ \delta s_3 \end{bmatrix} + \mathbf{J}_\theta \begin{bmatrix} \delta\theta_1 \\ \delta\theta_2 \\ \delta\theta_3 \end{bmatrix} + \mathbf{J}_\rho \begin{bmatrix} \delta\rho_1 \\ \delta\rho_2 \\ \delta\rho_3 \end{bmatrix} + \mathbf{J}_A \begin{bmatrix} \delta a_{1x} \\ \delta a_{1y} \\ \delta a_{2x} \\ \delta a_{2y} \\ \delta a_{3x} \\ \delta a_{3y} \end{bmatrix}
$$

$$
+ \mathbf{J}_B \begin{bmatrix} \delta b_{1x} \\ \delta b_{1y} \\ \delta b_{2x} \\ \delta b_{2y} \\ \delta b_{3x} \\ \delta b_{3y} \end{bmatrix} + \mathbf{J}_C \begin{bmatrix} \delta c_{1x} \\ \delta c_{1y} \\ \delta c_{2x} \\ \delta c_{2y} \\ \delta c_{3x} \\ \delta c_{3y} \end{bmatrix} + \mathbf{J}_D \begin{bmatrix} \delta d_{1x} \\ \delta d_{1y} \\ \delta d_{2x} \\ \delta d_{2y} \\ \delta d_{3x} \\ \delta d_{3y} \end{bmatrix} \tag{13}
$$

where δa_{ix} and δa_{iy} (δb_{ix} and δb_{iy}, δc_{ix}, and δc_{iy}, resp.) are the positioning errors of point A_i (B_i, C_i, resp.), $i = 1, 2, 3$, along x- and y-axes, namely, the variations in the Cartesian coordinates. Notice that δd_{ix} and δd_{iy} denote the positioning errors of points $Dι_i$ along X- and Y-axes, namely, the variations in the Cartesian coordinates of D_i'. The 3×6 matrices $\mathbf{J}_A, \mathbf{J}_B, \mathbf{J}_C$, and $\mathbf{J}_D$ can be found in Appendix A. Equation (13) can be written in the following form:

$$
\begin{bmatrix} \delta\mathbf{p} \\ \delta\phi \end{bmatrix} = \mathbf{J}_{\mathrm{err}}\boldsymbol{\delta}_{\mathrm{var}} \tag{14}
$$

where

$$
\mathbf{J}_{\mathrm{err}} = \begin{bmatrix} \mathbf{J} & \mathbf{J}_\theta & \mathbf{J}_\rho & \mathbf{J}_A & \mathbf{J}_B & \mathbf{J}_C & \mathbf{J}_D \end{bmatrix} \tag{15a}
$$

$$
\boldsymbol{\delta}_{\mathrm{var}} = \begin{bmatrix} \delta\mathbf{s}^T & \delta\boldsymbol{\theta}^T & \delta\boldsymbol{\rho}^T & \delta\mathbf{a}^T & \delta\mathbf{b}^T & \delta\mathbf{c}^T & \delta\mathbf{d}^T \end{bmatrix}^T \tag{15b}
$$

with

$$
\delta\mathbf{s} = \begin{bmatrix} \delta s_1 \\ \delta s_2 \\ \delta s_3 \end{bmatrix}, \quad \delta\boldsymbol{\theta} = \begin{bmatrix} \delta\theta_1 \\ \delta\theta_2 \\ \delta\theta_3 \end{bmatrix}, \quad \delta\boldsymbol{\rho} = \begin{bmatrix} \delta\rho_1 \\ \delta\rho_2 \\ \delta\rho_3 \end{bmatrix}, \quad \delta\mathbf{e} = \begin{bmatrix} \delta\mathbf{e}_1 \\ \delta\mathbf{e}_2 \\ \delta\mathbf{e}_3 \end{bmatrix}
$$

$$
\delta\mathbf{e}_i = \begin{bmatrix} \delta e_{ix} & \delta e_{iy} \end{bmatrix}^T, \quad e \in \{a, b, c, d\}, \quad i = 1, 2, 3
$$

where $\mathbf{J}_{\mathrm{err}}$ is the global sensitivity Jacobian matrix and $\boldsymbol{\delta}_{\mathrm{var}}$ is a vector containing all variations. For a given posture, all submatrices except $\mathbf{J}_\rho$ are known.

4.2 Modeling the Joint Clearances. Figure 5 illustrates the assembly errors and clearances in the prismatic and revolute joints. $\delta d_{ai}, \delta\beta_i, \delta\gamma_{ai}$ and $\delta\theta_{ai}$, $i = 1, 2, 3$, are the assembly errors while δd_{ix} and δd_{iy} correspond to the manufacturing errors. Moreover, $\Delta\sigma_{gi}, \Delta\tau_{gi}, \Delta\tau_{bi}$ and $\Delta\rho_i$ are the displacements due to joint clearances. Then, we have

$$
\delta d_i = \delta d_{ai} + \Delta\sigma_{gi}, \delta\gamma_i = \delta\gamma_{ai} + \Delta\tau_{gi}, \delta\theta_i = \delta\theta_{ai} + \Delta\tau_{bi}
$$

The errors due to the clearances in the linear guides are characterized by the following constraints [11]:

$$
-2\varepsilon_{gi} \leq L_g\Delta\tau_{gi} + 2\Delta\sigma_{gi} \leq 2\varepsilon_{gi} \tag{16a}
$$

$$
-2\varepsilon_{gi} \leq -L_g\Delta\tau_{gi} + 2\Delta\sigma_{gi} \leq 2\varepsilon_{gi} \tag{16b}
$$

where ε_{gi} specifies the lateral clearance and L_g is the length of the linear guide block. Alternatively, the errors in the linear bearing are constrained by the following condition:

$$-\varepsilon_{\theta i} \leq \Delta\tau_{bi} \leq \varepsilon_{\theta i} \tag{17}$$

where $\varepsilon_{\theta i}$ is the upper bound of $\Delta\tau_{bi}$. Figure 5(a) demonstrates the tolerances of the linear guides and bearing. The clearances in the three revolute joints meet the following constraint:

$$0 \leq \Delta\rho_i \leq \varepsilon_{ri}, \; i = 1, 2, 3 \tag{18}$$

where ε_{ri} is the range of variations $\Delta\rho_i$ due to the joint clearance shown in Fig. 5(b).

4.3 Maximum Pose Errors of the Moving Platform With Joint Clearances.

The pose errors due to the assembly and actuation errors can be determined from Eq. (14), while the errors due to joint clearances will be solved by virtue of an optimization method. When only joint clearances are considered, the relationship between the pose errors and joint clearances becomes:

$$\begin{bmatrix} \delta\mathbf{p} \\ \delta\phi \end{bmatrix} = \mathbf{J}_{err}^c \boldsymbol{\delta}_{var}^c \tag{19}$$

with

$$\mathbf{J}_{err}^c = [\, \mathbf{J}_\theta \quad \mathbf{J}_d \quad \mathbf{J}_\gamma \quad \mathbf{J}_\rho \,]_{3\times 12} \rightarrow \equiv \begin{bmatrix} \mathbf{J}_{err,x}^c \\ \mathbf{J}_{err,y}^c \\ \mathbf{J}_{err,\phi}^c \end{bmatrix} \tag{20a}$$

$$\boldsymbol{\delta}_{var}^c = [\, \Delta\tau_{b1} \quad \Delta\tau_{b2} \quad \Delta\tau_{b3} \quad \Delta\sigma_{g1} \quad \Delta\sigma_{g2} \quad \Delta\sigma_{g3} \quad \Delta\tau_{g1} \quad \Delta\tau_{g2} \quad \Delta\tau_{g3} \quad \Delta\rho_1 \quad \Delta\rho_2 \quad \Delta\rho_3 \,]^T \tag{20b}$$

where $\mathbf{J}_{err,x}^c, \mathbf{J}_{err,y}^c, \mathbf{J}_{err,\phi}^c$ are three 1×12 submatrices corresponding to the first, the second, and the third rows of $\mathbf{J}_{err}^c$. The maximum positioning error along x-axis, y-axis, and the maximum orientation error of the MP, namely, $\delta x_{max}, \delta y_{max}$ and $\delta\phi_{max}$, can be obtained by solving the following optimization problem:

$$\delta\zeta_{max}^2 \equiv \max\left(\mathbf{J}_{err,\zeta}^c \boldsymbol{\delta}_{var}^c\right)^2 \text{ for } x, y, \phi \in \Omega \tag{21}$$

$$\begin{aligned} \text{ST} \quad &-2\varepsilon_{gi} \leq L_g\Delta\tau_{gi} + 2\Delta\sigma_{gi} \leq 2\varepsilon_{gi} \\ &-2\varepsilon_{gi} \leq -L_g\Delta\tau_{gi} + 2\Delta\sigma_{gi} \leq 2\varepsilon_{gi} \\ &-\varepsilon_{\theta i} \leq \Delta\tau_{bi} \leq \varepsilon_{\theta i} \\ &0 \leq \Delta\rho_i \leq \varepsilon_{ri} \\ &0 \leq \varphi_i \leq 2\pi \\ &i = 1, 2, 3, \zeta \in \{x, y, \phi\} \end{aligned}$$

where Ω denotes the Cartesian workspace of the manipulator defined in Sec. 3. Optimization problem of Eq. (21) aims at finding separately the maximum positioning errors along the x-axis and y-axis and the maximum orientation error of the moving platform. Note that the three maximum errors are subject to the same constraints, hence, the optimization problems are written in a generalized form.

The maximum positioning error δp_{max} is obtained by solving the following optimization problem:

$$\delta p_{max}^2 \equiv \max\left(\mathbf{J}_{err,p}^c \boldsymbol{\delta}_{var}^c\right)^T \left(\mathbf{J}_{err,p}^c \boldsymbol{\delta}_{var}^c\right) \text{ for } x, y, \phi \in \Omega \tag{22}$$

$$\begin{aligned} \text{ST} \quad &-2\varepsilon_{gi} \leq L_g\Delta\tau_{gi} + 2\Delta\sigma_{gi} \leq 2\varepsilon_{gi} \\ &-2\varepsilon_{gi} \leq -L_g\Delta\tau_{gi} + 2\Delta\sigma_{gi} \leq 2\varepsilon_{gi} \\ &-\varepsilon_{\theta i} \leq \Delta\tau_{bi} \leq \varepsilon_{\theta i} \\ &0 \leq \Delta\rho_i \leq \varepsilon_{ri} \\ &0 \leq \varphi_i \leq 2\pi \\ &i = 1, 2, 3 \end{aligned}$$

where $\mathbf{J}_{err,p}^c = [\, \mathbf{J}_{err,x}^{c\;T} \quad \mathbf{J}_{err,y}^{c\;T} \,]^T$. The foregoing optimization problems are solved using the MATLAB *fmincon* function. According to the product catalogues, the clearance in the lateral direction of the linear guide is equal to $3\mu m$, namely, $2\varepsilon_{gi} = 2\varepsilon_g = 3\mu m$. As a consequence, the errors due to the linear guides are negligible. δa_{ix} and δa_{iy} are set to zero too. Finally, the maximum position

error and the maximum orientation error of the MP can be evaluated from Eqs. (21) and (22) for any configuration of the manipulator by known joint clearances and geometric tolerances.

5 Experimental Setup and Measurement Errors

A main purpose of the work is to experimentally validate the error model developed. To this end, experiments have been conducted in which the position and orientation of the MP were measured with a vision-based system composed of a single Charge-Coupled Device (CCD) camera. The experimental setup is shown in Fig. 6(a) and its specifications are given hereafter:

- DVT 554c smart camera with 1280×1024 pixel resolution ($7.4\mu m \times 7.4\mu m$ pixels) from Cognex [21] was fixed right above the MP for pose measurements.
- INTELLECT 1.5.1, a vision software from Cognex [22], was used to establish the communication with the camera via data cable as shown in Fig. 6(b). The Blobs are used to locate markers on the MP.

With this system, the position and orientation measurement accuracies are 0.01 mm and 0.01 deg, respectively.

5.1 Measurements.
Before the measurements, the system was calibrated. A standard calibration paper with markers of 2 cm spacing from Cognex was used to establish the reference frame. The calibration method is described in the INTELLECT 1.5 Guide [22].

5.1.1 Assembly Errors. In measuring configuration error, the first linear guide was used as the y-axis of the reference frame, which means $\delta\beta_1 = 0$. The measurement is illustrated in Fig. 7. Four holes on each linear guide were used as the markers. $\delta\beta_2$ and $\delta\beta_3$ can be obtained by means of the INTELLECT software. Similarly, a perfect regular component with four uniformly distributed holes was used to measure the assembly errors $\delta\gamma_{ai}$ and $\delta\theta_{ai}$ by means of face to face alignments. The measured assembly errors are listed in Table 2.

5.1.2 Joint Clearances. Figure 8 illustrates the method used to measure the clearance in the linear bearing. Pushing the right end of the shaft back and forth and measuring the difference of the two counts δ_{LB}, the value of δ_{LB}/L_s was adopted as the bound of angular clearance. For the revolute joint clearances, the diameters of the joint pin and the cylinder were measured, respectively. The half value of the difference of the two measurements was adopted as the clearance bound. The bounds of the joint clearances were found as
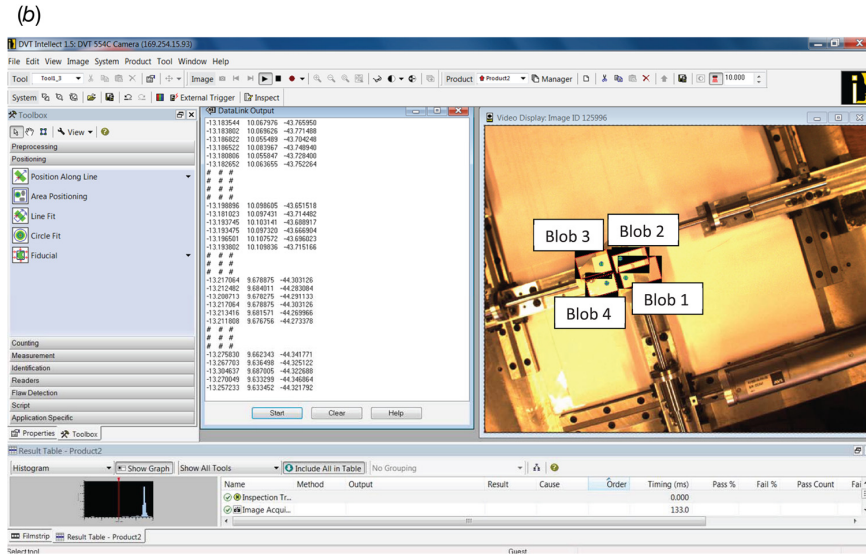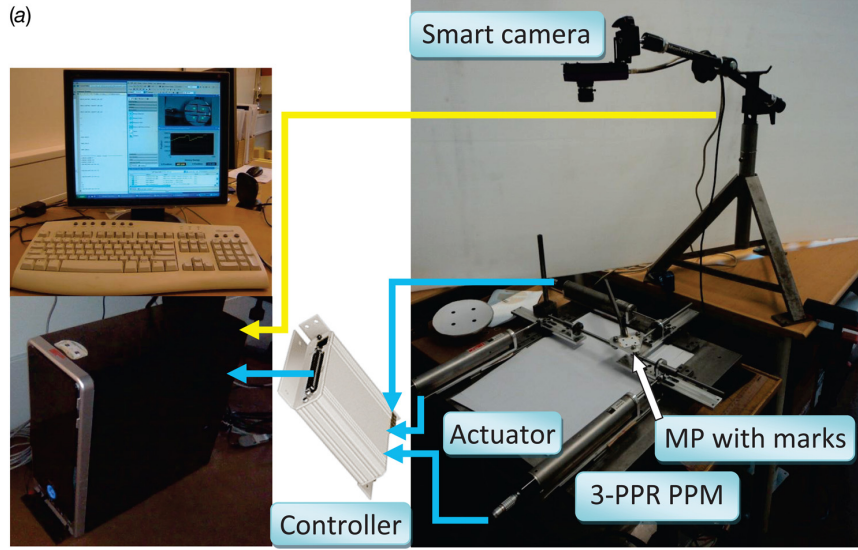
Fig. 6 A vision-based system for the moving platform pose measurement: (a) experimental setup and (b) measurement interface

$$\varepsilon_{\theta i} = \varepsilon_\theta = 0.0012 \text{ rad}, \quad i = 1, 2, 3$$

$$\varepsilon_{r1} = 0.039 \text{ mm}, \quad \varepsilon_{r2} = 0.036 \text{ mm}, \quad \varepsilon_{r3} = 0.037 \text{ mm}$$

5.2 Pose Errors of MP. The measurements were conducted with two cases:

- Case 1: a case with only clearances in the passive prismatic joints
- Case 2: a case with clearances in both passive prismatic and revolute joints

The two cases were physically implemented with two different shapes for the moving platform in Sec. 2, respectively, namely, the equilateral triangle MP (Δ-shape MP) and the disk-shape MP ($\bigcirc$-shape MP), which are associated with Cases 1 and 2. We first fixed on the MP a calibration paper with 2×2 marks of 2 cm separation in case 1. Then, $i \times j$ uniformly distributed points were measured throughout the Cartesian workspace of the manipulator.
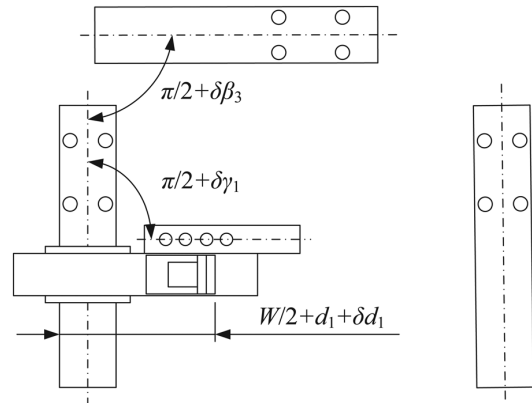
Fig. 7 Measurement of the assembly errors

Table 2 Measurements of assembly errors

i	$\delta\beta_i\,(\mathrm{rad})$	$\delta\gamma_{ai}\,(\mathrm{rad})$	$\delta\theta_{ai}\,(\mathrm{rad})$	$\delta d_{ai}\,(\mathrm{mm})$
1	0	0.016	−0.028	−0.12
2	0.014	0.020	−0.022	−0.08
3	−0.010	0.020	0.034	0.15

Fig. 8 Measurement of the angular clearance in the linear bearing

During the measurements, the actuators were locked to eliminate the errors in the actuators. At the (i, j) point, the MP was slightly pushed bidirectionally along the x-axis, y-axis, and rotated about the z-axis, respectively. The corresponding readings were noted as $(x, y, 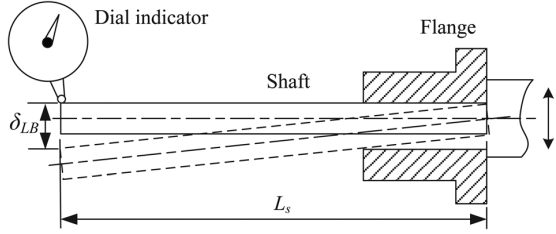\phi)^{ij}_{+t}$ and $(x, y, \phi)^{ij}_{-t}$, $t \in \{x, y, r\}$, respectively. The measured positioning and orientation errors at the (i, j) point are defined as:

$$\delta x^{ij} = \max\left\{x^{ij}_{+t}, x^{ij}_{-t}\right\} - \min\left\{x^{ij}_{+t}, x^{ij}_{-t}\right\} \qquad (23a)$$

$$\delta y^{ij} = \max\left\{y^{ij}_{+t}, y^{ij}_{-t}\right\} - \min\left\{y^{ij}_{+t}, y^{ij}_{-t}\right\} \qquad (23b)$$

$$\delta\phi^{ij} = \max\left\{\phi^{ij}_{+t}, \phi^{ij}_{-t}\right\} - \min\left\{\phi^{ij}_{+t}, \phi^{ij}_{-t}\right\} \qquad (23c)$$

$$\delta p^{ij} = \max\left\{\delta p^{ij}_t\right\}, \delta p^{ij}_t = \sqrt{(x^{ij}_{+t} - x^{ij}_{-t})^2 + (y^{ij}_{+t} - y^{ij}_{-t})^2} \qquad (23d)$$

6 Results and Discussion

In this section, the predicted maximum pose errors from the model and measured errors from the experiments are presented and compared.

6.1 Error Distributions for Case 1. Figure 6 represents the error distribution of the moving platform for a given orientation $\phi = 0$. Figure 9(a) shows that the simulated $\delta x_{\max}$ is constant for a given y-coordinate and decreases slightly with the y-coordinate. $\delta x_{\max}$ is bounded between 0.196 mm and 0.256 mm, while $\delta y_{\max}$ and $\delta\phi_{\max}$ are both constant, their values being equal to 0.100 mm and 0.221 deg, respectively. The y-coordinate of point P, the geometric center of the MP, and the orientation of the MP depend only on the first and second prismatic actuators because of the partial motion decoupling of the manipulator. Therefore, the maximum position error of the MP along the y-axis and its maximum rotation error occur when $\Delta\tau_{bi}$, $i = 1, 2$, reach their lower or upper bounds. As a result, both $\delta y_{\max}$ and $\delta\phi_{\max}$ remain constant throughout the Cartesian workspace of the manipulator. From Fig. 9(c), it is apparent that the maximum positioning error $\delta p_{\max}$ of the MP is symmetrical with respect to the x-axis. The root-mean-square deviation (RMSD) values between the simulations and measurements are equal to 50 μm, 30 μm, 51 μm, and 0.057 deg, for δx, δy, δp, and $\delta\phi$, respectively. From Fig. 6, it is noteworthy that there is a good correlation between the measured positioning errors and the simulated ones. On the other hand, the differences between the measured orientation errors of the MP and the
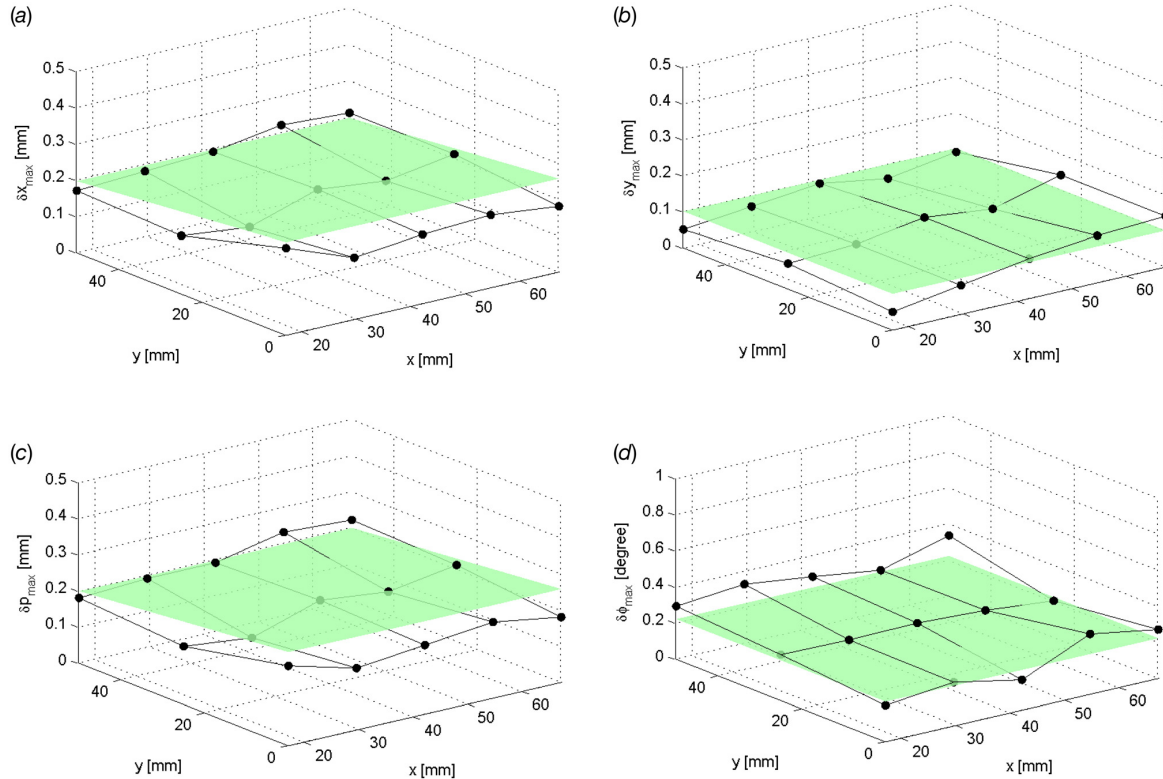
Fig. 9 Comparison of error distributions for case 1 with a constant orientation $\phi = 0$: The solid surface is obtained from simulation while dot points from measurements

Fig. 10 Comparison of error distributions for case 1 with a constant orientation $\phi = \pi/6$

Fig. 11 Comparison of error distributions for case 2 with a constant orientation $\phi = 0$

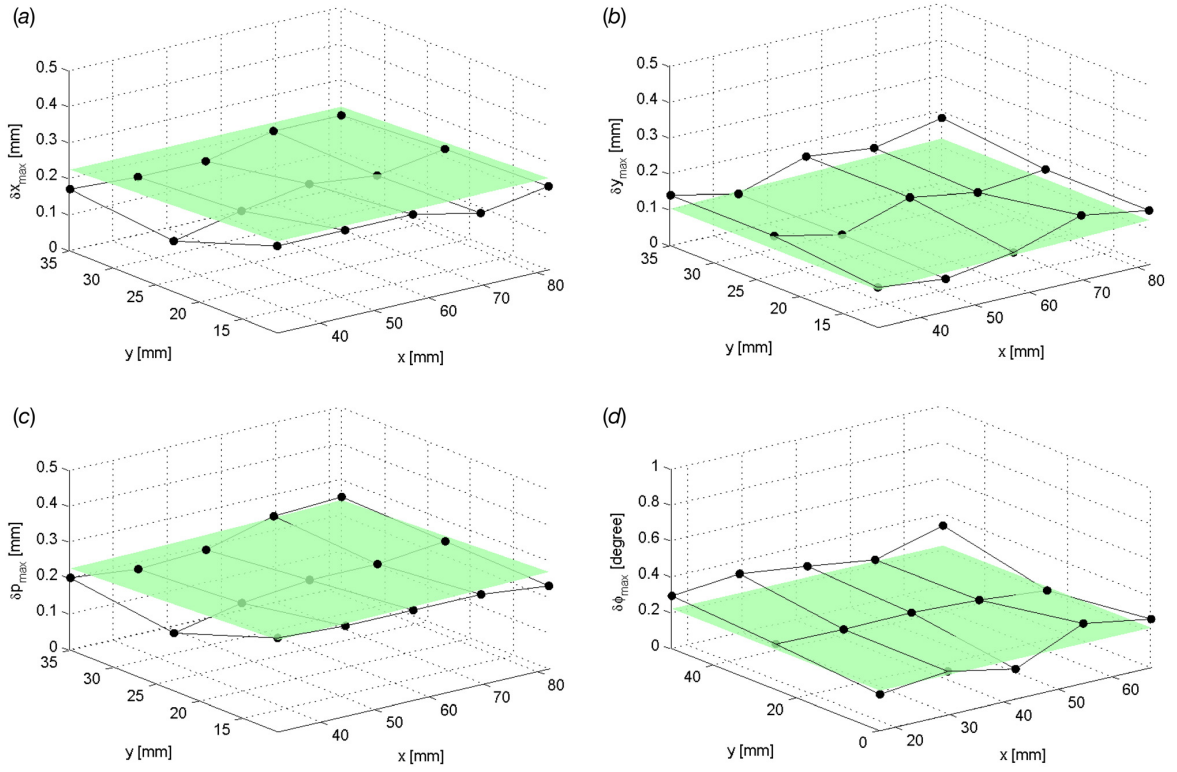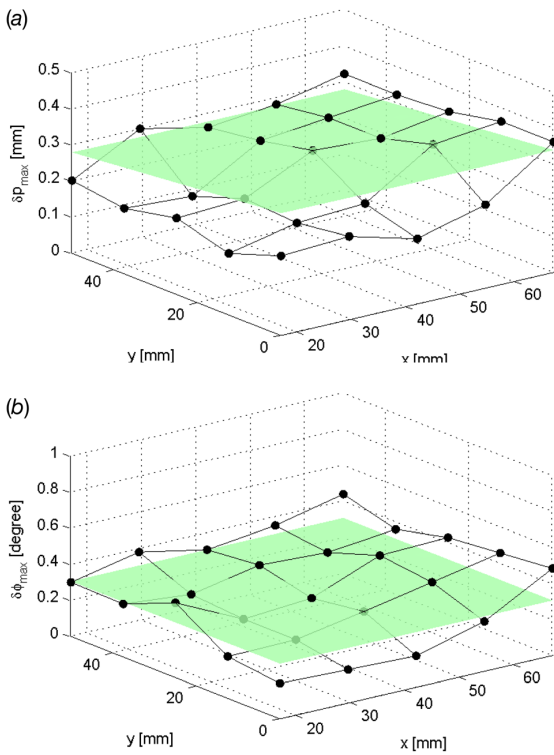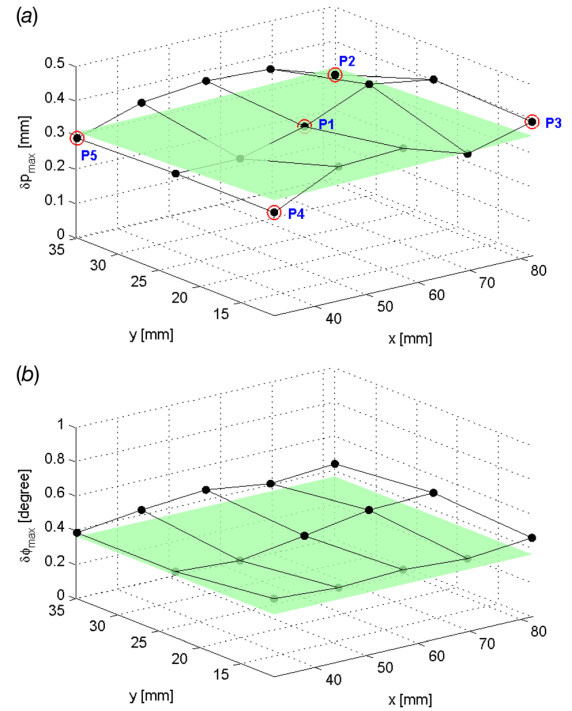**Fig. 12 Comparison of error distributions for case 2 with a constant orientation $\phi = \pi/6$**

simulated ones are noticeable. To some extent, this is due to the reason that angular measurement is more sensitive to the random error and influence of environments, etc., than the positional measurement.

The distributions of measured errors with constant orientation $\phi = \pi/6$ are shown in Fig. 10. The simulated δx_{max}, as shown in Fig. 10(a), varying from 0.224 mm to 0.253 mm, has a distribution similar to that corresponding to $\phi = 0$, while δy_{max} is constant along y-axis and increases gradually with the x-coordinate (see Fig. 10(b)), from 0.103 mm to 0.123 mm. In Fig. 10(d), the simulated orientation error $\delta\phi_{max}$ is constant and is equal to 0.264 deg. The positioning error δp_{max}, varying from 0.226 mm to 0.268 mm, increases when the measuring point moves from the upper left corner to the lower right corner throughout the workspace as displayed in Fig. 10(c). The RMSD values between the simulations and measurements of $\delta x, \delta y, \delta p$, and $\delta\phi$ are equal to 47 μm,

34 μm, 34 μm, and 0.103 deg, respectively. Therefore, the measurements have a good correlation with the simulations.

6.2 Error Distributions for Case 2. In case 2, both prismatic and revolute joint clearances are considered. The distributions of the maximum pose errors are shown in Figs. 11 and 12. By comparing Figs. 11 to 6, it can be found that the differences between the simulation results and measurements really depend on the orientation of the MP. For $\phi = 0$, the RMSD values between the simulations and measurements are equal to 77 μm, 62 μm, 81 μm, and 0.086 deg, for $\delta x, \delta y, \delta p$, and $\delta\phi$, respectively. Although the difference between the simulations and experiments in Fig. 11(b) under the given scale and unit seems larger than the other results, however, the maximum value is around 0.5 deg and the statistical analysis also shows that the difference is acceptable.
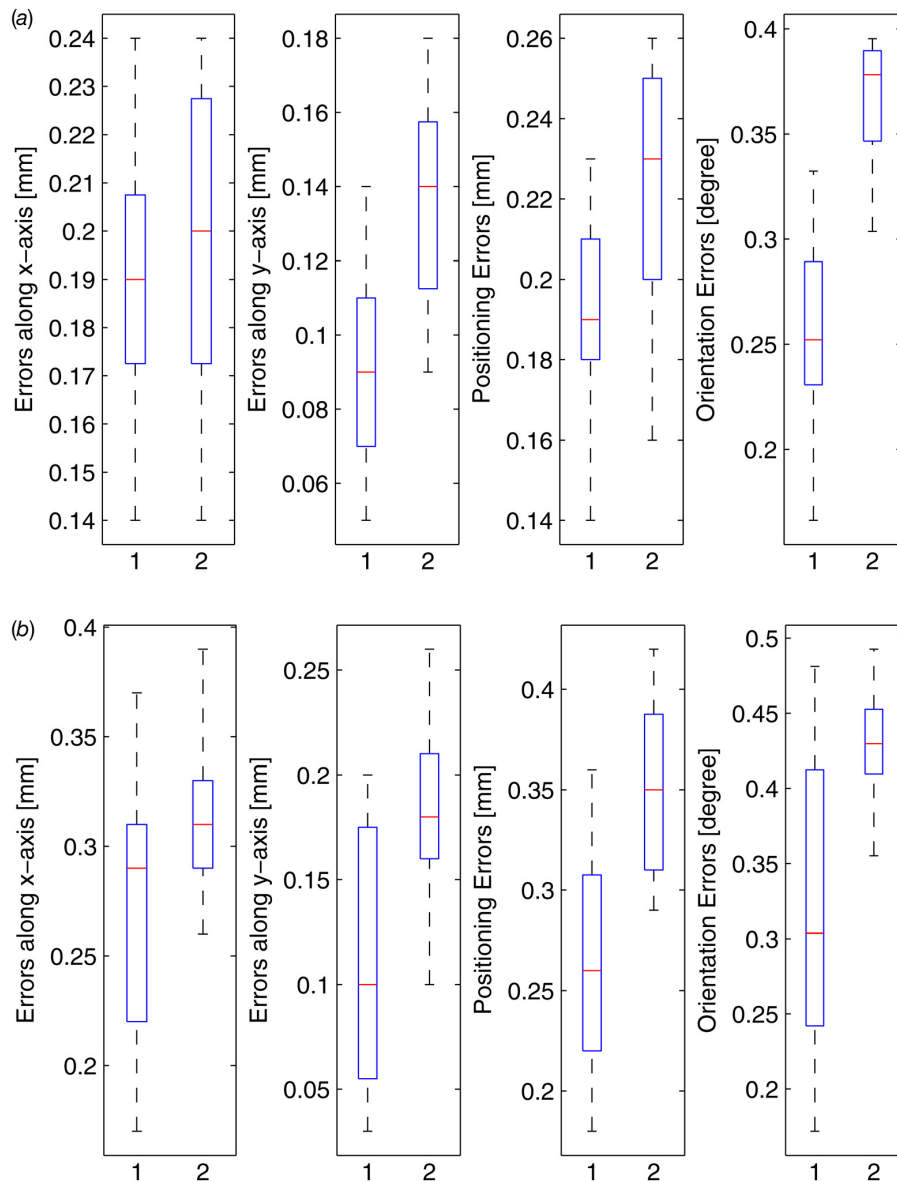
Fig. 13 Boxplot of the measurements for cases 1 and 2. Nos. 1 and 2 of horizontal axes stand for the measurements with constant orientations $\phi = 0$ and $\phi = \pi/6$, respectively.
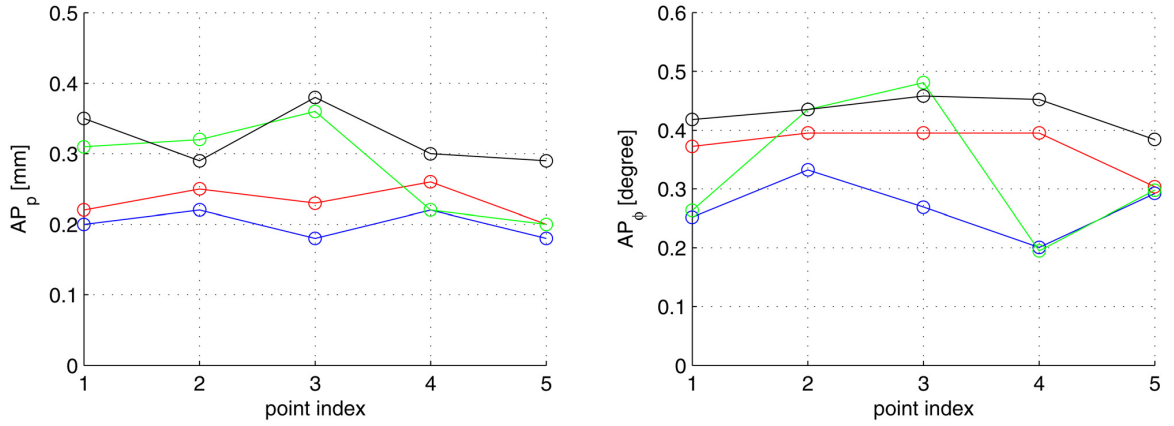
Fig. 14 Position and orientation accuracies at five poses

For $\phi = \pi/6$, the RMSD values between the simulations and measurements of $\delta x, \delta y, \delta p$ and $\delta \phi$, are equal to $26 \, \mu m$, $36 \, \mu m$, $34 \, \mu m$, and $0.063 \, \text{deg}$, respectively. Note that the correlation between the simulation results and the measurements is better with $\phi = \pi/6$ than $\phi = 0$.

6.3 Discussion on Measurement Results. As shown in Fig. 13, both for cases 1 and 2, the measurement errors with $\phi = \pi/6$ are larger than that of $\phi = 0$, which agrees with the distributions obtained from simulations. Moreover, the sample standard deviations (SSD) of the measured orientation errors are equal to 0.052, 0.029, 0.086, and 0.034 deg, respectively. This means

that the measured orientation errors have very small fluctuations among the discrete points. The positioning performance of the robot, namely, their accuracy, is defined in accordance to ISO 9283: 1998 [23] as

$$AP_p = \delta p, AP_\phi = \delta \phi \qquad (24)$$

where δp and $\delta \phi$ are the measured pose errors defined in Sec. 5.2. Figure 14 shows the accuracy of the manipulator, where the measured points covering the maximum workspace are demonstrated in Fig. 12(a). The position accuracy in measured points is $0.2 - 0.35 \, \text{mm}$, while the orientation accuracy is $0.2 - 0.45 \, \text{deg}$.
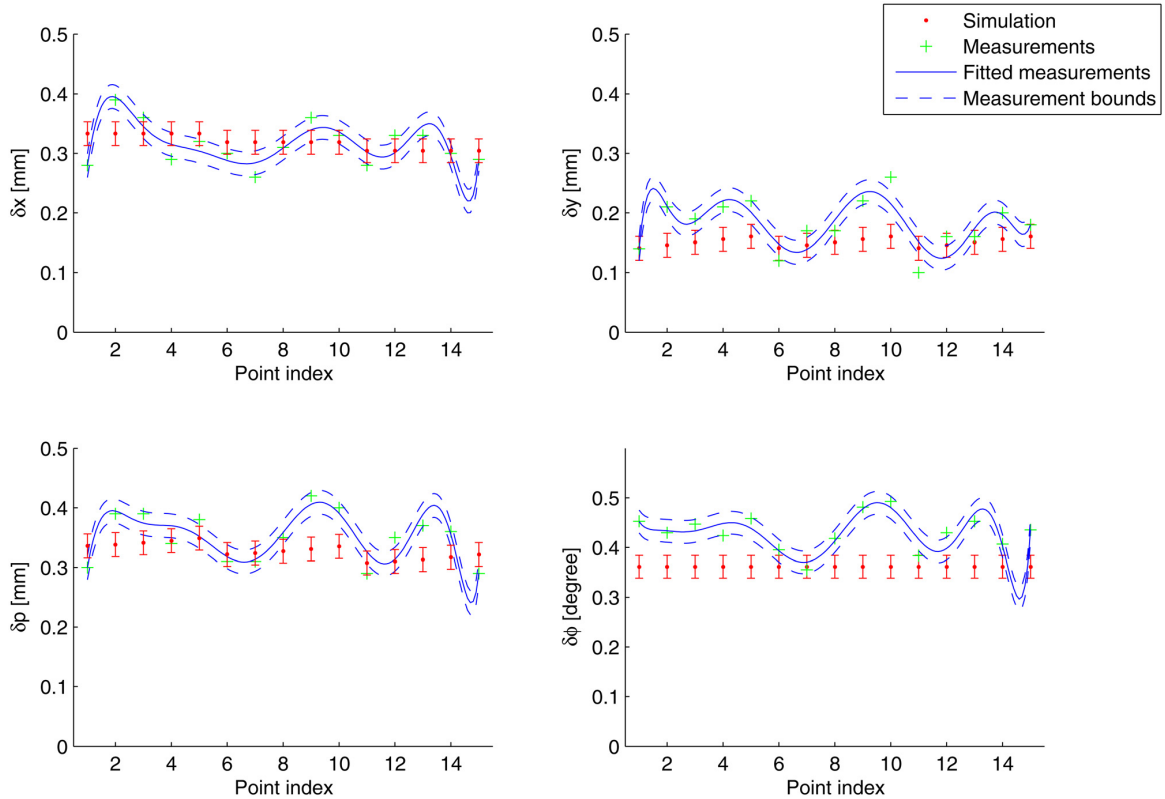
Fig. 15 Comparison between the measurements and simulation results for case 2 with a constant orientation $\phi = \pi/6$

The experiments show that most of the measurements line along the boundaries established with the mathematical model, with a few exceptions. In order to evaluate the comparison between the simulations and measurements, we made a statistical regression analysis [24], as shown in Fig. 15 for case 2 with a constant orientation $\phi = \pi/6$. Most of the simulation results are distributed in the measured error bands $\delta_{\mathrm{mea}} \pm 2A_{\mathrm{mea}}$ except the orientation errors, where δ_{mea} is the measurement error defined in Sec. 5.2 and A_{mea} is the accuracy of the measurement system in Sec. 5. The deviations in the simulation results are equal to 0.02 mm and 0.023 deg, respectively, as derived from the measurements of joint clearances. Although the simulated $\delta\phi$ are located beyond the measured error band for some points, the maximum difference between the two error bands is 0.086 deg, which means that the simulation results are quite close to the measurements. The possible reasons which cause disagreement between the simulations and measurements are random and systematic errors, the influence of the MP inclination and elastic deflection, etc.

7 Conclusions

In this paper, the pose error of a planar parallel manipulator was studied. A new error model was developed for PPMs with due considerations of both configuration errors and joint clearances. With the model, the pose error estimation problem was formulated as an optimization problem, which can estimate maximum pose errors. The error analysis method was deduced and explained in detail. This method can also be applied to planar serial mechanisms.

Another contribution lies in the experimental validation of the error model. Experiments were conducted to obtain the distribution of pose errors throughout the workspace, the results being compared with the errors estimated by the error model. It turns out that there is a good correlation between the pose error simulations and measurements. Moreover, the simulations show that the angular clearances in the passive prismatic joints have much more influence on the pose errors of the moving platform than the revolute joint clearances. This is associated with the experiments, in which the angular clearances in the linear bearings reach their tolerance bounds as much as possible. This suggests that one possible approach to eliminate the errors due to joint clearances is to preload the joint. The validated work can be used for error analysis and compensation in future work. Moreover, other error sources such as manufacturing errors will be considered.

Nomenclature

AP_p, AP_ϕ = position and orientation accuracy of the manipulator

$\Delta\rho_i, \varepsilon_{ri}$ = radial displacement at the ith revolute joint due to clearance and its tolerance

$\Delta\sigma_{gi}, \varepsilon_g$ = lateral displacement at the ith actuated prismatic joint (linear guide) due to clearance and its tolerance

$\Delta\tau_{bi}, \varepsilon_{\theta i}$ = angular displacement at the ith passive prismatic joint (linear bearing) due to clearance and its tolerance

$\Delta\tau_{gi}$ = angular displacement at the ith actuated prismatic joint (linear guide) due to clearance

$\boldsymbol{\delta}_{\mathrm{var}}^c$ = the vector of joint clearances

$\boldsymbol{\delta}_{\mathrm{var}}$ = the vector of variations in all design parameters

$\delta a_{ix}, \delta a_{iy} (\delta b_{ix}, \delta b_{iy},$ = variations in the Cartesian coordinates of

$\delta c_{ix}, \delta c_{iy}, \delta d_{ix}, \delta d_{iy})$ point $A_i(B_i, C_i, D_i)$

$\delta x, \delta y$ = MP positioning errors along x- and y-axis

$\delta x^{ij}, \delta y^{ij}, \delta \phi^{ij}, \delta p^{ij}$ = measured values of x, y, orientation and positioning errors of the MP at the (i, j)th measurement point

$\delta x_{\mathrm{max}}, \delta y_{\mathrm{max}},$ = simulated maximum values of x, y, orien-

$\delta\phi_{\mathrm{max}}, \delta p_{\mathrm{max}}$ tation and positioning errors of the MP

$\mathbf{A}, \mathbf{B}$ = forward and backward kinematic Jacobian matrices

$\mathbf{J}_{\mathrm{err}}^c$ = sensitivity Jacobian matrix to joint clearances

$\mathbf{J}_{\mathrm{err}}$ = global sensitivity Jacobian matrix

$\mathbf{p}, \delta\mathbf{p}$ = Cartesian coordinates vector of point P and its variations

$\phi, \delta\phi$ = orientation of the moving platform and its variation

$l_i, \delta l_i$ = displacement of the ith passive prismatic joint and its variation

$s_i, \delta s_i$ = displacement of the ith actuated prismatic joint and its variation

$\mathcal{F}_b(O, x, y)$ = base coordinate frame

$\mathcal{F}_p(P, X, Y)$ = coordinate frame attached to moving platform

Appendix

The matrices in Eq. (9) are given below

$$\mathbf{H}_a = \mathrm{diag}\left[\, \mathbf{w}_1^T \mathbf{E}^T \mathbf{h}_1 \quad \mathbf{w}_2^T \mathbf{E}^T \mathbf{h}_2 \quad \mathbf{w}_3^T \mathbf{E}^T \mathbf{h}_3 \,\right] \tag{A1a}$$

$$\mathbf{H}_\alpha = \mathrm{diag}\left[\, \mathbf{w}_1^T(a_1\mathbf{h}_1 + s_1\mathbf{u}_1 + d_1\mathbf{v}_1) + l_1 \quad \mathbf{w}_2^T(a_2\mathbf{h}_2 + s_2\mathbf{u}_2 + d_2\mathbf{v}_2) + l_2 \quad \mathbf{w}_3^T(a_3\mathbf{h}_3 + s_3\mathbf{u}_3 + d_3\mathbf{v}_3) + l_3 \,\right] \tag{A1b}$$

$$\mathbf{H}_\beta = \mathrm{diag}\left[\, \mathbf{w}_1^T(s_1\mathbf{u}_1 + d_1\mathbf{v}_1) + l_1 \quad \mathbf{w}_2^T(s_2\mathbf{u}_2 + d_2\mathbf{v}_2) + l_2 \quad \mathbf{w}_3^T(s_3\mathbf{u}_3 + d_3\mathbf{v}_3) + l_3 \,\right] \tag{A1c}$$

$$\mathbf{H}_d = \mathrm{diag}\left[\, \mathbf{w}_1^T \mathbf{E}^T \mathbf{v}_1 \quad \mathbf{w}_2^T \mathbf{E}^T \mathbf{v}_2 \quad \mathbf{w}_3^T \mathbf{E}^T \mathbf{v}_3 \,\right] \tag{A1d}$$

$$\mathbf{H}_\gamma = \mathrm{diag}\left[\, d_1\mathbf{w}_1^T \mathbf{v}_1 + l_1 \quad d_2\mathbf{w}_2^T \mathbf{v}_2 + l_2 \quad d_3\mathbf{w}_3^T \mathbf{v}_3 + l_3 \,\right] \tag{A1e}$$

$$\mathbf{H}_\theta = \mathrm{diag}\left[\, l_1 \quad l_2 \quad l_3 \,\right] \tag{A1f}$$

$$\mathbf{H}_\rho = \mathrm{diag}\left[\, \mathbf{w}_1^T \mathbf{E}^T \mathbf{n}_1 \quad \mathbf{w}_2^T \mathbf{E}^T \mathbf{n}_2 \quad \mathbf{w}_3^T \mathbf{E}^T \mathbf{n}_3 \,\right] \tag{A1g}$$

$$\mathbf{H}_r = \mathrm{diag}\left[\, \mathbf{w}_1^T \mathbf{E}^T \mathbf{k}_1 \quad \mathbf{w}_2^T \mathbf{E}^T \mathbf{k}_2 \quad \mathbf{w}_3^T \mathbf{E}^T \mathbf{k}_3 \,\right] \tag{A1h}$$

$$\mathbf{H}_\psi = \mathrm{diag}\left[\, r_1\mathbf{w}_1^T \mathbf{k}_1 \quad r_2\mathbf{w}_2^T \mathbf{k}_2 \quad r_3\mathbf{w}_3^T \mathbf{k}_3 \,\right] \tag{A1i}$$

The matrices $\mathbf{J}_A, \mathbf{J}_B, \mathbf{J}_C$, and $\mathbf{J}_D$ in Eq. (13) are expressed as

$$\mathbf{J}_A = \left[\mathbf{J}_a \quad \mathbf{J}_\alpha\right]\left[\mathbf{A}_a \quad \mathbf{A}_\alpha\right]_{6\times6}^{-1}, \mathbf{A}_a = \mathrm{diag}\left[\mathbf{h}_1 \quad \mathbf{h}_2 \quad \mathbf{h}_3\right], \mathbf{A}_\alpha = \mathrm{diag}\left[a_1\mathbf{E}\mathbf{h}_1 \quad a_2\mathbf{E}\mathbf{h}_2 \quad a_3\mathbf{E}\mathbf{h}_3\right] \tag{A2a}$$

$$\mathbf{J}_B = \left[\mathbf{0}_{3\times3} \quad \mathbf{J}_\beta\right]\left[\mathbf{B}_s \quad \mathbf{B}_\beta\right]_{6\times6}^{-1}, \mathbf{B}_s = \mathrm{diag}\left[\mathbf{u}'_1 \quad \mathbf{u}'_2 \quad \mathbf{u}'_3\right], \mathbf{B}_\beta = \mathrm{diag}\left[s_1\mathbf{E}\mathbf{u}'_1 \quad s_2\mathbf{E}\mathbf{u}'_2 \quad s_3\mathbf{E}\mathbf{u}'_3\right] \tag{A2b}$$

$$\mathbf{J}_C = \begin{bmatrix} \mathbf{J}_d & \mathbf{J}_\gamma \end{bmatrix} \begin{bmatrix} \mathbf{C}_d & \mathbf{C}_\gamma \end{bmatrix}_{6\times6}^{-1}, \mathbf{C}_d = \mathrm{diag}\begin{bmatrix} \mathbf{v}'_1 & \mathbf{v}'_2 & \mathbf{v}'_3 \end{bmatrix}, \mathbf{C}_\gamma = \mathrm{diag}\begin{bmatrix} d_1\mathbf{E}\mathbf{v}'_1 & d_2\mathbf{E}\mathbf{v}'_2 & d_3\mathbf{E}\mathbf{v}'_3 \end{bmatrix} \qquad (A2c)$$

$$\mathbf{J}_D = \begin{bmatrix} \mathbf{J}_r & \mathbf{J}_\psi \end{bmatrix} \begin{bmatrix} \mathbf{D}_r & \mathbf{D}_\psi \end{bmatrix}_{6\times6}^{-1}, \mathbf{D}_r = \mathrm{diag}\begin{bmatrix} \mathbf{k}'_1 & \mathbf{k}'_2 & \mathbf{k}'_3 \end{bmatrix}, \mathbf{D}_\psi = \mathrm{diag}\begin{bmatrix} r_1\mathbf{E}\mathbf{k}'_1 & r_2\mathbf{E}\mathbf{k}'_2 & r_3\mathbf{E}\mathbf{k}'_3 \end{bmatrix} \qquad (A2d)$$

with

$$\mathbf{u}'_i = \begin{bmatrix} \cos\beta_i \\ \sin\beta_i \end{bmatrix}, \mathbf{v}'_i = \begin{bmatrix} \cos\gamma_i \\ \sin\gamma_i \end{bmatrix}, \mathbf{k}'_i = \begin{bmatrix} \cos\psi_i \\ \sin\psi_i \end{bmatrix}$$

References

[1] Ryu, J., and Cha, J., 2003, "Volumetric Error Analysis and Architecture Optimization for Accuracy of HexaSlide Type Parallel Manipulators," Mech. Mach Theory, **38**, pp. 227–240.

[2] Liu, H., Huang, T., and Chetwynd, D. G., 2011, "A General Approach for Geometric Error Modeling of Lower Mobility Parallel Manipulators," ASME J. Mech. Rob., **3**(2), 021013.

[3] Yu, A., Bonev, I. A., and Murray, P. Z., 2008, "Geometric Approach to the Accuracy Analysis of a Class of 3-DOF Planar Parallel Robots," Mech. Mach. Theory, **43**, pp. 364–375.

[4] Briot, S., and Bonev, I. A., 2010, "Accuracy Analysis of 3T1R Fully-Parallel Robots," Mech. Mach. Theory, **45**, pp. 695–706.

[5] Lin, P. D., and Chen, J. F., 1992, "Accuracy Analysis of Planar Linkages by the Matrix Method," Mech. Mach. Theory, **35**, pp. 507–516.

[6] Ting, K., Zhu, J., and Watkins, D., 2000, "The Effects of Joint Clearance on Position and Orientation Deviation of Linkages and Manipulators," Mech. Mach. Theory, **35**, pp. 391–401.

[7] Fogarasy, A., and Smith, M., 1998, "The Influence of Manufacturing Tolerance on the Kinematic Performance of Mechanisms," Proc. Inst. Mech. Eng. Part C: Mech. Eng. Sci., **212**, pp. 35–47.

[8] Lim, S. R., Kang, K., Park, S., Choi, W. C., Jae-Bok, S., Hong, D., and Shim, J. K., 2002, "Error Analysis of a Parallel Mechanism Considering Link Stiffness and Joint Clearances," J. Mech. Sci. Technol., **16**(6), pp. 799–809.

[9] Castelli, V. P., and Venanzi, S., 2005, "Clearance Influence Analysis on Mechanisms," Mech. Mach. Theory, **40**, pp. 1316–1329.

[10] Venanzi, S., and Castelli, V. P., 2005, "A New Technique for Clearance Influence Analysis in Spatial Mechanisims," ASME J. Mech. Des., **127**, pp. 446–455.

[11] Meng, J., Zhang, D., and Li, Z., 2009, "Accuracy Analysis of Parallel Manipulators With Joint Clearance," ASME J. Mech. Des., **131**, 011013.

[12] Binaud, N., Cardou, P., Caro, S., and Wenger, P., 2010, "The Kinematic Sensitivity of Robotic Manipulators to Joint Clearance," Proceedings of ASME Design Engineering Technical Conferences, Aug. 15–18, Montreal, QC, Canada.

[13] Binaud, N., Caro, S., Bai, S., and Wenger, P., 2010, "Comparison of 3-PPR Parallel Planar Manipulators Based on Their Sensitivity to Joint Clearances," Proceedings of IEEE/RSJ International Conference on Intelligent Robots and Systems (IROS), Taipei, Oct. 18–22, pp. 2778–2783.

[14] Wei, W., and Simaan, N., 2010, "Design of Planar Parallel Robots With Preloaded Flexures for Guaranteed Backlash Prevention," ASME J. Mech. Rob., **2**(1), 011012.

[15] Carusone, J., and D'Eleuterio, G. M., 1993, "Tracking Control for End-Effector Position and Orientation of Structurelly Flexible Manipulators," J. Rob. Syst., **10**(6), pp. 847–870.

[16] Zhuang, H., 1997, "Self-Calibration of Parallel Mechanisms With a Case Study on Stewart Platforms," IEEE Trans. Rob. Autom., **13**(3), pp. 387–397.

[17] Voglewede, P., and Uphoff, I., 2004, "Application of Workspace Generation Techniques to Determine the Unconstrained Motion of Parallel Manipulators," ASME J. Mech. Des., **126**, pp. 283–290.

[18] Bai, S., and Caro, S., 2009, "Design and Analysis of a 3-PPR Planar Robot With U-Shape Base," Proceedings of 14th International Conference on Advanced Robotics, Munich, Germany, June 22–26.

[19] SMAC Product Catalog version 2009 on the WWW, at http://www.smac-mca.com/

[20] Caro, S., Binaud, N., and Wenger, P., 2009, "Sensitivity Analysis of 3-RPR Planar Parallel Manipulators," J. Mech. Des., **131**, 121005.

[21] http://www.pdfsupply.com/pdfs/dvt-554c.pdf

[22] http://www.cognex.com/support/files/DVT/Intellect_Manual.pdf

[23] International Standard, Manipulating Industrial Robots-Performance Criteria and Related Test Methods, ISO 9283: 1998.

[24] Douglas, C. M., 2009, *Design and Analysis of Experiments*, 7th ed., John Wiley & Sons.

5

Paper II

G. Wu, S. Caro, S. Bai, J.A. Kepler, 2014. Mobile platform center shift in spherical parallel manipulators with flexible limbs, *Mechanism and Machine Theory*, 75: 12-26, DOI:10.1016/j.mechmachtheory.2014.01.001.

Mobile platform center shift in spherical parallel manipulators with flexible limbs

CrossMark

Guanglei Wu, Shaoping Bai *, Jørgen Kepler

Department of Mechanical and Manufacturing Engineering, Aalborg University, DK-9220 Aalborg, Denmark

ARTICLE INFO

ABSTRACT

Spherical parallel manipulators (SPMs) with revolute joints work under the condition that all joint axes intersect at the manipulator center, where the mobile platform (MP) center is coincident with the center of the base platform. The center of each platform is the point of concurrence of the axes of the three revolute joints attached to the platform. When limb flexibility is considered, however, the MP center will shift away from the base platform center, which consequently influences the manipulator performance, e.g., its orientation accuracy. In this work, the stiffness of SPMs is analyzed, with focus on the MP center shift. The stiffness is modeled by adopting the virtual-spring method. Castigliano's theorem is used to calculate the limb deflection. The model is validated via FE analysis. Examples are included to show the center shift of SPMs with different designs.

1. Introduction

A fundamental assumption for spherical parallel manipulators (SPMs) is that all links of the manipulator rotate about the manipulator center [1], i.e., the point of concurrency of the axes of all nine revolute joints. This assumption is valid for rigid-body motion or manipulators consisting of a ball-and-socket joint as the center of rotation. However, in the presence of link flexibility, the axes of all joints may not intersect at one common point. In other words, the center of the mobile platform (MP) will shift away from the center of the base platform. As this shift will consequently influence the performance of the manipulator orientation accuracy, it is important to investigate this shift from a design perspective.

The center shift in question is the result of limb deformation, which can be quantified based on stiffness analysis. Of the existing methods of stiffness modeling, the Virtual Joint Method (VJM), which is often called lumped modeling, has been widely used to establish the stiffness model for parallel manipulators (PMs), as it provides acceptable accuracy in short computational time. Gosselin first applied this approach to parallel manipulators [2], in which only actuator compliance was taken into account under an unloaded equilibrium condition. Chen and Kao proposed the Conservative Congruence Transformation (CCT) [3] to analyze the influence of changes of the robot geometry on the manipulator stiffness due to an external wrench. In general, link flexibility was considered in the stiffness modeling. In Gosselin and Zhang's work [4], the flexible links were replaced with rigid beams mounted on revolute joints supplied with torsional springs. This flexible-link, lumped-parameter model was also used by Majou et al. [5] to characterize the stiffness of the Orthoglide robot. Quennouelle and Gosselin considered the influence of the passive joints during stiffness modeling [6]. Combining the advantages of the existing methods, a systematic virtual-spring method was proposed to analyze translational parallel manipulators [7], which considers the link deflection and the influence of the passive joints simultaneously. The difference among the various VJM approaches lies in both the modeling assumptions and the numerical techniques. The stiffness of different types of PMs has been extensively investigated, whereas the stiffness modeling and analysis of this class of SPM have received less attention. Liu et al. [8] developed a stiffness model based on

---

Gosselin's work [2], in which only the actuation compliance is considered. Recently, the stiffness analysis of a 3-RRP SPM was conducted on the basis of strain energy and Castigliano's theorem, while ignoring the influence of the passive joints and strain energy due to shear forces [9]. As SPMs are widely used as orientating devices, the previous stiffness analyses were limited to investigate the orientational deformation. However, the translational deformation of SPMs is an important consideration [10]. It is known that in the VJM approach, the Cartesian stiffness matrix relies on the calculation of both the mechanism Jacobian and stiffness matrices in joint space. When applying the virtual spring method to SPMs, one challenge is the computational burden of the complicated kinematics problem due to the products of trigonometric functions, since the inverse-kinematics solutions of all the limbs are to be solved in advance, to derive the Jacobian, as in Pashkevich's approach [7]. Thus, a simple and fast procedure is needed for modeling the stiffness of SPMs to investigate both the position and orientation accuracies.

In this paper, the MP center shift of spherical parallel manipulators is studied. A method to model the stiffness of SPMs for the analysis of the shift is developed and validated through FE analysis. We adopted the virtual-spring method in connection with Castigliano's theorem to calculate the limb stiffness in SPMs. Examples are included to illustrate the application of the method.

2. Problem formulation

A general spherical parallel manipulator is shown in Fig. 1. The ith limb consists of three revolute joints, whose axes are parallel to the unit vectors $\mathbf{u}_i$, $\mathbf{v}_i$, and $\mathbf{w}_i$. All three limbs have identical architectures, defined by angles α_1 and α_2. Moreover, β and γ define the geometry of two triangular pyramids on the base and the mobile platforms, respectively. The origin O of the base coordinate system xyz is located at point O. The z axis is normal to the bottom surface of the base pyramid and points upwards, while the y axis is located in the plane made by the z-axis and $\mathbf{u}_1$.

Under rigid-body motion, all the joint axes intersect at one point, namely, point O in Fig. 2(a). In a real-life system the manipulator will deform when subjected to external loads. Assuming that both the MP and the base platform are rigid, while the limb links are linearly elastic, the SPM will have two centers, one on the base platform, and one on the MP, which is movable, as illustrated in Fig. 2(b). The modeling of the shift of the MP center and the associated orientation error are the main issues studied here.

3. Error modeling of SPMs

Under the prescribed coordinate system, unit vector $\mathbf{u}_i$ is derived as

$$\mathbf{u}_i = \begin{bmatrix} -\sin\eta_i\sin\gamma & \cos\eta_i\sin\gamma & -\cos\gamma \end{bmatrix}^T \tag{1}$$

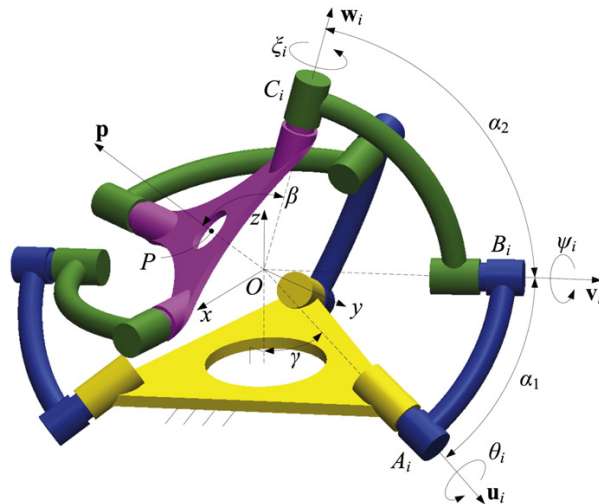where $\eta_i = 2(i-1)\pi/3$, $i = 1, 2, 3$.

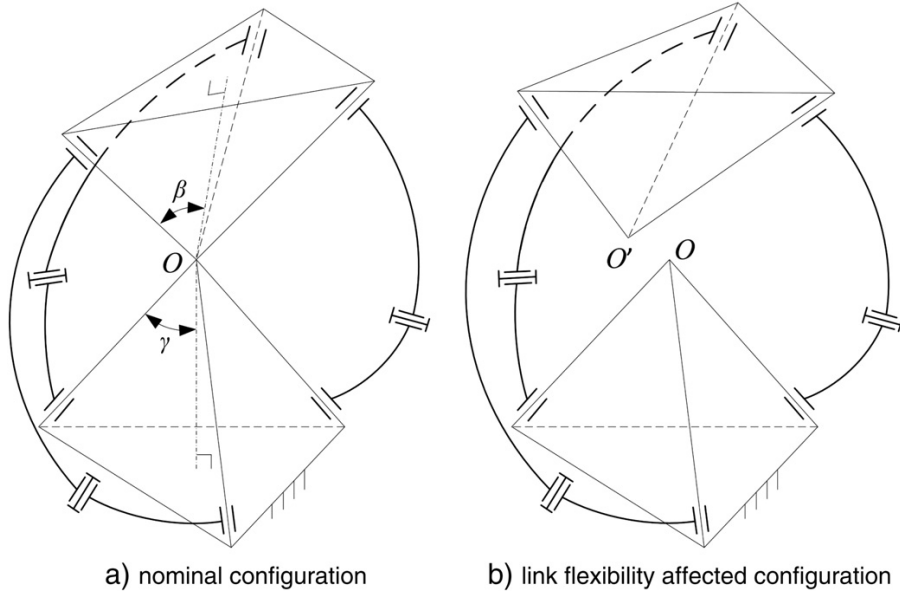**Fig. 1.** Architecture of a general SPM.

Fig. 2. Center separation of a SPM under an external wrench due to link flexibility.

The unit vector $\mathbf{v}_i$ of the axis of the intermediate revolute joint in the ith leg is expressed as:

$$\mathbf{v}_i = \begin{bmatrix} -s\eta_i s\gamma c\alpha_1 + (c\eta_i s\theta_i - s\eta_i c\gamma c\theta_i)s\alpha_1 \\ c\eta_i s\gamma c\alpha_1 + (s\eta_i s\theta_i + c\eta_i c\gamma c\theta_i)s\alpha_1 \\ -c\gamma c\alpha_1 + s\gamma c\theta_i s\alpha_1 \end{bmatrix} \tag{2}$$

The unit vector $\mathbf{w}_i$ of the top revolute joint in the ith leg is a function of the orientation of the mobile platform, namely,

$$\mathbf{w}_i = \begin{bmatrix} w_{\mathrm{ix}} & w_{\mathrm{iy}} & w_{\mathrm{iz}} \end{bmatrix}^T = \mathbf{Q}\mathbf{w}_i^* \tag{3}$$

where $\mathbf{Q}$ is the rotation matrix that carries the MP from its reference orientation to the current one and $\mathbf{w}_i^*$ is the unit vector of the axis of the top revolute joint in the ith leg when the mobile platform is in its reference orientation, which is given as

$$\mathbf{w}_i^* = [-\sin\eta_i\sin\beta \quad \cos\eta_i\sin\beta \quad \cos\beta]^T \tag{4}$$

Let the input error of the SPMs be $\Delta\mathbf{x}$, the orientation error of the mobile platform $\Delta\boldsymbol{\varphi}$ under rigid-body motion being derived from

$$\mathbf{J}\Delta\boldsymbol{\varphi} = \Delta\mathbf{x} \tag{5}$$

where $\Delta\mathbf{x} = [\Delta\theta_1 \ \Delta\theta_2 \ \Delta\theta_3]^T$ and $\Delta\boldsymbol{\varphi} = [\Delta\varphi_x \ \Delta\varphi_y \ \Delta\varphi_z]^T$. Moreover, $\mathbf{J} = [\mathbf{j}_1 \ \mathbf{j}_2 \ \mathbf{j}_3]^T$ is the kinematic Jacobian matrix of the manipulator [11], and $\mathbf{j}_i = (\mathbf{v}_i \times \mathbf{w}_i)/(\mathbf{u}_i \times \mathbf{v}_i \cdot \mathbf{w}_i)$.

3.1. The Cartesian stiffness matrix

To model the center shift and orientation error for SPMs with flexible limbs, we need to find the overall stiffness of the manipulator structure. The virtual-spring method is adopted in this work for stiffness modeling. In this method, link flexibility is replaced by an n-dof virtual spring associated with the mobility freedoms describing both the static translational and rotational deflections and the coupling between them, where the spring compliance is calculated by means of Euler–Bernoulli beam theory. The flexibility of the single kinematic leg of the SPM in question is illustrated in Fig. 3(a), in accordance to the force diagram of Fig. 3(b) and the associated deflection and joint displacements in Fig. 3(c), the corresponding virtual springs and passive joints being described below:

• a 1-dof virtual spring representing the actuator stiffness defined by the deflection $\Delta\theta_i$;
• a 6-dof virtual spring describing the stiffness of the proximal curved link defined by the rotational deflection $\Delta\mathbf{u}_{i1} = [\Delta u_1^i, \Delta u_2^i, \Delta u_3^i]^T$ and translational deflection $\Delta\mathbf{u}_{i2} = [\Delta u_4^i, \Delta u_5^i, \Delta u_6^i]^T$;
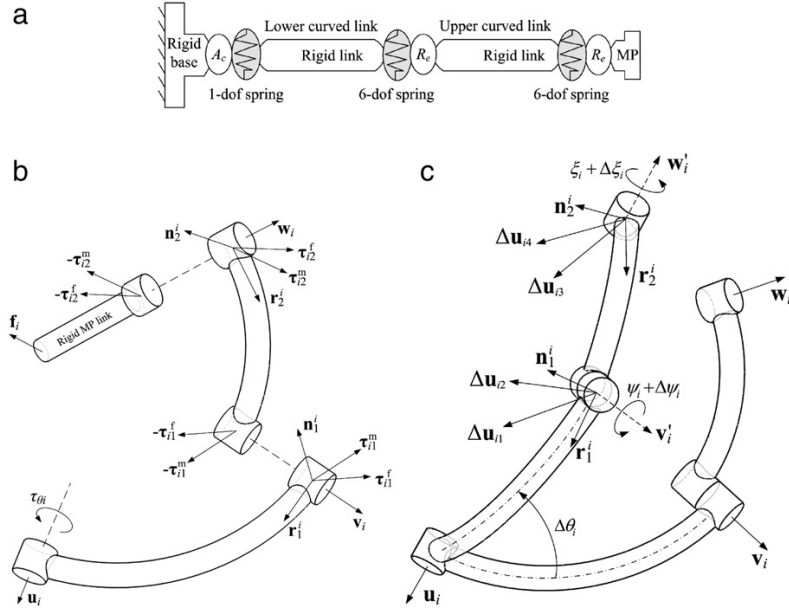
Fig. 3. Flexible model of a single limb: (a) virtual spring model, where A_c stands for the actuator, R_e for revolute joint; (b) force diagram of the ith limb, where τ^{m} and τ^{f} stand for the moments and forces in frame $\mathbf{r}_1^i\mathbf{v}_i\mathbf{n}_1^i(\mathbf{r}_2^i\mathbf{w}_i\mathbf{n}_2^i)$; (c) link deflections and joint displacements in the ith leg.

- a 1-dof passive R-joint between the two links in each leg, allowing one rotational displacement $\Delta\psi_i$;
- a 6-dof virtual spring describing the stiffness of the distal curved link defined by the rotational deflection $\Delta\mathbf{u}_{i3} = [\Delta u_7^i, \Delta u_8^i, \Delta u_9^i]^T$ and translational deflection $\Delta\mathbf{u}_{i4} = [\Delta u_{10}^i, \Delta u_{11}^i, \Delta u_{12}^i]^T$;
- a 1-dof passive R-joint between the distal curved link and the moving platform, allowing one rotational displacement $\Delta\xi_i$.

The center of the SPM, or the center of the base frame, is the designated origin of the reference frame of the mobile platform. The small-amplitude deformation screw of the MP can be expressed as:

$$\mathbf{S}_O^i = \begin{bmatrix} \Delta\boldsymbol{\varphi} \\ \Delta\mathbf{p} \end{bmatrix} = \mathbf{J}_\phi^i \Delta\boldsymbol{\phi}_i + \mathbf{J}_u^i \Delta\mathbf{u}_i \tag{6}$$

with

$$\mathbf{J}_\phi^i = \begin{bmatrix} \hat{\mathbf{S}}_A^i & \hat{\mathbf{S}}_B^i & \hat{\mathbf{S}}_C^i \end{bmatrix}, \quad \Delta\boldsymbol{\phi}_i = \begin{bmatrix} \Delta\theta_i & \Delta\psi_i & \Delta\xi_i \end{bmatrix}^T \tag{7a}$$

$$\mathbf{J}_u^i = \begin{bmatrix} \hat{\mathbf{S}}_{u1}^i & \hat{\mathbf{S}}_{u2}^i & \dots & \hat{\mathbf{S}}_{u12}^i \end{bmatrix}, \quad \Delta\mathbf{u}_i = \begin{bmatrix} \Delta u_1^i & \Delta u_2^i & \dots & \Delta u_{12}^i \end{bmatrix}^T \tag{7b}$$

The corresponding unit screws are expressed as

$$\hat{\mathbf{S}}_A^i = \begin{bmatrix} \mathbf{u}_i \\ \mathbf{0} \end{bmatrix}, \quad \hat{\mathbf{S}}_B^i = \begin{bmatrix} \mathbf{v}_i \\ \mathbf{0} \end{bmatrix}, \quad \hat{\mathbf{S}}_C^i = \begin{bmatrix} \mathbf{w}_i \\ \mathbf{0} \end{bmatrix}$$

$$\hat{\mathbf{S}}_{u1}^i = \begin{bmatrix} \mathbf{r}_1^i \\ \mathbf{b}_i\times\mathbf{r}_1^i \end{bmatrix}, \quad \hat{\mathbf{S}}_{u2}^i = \hat{\mathbf{S}}_B^i, \quad \hat{\mathbf{S}}_{u3}^i = \begin{bmatrix} \mathbf{n}_1^i \\ \mathbf{b}_i\times\mathbf{n}_1^i \end{bmatrix}, \quad \hat{\mathbf{S}}_{u4}^i = \begin{bmatrix} \mathbf{0} \\ \mathbf{r}_1^i \end{bmatrix}, \quad \hat{\mathbf{S}}_{u5}^i = \begin{bmatrix} \mathbf{0} \\ \mathbf{v}_i \end{bmatrix}, \quad \hat{\mathbf{S}}_{u6}^i = \begin{bmatrix} \mathbf{0} \\ \mathbf{n}_1^i \end{bmatrix}$$

$$\hat{\mathbf{S}}_{u7}^i = \begin{bmatrix} \mathbf{r}_2^i \\ \mathbf{c}_i\times\mathbf{r}_2^i \end{bmatrix}, \quad \hat{\mathbf{S}}_{u8}^i = \hat{\mathbf{S}}_C^i, \quad \hat{\mathbf{S}}_{u9}^i = \begin{bmatrix} \mathbf{n}_2^i \\ \mathbf{c}_i\times\mathbf{n}_2^i \end{bmatrix}, \quad \hat{\mathbf{S}}_{u10}^i = \begin{bmatrix} \mathbf{0} \\ \mathbf{r}_2^i \end{bmatrix}, \quad \hat{\mathbf{S}}_{u11}^i = \begin{bmatrix} \mathbf{0} \\ \mathbf{w}_i \end{bmatrix}, \quad \hat{\mathbf{S}}_{u12}^i = \begin{bmatrix} \mathbf{0} \\ \mathbf{n}_2^i \end{bmatrix} \tag{8}$$

with

$$\mathbf{n}_1^i = \frac{\mathbf{u}_i\times\mathbf{v}_i}{\|\mathbf{u}_i\times\mathbf{v}_i\|}, \quad \mathbf{r}_1^i = \frac{\mathbf{v}_i\times\mathbf{n}_1^i}{\|\mathbf{v}_i\times\mathbf{n}_1^i\|}; \quad \mathbf{n}_2^i = \frac{\mathbf{v}_i\times\mathbf{w}_i}{\|\mathbf{v}_i\times\mathbf{w}_i\|}, \quad \mathbf{r}_2^i = \frac{\mathbf{w}_i\times\mathbf{n}_2^i}{\|\mathbf{w}_i\times\mathbf{n}_2^i\|} \tag{9}$$

where $\Delta\mathbf{p} = [\Delta x, \Delta y, \Delta z]^T$ is the vector of positional error of the center of rotation. Moreover, $\mathbf{b}_i$ and $\mathbf{c}_i$ are the position vectors of points B_i and C_i, respectively. Obviously, $\Delta\mathbf{p}$ is zero when only joint displacements are considered, by virtue of the zero vectors in the lower parts of $\hat{\mathbf{S}}_A^i, \hat{\mathbf{S}}_B^i$ and $\hat{\mathbf{S}}_C^i$. This means that the joint variations due to rigid-body motions of the links have no influence on the position of the rotation center.

Eq. (6) relates the end-effector deflection to the articulated joint displacements and elastic deformations in the ith leg, which can be rewritten by separating all the variation terms into those of the passive joints and the ones due to elastic deflections and actuator compliance,

$$\mathbf{S}_O^i = \mathbf{J}_\theta^i \Delta\boldsymbol{\theta}_i + \mathbf{J}_q^i \Delta\mathbf{q}_i \tag{10}$$

with

$$\mathbf{J}_\theta^i = \begin{bmatrix} \hat{\mathbf{S}}_A^i & \hat{\mathbf{S}}_{u1}^i & \dots & \hat{\mathbf{S}}_{u12}^i \end{bmatrix} \in \mathbf{R}^{6\times13}, \ \ \Delta\boldsymbol{\theta}_i = \begin{bmatrix} \Delta\theta_i & \Delta u_1^i & \dots \Delta u_{12}^i \end{bmatrix}^T \tag{11a}$$

$$\mathbf{J}_q^i = \begin{bmatrix} \hat{\mathbf{S}}_B^i & \hat{\mathbf{S}}_C^i \end{bmatrix} \in \mathbf{R}^{6\times2}, \ \ \Delta\mathbf{q_i} = [\Delta\psi_i \ \ \Delta\xi_i]^T \tag{11b}$$

Let the external wrench (six-dimensional array of force and moment) applied to the end of the ith leg be $\mathbf{f}_i = [\mathbf{m}_{ex,i}^T \ \mathbf{f}_{ex,i}^T]^T$. On the other hand, in accordance to Fig. 3(b), the force/torque causing the deflection $\Delta\boldsymbol{\theta}_i$ in the ith leg being denoted by $\boldsymbol{\tau}_i = [\tau_{\theta i} (\boldsymbol{\tau}_{i1}^m)^T (\boldsymbol{\tau}_{i1}^f)^T (\boldsymbol{\tau}_{i2}^m)^T (\boldsymbol{\tau}_{i2}^f)^T]^T$, the equilibrium condition for the system is written as

$$\mathbf{J}_\theta^{i\,T} \mathbf{f}_i = \boldsymbol{\tau}_i, \ \ \boldsymbol{\tau}_i = \mathbf{K}_\theta^i \Delta\boldsymbol{\theta}_i \tag{12a}$$

$$\mathbf{J}_q^{i\,T} \mathbf{f}_i = \mathbf{0} \tag{12b}$$

where $\mathbf{K}_\theta^i$ is the stiffness matrix in joint space. Combining Eqs. (10), (12a) and (12b), the kinetostatic model of the ith leg is reduced to

$$\begin{bmatrix} \mathbf{S}_\theta^i & \mathbf{J}_q^i \\ \mathbf{J}_q^{i\,T} & \mathbf{0}_{2\times2} \end{bmatrix} \begin{bmatrix} \mathbf{f}_i \\ \Delta\mathbf{q}_i \end{bmatrix} = \begin{bmatrix} \mathbf{S}_O^i \\ \mathbf{0}_{2\times1} \end{bmatrix} \tag{13}$$

where the 6×6 block $\mathbf{S}_\theta^i = \mathbf{J}_\theta^i (\mathbf{K}_\theta^i)^{-1} \mathbf{J}_\theta^{i\,T}$ represents the spring compliance relative to the reference frame on the moving platform, and the block $\mathbf{J}_q^i$ takes into account the passive-joint influence on the MP motions.

Moreover, $\mathbf{K}_\theta^i$ is a 13×13 matrix, describing the stiffness of the virtual springs and the actuators, which takes the form:

$$\mathbf{K}_\theta^i = \begin{bmatrix} K_{act}^i & \mathbf{0}_{1\times6} & \mathbf{0}_{1\times6} \\ \mathbf{0}_{6\times1} & \mathbf{K}_{L_1}^i & \mathbf{0}_{6\times6} \\ \mathbf{0}_{6\times1} & \mathbf{0}_{6\times6} & \mathbf{K}_{L_2}^i \end{bmatrix} \tag{14}$$

where K_{act}^i describes the ith actuator stiffness, while $\mathbf{K}_{L_1}^i$ and $\mathbf{K}_{L_2}^i$, respectively, are the 6×6 stiffness matrices of the proximal and distal curved links in the ith leg. The compliance matrix $\left(\mathbf{K}_{L_{1(2)}}^i \right)^{-1} = \mathbf{C}_{1(2)}^i$, $i = 1, 2, 3$, of the proximal (distal) curved link can be found using Castigliano's theorem, as presented in Section 3.2.

The matrix $\mathbf{J}_\theta^i \in \mathbb{R}^{6\times13}$ is the Jacobian matrix associated with the virtual springs and $\mathbf{J}_q^i \in \mathbb{R}^{6\times2}$ the one associated with the passive joints. The Cartesian stiffness matrix $\mathbf{K}_i$ of the ith leg is extracted from the inverse of the matrix in Eq. (13)

$$\mathbf{K}_i' = \begin{bmatrix} \mathbf{S}_\theta^i & \mathbf{J}_q^i \\ \mathbf{J}_q^{i\,T} & \mathbf{0}_{2\times2} \end{bmatrix}^{-1} \tag{15}$$

As a result, the Cartesian stiffness matrix $\mathbf{K}_i$ mapping displacement screw to wrench is obtained as the first 6×6 block in $\mathbf{K}_i'$. From $\mathbf{f} = \sum_{i=1}^3 \mathbf{f}_i, \mathbf{S}_O^i = \mathbf{S}_O$ and $\mathbf{f}_i = \mathbf{K}_i \mathbf{S}_O^i$, the Cartesian stiffness matrix $\mathbf{K}$ of the system is found by simple addition in accordance to $\mathbf{f} = \mathbf{K}\mathbf{S}_O$, namely,

$$\mathbf{K} = \sum_{i=1}^3 \mathbf{K}_i \tag{16}$$

The stiffness matrix $\mathbf{K}$ consists of rotational, translational and coupling blocks. Liu's stiffness matrix [8], $\mathbf{K} = \mathbf{J}\mathbf{K}_{act}\mathbf{J}^T$, and Enferadi's [9] only considered the rotational block. Compared to Liu's and Enferadi's models developed through force analysis, matrix Eq. (16) can be readily used for SPM parameterization and design optimization.
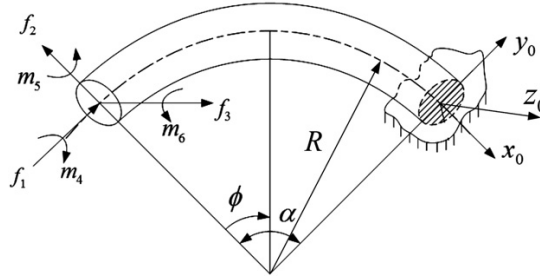
Fig. 4. A curved beam element acted upon by an external wrench.

The SPM deformation screw is found as:

$$\mathbf{S}_O = \begin{bmatrix} \Delta\boldsymbol{\varphi}^T & \Delta\mathbf{p}^T \end{bmatrix}^T = \mathbf{K}^{-1}\mathbf{f} \tag{17}$$

Compared to the conventional error formulation of Eq. (5), the derived error model Eq. (17) includes not only the orientational deflection but also the positional deflection as expressed by Eq. (6). The translational displacement $\Delta\mathbf{p}$ in $\mathbf{S}_O$ will not necessarily vanish when an external wrench is applied to the end-effector. This means that the centers of the two plates have separated. To make it clear, we denote the separation of the two centers as the *MP center shift*.

3.2. Compliance matrix formulation of curved beam

To derive the stiffness of the SPM limb, the compliance of a circular curved beam is to be formulated. A cantilever with forces and moments applied onto the free end is shown in Fig. 4, the corresponding compliance matrix **C** being calculated by means of Euler–Bernoulli beam theory. To this end, the strain energy is expressed as

$$U = \frac{R}{2}\int_0^\alpha \left[\frac{(f_1')^2}{EA} + \frac{(f_2')^2}{GA} + \frac{(f_3')^2}{GA} + \frac{(m_4')^2}{GI_x} + \frac{(m_5')^2}{EI_y} + \frac{(m_6')^2}{EI_z} \right] \mathrm{d}\phi \tag{18}$$

with the forces and moments defined as

$$f_1' = f_1\cos\phi - f_2\sin\phi$$
$$f_2' = f_1\sin\phi + f_2\cos\phi$$
$$f_3' = f_3$$
$$m_4' = m_4\cos\phi - m_5\sin\phi - f_3R(1-\cos\phi)$$
$$m_5' = m_4\sin\phi + m_5\cos\phi + f_3R\sin\phi$$
$$m_6' = m_6 - f_1R(1-\cos\phi) - f_2R\sin\phi.$$

Using Castigliano's theorem [12], the deflections are obtained by differentiation of Eq. (18):

$$\Delta u_1 = \frac{\partial U}{\partial m_4}, \quad \Delta u_2 = \frac{\partial U}{\partial m_5}, \quad \Delta u_3 = \frac{\partial U}{\partial m_6}, \quad \Delta u_4 = \frac{\partial U}{\partial f_1}, \quad \Delta u_5 = \frac{\partial U}{\partial f_2}, \quad \Delta u_6 = \frac{\partial U}{\partial f_3}. \tag{19}$$

Subsequently, the relationship between the deflections and wrench is established as

$$\begin{bmatrix} \Delta u_1 \\ \Delta u_2 \\ \Delta u_3 \\ \Delta u_4 \\ \Delta u_5 \\ \Delta u_6 \end{bmatrix} = \begin{bmatrix} C_{11} & C_{12} & 0 & 0 & 0 & C_{16} \\ C_{12} & C_{22} & 0 & 0 & 0 & C_{26} \\ 0 & 0 & C_{33} & C_{34} & C_{35} & 0 \\ 0 & 0 & C_{34} & C_{44} & C_{45} & 0 \\ 0 & 0 & C_{35} & C_{45} & C_{55} & 0 \\ C_{16} & C_{26} & 0 & 0 & 0 & C_{66} \end{bmatrix} \begin{bmatrix} m_4 \\ m_5 \\ m_6 \\ f_1 \\ f_2 \\ f_3 \end{bmatrix} \quad \text{or} \quad \Delta\mathbf{u} = \mathbf{C}\mathbf{f} \tag{20}$$

The entries of the compliance matrix C are given in Appendix A.
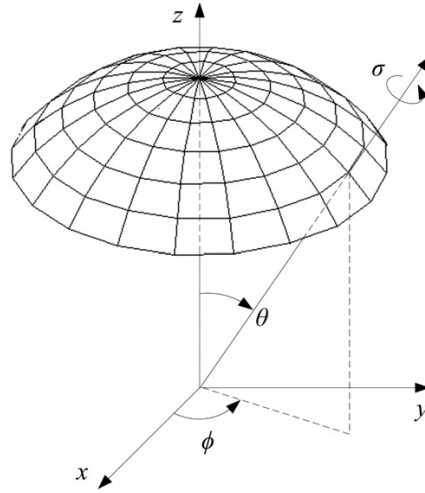
Fig. 5. Orientation representation of the *azimuth–tilt–torsion* angles.

4. Case studies

Henceforth, the MP orientation is represented by *azimuth–tilt–torsion* (ϕ–θ–σ) angles [13], as shown in Fig. 5, the analysis being carried out under one given working mode [14], characterized by $(\mathbf{u}_i \times \mathbf{v}_i) \cdot \mathbf{w}_i \leq 0$, $i = 1, 2, 3$. Moreover, the actuator stiffness is set to $K_{act}^i = 10^6$ Nm/rad for examples I and II.

4.1. Example I: unlimited-roll SPM

The first example pertains to an unlimited-roll SPM [15,16] shown in Fig. 6(a), that consists only of three curved links connected to the MP. The three links are driven by actuators moving independently on a circular guide. The dimensions and link parameters of the SPM, which admits a relatively large dexterous workspace [16], are listed in Table 1, where r is the radius of the circular cross section of the curved link and R is the radius of the midcurve.
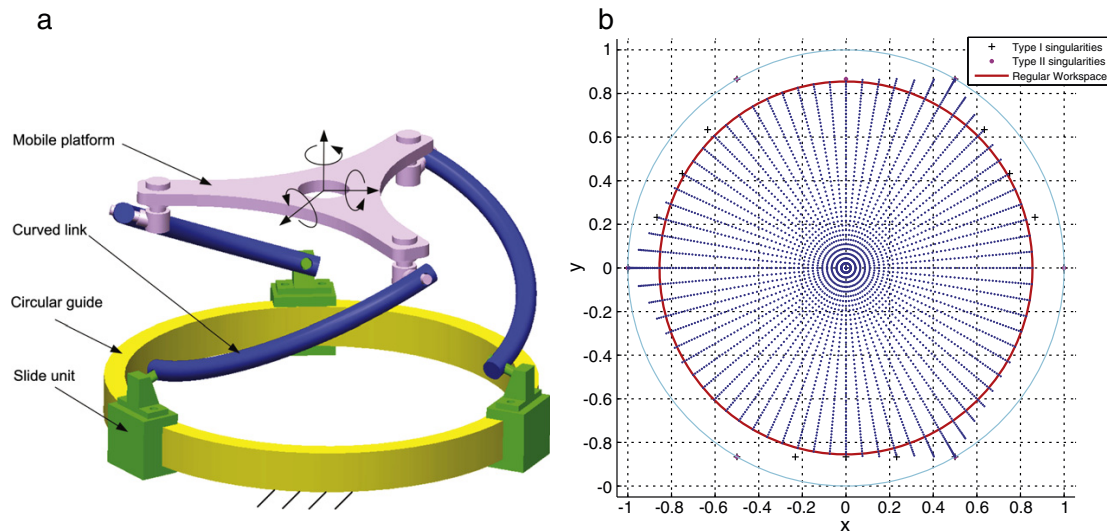
Fig. 6. A spherical parallel manipulator with unlimited roll: (a) schematic diagram; (b) its regular workspace with $\sigma = 0$.

Table 1
Dimensions and parameters of the special SPM.

SPM			Link			
a_1	a_2	β	R [m]	r [m]	E [GPa]	v
60°	90°	90°	0.200	0.0075	210	0.3

Fig. 6(b) shows the workspace on a unit sphere projected in the xy plane for the SPM with $\sigma = 0$. Similarly, the workspace can be obtained for different values of σ. The link is made of steel of Young's modulus E, Poisson's ratio v and shear modulus $G = E/(2 + 2v)$. From Eq. (20), the compliance matrix of the distal curved link is calculated as

$$
\mathbf{C}_2 = \left[\begin{array}{ccc|ccc}
6.923 & -0.575 & 0 & 0 & 0 & 0.388 \\
-0.575 & 6.923 & 0 & 0 & 0 & 0.632 \\
0 & 0 & 6.020 & -0.438 & -0.767 & 0 \\
\hline
0 & 0 & -0.438 & 0.055 & 0.077 & 0 \\
0 & 0 & -0.767 & 0.077 & 0.121 & 0 \\
0.388 & 0.632 & 0 & 0 & 0 & 0.192
\end{array}\right] \cdot 10^{-4}
\tag{21}
$$

The blocks corresponding to rotation, translation and coupling are given in rad/Nm, m/N and rad/N, respectively.
For configurations with *tilt* angle $\theta = 0$, the stiffness matrix is constantly equal to

$$
\mathbf{K} = \begin{bmatrix} \mathbf{K}_{rr} & \mathbf{K}_{rt} \\ \mathbf{K}_{rt}^{T} & \mathbf{K}_{tt} \end{bmatrix} = \left[\begin{array}{ccc|ccc}
0.055 & 0 & 0 & -0.373 & 0.430 & 0 \\
0 & 0.055 & 0 & -0.430 & -0.373 & 0 \\
0 & 0 & 0.332 & 0 & 0 & 0.745 \\
\hline
-0.373 & -0.430 & 0 & 6.233 & 0 & 0 \\
0.430 & -0.373 & 0 & 0 & 6.233 & 0 \\
0 & 0 & 0.745 & 0 & 0 & 1.849
\end{array}\right] \cdot 10^6
\tag{22}
$$

The entries $\mathbf{K}_{rr}$, $\mathbf{K}_{rt}$ and $\mathbf{K}_{tt}$ are given in Nm/rad, N/rad and N/m, respectively. For any applied external wrench, the deformation of the SPM can be determined. An example is given for a vector of pure moments $\mathbf{m} = [10, 10, 10]^T$ Nm, which induce the deformation screw

$$
\mathbf{S}_O = [2.985 \quad 2.985 \quad 0.314; \quad 0.385 \quad -0.028 \quad -0.127]^T
$$

where the angular deflection is given hereafter within the deformation screw in μrad, which leads to $\|\Delta\varphi\| = 4.232$ μrad $= 0.243°$ and $\|\Delta\mathbf{p}\| = 0.406$ mm.
The stiffness matrix Eq. (22) is obtained for curved links of uniform cross-section, as shown in Fig. 6(a). In a real design, the curved link can have embodiment of cylindrical ends, as shown in Fig. 1. For this type of links, the diagonal entries of the stiffness can slightly increase, leading to a smaller deflection.

4.1.1. SPM compliance at singular configurations
The stiffness matrix at certain configurations may become singular. Taking [90°, 60°, 0], for example, the SPM encounters a parallel singularity, where det($\mathbf{A}$) = 0, as depicted in Fig. 6(b), and the stiffness matrix is

$$
\mathbf{K} = \left[\begin{array}{ccc|ccc}
0.067 & 0.101 & -0.007 & -0.523 & -0.333 & 0.084 \\
0.101 & 0.192 & 0.082 & -0.832 & -0.608 & 0.637 \\
-0.007 & 0.082 & 0.205 & -0.061 & -0.210 & 1.130 \\
\hline
-0.523 & -0.832 & -0.061 & 4.602 & 2.287 & -1.320 \\
-0.333 & -0.608 & -0.210 & 2.287 & 3.475 & -1.269 \\
0.084 & 0.637 & 1.130 & -1.320 & -1.269 & 6.876
\end{array}\right] \cdot 10^6
\tag{23}
$$

In matrix Eq. (23), rank($\mathbf{K}_{rr}$) = 2, the stiffness matrix thus being singular. The problem of calculating the displacements can be solved by means of least squares based on the QR decomposition [17], namely,

$$
\begin{bmatrix} \mathbf{K} \\ \mathbf{a}^T \end{bmatrix} \mathbf{S}_O = \begin{bmatrix} \mathbf{f} \\ 0 \end{bmatrix}
\tag{24}
$$

where $\mathbf{a}$ is the last column of matrix $\mathbf{R}$ from $\mathbf{K}$, which spans the null space of $\mathbf{K}$. The solution sought that lies outside the null space of $\mathbf{K}$. With the moment $\mathbf{m}$ applied on the MP, the twist deflections are calculated as:

$$
\mathbf{S}_O = [11.502 \quad -4.747 \quad 4.782; \quad 0.285 \quad 0.234 \quad -0.390]^T
\tag{25}
$$

As **K** is singular, the deformation screws will not be definite. By means of the least square method after spanning the null space, the deformation screws are approximated via linear regression. From kinematics, the MP generates a finite rotation about its center of rotation O at this type of singularity. Another example is the case of a serial singularity, for instance, [45°, 60°, 0], where the stiffness matrix is invertible at this type of singularity. The displacements are found as:

$$\mathbf{S}_O = [15.307 \quad -3.246 \quad -2.443; \quad 0.449 \quad -0.315 \quad 0.332]^T \tag{26}$$

4.1.2. Comparison with FEA results

With the parameters in Table 1, the FE model displayed in Fig. 7 was created in Ansys/Workbench to verify the foregoing model; rib stiffeners were used to make the mobile platform rigid and two passive revolute joints in each limb were used to connect the components; while a revolute joint with torsional stiffness of 10^6 Nm/rad is used to describe the actuation stiffness. The material of the model is structural steel with the same Young's and shear modulus as shown in Table 1.

To validate the model effectively, 125 orientations of $\phi \in \mathcal{S}, \phi \in \mathcal{S}$, and $\theta \in \{0, 15°, 30°, 45°, 50°\}$, where $\mathcal{S} = \{0, 45°, 90°, 120°, 180°\}$, under the external moments $\mathbf{m} = [10, 10, 10]^T$ Nm, were analyzed. The corresponding translational and rotational displacements, $\|\Delta \mathbf{p}\|$ and $\|\Delta \boldsymbol{\varphi}\|$, are shown in Fig. 8. At configurations with *tilt* angle $\theta = 0$, the FE solved deflections are $\|\Delta \mathbf{p}\| = 0.401 \pm 0.0004$ mm and $\|\Delta \boldsymbol{\varphi}\| = 0.237 \pm 0.022°$, which are quite close to the analytical solutions. Henceforth, the relative error (%) between the developed model and FE analysis results is defined as

$$Err = |\delta_{Ana} - \delta_{Fea}| / \delta_{Fea} \cdot 100\% \tag{27}$$

where δ stands for the δp or $\delta \phi$. The average relative error for $\|\Delta \mathbf{p}\|$ is 1.48% and the average difference is 0.014 mm. For $\|\Delta \boldsymbol{\varphi}\|$, the average difference is 0.035° or 4.17% of relative error. In contrast, the difference of the results obtained from the FEA approach and the developed model for the most workspace points is below 5%. An exception is the SPM at singular configuration. For instance, at the singular configuration of [45°, 60°, 0] under $\mathbf{m} = [10, 10, 10]^T$ Nm, the FE solved deflections are $\|\Delta \mathbf{p}\| = 0.635$ mm and $\|\Delta \boldsymbol{\varphi}\| = 1.041°$. Compared to the analytical solution Eq. (26), the difference for the orientation error rises up to about 13%. The comparison shows that the developed stiffness model can effectively calculate the manipulator stiffness.

In the FE model, we consider only major geometric dimensions. Details such as round corner or chamfers are not included. While such details affect the stress, they have less influence on the deflection.

4.1.3. Isocontours of MP center shift and orientation error

Fig. 9(a) and (b) illustrate the isocontours of the MP center shift and orientation error throughout the regular workspace. The maps are formulated with the maximum magnitude at each discrete point among the eight combinations of moment $\mathbf{m} = [\pm 10, \pm 10, \pm 10]^T$ Nm. It is apparent that the largest displacements occur at the workspace boundary and the three peaks of the contours appear symmetrically distributed at intervals of 120°. The maximum orientation error and center shift are 3.5° and 2 mm, respectively, for the link properties given, the MP oriented at $\phi = -70°$. Within the region $\theta \leq 30°$, the orientation accuracy due to the elastic deformation can reach 1°, whereas the center shift can reach up to 1.5 mm, which cannot be ignored when high positional accuracy is needed. Given the SPM symmetry, the other cases of σ-orientations generate the same isocontour maps with rotational symmetry to Fig. 9(a) and (b), respectively. It can be predicted that the global stiffness becomes weaker from the center region of the workspace to the boundary and its 3D contour map resembling a conical surface.

Fig. 9(c) displays the orientation error when only the actuation compliance is considered. By comparison to Fig. 9(b), it is seen that the limb flexibility strongly influences the orientation error. The link properties should thus be an important consideration in the SPM design.
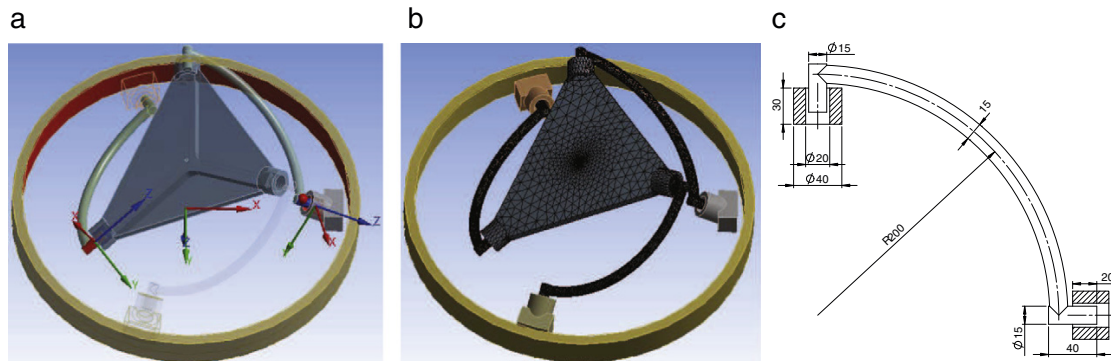

Fig. 7. SPM model for FE analysis: (a) revolute joints; (b) link meshing; (c) link detail, where bearings mounted between the shaft and the hole are not displayed.
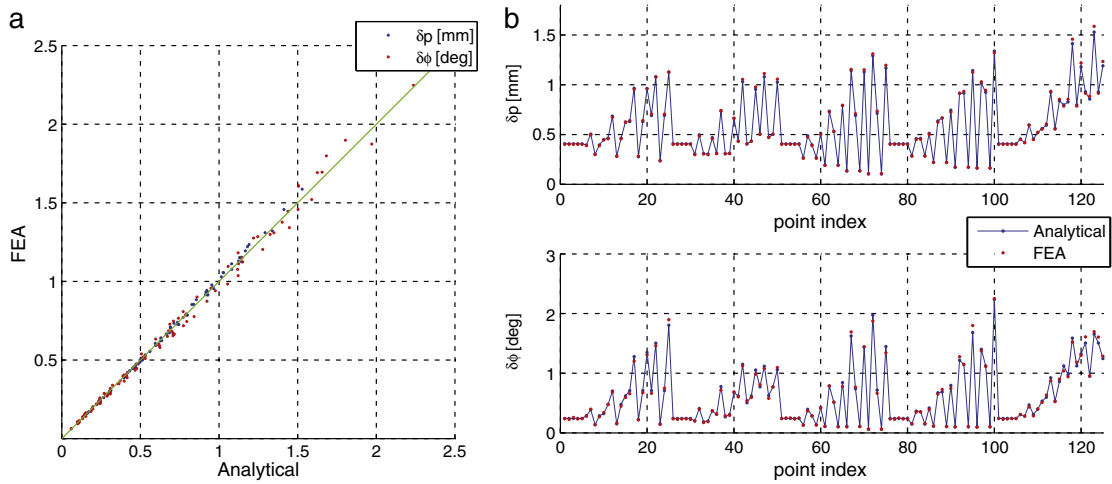
Fig. 8. Comparison of the linear and angular deflections between the FEA and analytical approaches: (a) correlations; (b) error variations, where $\delta p = \|\Delta \mathbf{p}\|$, $\delta \phi = \|\Delta \boldsymbol{\varphi}\|$.

4.2. Example II: an alternative structure of a co-axial SPM

In this example, an alternative structure of the SPM in Example I, shown in Fig. 10, is studied. At the orientation [0, 0, 0], the Cartesian stiffness matrix is computed as:

$$\mathbf{K} = \begin{bmatrix} 0.021 & 0 & 0 & -0.092 & 0.183 & 0 \\ 0 & 0.021 & 0 & -0.183 & -0.092 & 0 \\ 0 & 0 & 0.127 & 0 & 0 & 0.247 \\ -0.092 & -0.183 & 0 & 3.253 & 0 & 0 \\ 0.183 & -0.092 & 0 & 0 & 3.253 & 0 \\ 0 & 0 & 0.247 & 0 & 0 & 1.808 \end{bmatrix} \cdot 10^5 \tag{28}$$

Compared to matrix Eq. (22), the diagonal elements are much smaller, which imply that this SPM will generate large twist deformation under moment m:

$$\mathbf{S}_O = \begin{bmatrix} 12.043 & 12.043 & 1.0647; & 1.019 & -0.336 & -0.146 \end{bmatrix}^T$$

The isocontours for the orientation error and center shift are displayed in Fig. 11. It is seen that both the MP center shift and orientation error are larger than the SPM in Example I, which indicates that the presence of the circular guide of SPM in Fig. 6(a) effectively reduces the positioning errors.

4.3. Example III: Agile Wrist

This example borrows the geometric parameters of the Agile Wrist [18], i.e., $\alpha_1 = \alpha_2 = 90^o, \beta = \gamma = sin^{-1}(\sqrt{6}/3)$, as shown in Fig. 12, whose architecture determines a large workspace with $\sigma = 30^o$, but keeps the same properties of the circular curved beam. The actuation stiffness is $K_{act} = 5.44 \cdot 10^5$ Nm/rad. The isocontours for the center shift and orientation error are mapped within a dexterous workspace, as seen in Fig. 13. When $\sigma = 0$, the maximum orientation error can reach up to 12° at the workspace bounds while the center shift is 4.5 mm. With *torsion* angle σ increasing, the MP center shift and orientation error become smaller.

5. Conclusions

This paper investigates the MP center shift in spherical parallel manipulators with the consideration of limb flexibility. On the basis of screw theory, the virtual-spring method, supported with Castigliano's theorem is adopted for the stiffness modeling of SPMs. The model developed is validated by means of FEA. The elastic deformation for the SPMs at singular configurations is given due attention, which is handled by means of least square method, based on the QR decomposition.

a $\|\triangle p\|$ (mm)

b $\|\triangle \varphi\|$ (deg)

c $\|\triangle \varphi\|$ (deg)
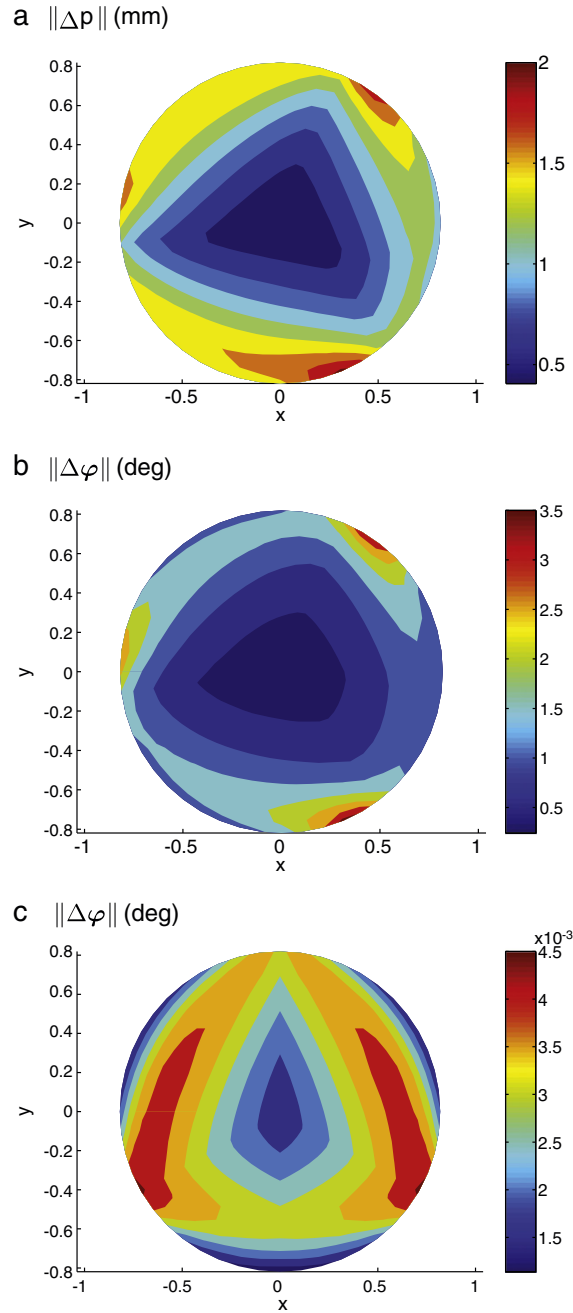
Fig. 9. MP center shift and orientation error for the unlimited-roll SPM throughout the regular workspace with orientation $\sigma = 0$: (a) and (b) both actuation and link compliance are considered; (c) only actuation compliance is considered.

A major contribution of the paper is the development of a method for qualifying the MP center shift of SPMs. The method addresses a common problem with SPMs of revolute joints. The proposed approach is illustrated with case studies of SPMs with different structures, whose isocontours for the MP center shift and orientation errors within a prescribed workspace were mapped. Moreover, the isocontours can be used for stiffness maps of SPMs. Through comparison, it is found that the SPM with the
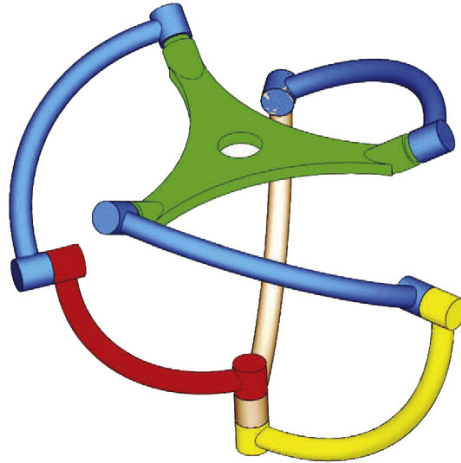
Fig. 10. An alternative structure of the unlimited-roll SPM.

circular guide yields a smaller center shift and error. The study shows that the deflection due to the limb flexibility causes large errors, in particular, the MP center shift, which could be considered in the design of SPMs, with the method developed in this work.

Supplementary data to this article can be found online at http://dx.doi.org/10.1016/j.mechmachtheory.2014.01.001.
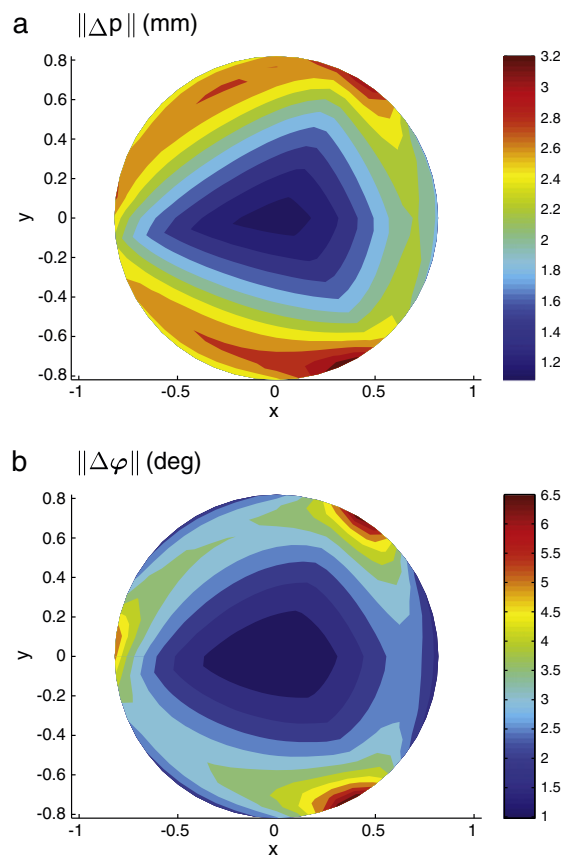
Fig. 11. MP center shift and orientation error for an alternative structure of the co-axial SPM throughout the regular workspace with orientation $\sigma = 0$.
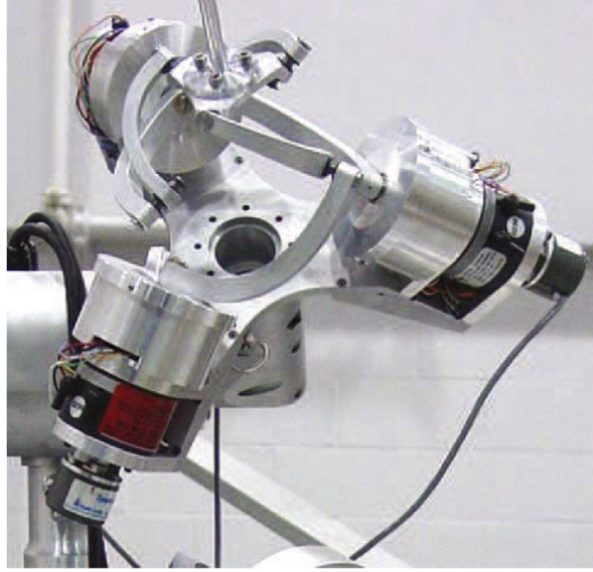
Fig. 12. Prototype of the Agile Wrist, McGill University, Canada.
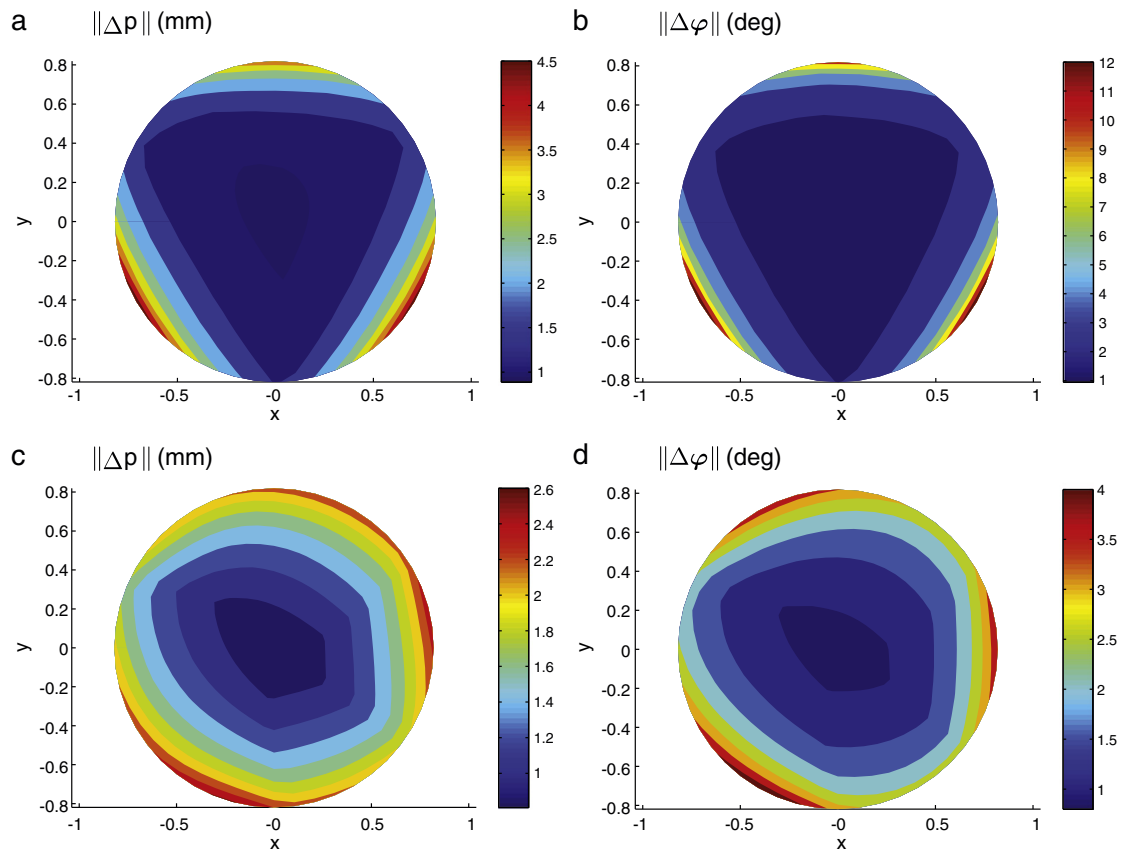
Fig. 13. MP center shift and orientation error for the Agile Wrist throughout the regular dexterous workspace with orientation: (a) and (b) $\sigma = 0$; (c) and (d) $\sigma = 30°$.

Acknowledgment

Appendix A

The elements of the compliance matrix of the curved beam in Eq. (20) are given as:

$$C_{11} = \frac{R}{2}\left(\frac{s_1}{GI_x} + \frac{s_2}{EI_y}\right) \tag{A-1a}$$

$$C_{12} = \frac{s_8 R}{2}\left(\frac{1}{GI_x} - \frac{1}{EI_y}\right) \tag{A-1b}$$

$$C_{16} = \frac{R^2}{2}\left(\frac{s_2}{EI_y} - \frac{s_7}{GI_x}\right) \tag{A-1c}$$

$$C_{22} = \frac{R}{2}\left(\frac{s_2}{GI_x} + \frac{s_1}{EI_y}\right) \tag{A-1d}$$

$$C_{26} = \frac{R^2}{2}\left(\frac{s_4}{GI_x} - \frac{s_2}{EI_y}\right) \tag{A-1e}$$

$$C_{33} = \frac{R\alpha}{EI_z} \tag{A-1f}$$

$$C_{34} = \frac{s_5 R^2}{EI_z} \tag{A-1g}$$

$$C_{35} = \frac{s_6 R^2}{EI_z} \tag{A-1h}$$

$$C_{44} = \frac{R}{2A}\left(\frac{s_1}{E} + \frac{s_2}{G}\right) + \frac{s_3 R^3}{2EI_z} \tag{A-1i}$$

$$C_{45} = \frac{s_8 R}{2A}\left(\frac{1}{E} - \frac{1}{G}\right) + \frac{s_4 R^3}{2EI_z} \tag{A-1j}$$

$$C_{55} = \frac{R}{2A}\left(\frac{s_1}{G} + \frac{s_2}{E}\right) + \frac{s_2 R^3}{2EI_z} \tag{A-1k}$$

$$C_{66} = \frac{R\alpha}{GA} + \frac{R^3}{2}\left(\frac{s_3}{GI_x} + \frac{s_2}{EI_y}\right) \tag{A-1l}$$

where A is the area of the beam cross section, I_x, I_y and I_z are the moments of inertia. Moreover,

$$s_1 = \alpha + \sin\alpha\cos\alpha \tag{A-2a}$$

$$s_2 = \alpha - \sin\alpha\cos\alpha \tag{A-2b}$$

$$s_3 = 3\alpha + \sin\alpha\cos\alpha/2 - 4\sin\alpha \tag{A-2c}$$

$$s_4 = 1 - \cos\alpha - \sin^2\alpha/2 \tag{A-2d}$$

$$s_5 = \sin\alpha - \alpha \tag{A-2e}$$

$$s_6 = \cos\alpha - 1 \tag{A-2f}$$

$$s_7 = 2\sin\alpha - \alpha - \sin\alpha\cos\alpha \tag{A-2g}$$

$$s_8 = -\sin^2\alpha. \tag{A-2h}$$

References

[1] C.M. Gosselin, J.-F. Hamel, The Agile Eye: a high-performance three-degree-of-freedom camera-orienting device, IEEE Int. Conf. Robot. Autom. 1 (1994) 781–786, http://dx.doi.org/10.1109/ROBOT.1994.351393.

[2] C. Gosselin, Stiffness mapping for parallel manipulators, IEEE Trans. Robot. Autom. 6 (3) (1990) 377–382, http://dx.doi.org/10.1109/70.56657.

[3] S.-F. Chen, I. Kao, Conservative congruence transformation for joint and Cartesian stiffness matrices of robotic hands and fingers, Int. J. Robot. Res. 19 (2000) 835–847, http://dx.doi.org/10.1177/02783640022067201.

[4] C.M. Gosselin, D. Zhang, Stiffness analysis of parallel mechanisms using a lumped model, Int. J. Robot. Autom. 17 (1) (2003) 17–27.

[5] F. Majou, C. Gosselin, P. Wenger, D. Chablat, Parametric stiffness analysis of the orthoglide, Mech. Mach. Theory 42 (3) (2007) 296–311, http://dx.doi.org/10.1016/j.mechmachtheory.2006.03.018.

[6] C. Quennouelle, C.M. Gosselin, Stiffness matrix of compliant parallel mechanisms, in: J. Lenarčič, P. Wenger (Eds.), Advances in Robot Kinematics: Analysis and Design, Springer, Netherlands, 2008, pp. 331–341, http://dx.doi.org/10.1007/978-1-4020-8600-7_35.

[7] A. Pashkevich, D. Chablat, P. Wenger, Stiffness analysis of overconstrained parallel manipulators, Mech. Mach. Theory 44 (5) (2009) 966–982, http://dx.doi.org/10.1016/j.mechmachtheory.2008.05.017.

[8] X.J. Liu, Z.L. Jin, F. Gao, Optimum design of 3-DOF spherical parallel manipulators with respect to the conditioning and stiffness indices, Mech. Mach. Theory 35 (9) (2000) 1257–1267, http://dx.doi.org/10.1016/S0094-114X(99)00072-5.

[9] J. Enferadi, A.A. Tootoonchi, Accuracy and stiffness analysis of a 3-RRP spherical parallel manipulator, Robotica 29 (2) (2011) 193–209, http://dx.doi.org/10.1017/S0263574710000032.

[10] H. Asada, J. Granito, Kinematic and static characterization of wrist joints and their optimal design, IEEE Int. Conf. Robot. Autom. 2 (1985) 244–250, http://dx.doi.org/10.1109/ROBOT.1985.1087324.

[11] C.M. Gosselin, E. Lavoie, On the kinematic design of spherical three-degree-of-freedom parallel manipulators, Int. J. Robot. Res. 12 (4) (1993) 394–402, http://dx.doi.org/10.1177/027836499301200406.

[12] R.C. Hibbeler, Mechanics of Materials, Pearson Prentice Hall, 2011.

[13] I.A. Bonev, Direct kinematics of zero-torsion parallel mechanisms, International Conference on Robotics and Automation, IEEE, 2008, pp. 3851–3856, http://dx.doi.org/10.1109/ROBOT.2008.4543802, (Pasadena, California, USA).

[14] I.A. Bonev, D. Chablat, P. Wenger, Working and assembly modes of the Agile Eye, International Conference on Robotics and Automation, 2006, pp. 2317–2322, http://dx.doi.org/10.1109/ROBOT.2006.1642048.

[15] S. Bai, M.R. Hansen, T.O. Andersen, Modelling of a special class of spherical parallel manipulators with Euler parameters, Robotica 27 (2) (2009) 161–170, http://dx.doi.org/10.1017/S0263574708004402.

[16] S. Bai, Optimum design of spherical parallel manipulators for a prescribed workspace, Mech. Mach. Theory 45 (2) (2010) 200–211, http://dx.doi.org/10.1016/j.mechmachtheory.2009.06.007.

[17] G.H. Golub, C.F. Van Loan, Matrix Computations, 3rd ed. Johns Hopkins University Press, Baltimore, MD, USA, 1996.

[18] F. Bidault, C.-P. Teng, J. Angeles, Structural optimization of a spherical parallel manipulator using a two-level approach, Proc. ASME 2001 Design Engineering Technical Conferences, DETC2001/DAC-21030, Pittsburgh, Pennsylvania, 2001.
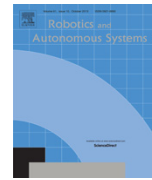
6

Paper III

G. Wu, S. Caro, S. Bai, J.A. Kepler, 2014. Dynamic modeling and design optimization of a 3-DOF spherical parallel manipulator, *Robotics and Autonomous Systems*, 62(10): 1377–1386, DOI: 10.1016/j.robot.2014.06.006.

Dynamic modeling and design optimization of a 3-DOF spherical parallel manipulator

Guanglei Wu [a], Stéphane Caro [b], Shaoping Bai [a,*], Jørgen Kepler [a]

[a] Department of Mechanical and Manufacturing Engineering, Aalborg University, DK-9220 Aalborg, Denmark
[b] CNRS, Institut de Recherche en Communications et Cybernétique de Nantes, UMR CNRS n° 6597, 44321 Nantes, France

HIGHLIGHTS

- A dynamic model is derived by considering the motion characteristics of spherical parallel manipulators (SPMs).
- A comprehensive multiobjective optimization approach is formulated for SPMs.
- A Pareto-front is obtained to show the Pareto optimal solutions for selected design criteria.
- A scatter matrix is generated to show the inter-dependencies between the decision variables.

ARTICLE INFO

ABSTRACT

This paper deals with the dynamic modeling and design optimization of a three Degree-of-Freedom spherical parallel manipulator. Using the method of Lagrange multipliers, the equations of motion of the manipulator are derived by considering its motion characteristics, namely, all the components rotating about the center of rotation. Using the derived dynamic model, a multiobjective optimization problem is formulated to optimize the structural and geometric parameters of the spherical parallel manipulator. The proposed approach is illustrated with the design optimization of an unlimited-roll spherical parallel manipulator with a main objective to minimize the mechanism mass in order to enhance both kinematic and dynamic performances.

© 2014 Elsevier B.V. All rights reserved.

1. Introduction

The design of three Degree-of-Freedom (3-DOF) spherical parallel manipulators (SPMs) can consider many criteria, such as workspace [1–3], dexterity [4–6], dynamics [7], singularity avoidance [8], stiffness [9,10]. These evaluation criteria can be classified into two groups: one relates to the kinematic performance while the other relates to the kinetostatic/dynamic performance of the manipulator [11]. Most of the SPMs find their applications as orienting devices, such as camera orienting and medical instrument alignment [12,13], therefore, the kinematic aspects, mainly, workspace and dexterity, were extensively studied in the literature. On the other hand, the dynamics received less attention. Staicu [7] used the principle of virtual work to derive the inverse

dynamics of the Agile Wrist [10], in which recursive matrix relations for kinematics and dynamics were established. When the SPMs are used to build active spherical manipulators, for instance, wrist joint [14], the dynamic characteristics are of importance in their design and applications.

This work develops a dynamic model with the classical approach of Lagrange multipliers, which takes all the mobile components into consideration to calculate the power consumption effectively. The equations of motion for the SPMs are modeled with the motion characteristics, namely, all the bodies rotating about a fixed point (center of rotation). The derived dynamic model can be used either to assess the dynamic performance or in the design optimization.

In general, a robot design process has to simultaneously deal with the kinematic and kinetostatic/dynamic aspects, both of which include a number of performance measures that essentially vary throughout the workspace. This can be effectively achieved by virtue of multiobjective optimization method. The multiobjective optimization problems of parallel manipulators (PMs) have been reported in the literature, where various approaches of

* Corresponding author. Tel.: +45 9940 9291; fax: +45 9940 7110.
E-mail addresses: gwu@m-tech.aau.dk (G. Wu),
Stephane.Caro@irccyn.ec-nantes.fr (S. Caro), shb@m-tech.aau.dk (S. Bai),
jk@m-tech.aau.dk (J. Kepler).
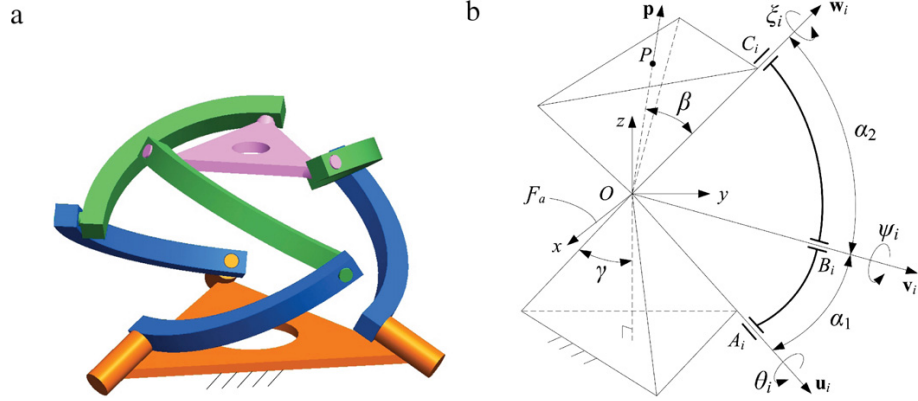
a

b

Fig. 1. Architecture of a general SPM: (a) overview, (b) parameterization of the ith leg.
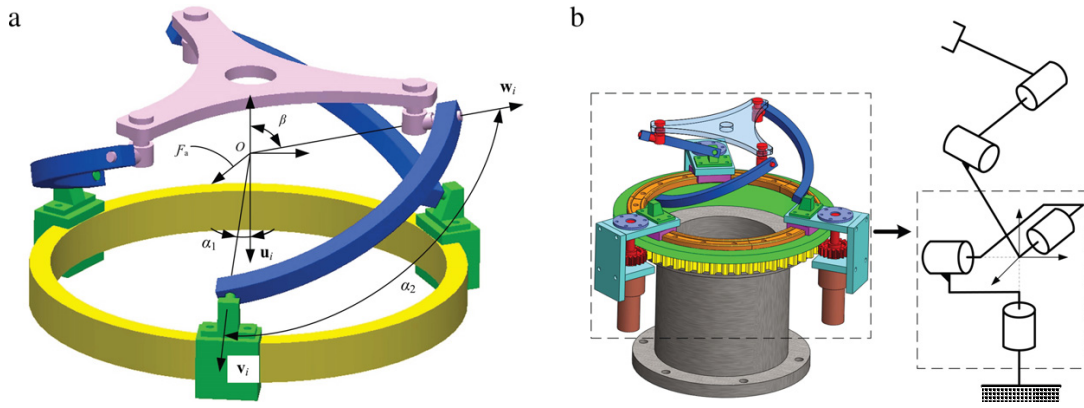
a

b

Fig. 2. (a) 3-DOF unlimited-roll SPM, which is a special case of the general SPM with $\gamma = 0$; (b) its application as spherically actuated joint.

multiobjective optimization have been applied to different types of PMs, while considering kinematic, dynamic and static criteria [11, 15–18]. However, a systematic approach lacks in the optimum design for this class of SPMs, as the static/dynamic performance received relatively less attention as mentioned above.

This paper focuses on the dynamic modeling and design optimization of the SPMs. A dynamic model of the SPM is derived based on the Lagrange equations. Based on the dynamics, together with the kinematics and stiffness of the manipulator, a multiobjective design optimization method is proposed for SPMs, aiming to formulate a general approach for the SPMs in the early design stage. The multi-objective design optimization problem is applied to a 3-DOF unlimited-roll SPM, for which the Pareto-optimal solutions are obtained with a genetic algorithm.

2. Architecture of SPMs

A general spherical parallel manipulator is shown in Fig. 1. The ith leg consists of three revolute joints, whose axes are parallel to the unit vectors $\mathbf{u}_i$, $\mathbf{v}_i$, and $\mathbf{w}_i$. All three legs have identical architectures, defined by angles $\alpha_1, \alpha_2, \beta$ and γ, where β and γ define the geometry of two regular pyramids of the base and mobile platforms. Both the two platforms are assumed to be rigid. The origin O of the base coordinate system $\mathcal{F}_a$ is located at the center of rotation. The z axis is normal to the bottom surface of the base pyramid and points upwards, while the y axis is located in the plane spanned by the z axis and $\mathbf{u}_1$ vector.

The SPM under study is a special case of $\gamma = 0$ [3], where the pyramids of the base platform is degenerated to a line segment, as shown in Fig. 2(a). The axes of the three active revolute joints are coincident with the z axis and it consists only of three curved links connected to its mobile platform. The links are driven by actuators moving independently on a circular guide via pinion and gear-ring transmissions, which can replace the serial chains based wrist mechanisms as displayed Fig. 2(b).

3. Dynamic modeling of SPMs

The orientation of the mobile platform (MP) is described by the azimuth–tilt–torsion (ϕ–θ–σ) angles [19] as displayed in Fig. 3, for which the rotation matrix is expressed as:

$$\mathbf{Q} = \mathbf{R}_z(\phi)\mathbf{R}_y(\theta)\mathbf{R}_z(\sigma - \phi) \tag{1}$$

where $\phi \in (-\pi, \pi], \theta \in [0, \pi), \sigma \in (-\pi, \pi]$.

Under the prescribed coordinate system, unit vector $\mathbf{u}_i$ is derived as

$$\mathbf{u}_i = \begin{bmatrix} -\sin\eta_i \sin\gamma & \cos\eta_i \sin\gamma & -\cos\gamma \end{bmatrix}^T \tag{2}$$

where $\eta_i = 2(i-1)\pi/3, i = 1, 2, 3$.

Unit vector $\mathbf{v}_i$ of the axis of the intermediate revolute joint in the ith leg is expressed as:

$$\mathbf{v}_i = \begin{bmatrix} -s\eta_i s\gamma c\alpha_1 + (c\eta_i s\theta_i - s\eta_i c\gamma c\theta_i)s\alpha_1 \\ c\eta_i s\gamma c\alpha_1 + (s\eta_i s\theta_i + c\eta_i c\gamma c\theta_i)s\alpha_1 \\ -c\gamma c\alpha_1 + s\gamma c\theta_i s\alpha_1 \end{bmatrix} \tag{3}$$
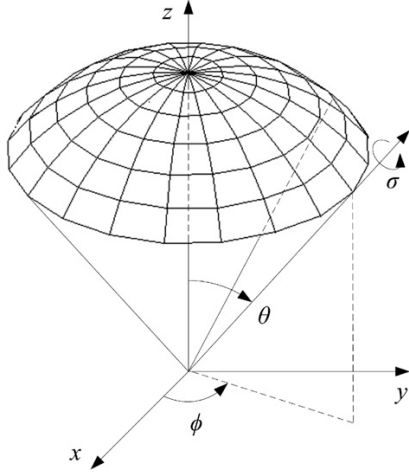
Fig. 3. Orientation representation of the *azimuth–tilt–torsion* angles.

Fig. 4. The movements of the mobile platform and a single leg.

Unit vector $\mathbf{w}_i$ of the top revolute joint in the ith leg, is a function of the orientation of the mobile platform described as

$$\mathbf{w}_i = \begin{bmatrix} w_{ix} & w_{iy} & w_{iz} \end{bmatrix}^T = \mathbf{Q}\mathbf{w}_i^* \tag{4}$$

where $\mathbf{w}_i^*$ is the unit vector for the axis of the top revolute joint of the ith leg when the mobile platform (MP) reaches its home configuration, i.e., the MP orientation in the reference frame, which is given as

$$\mathbf{w}_i^* = \begin{bmatrix} -\sin\eta_i \sin\beta & \cos\eta_i \sin\beta & \cos\beta \end{bmatrix}^T \tag{5}$$

3.1. Kinematic Jacobian matrix

The relationship between the angular velocity of the mobile platform $\boldsymbol{\omega} = [\omega_x\ \omega_y\ \omega_z]^T$ and the input angle velocity $\dot{\boldsymbol{\theta}} = [\dot{\theta}_1\ \dot{\theta}_2\ \dot{\theta}_3]^T$ is expressed as

$$\mathbf{A}\boldsymbol{\omega} = \mathbf{B}\dot{\boldsymbol{\theta}} \tag{6}$$

with

$$\mathbf{A} = \begin{bmatrix} \mathbf{a}_1 & \mathbf{a}_2 & \mathbf{a}_3 \end{bmatrix}^T; \quad \mathbf{a}_i = \mathbf{v}_i \times \mathbf{w}_i \tag{7a}$$

$$\mathbf{B} = \mathrm{diag}\begin{bmatrix} b_1 & b_2 & b_3 \end{bmatrix}; \quad b_i = (\mathbf{u}_i \times \mathbf{v}_i) \cdot \mathbf{w}_i \tag{7b}$$

where matrices $\mathbf{A}$ and $\mathbf{B}$ are named the forward and inverse Jacobian matrices of the manipulator, respectively. The kinematic Jacobian matrix $\mathbf{J}$ of the manipulator [1] is obtained as

$$\mathbf{J} = \mathbf{B}^{-1}\mathbf{A} = \begin{bmatrix} \mathbf{j}_1 & \mathbf{j}_2 & \mathbf{j}_3 \end{bmatrix}^T; \quad \mathbf{j}_i = \mathbf{a}_i/b_i \tag{8}$$

3.2. Inverse dynamic modeling

The motions of the SPM bodies are shown in Fig. 4. The relationship between the angle rates $\dot{\boldsymbol{\varphi}} = [\dot{\phi}\ \dot{\theta}\ \dot{\sigma}]^T$ and the angular velocity $\boldsymbol{\omega}$ is found as [20]:

$$\begin{bmatrix} \omega_x \\ \omega_y \\ \omega_z \end{bmatrix} = \begin{bmatrix} -\mathrm{s}\theta\mathrm{c}\phi & -\mathrm{s}\phi & \mathrm{s}\theta\mathrm{c}\phi \\ -\mathrm{s}\theta\mathrm{s}\phi & \mathrm{c}\phi & \mathrm{s}\theta\mathrm{s}\phi \\ 1-\mathrm{c}\theta & 0 & \mathrm{c}\theta \end{bmatrix} \begin{bmatrix} \dot{\phi} \\ \dot{\theta} \\ \dot{\sigma} \end{bmatrix} \quad \text{or} \quad \boldsymbol{\omega} = \boldsymbol{\Phi}\dot{\boldsymbol{\varphi}} \tag{9}$$

The dynamics of the SPM can be solved by using the Lagrange equations [21] below

$$\frac{\mathrm{d}}{\mathrm{d}t}\left(\frac{\partial L}{\partial \dot{\mathbf{q}}}\right) - \frac{\partial L}{\partial \mathbf{q}} + \mathbf{C}_q^T\boldsymbol{\lambda} = \mathbf{Q}_{ex} \tag{10}$$
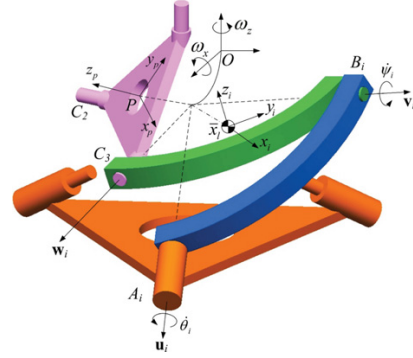
where $L \equiv T - V$ is the Lagrangian of the system, including the mobile platform and the three legs, and $\mathbf{q} = [\theta_1,\ \theta_2,\ \theta_3,\ \phi,\ \theta,\ \sigma]^T$. Moreover, $\mathbf{Q}_{ex} = [\boldsymbol{\tau}^T,\ \mathbf{0}]^T \in \mathbb{R}^6$ is the vector of external forces and vector $\boldsymbol{\tau} = [\tau_1,\ \tau_2,\ \tau_3]^T$ characterizes the actuator torques. Matrix $\mathbf{C}_q$ is the system's constraint Jacobian, which can be found from the velocity Eq. (6), namely,

$$\mathbf{B}\dot{\boldsymbol{\theta}} - \mathbf{A}\boldsymbol{\omega} = \begin{bmatrix} \mathbf{B} & -\mathbf{A}\boldsymbol{\Phi} \end{bmatrix}\begin{bmatrix} \dot{\boldsymbol{\theta}}^T & \dot{\boldsymbol{\varphi}}^T \end{bmatrix}^T = \mathbf{0} \tag{11}$$

therefore, the matrix of constraints is found as $\mathbf{C}_q = [\mathbf{B}\ -\mathbf{A}\boldsymbol{\Phi}]$. Moreover, $\boldsymbol{\lambda} = [\lambda_1,\ \lambda_2,\ \lambda_3]^T$ is a vector of Lagrange multipliers.

3.2.1. Lagrangian of the mobile platform

The local frame (x_p, y_p, z_p) attached to the MP is established with the origin located at point P, i.e., the center of mass of the MP. Henceforth, the Lagrangian of the mobile platform is obtained as

$$L_p = T_p - V_p = \frac{1}{2}\boldsymbol{\omega}^T\mathbf{I}_p\boldsymbol{\omega} - m_pR\cos\beta\mathbf{g}^T\mathbf{p} \tag{12}$$

where $\mathbf{I}_p$ denotes the global inertia tensor of the mobile platform, which can be found in Appendix A. Moreover, $\mathbf{g} = [0,\ 0,\ 9.81\,\mathrm{m/s}^2]^T$.

3.2.2. Lagrangian of a single leg

The velocity $\dot{\psi}$ of the intermediate joint in ith leg is found using the following equation

$$\boldsymbol{\omega} = \dot{\theta}_i\mathbf{u}_i + \dot{\psi}_i\mathbf{v}_i + \dot{\xi}_i\mathbf{w}_i \tag{13}$$

To eliminate $\dot{\theta}_i$ and $\dot{\xi}_i$, dot-multiplying Eq. (13) on both sides with $\mathbf{u}_i \times \mathbf{w}_i$ yields

$$(\mathbf{u}_i \times \mathbf{w}_i) \cdot \boldsymbol{\omega} = \dot{\psi}(\mathbf{u}_i \times \mathbf{w}_i) \cdot \mathbf{v}_i \quad \text{or} \quad \dot{\psi} = \mathbf{j}_{\psi i}^T\boldsymbol{\omega}$$

$$= \frac{(\mathbf{u}_i \times \mathbf{w}_i)^T}{(\mathbf{u}_i \times \mathbf{w}_i) \cdot \mathbf{v}_i}\boldsymbol{\omega} \tag{14}$$

The angular velocity of the distal link in the ith leg in the reference frame (x, y, z) is found as $\boldsymbol{\varpi}_i = \dot{\theta}_i\mathbf{u}_i + \dot{\psi}_i\mathbf{v}_i$. Let $\boldsymbol{\varpi}_{li}$ denote the corresponding angular velocity in the local frame (x_i, y_i, z_i), we have

$$\boldsymbol{\varpi}_i = \begin{bmatrix} \mathbf{e}_{ix} & \mathbf{e}_{iy} & \mathbf{e}_{iz} \end{bmatrix}\boldsymbol{\varpi}_{li} \quad \text{or} \quad \boldsymbol{\varpi}_i = \mathbf{E}_i\boldsymbol{\varpi}_{li} \tag{15}$$

with

$$\mathbf{e}_{ix} = \frac{\mathbf{v}_i + \mathbf{w}_i}{\|\mathbf{v}_i + \mathbf{w}_i\|}, \qquad \mathbf{e}_{iy} = \frac{\mathbf{v}_i - \mathbf{w}_i}{\|\mathbf{v}_i - \mathbf{w}_i\|}, \qquad \mathbf{e}_{iz} = \frac{\mathbf{v}_i \times \mathbf{w}_i}{\|\mathbf{v}_i \times \mathbf{w}_i\|} \tag{16}$$

From Eq. (15), we have $\boldsymbol{\varpi}_{li} = \mathbf{E}_i^T\boldsymbol{\varpi}_i$. The Lagrangian of the ith leg is derived as below

$$L_i = T_i - V_i = \frac{1}{2}I_{l1}\dot{\theta}_i^2 + \frac{1}{2}\boldsymbol{\varpi}_i^T\mathbf{I}_{l2}\boldsymbol{\varpi}_i - m_{l1}\bar{x}_1\mathbf{g}^T\mathbf{h}_i - m_{l2}\bar{x}_2\mathbf{g}^T\mathbf{e}_{ix} \tag{17}$$

where I_{l1} is the proximal link's mass moment of inertia about $\mathbf{u}_i$, and $\mathbf{I}_{l2}$ is the distal link's mass moment of inertia about point O. Moreover, $\bar{x}_1$ and $\bar{x}_2$ indicate the centers of the mass of the proximal and distal links, respectively, and $\mathbf{h}_i = (\mathbf{u}_i + \mathbf{v}_i)/\|\mathbf{u}_i + \mathbf{v}_i\|$. The details for a curved link can be found in Appendix A.

Substituting the Lagrangian L_p and $L_i, i = 1, 2, 3$, into Eq. (10), the terms in the equation of motion for this dynamic system [21] can be derived. With an external moment vector $\mathbf{m}$, the actuator torques are expressed as:

$$\boldsymbol{\tau}_a = \boldsymbol{\tau} - \mathbf{J}^{-T}\mathbf{m} \tag{18}$$

This developed dynamic model can effectively compute the active forces/torques as it takes into account all the mobile components and external forces/moments. Compared to Staicu's work [7], the model developed in this work has a more compact form, which takes advantages of the unique feature of SPMs that involves only rotations. Such a formulation can be easily understood and implemented.

4. Optimization problem of the SPMs design

The foregoing derived dynamic model can be applied in the optimization procedure to obtain a design with optimal dynamic performance. Henceforth, this section formulates a design optimization problem for the SPMs based on their dynamic modeling. Besides, the kinematic and elastic performances are also employed to evaluate the SPM design. A predefined workspace is specified as a minimum pointing cone of 90° opening with 360° full rotation, i.e., $\theta \in [0, \theta_{\min}], \theta_{\min} \geq 45°, \{\phi, \sigma\} \in (-180°, 180°]$.

4.1. Design variables

Variables α_1, α_2 and β are part of the geometric parameters of the SPM under study. Moreover, the radius R of the link midcurve and the side length a of a square cross section of the uniform curved links are included as design parameters as well. This implies that the curved link does not include details such as slots that may affect the total mass and structural strength [22]. As a consequence, the design variables of the optimization problem at hand are:

$$\mathbf{x} = [\alpha_1, \alpha_2, \beta, a, R] \tag{19}$$

4.2. Objective functions

The mechanism mass influences the dynamic performance, such as inertia, acceleration, etc., hence, minimizing the mass of moving bodies is one important consideration. The mass m_{spm} of the SPM includes the mass m_p of the platform, the mass m_l of the distal links, and the mass m_s of the sliding units (or proximal links). The mass of the revolute joints is not considered for simplification, thus, the mass function is given as:

$$m_{spm} = m_p + 3m_l + 3m_s \tag{20}$$

As a result, the first objective function of the optimization problem is written as:

$$f_1(\mathbf{x}) = m_{spm} \to \min \tag{21}$$

The dexterity of SPMs is another major concern in the manipulator design. A commonly used criterion to evaluate this kinematic performance is the global conditioning index (GCI) [4], which describes the isotropy of the kinematic performance. The GCI is defined over a workspace Ω, which is calculated through a discrete approach in practice, namely,

$$\text{GCI} = \frac{\int_\Omega \kappa^{-1}(\mathbf{J})dW}{\int_\Omega dW} \quad \text{or} \quad \text{GCI} = \frac{1}{n}\sum_{k=1}^{n}\frac{1}{\kappa_k(\mathbf{J})} \tag{22}$$

where $\kappa(\mathbf{J})$ is the condition number of the kinematic Jacobian matrix (8) and $n = n_1 n_2 n_3$ is the number of the workspace points, n_1, n_2, n_3 being the numbers of discrete points along ϕ, θ, σ, respectively. It is known that the higher the GCI, the better the performance. Hereby, the second objective function of the optimization problem is written as:

$$f_2(\mathbf{x}) = 1 - \text{GCI} = \text{MGCI} \to \min \tag{23}$$

Henceforth, a modified global conditioning index (MGCI) is introduced for the purpose of optimization.

4.3. Optimization constraints

In this section, the kinematic constraints, condition number of the kinematic Jacobian matrix, elastic and dynamic performances of the manipulator are considered. Constraining the condition number of the Jacobian matrix aims to obtain a dexterous workspace free of singularity. Moreover, the constraints on the link strength and the actuator torque are also considered.

4.3.1. Geometric constraints

According to the determination of the design space reported in [3], the bounds of the parameters α_1, α_2 and β subject to the prescribed workspace are stated as:

$$45° \leq \alpha_1 \leq 135°, \qquad 45° \leq \alpha_2 \leq 135°, \qquad 45° \leq \beta \leq 90° \tag{24}$$

In accordance with Fig. 5, the following constraints should be satisfied to avoid any collision,

$$\theta_{ij} \geq \epsilon_\theta, \quad \forall \theta_{ij} \in \{\theta_{12}, \theta_{23}, \theta_{31}\} \tag{25a}$$

$$R\sin\alpha_1 \geq R_0 \tag{25b}$$

where $\epsilon_\theta = 10°$ and $R_0 = 0.120\,\text{m}$ are geometric parameters relative to the size of curved links.

4.3.2. Condition number of the kinematic Jacobian matrix

Minimizing MGCI, i.e., maximizing GCI, cannot prevent the prescribed workspace away from ill-conditioned configurations. For the design optimization to achieve a dexterous workspace, the minimum of the inverse condition number of the kinematic Jacobian matrix $\kappa^{-1}(\mathbf{J})$, based on the 2-norm, should be higher than a prescribed value throughout the workspace, say 0.1, namely,

$$\min(\kappa^{-1}(\mathbf{J})) \geq 0.1 \tag{26}$$

4.3.3. Strength constraints

The strength constraints are to ensure the SPM to produce allowable maximum point-displacement of the rotation center and angular deflection of the mobile platform subject to a given wrench. The deflections are computed by

$$\Delta\mathbf{x} = \mathbf{K}^{-1}\mathbf{w}; \qquad \Delta\mathbf{x} = \begin{bmatrix}\Delta\mathbf{p}^T & \Delta\boldsymbol{\varphi}^T\end{bmatrix}^T, \quad \mathbf{w} = \begin{bmatrix}\mathbf{0} & \mathbf{m}^T\end{bmatrix}^T \tag{27}$$

where $\Delta\mathbf{p} = [\Delta x, \Delta y, \Delta z]^T$ and $\Delta\boldsymbol{\varphi} = [\Delta\varphi_x, \Delta\varphi_y, \Delta\varphi_z]^T$ are the translational and rotational displacements, respectively, and $\mathbf{K}$ is the Cartesian stiffness matrix given in Appendix B. Let the static torque of the SPM within the range $\mathbf{m} = [\pm m_{x,\max}, \pm m_{y,\max}, \pm m_{z,\max}]$, the strength constraints can be written as:

$$-\epsilon_p \leq \Delta t \leq \epsilon_p, \quad \forall \Delta t \in \{\Delta x_k, \Delta y_k, \Delta z_k\} \tag{28a}$$

$$-\epsilon_r \leq \Delta r \leq \epsilon_r, \quad \forall \Delta r \in \{\Delta\varphi_{x,k}, \Delta\varphi_{y,k}, \Delta\varphi_{z,k}\} \tag{28b}$$

where ϵ_p and ϵ_r are acceptable translational and rotational errors, respectively, and $k = 1, \ldots, n$ is the number of the discrete points defined in Eq. (22).
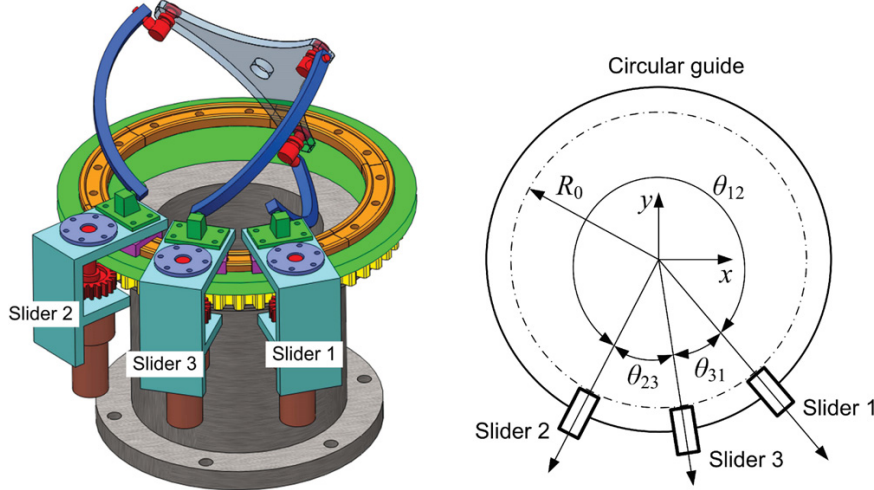
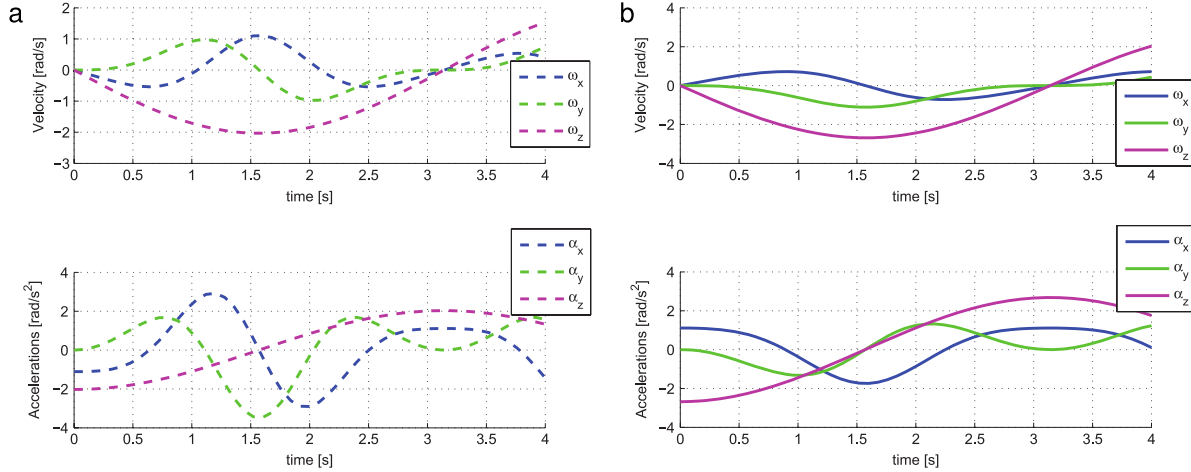**Fig. 5.** One extreme configuration of the sliding units.

Fig. 6. The angular velocity and acceleration profiles of the mobile platform: (a) trajectory 1; (b) trajectory 2.

It is noted that the model in Eq. (27) includes only the compliances of curved links. The base and MP are considered rigid. Moreover, the joint compliance is not addressed in this paper, as revolute joints are not easily characterized by a generic representative stiffness due to the nonlinear kinematic joint stiffness upon the specific design. Such an issue could be well addressed through stiffness modeling researches.

4.3.4. Actuation torque constraints

With an external moment $\mathbf{m} = [m_x,\ m_y,\ m_z]^T$ applied on the MP, in accordance to Eq. (18), the actuator torques are redefined as: $\boldsymbol{\tau}_a = |\boldsymbol{\tau}| + |\mathbf{J}^{-T}\mathbf{m}|$. At any time, the components of the actuator torque vector $\boldsymbol{\tau}_a$ should be smaller than the maximum continuous torque $T_{\max}$ of each actuator. As a result, the actuation torque constraints can be written as:

$$\max\{\boldsymbol{\tau}_a\} \leq T_{\max} \tag{29}$$

Henceforth, two alternative trajectories describing the MP orientation:

$$(1)\ \phi(t) = \pi \cos t, \qquad \theta(t) = \frac{\pi}{4}, \qquad \sigma(t) = \frac{\pi}{2}\cos t \tag{30}$$

$$(2)\ \phi(t) = \frac{\pi}{2}\cos t, \qquad \theta(t) = \frac{\pi}{4}, \qquad \sigma(t) = \pi \cos t$$

are integrated into the optimization procedure implemented with the *Matlab/simulink* package. The corresponding angular velocity and acceleration profiles of the mobile platform are shown in Fig. 6.

4.4. Formulation of the multi-objective design optimization problem

The multi-objective design optimization problem for the SPM is formulated as:

$$\begin{aligned}
\text{minimize} \quad & f_1(\mathbf{x}) = m_{spm} && (31)\\
\text{minimize} \quad & f_2(\mathbf{x}) = MGCI \\
\text{over} \quad & \mathbf{x} = [\alpha_1;\ \alpha_2;\ \beta;\ a;\ R] \\
\text{subject to} \quad & g_1 :\ R\sin\alpha_1 \geq R_0 \\
& g_2 :\ \theta_{ij} \geq \epsilon_\theta, \quad \forall \theta_{ij} \in \{\theta_{12},\ \theta_{23},\ \theta_{31}\} \\
& g_3 :\ \theta_{\min} \geq 45° \\
& g_4 :\ \min(\kappa^{-1}(\mathbf{J})) \geq 0.1 \\
& g_5 :\ -\epsilon_p \leq \Delta t \leq \epsilon_p, \quad \forall \Delta t \in \{\Delta x_k,\ \Delta y_k,\ \Delta z_k\} \\
& g_6 :\ -\epsilon_r \leq \Delta r \leq \epsilon_r, \quad \forall \Delta r \in \{\Delta\varphi_{x,k},\ \Delta\varphi_{y,k},\ \Delta\varphi_{z,k}\} \\
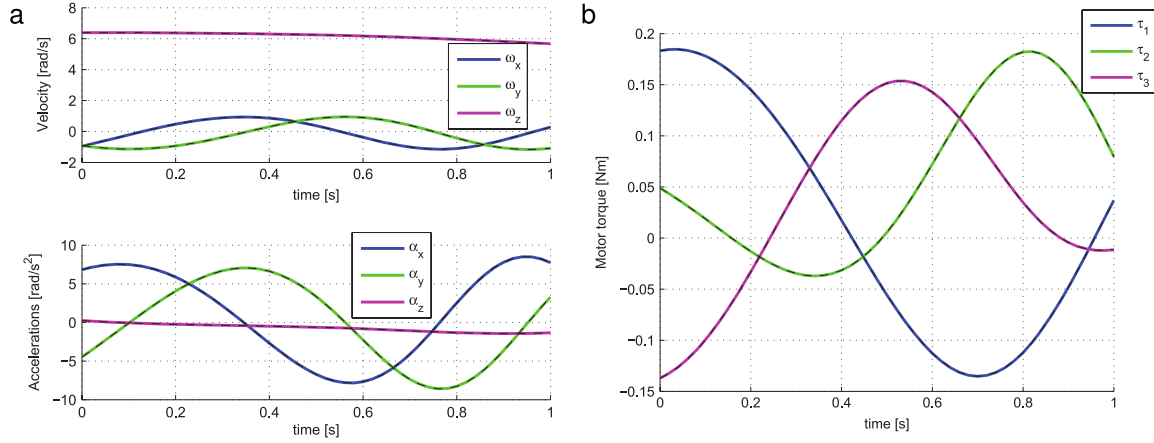& g_7 :\ \max\{\boldsymbol{\tau}_a\} \leq T_{\max}
\end{aligned}$$

Fig. 7. Simulation results (solid line stands for Matlab solver, dashed line for Adams): (a) motion of the mobile platform; (b) actuator torques.

Table 1
Parameters of the SPM and the initial simulation condition.

α_1 (deg)	α_2 (deg)	β (deg)	$[\phi, \theta, \sigma]$ (rad)	$[\dot{\theta}_1, \dot{\theta}_2, \dot{\theta}_3]$ (rad/s)	$\mathbf{m}$ (N m)
60	75	75	$[0, \pi/6, 0]$	$[-6, -5, -7]$	$[0.1, 0.1, 0.1]$

Table 2
Mass and inertia properties of the SPM model.

Mobile platform		Curved link		Sliding unit
m_p (kg)	$\mathbf{I}_p$ (10^{-4} kg m^2)	m_l (kg)	$\mathbf{I}_l$ (10^{-4} kg m^2)	m_s (kg)
0.332	[3.855 3.855 7.688]	0.107	[1.816 0.081 1.894]	0.123

5. Results and discussion

5.1. Validation of dynamic model

Dynamic simulations were conducted with the developed SPM dynamic model, the obtained results being compared with those obtained with *MSC Adams*, utilizing the properties and simulation conditions given in Tables 1 and 2. The corresponding simulation results from the developed model and the Adams simulation are shown in Fig. 7, which shows a good agreement with each other.

5.2. Design optimization

The optimization procedure is applied to the SPM shown in Fig. 2(b). The actuation transmission mechanism is a combination of RE 35 GB actuator and GP 42 C gearhead from Maxon [23]. The components are supposed to be made up of steel, and the mobile platform is supposed to be a regular triangle. The total mass m_s of each slide unit, including the mass of the actuator, gearhead, pinions and the manufactured components, is equal to $m_s = 2.1$ kg. Henceforth, the actuation stiffness is $K_{act}^i = 10^6$ N m/rad and the range of the static moment in Eq. (27) is $\mathbf{m} = [\pm 10, \pm 10, \pm 10]$ N m, while the acceptable translational and rotational errors are $\epsilon_p = 1$ mm and $\epsilon_r = 0.0349$ rad, respectively. Moreover, the maximum continuous torque of the actuator is $T_{max} = 15$ N m and the external moment applied on the mobile platform and expressed in the base frame along the trajectories defined by Eq. (30) is $\mathbf{m} = [5, 5, 5]^T$ N m.

The solutions of the previous optimization problem are non-dominated solutions, also called Pareto-optimal solutions, which stand for solutions for which the corresponding objectives cannot be further improved without degrading others. Problem (31) is
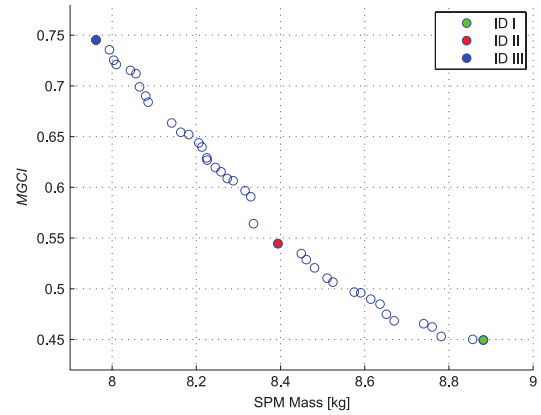
Fig. 8. The Pareto-front of the multiobjective optimization problem (31).

solved by the genetic algorithm NSGA-II [24] implemented in *Matlab*, for which the algorithm parameters are given in Table 3. The lower and upper bounds of the design variables are shown in Table 4, denoted by $\mathbf{x}_{lb}$ and $\mathbf{x}_{ub}$, respectively.

The Pareto-front of the optimization problem at hand is shown in Fig. 8. Three Pareto-optimal solutions named ID-I, ID-II and ID-III on the Pareto-fronts, i.e., two extreme solutions and one intermediate solution, described in Table 5, are selected for further consideration. The CAD designs of these three Pareto-optimal solutions are shown in Fig. 9 and the corresponding dynamic simulations are illustrated in Fig. 10, respectively, from which it is seen that from ID-I to III, the maximum actuating torque increases. By comparison among the three groups of design variables in Table 5, smaller α_1 and larger α_2 yield higher wrench capability under given input torques. Although the design ID-III has the lowest mass, it has the highest requirements on the actuators. From the kinematic and dynamic considerations, design ID-I can be selected for further application as an active joint.

Fig. 11, obtained with *plotmatrix* and *corrcoef* functions in *Matlab*, illustrates the variational trends as well as the inter-dependency between the objective functions and design variables by means of a scatter matrix [11,18]. The lower triangular part of the matrix represents the correlation coefficients whereas the upper one shows the corresponding scatter plots. The diagonal elements represent the probability density charts of each variable. The correlation coefficients vary from -1 to 1. Two variables are
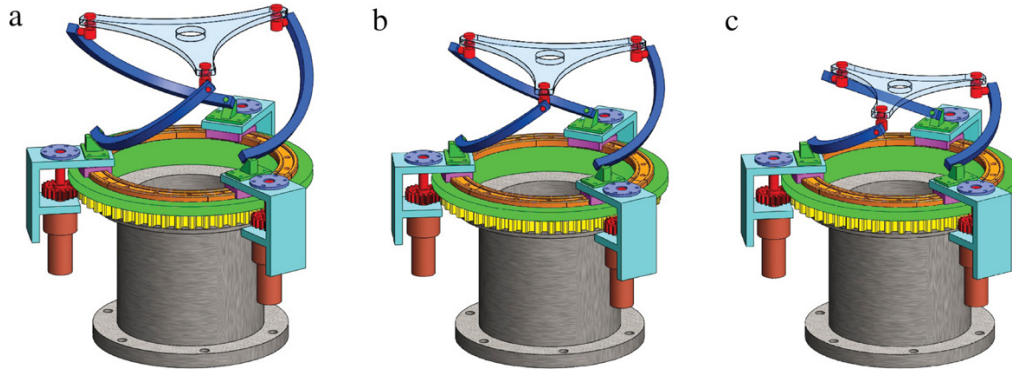
Fig. 9. CAD designs of three Pareto-optimal solutions: (a) ID-I, (b) ID-II, (c) ID-III.

Table 3
Algorithm parameters of the implemented NSGA-II.

Population size	Number of generations	Directional crossover probability	Crossover probability	Distribution index
40	200	0.5	0.9	20

Table 4
The lower and upper bounds of the design variables.

	α_1 (deg)	α_2 (deg)	β (deg)	a (m)	R (m)
$\mathbf{x}_{lb}$	45	45	45	0.005	0.120
$\mathbf{x}_{ub}$	135	135	90	0.030	0.300

strongly dependent when their correlation coefficient is close to −1 or 1 and independent when the latter is null. Fig. 11 shows that:

- m_{spm} and *MGCI* are strongly dependent as their correlation coefficient is equal to −0.984;
- m_{spm} and *MGCI* are strongly dependent on the design variables except a as the mass of the sliding units mainly affects the total mass, thus, a slightly affects m_{spm};
- both objective functions are approximately linearly related to variables α_1, α_2 and R;
- all the variables are strongly dependent on each other except a;
- the results show that β is close to 90° for all Pareto-optimal solutions;
- it is noteworthy that the higher m_{spm}, the lower α_1. Conversely, the higher m_{spm}, the higher α_2. Higher R results in higher m_{spm}.

6. Conclusions

In this paper, the inverse dynamics and geometric synthesis of spherical parallel manipulators were discussed. Using the classical method of Lagrange multipliers, the equations of motion for the SPMs were derived. The expressions for the kinetic energy are associated with the characteristics of motion, namely, all the SPM bodies rotating about the center of rotation. All the moving bodies are taken into account to describe this dynamic system effectively and clearly. The developed dynamic model is integrated into the design optimization procedure of the SPMs.

A multiobjective design optimization problem was formulated in order to determine the mechanism optimum structural and geometric parameters. The objective functions were evaluated based on the kinematic and kinetostatic/dynamic performances of the manipulators. This approach has been illustrated with the optimum design of an unlimited-roll spherical parallel manipulator, aiming at minimizing the mechanism mass and increasing its dexterity. As a result, the Pareto-front was obtained to show the approximation of the optimal solutions between the various (antagonistic) criteria, subject to the dependency of the performance. It turns out that the manipulator has the best performance with $\beta = 90°$.

As a matter of fact, the method offers a great flexibility to select any criterion as an objective function based on requirements. A contribution of the work is the formulation of different kinds of performances ranging from kinematics, statics to dynamics. All these formulations ease the modeling and simulation, and can be used for other design optimization tasks in future work.

Appendix A. Mass moment of inertia

The mass moment of inertia of the mobile platform about point O [25] is given by

$$\mathbf{I}_p = m_p R^2 \cos^2 \beta [\mathbf{p}]_\times [\mathbf{p}]_\times^T + \mathbf{Q}\mathbf{I}_p'\mathbf{Q}^T \quad (A.1)$$

where m_p is the mass, $\mathbf{I}_p'$ is the inertia tensor in its local frame (x_p, y_p, z_p), and $[\mathbf{p}]_\times = \text{CPM}(\mathbf{p})$ is the skew-symmetric matrix, $\mathbf{p}$ being the unit vector of z_p axis in Fig. 4.

A parameterized curved link with uniform cross-section is shown in Fig. 12, its center of mass being found as

$$R\alpha\bar{x} = R^2 \int_{-\frac{\alpha}{2}}^{\frac{\alpha}{2}} \cos \varphi \mathrm{d}\varphi \quad \text{or} \quad \bar{x} = \frac{2R}{\alpha} \sin \frac{\alpha}{2} \quad (A.2)$$

Table 5
Three Pareto-optimal solutions.

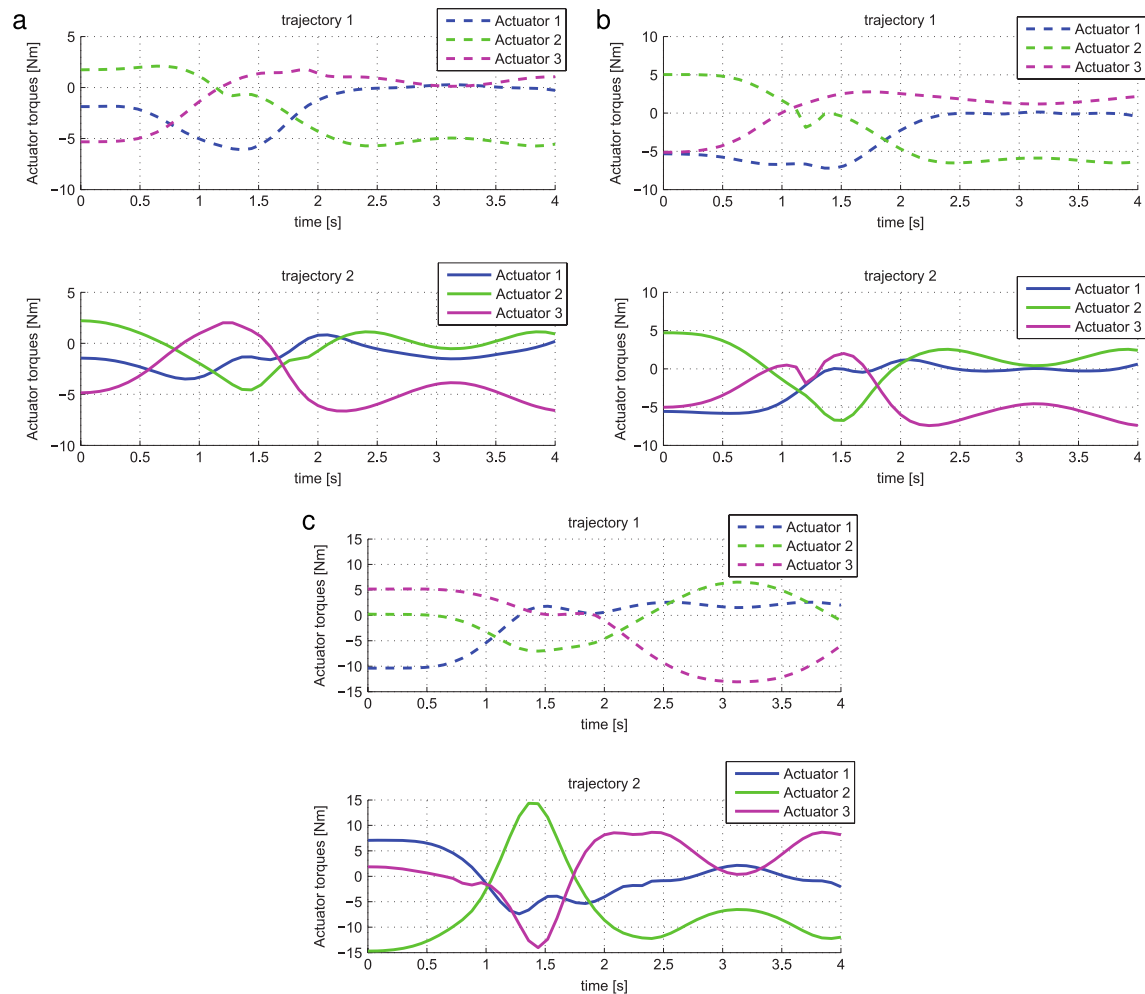| Design ID	Variables					Objectives		
	α_1 (deg)	α_2 (deg)	β (deg)	a (m)	R (m)	m_{spm} (kg)	*MGCI*	$\min(\kappa^{-1}(\mathbf{J}))$
I	47.2	91.7	88.4	0.0120	0.1659	8.882	0.449	0.253
II	51.9	85.0	88.3	0.0113	0.1525	8.394	0.545	0.240
III	63.5	72.2	89.6	0.0119	0.1342	7.962	0.745	0.102

Fig. 10. The dynamic simulation results for the three Pareto-optimal solutions: (a) ID-I; (b) ID-II; (c) ID-III.
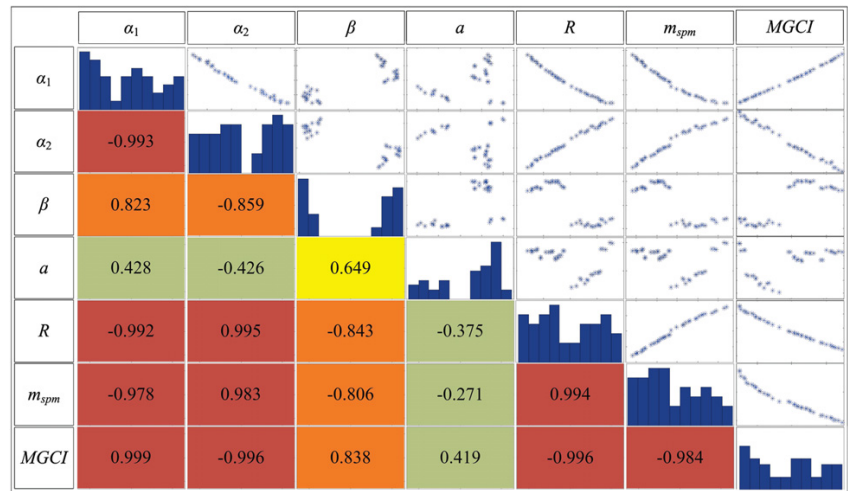

Fig. 11. Scatter matrix for the objective functions and the design variables.
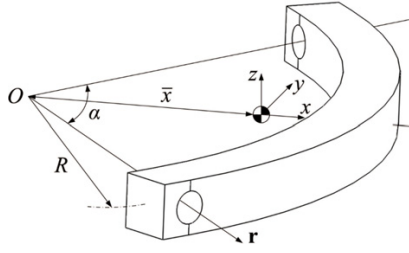
Fig. 12. A curved link.

Let the link's mass be m_l, its moment of inertia about point O is found as [25]:

$$\mathbf{I}_l = m_l \bar{x}^2 [\mathbf{i}]_\times [\mathbf{i}]_\times^T + \mathbf{E}\mathbf{I}_l' \mathbf{E}^T \tag{A.3}$$

where $[\mathbf{i}]_\times = \mathrm{CPM}(\mathbf{i})$, and $\mathbf{E} = [\mathbf{i}\ \mathbf{j}\ \mathbf{k}]$, $\mathbf{i}$, $\mathbf{j}$, $\mathbf{k}$ being the unit vectors of x, y and z-axes. Moreover, the mass moments of inertia $\mathbf{I}_l' = \mathrm{diag}[L_{xx}\ L_{yy}\ L_{zz}]$ in the frame (x, y, z) are expressed as:

$$L_{xx} = \int_{-\frac{\alpha}{2}}^{\frac{\alpha}{2}} (R\sin\varphi)^2 \cdot \frac{m_l}{R\alpha} \cdot R\mathrm{d}\varphi = \frac{1}{2} m_l R^2 \left(1 - \frac{\sin\alpha}{\alpha} \right) \tag{A.4a}$$

$$\begin{aligned} L_{yy} &= \int_{-\frac{\alpha}{2}}^{\frac{\alpha}{2}} (R\sin\varphi - \bar{x})^2 \cdot \frac{m_l}{R\alpha} \cdot R\mathrm{d}\varphi \\ &= \frac{1}{2} m_l \left(\frac{R^2 \sin\alpha}{\alpha} - \frac{8R\bar{x}}{\alpha} \sin\frac{\alpha}{2} + R^2 + 2\bar{x}^2 \right) \end{aligned} \tag{A.4b}$$

$$\begin{aligned} L_{zz} &= \int_{-\frac{\alpha}{2}}^{\frac{\alpha}{2}} \left[(R\sin\varphi)^2 + (R\cos\varphi - \bar{x})^2 \right] \cdot \frac{m_l}{R\alpha} \cdot R\mathrm{d}\varphi \\ &= \frac{1}{2} m_l \left(R^2 + \bar{x}^2 - \frac{4R\bar{x}}{\alpha} \sin\frac{\alpha}{2} \right) \end{aligned} \tag{A.4c}$$

Moreover, the mass moment of inertia about $\mathbf{r}$ is derived as

$$\begin{aligned} I_l &= m_l \left(\bar{x}\sin\frac{\alpha}{2} \right)^2 + \int_0^\alpha (R\sin\varphi)^2 \cdot \frac{m_l}{R\alpha} \cdot R\mathrm{d}\varphi \\ &= \frac{1}{4} m_l R^2 \left[\frac{(1 - \cos\alpha)^2}{\alpha^2} + 2 - \frac{\sin 2\alpha}{\alpha} \right] \end{aligned} \tag{A.5}$$

Appendix B. Cartesian stiffness matrix

With the virtual-spring approach [26], the Cartesian stiffness matrix $\mathbf{K}$ of the SPM is found as

$$\mathbf{K} = \sum_{i=1}^3 \mathbf{K}_i \tag{B.1}$$

Here $\mathbf{K}_i \in \mathbb{R}^6$ is the Cartesian stiffness matrix of the ith leg, extracted from the first six-dimensional block of matrix $\mathbf{K}_i'$

$$\mathbf{K}_i' = \begin{bmatrix} \mathbf{J}_\theta^i (\mathbf{K}_\theta^i)^{-1} \mathbf{J}_\theta^{iT} & \mathbf{J}_q^i \\ \mathbf{J}_q^{iT} & \mathbf{0}_2 \end{bmatrix}^{-1} \tag{B.2}$$

with

$$\mathbf{J}_\theta^i = \begin{bmatrix} \hat{\mathbf{S}}_A^i & \hat{\mathbf{S}}_{u1}^i & \dots & \hat{\mathbf{S}}_{u12}^i \end{bmatrix} \in \mathbb{R}^{6\times 13} \tag{B.3a}$$

$$\mathbf{J}_q^i = \begin{bmatrix} \hat{\mathbf{S}}_B^i & \hat{\mathbf{S}}_C^i \end{bmatrix} \in \mathbb{R}^{6\times 2} \tag{B.3b}$$

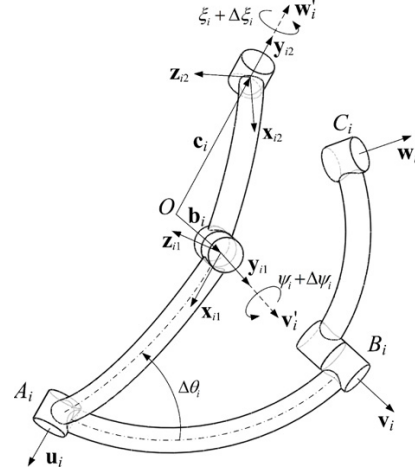**Fig. 13.** Link deflections and joint displacements of a flexible leg.

According to Fig. 13, the unit screws are given by

$$\hat{\mathbf{S}}_A^i = \begin{bmatrix} \mathbf{u}_i \\ \mathbf{0} \end{bmatrix}, \qquad \hat{\mathbf{S}}_B^i = \begin{bmatrix} \mathbf{v}_i \\ \mathbf{0} \end{bmatrix}, \qquad \hat{\mathbf{S}}_C^i = \begin{bmatrix} \mathbf{w}_i \\ \mathbf{0} \end{bmatrix}$$

$$\hat{\mathbf{S}}_{u1}^i = \begin{bmatrix} \mathbf{x}_{i1} \\ \mathbf{b}_i \times \mathbf{x}_{i1} \end{bmatrix}, \qquad \hat{\mathbf{S}}_{u2}^i = \hat{\mathbf{S}}_B^i, \qquad \hat{\mathbf{S}}_{u3}^i = \begin{bmatrix} \mathbf{z}_{i1} \\ \mathbf{b}_i \times \mathbf{z}_{i1} \end{bmatrix},$$

$$\hat{\mathbf{S}}_{u4}^i = \begin{bmatrix} \mathbf{0} \\ \mathbf{x}_{i1} \end{bmatrix}, \qquad \hat{\mathbf{S}}_{u5}^i = \begin{bmatrix} \mathbf{0} \\ \mathbf{v}_i \end{bmatrix}, \qquad \hat{\mathbf{S}}_{u6}^i = \begin{bmatrix} \mathbf{0} \\ \mathbf{z}_{i1} \end{bmatrix}$$

$$\hat{\mathbf{S}}_{u7}^i = \begin{bmatrix} \mathbf{x}_{i2} \\ \mathbf{c}_i \times \mathbf{x}_{i2} \end{bmatrix}, \qquad \hat{\mathbf{S}}_{u8}^i = \hat{\mathbf{S}}_C^i, \qquad \hat{\mathbf{S}}_{u9}^i = \begin{bmatrix} \mathbf{z}_{i2} \\ \mathbf{c}_i \times \mathbf{z}_{i2} \end{bmatrix},$$

$$\hat{\mathbf{S}}_{u10}^i = \begin{bmatrix} \mathbf{0} \\ \mathbf{x}_{i2} \end{bmatrix}, \qquad \hat{\mathbf{S}}_{u11}^i = \begin{bmatrix} \mathbf{0} \\ \mathbf{w}_i \end{bmatrix}, \qquad \hat{\mathbf{S}}_{u12}^i = \begin{bmatrix} \mathbf{0} \\ \mathbf{z}_{i2} \end{bmatrix} \tag{B.4}$$

and $\mathbf{K}_\theta^i \in \mathbb{R}^{13}$ describes the stiffness of the actuation and virtual springs, taking the form:

$$\mathbf{K}_\theta^i = \mathrm{diag} \begin{bmatrix} K_{act}^i & \mathbf{K}_{L_1}^i & \mathbf{K}_{L_2}^i \end{bmatrix} \tag{B.5}$$

where K_{act}^i is the ith actuator stiffness, $\mathbf{K}_{L_1}^i$ and $\mathbf{K}_{L_2}^i$, respectively, are the 6×6 stiffness matrices of the proximal and distal curved links in the ith leg, which can be found in [27].

References

[1] C.M. Gosselin, J. Angeles, The optimum kinematic design of a spherical three-degree-of-freedom parallel manipulator, ASME J. Mech. Transm. Autom. Des. 111 (1989) 202–207.

[2] F. Bulca, J. Angeles, P.J. Zsombor-Murray, On the workspace determination of spherical serial and platform mechanisms, Mech. Mach. Theory 34 (3) (1999) 497–512.

[3] S. Bai, Optimum design of spherical parallel manipulators for a prescribed workspace, Mech. Mach. Theory 45 (2) (2010) 200–211.

[4] C.M. Gosselin, J. Angeles, A global performance index for the kinematic optimization of robotic manipulators, ASME J. Mech. Des. 113 (3) (1991) 220–226.

[5] C.M. Gosselin, E. Lavoie, On the kinematic design of spherical three-degree-of-freedom parallel manipulators, Int. J. Robot. Res. 12 (4) (1993) 394–402.

[6] S. Bai, M.R. Hansen, T.O. Andersen, Modelling of a special class of spherical parallel manipulators with Euler parameters, Robotica 27 (2) (2009) 161–170.

[7] S. Staicu, Recursive modelling in dynamics of Agile Wrist spherical parallel robot, Robot. Comput.-Integr. Manuf. 25 (2) (2009) 409–416.

[8] I.A. Bonev, C.M. Gosselin, Singularity loci of spherical parallel mechanisms, IEEE International Conference on Robotics and Automation, Barcelona, Spain, 2005, pp. 2957–2962.

[9] X.J. Liu, Z.L. Jin, F. Gao, Optimum design of 3-DOF spherical parallel manipulators with respect to the conditioning and stiffness indices, Mech. Mach. Theory 35 (9) (2000) 1257–1267.

[10] F. Bidault, C.-P. Teng, J. Angeles, Structural optimization of a spherical parallel manipulator using a two-level approach, Proc. ASME 2001 Design Engineering Technical Conferences, Pittsburgh, Pennsylvania, 2001, pp. 9–12.

[11] S. Caro, D. Chablat, R. Ur-Rehman, P. Wenger, Multiobjective design optimization of 3-PRR planar parallel manipulators, Glob. Prod. Dev. (2011) 373–383.

[12] C.M. Gosselin, J.F. Hamel, The Agile Eye: a high-performance three-degree-of-freedom camera-orienting device, IEEE International Conference on Robotics and Automation, San Diego, CA, 1994, pp. 781–786.

[13] T. Li, S. Payandeh, Design of spherical parallel mechanisms for application to laparoscopic surgery, Robotica 20 (2) (2002) 133–138.

[14] H. Asada, J. Granito, Kinematic and static characterization of wrist joints and their optimal design, IEEE International Conference on Robotics and Automation, 1985, pp. 244–250.

[15] M. Ceccarelli, G. Carbone, E. Ottaviano, Multi criteria optimum design of manipulators, Bull. Pol. Acad. Tech. Sci. 53 (1) (2005) 9–18.

[16] O. Altuzarra, O. Salgado, A. Hernandez, J. Angeles, Multiobjective optimum design of a symmetric parallel schönflies-motion generator, ASME J. Mech. Des. 131 (3) (2009) 031002.

[17] D. Chablat, S. Caro, R. Ur-Rehman, P. Wenger, Comparison of planar parallel manipulator architectures based on a multi-objective design optimization approach, ASME 2010 International Design Engineering Technical Conferences and Computers and Information in Engineering Conference, Montreal, Quebec, Canada, 2010, pp. 861–870.

[18] R. Ur-Rehman, S. Caro, D. Chablat, P. Wenger, Multi-objective path placement optimization of parallel kinematics machines based on energy consumption, shaking forces and maximum actuator torques: Application to the Orthoglide, Mech. Mach. Theory 45 (8) (2010) 1125–1141.

[19] I.A. Bonev, Direct kinematics of zero-torsion parallel mechanisms, IEEE International Conference on Robotics and Automation, Pasadena, California, USA, 2008, pp. 3851–3856.

[20] J. Diebel, Representing attitude: Euler angles, unit quaternions, and rotation vectors, Stanford University Technical Report, Stanford University, Stanford, CA, 2006.

[21] J.G. Jalón, E. Bayo, Kinematic and Dynamic Simulation of Multibody Systems: The Real-Time Challenge, Springer-Verlag, New-York, 1994.

[22] L. Zhou, S. Bai, M.R. Hansen, Integrated dimensional and drive-train design optimization of a light-weight anthropomorphic arm, Robot. Auton. Syst. 60 (1) (2012) 113–122.

[23] Maxon products catalog (2012), http://www.maxonmotor.com/maxon/view/catalog/.

[24] K. Deb, A. Pratap, S. Agarwal, T. Meyarivan, A fast and elitist multiobjective genetic algorithm: NSGA-II, IEEE Trans. Evol. Comput. 6 (2) (2002) 182–197.

[25] J. Awrejcewicz, Z. Koruba, Equations of motion of a rigid spherical body, Adv. Mech. Math.: Class. Mech. 30 (2012) 87–123.

[26] A. Pashkevich, D. Chablat, P. Wenger, Stiffness analysis of overconstrained parallel manipulators, Mech. Mach. Theory 44 (5) (2009) 966–982.

[27] G. Wu, S. Bai, J. Kepler, Mobile platform center shift in spherical parallel manipulators with flexible limbs, Mech. Mach. Theory 75 (2014) 12–26.

Guanglei Wu received his B.Eng. in Machinery Design, Manufacturing and Automation from Yantai University, China, in 2007 and M.Eng. in Machinery Manufacturing and Automation from Northeastern University, China, in 2009. He is currently a Ph.D. Student in the Department of Mechanical and Manufacturing Engineering at Aalborg University, Denmark. His main research interest is in modeling and design of parallel manipulators.

Stéphane Caro received the Engineering and M.Sc. degrees in mechanical engineering from Ecole Centrale Nantes (ECN), Nantes, France, in 2001, and the Doctorate degree in mechanical engineering from the University of Nantes in 2004. He was a Post-doctoral Fellow in the Centre for Intelligent Machines, McGill University, Montreal, QC, Canada from 2005 to 2006. He is currently a full-time researcher of the National Centre for Scientific Research (CNRS) and works in the Research Institute in Communications and Cybernetics of Nantes (IRCCyN) and at the French Technological Research Institute (IRT) Jules Verne. His research interests include conceptual design of robots, robust design, kinematic analysis and synthesis, singularity analysis, sensitivity analysis, tolerance synthesis, and design optimization.

Shaoping Bai is an associate professor at the Department of Mechanical and Manufacturing Engineering, Aalborg University (AAU), Denmark. His research interests include medical and assistive robots, parallel manipulators, walking robots, dynamics and design.

Jørgen A. Kepler, Ph.D., is an associate professor at the Department of Mechanical and Manufacturing Engineering, Aalborg University, Denmark. His research interests include mechanical systems, impact dynamics, elasticity theory.

7

Paper IV

Multiobjective Optimum Design of a 3-RRR Spherical Parallel Manipulator with Kinematic and Dynamic Dexterities

Guanglei Wu [1]

[1]*Department of Mechanical and Manufacturing Engineering, Aalborg University, 9220 Aalborg, Denmark.*
E-mail: gwu@m-tech.aau.dk

Abstract

This paper deals with the kinematic synthesis problem of a 3-RRR spherical parallel manipulator, based on the evaluation criteria of the kinematic, kinetostatic and dynamic performances of the manipulator. A multiobjective optimization problem is formulated to optimize the structural and geometric parameters of the spherical parallel manipulator. The proposed approach is illustrated with the optimum design of a special spherical parallel manipulator with unlimited rolling motion. The corresponding optimization problem aims to maximize the kinematic and dynamic dexterities over its regular shaped workspace.

Keywords: Spherical parallel manipulator, multiobjective optimization, Cartesian stiffness matrix, dexterity, Generalized Inertia Ellipsoid

1 Introduction

A three Degrees of Freedom (3-DOF) spherical parallel manipulator (SPM) is generally composed of two pyramid-shaped platforms, namely, a mobile platform (MP) and a fixed base that are connected together by three identical legs, each one consisting of two curved links and three revolute joints. The axes of all joints intersect at a common point, namely, the center of rotation. Such a spherical parallel manipulator provides a three degrees of freedom rotational motion. Most of the SPMs find their applications as orienting devices, such as camera orienting and medical instrument alignment (Gosselin and Hamel, 1994; Li and Payandeh, 2002; Cavallo and Michelini, 2004; Chaker et al., 2012). Besides, they can also be used to develop active spherical manipulators, i.e., wrist joint (Asada and Granito, 1985).

In designing parallel manipulators, a fundamental problem is that their performance heavily depends on their geometry (Hay and Snyman, 2004) and the mu-

tual dependency of the performance measures. The manipulator performance depends on its dimensions while the mutual dependency among the performances is related to manipulator applications (Merlet, 2006b). The evaluation criteria for design optimization can be classified into two groups: one relates to the kinematic performance of the manipulator while the other relates to the kinetostatic/dynamic performance of the manipulator (Caro et al., 2011). In the kinematic considerations, a common concern is the workspace (Merlet, 2006a; Kong and Gosselin, 2004; Liu et al., 2000; Bonev and Gosselin, 2006). The size and shape of the workspace are of primary importance. Workspace based design optimization can usually be solved with two different formulations, the first formulation aiming to design a manipulator whose workspace contains a prescribed workspace (Hay and Snyman, 2004) and the second approach being to design a manipulator whose workspace is as large as possible (Lou et al., 2005). In Ref. (Bai, 2010), the SPM dexterity was optimized within a prescribed workspace by identifying
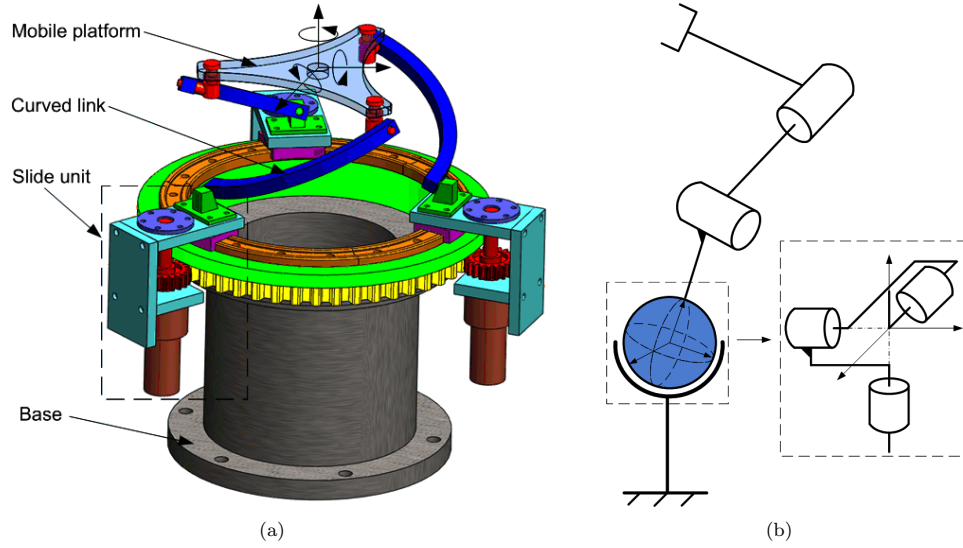
Figure 1: 3-<u>R</u>RR unlimited-roll SPM: (a) CAD model, (b) application as spherically actuated joint.

the design space. It is known from (Gosselin and Angeles, 1989) that the orientation workspace of a SPM is a maximum when the geometric angles of the links are equal to 90°. However, maximizing the workspace may lead to a poor design with regard to the manipulator dexterity and manipulability (Stamper et al., 1997; Durand and Reboulet, 1997). This problem can be solved by properly defining the constraints on dexterity (Merlet, 2006a; Huang et al., 2003). For the optimum design of SPMs, a number of works focusing on the kinematic performance, mainly the dexterity and workspace, have been reported, whereas, the kinetostatic/dynamic aspects receive relatively less attention. In general, the design process simultaneously deals with the two previously mentioned groups, both of which include a number of performance measures that essentially vary throughout the workspace. On the kinetostatic aspect, the SPM stiffness is an important consideration (Liu et al., 2000) to characterize its elastostatic performance. When they are used to develop spherically actuated joint, not only the MP angular displacement but also the translational displacement of the rotation center should be evaluated from the Cartesian stiffness matrix of the manipulator and should be minimized. Moreover, the dynamic performance of the manipulator should be as high as possible.

Among the evaluation criteria for optimum geometric parameters design, an efficient approach is to solve a multiobjective optimization problem, which takes all or most of the evaluation criteria into account. As the objective functions are usually conflicting, no single solution can be achieved in this process. The solutions

of such a problem are non-dominated solutions, also called Pareto-optimal solutions. Some multiobjective optimization problems of parallel manipulators (PMs) have been reported in the last few years. Hao and Merlet proposed a method different from the classical approaches to obtain all the possible design solutions that satisfy a set of compulsory design requirements, where the design space is identified via the interval analysis based approach (Hao and Merlet, 2005). Ceccarelli et al. focused on the workspace, singularity and stiffness properties to formulate a multi-criterion optimum design procedure for both parallel and serial manipulators (Ceccarelli et al., 2005). Stock and Miller formulated a weighted sum multi-criterion optimization problem with manipulability and workspace as two objective functions (Stock and Miller, 2003). Krefft and Hesselbach formulated a multi-criterion elastodynamic optimization problem for parallel mechanisms while considering workspace, velocity transmission, inertia, stiffness and the first natural frequency as optimization objectives (Krefft and Hesselbach, 2005). Altuzarra et al. dealt with the multiobjective optimum design of a parallel Schönflies motion generator, in which the manipulator workspace volume and dexterity were considered as objective functions (Altuzarra et al., 2009).

In this work, a multiobjective design optimization problem is formulated. The design optimization problem of the 3-DOF spherical parallel manipulator considers the kinematic performance, the accuracy and the dynamic dexterity of the mechanism under design. The performances of the mechanism are also optimized over a regular shaped workspace. The multiobjective de-
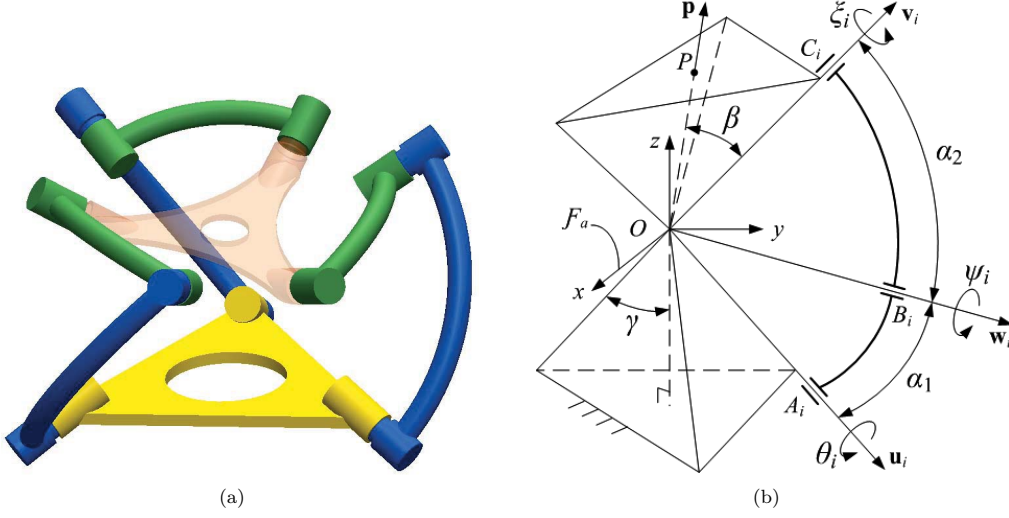
112

Figure 2: Architecture of a general SPM: (a) overview, (b) parameterization of the ith leg.

sign optimization problem is illustrated with a 3-$\underline{\text{R}}$RR SPM shown in Figure 1, which can replace the serial chains based wrist mechanisms. The non-dominated solutions, also called Pareto-optimal solutions, of the multiobjective optimization problem are obtained with a genetic algorithm.

2 Manipulator Architecture

The spherical parallel manipulator under study is a novel robotic wrist with an unlimited roll motion (Bai, 2010; Bai et al., 2009), which only consists of three curved links connected to a mobile platform (MP). The mobile platform is supposed to be quite stiffer than the links, which is considered as a rigid body. The three links are driven by three actuators moving independently on a circular rail of model HCR 150 from THK via pinion and gear-ring transmissions. Thanks to the circular guide, the overall stiffness of the mechanism is increased. Moreover, such a design enables the SPM to generate an unlimited rolling motion, in addition to limited pitch and yaw rotations.

A general spherical parallel manipulator is shown in Figure 2(a) (Liu et al., 2000). Figure 2(b) represents the parameters associated with the ith leg of the SPM,

$i = 1, 2, 3$. The SPM is composed of three legs that connect the mobile-platform to the base. Each leg is composed of three revolute joints. The axes of the revolute joints intersect and their unit vectors are denoted by $\mathbf{u}_i$, $\mathbf{w}_i$ and $\mathbf{v}_i$, $i = 1, 2, 3$. The arc angles of the three proximal curved links are the same and equal to α_1. Likewise, the arc angles of the three distal curved links are the same and equal to α_2. The radii of the link midcurves are the same and equal to R. Geometric angles β and γ define the geometry of the two pyramidal base and mobile platforms. The presented SPM in Figure 1(a) is a special case with $\gamma = 0$. The origin O of the reference coordinate system $\mathcal{F}_a$ is located at the center of rotation.

3 Kinematic and Kinetostatic Modeling of the SPM

The kinematics of the SPMs has been well documented (Gosselin and Angeles, 1989), which is not repeated in detail here. Hereafter, the orientation of the mobile platform is described by the orientation representation of *azimuth-tilt-torsion* $(\phi - \theta - \sigma)$ (Bonev, 2008), for which the rotation matrix is expressed as

$$\mathbf{Q} = \begin{bmatrix} \text{c}\phi\text{c}\theta\text{c}(\phi-\sigma) + \text{s}\phi s(\phi-\sigma) & \text{c}\phi\text{c}\theta\text{s}(\phi-\sigma) - \text{s}\phi\text{c}(\phi-\sigma) & \text{c}\phi\text{s}\theta \\ \text{s}\phi\text{c}\theta\text{c}(\phi-\sigma) - \text{c}\phi\text{s}(\phi-\sigma) & \text{s}\phi\text{c}\theta\text{s}(\phi-\sigma) + \text{c}\phi\text{c}(\phi-\sigma) & \text{s}\phi\text{s}\theta \\ -\text{s}\theta\text{c}(\phi-\sigma) & -\text{s}\theta\text{s}(\phi-\sigma) & \text{c}\theta \end{bmatrix} \tag{1}$$

where $\phi \in (-\pi, \pi]$, $\theta \in [0, \pi)$, $\sigma \in (-\pi, \pi]$, and $s(\cdot) = \sin(\cdot)$, $c(\cdot) = \cos(\cdot)$.

Under the prescribed coordinate system, unit vector $\mathbf{u}_i$ is expressed in the base frame $\mathcal{F}_a$ below:

$$\mathbf{u}_i = \begin{bmatrix} -\sin \eta_i \sin \gamma & \cos \eta_i \sin \gamma & -\cos \gamma \end{bmatrix}^T \quad (2)$$

where $\eta_i = 2(i-1)\pi/3$, $i = 1, 2, 3$.

Unit vector $\mathbf{w}_i$ of the intermediate revolute joint axis in the ith leg is expressed in $\mathcal{F}_a$ as:

$$\mathbf{w}_i = \begin{bmatrix} -s\eta_i s\gamma c\alpha_1 + (c\eta_i s\theta_i - s\eta_i c\gamma c\theta_i)s\alpha_1 \\ c\eta_i s\gamma c\alpha_1 + (s\eta_i s\theta_i + c\eta_i c\gamma c\theta_i)s\alpha_1 \\ -c\gamma c\alpha_1 + s\gamma c\theta_i s\alpha_1 \end{bmatrix} \quad (3)$$

The unit vector $\mathbf{v}_i$ of the last revolute joint axis in the ith leg, is a function of the mobile-platform orientation, namely,

$$\mathbf{v}_i = \mathbf{Q}\mathbf{v}_i^* \quad (4)$$

where $\mathbf{v}_i^*$ corresponds to the unit vector of the last revolute joint axis in the ith leg when the mobile platform is in its home configuration:

$$\mathbf{v}_i^* = \begin{bmatrix} -\sin \eta_i \sin \beta & \cos \eta_i \sin \beta & \cos \beta \end{bmatrix}^T \quad (5)$$

3.1 Kinematic Jacobian matrix

Let $\boldsymbol{\omega}$ denote the angular velocity of the mobile-platform, the screws velocity equation via the ith leg can be stated as

$$\mathbf{\$}_\omega = \begin{bmatrix} \boldsymbol{\omega} \\ \mathbf{0} \end{bmatrix} = \dot{\theta}_i \hat{\mathbf{\$}}_A^i + \dot{\psi}_i \hat{\mathbf{\$}}_B^i + \dot{\xi}_i \hat{\mathbf{\$}}_C^i \quad (6)$$

with the screws for the revolute joints at points A_i, B_i and C_i expressed as

$$\hat{\mathbf{\$}}_A^i = \begin{bmatrix} \mathbf{u}_i \\ \mathbf{0} \end{bmatrix}, \hat{\mathbf{\$}}_B^i = \begin{bmatrix} \mathbf{w}_i \\ \mathbf{0} \end{bmatrix}, \hat{\mathbf{\$}}_C^i = \begin{bmatrix} \mathbf{v}_i \\ \mathbf{0} \end{bmatrix}$$

Since the axes of the two passive revolute joints in each leg lie in the plane B_iOC_i, the following screw is reciprocal to all the revolute joint screws of the ith leg and does not lie in its constraint wrench system:

$$\hat{\mathbf{\$}}_r^i = \begin{bmatrix} \mathbf{0} \\ \mathbf{w}_i \times \mathbf{v}_i \end{bmatrix} \quad (7)$$

Applying the orthogonal product ($\circ$) (Tsai, 1998) to both sides of Eqn. (6) yields

$$\hat{\mathbf{\$}}_r^i \circ \mathbf{\$}_\omega = (\mathbf{w}_i \times \mathbf{v}_i)^T \boldsymbol{\omega} = (\mathbf{u}_i \times \mathbf{w}_i) \cdot \mathbf{v}_i \dot{\theta}_i \quad (8)$$

As a consequence, the expression mapping from the mobile platform twist to the input angular velocities is stated as:

$$\mathbf{A}\boldsymbol{\omega} = \mathbf{B}\dot{\boldsymbol{\theta}} \quad (9)$$

with

$$\mathbf{A} = \begin{bmatrix} \mathbf{a}_1 & \mathbf{a}_2 & \mathbf{a}_3 \end{bmatrix}, \mathbf{a}_i = \mathbf{w}_i \times \mathbf{v}_i \quad (10a)$$

$$\mathbf{B} = \mathrm{diag} \begin{bmatrix} b_1 & b_2 & b_3 \end{bmatrix}, b_i = (\mathbf{u}_i \times \mathbf{w}_i) \cdot \mathbf{v}_i \quad (10b)$$

where $\dot{\boldsymbol{\theta}} = \begin{bmatrix} \dot{\theta}_1 & \dot{\theta}_2 & \dot{\theta}_3 \end{bmatrix}^T$. Matrices $\mathbf{A}$ and $\mathbf{B}$ are the forward and inverse Jacobian matrices of the manipulator, respectively. If $\mathbf{B}$ is nonsingular, the kinematic Jacobian matrix $\mathbf{J}$ is obtained as

$$\mathbf{J} = \mathbf{B}^{-1}\mathbf{A} \quad (11)$$

3.2 Cartesian stiffness matrix

The stiffness model of the SPM under study is established with virtual spring approach (Pashkevich et al., 2009), by considering the actuation stiffness, link deformation and the influence of the passive joints. The flexible model of the ith leg is represented in Figure 3. Figure 3(b) illustrates the link deflections and variations in passive revolute joint angles.

Let the center of rotation be the reference point of the mobile platform. Analog to Eqn. (6), the small displacement screw of the mobile-platform can be expressed as:

$$\mathbf{\$}_O^i = \begin{bmatrix} \Delta\boldsymbol{\phi} \\ \Delta\mathbf{p} \end{bmatrix} = \Delta\theta_i \hat{\mathbf{\$}}_A^i + \Delta\psi_i \hat{\mathbf{\$}}_B^i + \Delta\xi_i \hat{\mathbf{\$}}_C^i \quad (12)$$

where $\Delta\mathbf{p} = [\Delta x, \Delta y, \Delta z]^T$ is linear displacement of the rotation center and $\Delta\boldsymbol{\phi} = [\Delta\phi_x, \Delta\phi_y, \Delta\phi_z]^T$ is the MP orientation error. Note that this equation only includes the joint variations, while for the real manipulator, link deflections should be considered as well.

The screws associated with the link deflections are formulated as follows:

$$\hat{\mathbf{\$}}_{u1}^i = \begin{bmatrix} \mathbf{r}_i \\ \mathbf{r}_C^i \times \mathbf{r}_i \end{bmatrix}, \hat{\mathbf{\$}}_{u2}^i = \hat{\mathbf{\$}}_C^i, \hat{\mathbf{\$}}_{u3}^i = \begin{bmatrix} \mathbf{n}_i \\ \mathbf{r}_C^i \times \mathbf{n}_i \end{bmatrix} \quad (13)$$

$$\hat{\mathbf{\$}}_{u4}^i = \begin{bmatrix} \mathbf{0} \\ \mathbf{r}_i \end{bmatrix}, \hat{\mathbf{\$}}_{u5}^i = \begin{bmatrix} \mathbf{0} \\ \mathbf{v}_i \end{bmatrix}, \hat{\mathbf{\$}}_{u6}^i = \begin{bmatrix} \mathbf{0} \\ \mathbf{n}_i \end{bmatrix}$$

where $\mathbf{n}_i = \mathbf{w}_i \times \mathbf{v}_i$ is the normal vectors of plane B_iOC_i, $\mathbf{r}_i = \mathbf{w}_i \times \mathbf{n}_i$, and $\mathbf{r}_C^i$ is the position vector of point C_i from O. The directions of the vectors $\mathbf{r}_i$ and $\mathbf{n}_i$ are identical to Δu_4^i and Δu_6^i, respectively.

By considering the link deflections $\Delta u_1^i...\Delta u_6^i$ and variations in passive joint angles and adding all the deflection freedoms to Eqn. (12), the mobile platform deflection in the ith leg is stated as

$$\mathbf{\$}_O^i = \Delta\theta_i \hat{\mathbf{\$}}_A^i + \Delta\psi_i \hat{\mathbf{\$}}_B^i + \Delta\xi_i \hat{\mathbf{\$}}_C^i + \Delta u_1^i \hat{\mathbf{\$}}_{u1}^i + \Delta u_2^i \hat{\mathbf{\$}}_{u2}^i$$
$$+ \Delta u_3^i \hat{\mathbf{\$}}_{u3}^i + \Delta u_4^i \hat{\mathbf{\$}}_{u4}^i + \Delta u_5^i \hat{\mathbf{\$}}_{u5}^i + \Delta u_6^i \hat{\mathbf{\$}}_{u6}^i \quad (14)$$

The previous equation can be written in a compact form by separating the terms related to the variations
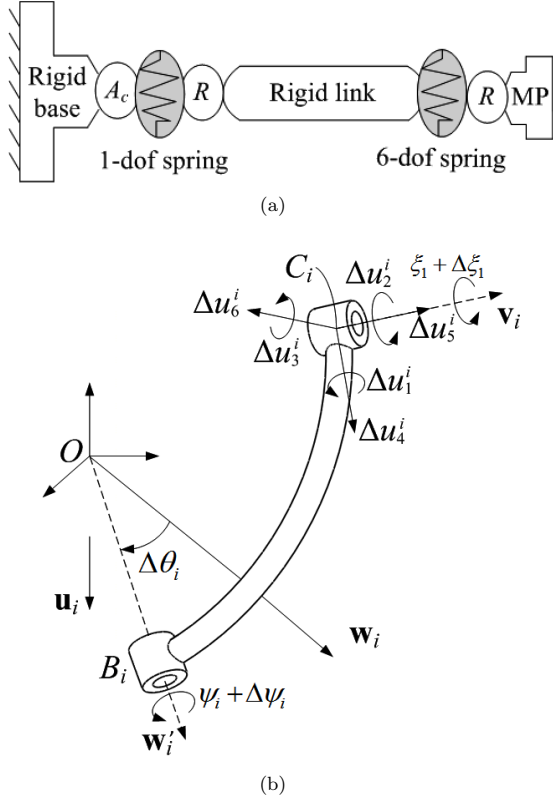
(a)

(b)

Figure 3: Flexible model of a single leg: (a) virtual spring model, where A_c stands for the actuator, R for revolute joints and MP for the mobile platform, (b) link deflections and joint variations in the ith leg.

in the passive revolute joint angles and those related to the actuator and link deflections, namely,

$$\$_O^i = \mathbf{J}_\theta^i \Delta\mathbf{u}_i + \mathbf{J}_q^i \Delta\mathbf{q}_i \qquad (15)$$

with

$$\mathbf{J}_\theta^i = \begin{bmatrix} \hat{\$}_A^i & \hat{\$}_{u1}^i & \hat{\$}_{u2}^i & \hat{\$}_{u3}^i & \hat{\$}_{u4}^i & \hat{\$}_{u5}^i & \hat{\$}_{u6}^i \end{bmatrix} \quad (16a)$$

$$\mathbf{J}_q^i = \begin{bmatrix} \hat{\$}_B^i & \hat{\$}_C^i \end{bmatrix} \qquad (16b)$$

$$\Delta\mathbf{u}_i = \begin{bmatrix} \Delta\theta_i & \Delta u_1^i & \Delta u_2^i & \Delta u_3^i & \Delta u_4^i & \Delta u_5^i & \Delta u_6^i \end{bmatrix}^T \ (16c)$$

$$\Delta\mathbf{q}_i = \begin{bmatrix} \Delta\psi_i & \Delta\xi_i \end{bmatrix}^T \qquad (16d)$$

Let the external wrench applied to the end of the ith leg be denoted by $\mathbf{f}_i$, the constitutive law of the ith leg can be expressed as

$$\mathbf{f}_i = \begin{bmatrix} \mathbf{K}_{rr} & \mathbf{K}_{rt} \\ \mathbf{K}_{rt}^T & \mathbf{K}_{tt} \end{bmatrix}_i \begin{bmatrix} \Delta\boldsymbol{\phi} \\ \Delta\mathbf{p} \end{bmatrix} \quad \rightarrow \quad \mathbf{f}_i = \mathbf{K}_i \$_O^i \quad (17)$$

On the other hand, the wrench applied to the articulated joints in the ith leg being denoted by a vector $\boldsymbol{\tau}_i$, the equilibrium condition for the system is written as,

$$\mathbf{J}_\theta^{i^T} \mathbf{f}_i = \boldsymbol{\tau}_i, \ \mathbf{J}_q^{i^T} \mathbf{f}_i = \mathbf{0}, \ \Delta\mathbf{u}_i = \mathbf{K}_\theta^{i^{-1}} \boldsymbol{\tau}_i \qquad (18)$$

Combining Eqns. (15), (17) and (18), the kinetostatic model of the ith leg can be reduced to a system of two matrix equations, namely,

$$\begin{bmatrix} \mathbf{S}_\theta^i & \mathbf{J}_q^i \\ \mathbf{J}_q^{i^T} & \mathbf{0}_{2\times2} \end{bmatrix} \begin{bmatrix} \mathbf{f}_i \\ \Delta\mathbf{q}_i \end{bmatrix} = \begin{bmatrix} \$_O^i \\ \mathbf{0}_{2\times1} \end{bmatrix} \qquad (19)$$

where the sub-matrix $\mathbf{S}_\theta^i = \mathbf{J}_\theta^i \mathbf{K}_\theta^{i^{-1}} \mathbf{J}_\theta^{i^T}$ describes the spring compliance relative to the center of rotation, and the sub-matrix $\mathbf{J}_q^i$ takes into account the passive joint influence on the mobile platform motions.

$\mathbf{K}_\theta^{i^{-1}}$ is a 7×7 matrix, describing the compliance of the virtual springs and taking the form:

$$\mathbf{K}_\theta^{i^{-1}} = \begin{bmatrix} \mathbf{K}_{act}^{i^{-1}} & \mathbf{0}_{1\times6} \\ \mathbf{0}_{6\times1} & \mathbf{K}_L^{i^{-1}} \end{bmatrix} \qquad (20)$$

where $\mathbf{K}_{act}^i$ corresponds to the stiffness of the ith actuator. $\mathbf{K}_L^i$ of size 6×6 is the stiffness matrix of the curved link in the ith leg, which is calculated by means of the Euler-Bernoulli stiffness model of a cantilever. In Figure 3(b), Δu_1, Δu_2 and Δu_3 show the three moment directions while Δu_4, Δu_5 and Δu_6 show the three force directions, thus, using Castigliano's theorem (Hibbeler, 1997), the compliance matrix of the curved link takes the form:

$$\mathbf{K}_L^{i^{-1}} = \begin{bmatrix} C_{11} & C_{12} & 0 & 0 & 0 & C_{16} \\ C_{12} & C_{22} & 0 & 0 & 0 & C_{26} \\ 0 & 0 & C_{33} & C_{34} & C_{35} & 0 \\ 0 & 0 & C_{34} & C_{44} & C_{45} & 0 \\ 0 & 0 & C_{35} & C_{45} & C_{55} & 0 \\ C_{16} & C_{26} & 0 & 0 & 0 & C_{66} \end{bmatrix} \quad (21)$$

where the corresponding elements are given in Appendix A.

The matrix $\mathbf{J}_\theta^i$ of size 6×7 is the Jacobian matrix related to the virtual springs and $\mathbf{J}_q^i$ of 6×2, the one related to revolute joints in the ith leg. The Cartesian stiffness matrix $\mathbf{K}_i$ of the ith leg is obtained from Eqn. (19),

$$\mathbf{f}_i = \mathbf{K}_i \$_O^i \qquad (22)$$

where $\mathbf{K}_i$ is a 6×6 sub-matrix, which is extracted from the inverse of the 8×8 matrix on the left-hand side of Eqn. (19). From $\mathbf{f} = \sum_{i=1}^{3} \mathbf{f}_i$, $\$_O = \$_O^i$ and $\mathbf{f} = \mathbf{K}\$_O$, the Cartesian stiffness matrix $\mathbf{K}$ of the system is found by simple addition, namely,

$$\mathbf{K} = \sum_{i=1}^{3} \mathbf{K}_i \qquad (23)$$

115

3.3 Mass matrix

The mass in motion of the mechanism influences the dynamic performance, such as inertia, acceleration, etc., hence, formulating the mass matrix is one important procedure in the dynamic analysis. Mass matrix is the function of manipulator dimensions and material properties, i.e., link lengths, cross-sectional area, mass density. Generally, the manipulator mass matrix (inertia matrix) can be obtained on the basis of its kinetic energy. The total kinetic energy T includes the energy T_p of the mobile platform, T_l of the curved links and T_s of the slide units:

- The kinetic energy of the mobile platform is

$$T_p = \frac{1}{2} m_p \mathbf{v}_p^T \mathbf{v}_p + \frac{1}{2} \boldsymbol{\omega}^T \mathbf{I}_p \boldsymbol{\omega} \qquad (24)$$

with

$$\mathbf{v}_p = R \cos \beta \mathbf{p} \times \boldsymbol{\omega}, \ \mathbf{I}_p = \text{diag} \left[I_{xx} \ I_{yy} \ I_{zz} \right] \ (25)$$

where m_p is the mass of the mobile-platform and I_{xx}, I_{yy}, I_{zz} are the mass moments of inertia of the mobile-platform about x-, y-, z-axes, respectively.

- The kinetic energy of the curved links is

$$T_l = \frac{1}{2} \sum_{i=1}^{3} \left(m_l \mathbf{v}_l^{i^T} \mathbf{v}_l^i + I_l \dot{\psi}_i^2 \right) \qquad (26)$$

with

$$\mathbf{v}_l^i = \frac{1}{2} R \left(\dot{\theta}_i \mathbf{w}_i \times \mathbf{u}_i + \mathbf{v}_i \times \boldsymbol{\omega} \right) \qquad (27a)$$

$$I_l = \frac{1}{2} m_l R^2 \left(1 - \frac{\sin \alpha_2 \cos \alpha_2}{\alpha_2} \right) \qquad (27b)$$

$$\dot{\psi}_i = -\frac{(\mathbf{u}_i \times \mathbf{v}_i) \cdot \boldsymbol{\omega}}{(\mathbf{u}_i \times \mathbf{w}_i) \cdot \mathbf{v}_i} = \mathbf{j}_{\psi i} \cdot \boldsymbol{\omega} \qquad (27c)$$

where m_l is the link mass and I_l is its mass moment of inertia about $\mathbf{w}_i$.

- The kinetic energy of the slide units is

$$T_s = \frac{1}{2} \left(I_g n_g^2 + m_s R_s^2 \right) \dot{\boldsymbol{\theta}}^T \dot{\boldsymbol{\theta}} \qquad (28)$$

where m_s is the mass of the slide unit and R_s is the distance from its mass center to z-axis. I_g is the mass moment of inertia of the pinion and n_g is the gear ratio.

Consequently, the SPM kinetic energy can be written in the following form

$$T = T_p + T_l + T_s = \frac{1}{2} \dot{\boldsymbol{\theta}}^T \mathbf{M} \dot{\boldsymbol{\theta}} \qquad (29)$$
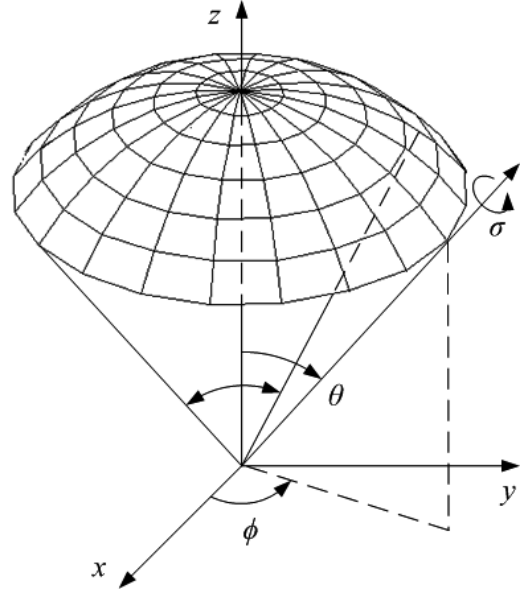
Figure 4: The representation of the regular workspace for the SPM with a pointing cone.

with the mass matrix $\mathbf{M}$ of the system is expressed as

$$\begin{aligned}
\mathbf{M} = &\left(m_s R_s^2 + I_g n_g^2 + \frac{1}{4} m_l R^2 \sin^2 \alpha_1 \right) \mathbf{1}_3 \\
&+ \mathbf{J}^T \left(\mathbf{I}_p + m_p R^2 \cos^2 \beta [\mathbf{p}]_\times^T [\mathbf{p}]_\times \right. \\
&\left. + \frac{1}{4} m_l R^2 \sum_{i=1}^{3} [\mathbf{v}_i]_\times^T [\mathbf{v}_i]_\times + I_l \sum_{i=1}^{3} \mathbf{j}_{\psi i} \mathbf{j}_{\psi i}^T \right) \mathbf{J} \quad (30)
\end{aligned}$$

where $[\cdot]_\times$ stands for the skew-symmetric matrix whose elements are from the corresponding vector and $\mathbf{1}_3$ is the Identity matrix.

4 Design Optimization of the Spherical Parallel Manipulator

The inverse kinematic problem of the SPM can have up to eight solutions, i.e., the SPM can have up to eight working modes. Here, the diagonal terms b_i of the inverse Jacobian matrix $\mathbf{B}$ are supposed to be all negative for the SPM to stay in a given working mode. In the optimization procedure, criteria involving kinematic and kinetostatic/dynamic performances are considered to determine the mechanism configuration and the dimension and mass properties of the links. Moreover, the performances are evaluated over a regular shaped workspace free of singularity, which is specified as a minimum pointing cone of 90° opening with

Figure 5: Design variables of the 3-RRR SPM.

360º full rotation, i.e., $\theta \geq 45º$ and $\sigma \in (-180º, 180º]$, see Figure 4.

4.1 Design variables

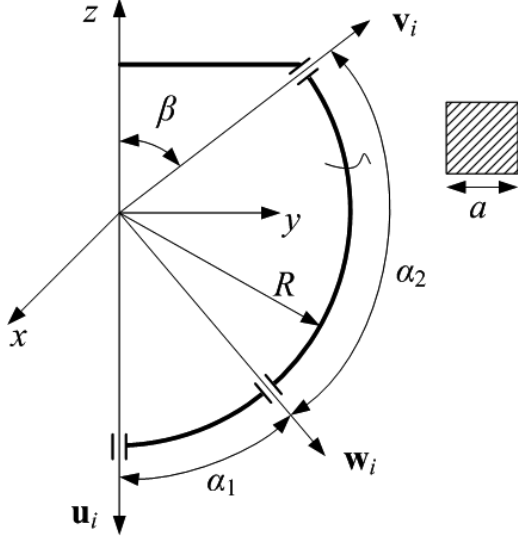Variables α_1, α_2, β and γ are part of the geometric parameters of a 3-RRR SPM and $\gamma = 0$ for the manipulator under study. Moreover, the radius R of the link midcurve is another design variable and the cross section of the links is supposed to be a square of side length a. These variables are shown in Figure 5. As a consequence, the design variable vector is expressed as follows:

$$\mathbf{x} = [\alpha_1, \, \alpha_2, \, \beta, \, a, \, R] \qquad (31)$$

4.2 Objective functions

The kinematic performance is one of the major concerns in the manipulator design, of which a criterion is the evaluation of the dexterity of SPMs. A commonly used criterion to evaluate this kinematic performance is the global conditioning index (GCI) (Gosselin and Angeles, 1991), which describes the isotropy of the kinematic performance. The GCI is defined over a workspace Ω as

$$GCI = \frac{\int_{\Omega} \kappa^{-1}(\mathbf{J}) \mathrm{d}W}{\int_{\Omega} \mathrm{d}W} \qquad (32)$$

where $\kappa(\mathbf{J})$ is the condition number of the kinematic Jacobian matrix (11). In practice, the GCI of a robotic

manipulator is calculated through a discrete approach as

$$GCI = \frac{1}{n} \sum_{i=1}^{n} \frac{1}{\kappa_i(\mathbf{J})} \qquad (33)$$

where n is the number of the discrete workspace points. As a result, the first objective function of the optimization problem is written as:

$$f_1(\mathbf{x}) = GCI \quad \rightarrow \quad \max \qquad (34)$$

Referring to the kinematic dexterity, an important criterion to evaluate the dynamic performance is dynamic dexterity, which is made on the basis of the concept of Generalized Inertia Ellipsoid (GIE) (Asada, 1983). In order to enhance the dynamic performance and to make acceleration isotropic, the mass matrix (30) should be optimized to obtain a better dynamic dexterity. Similar to GCI, a global dynamic index (GDI) is used to evaluate the dynamic dexterity, namely,

$$GDI = \frac{1}{n} \sum_{i=1}^{n} \frac{1}{\kappa_i(\mathbf{M})} \qquad (35)$$

where $\kappa_i(\mathbf{M})$ is the condition number of the mass matrix of the ith workspace point. Thus, the second objective function of the optimization problem is written as:

$$f_2(\mathbf{x}) = GDI \quad \rightarrow \quad \max \qquad (36)$$

4.3 Optimization constraints

In this section, the kinematic constraints, conditioning of the kinematic Jacobian matrix and accuracies due to the elastic deformation are considered. Constraining the conditioning of the Jacobian matrix aims to guarantee dexterous workspace free of singularity, whereas limits on accuracy consideration ensures that the mechanism is sufficiently stiff.

4.3.1 Kinematic constraints

According to the determination of design space reported in (Bai, 2010), the bounds of the parameter α_1, α_2 and β subject to the prescribed workspace are stated as:

$$45º \leq \beta \leq 90º, \ 45º \leq \alpha_1, \alpha_2 \leq 135º \qquad (37)$$

The sequence of the first, second and third slide units appearing on the circular guide counterclockwise is constant. In order to avoid collision, the angles θ_{ij} between the projections of vectors $\mathbf{w}_i$ and $\mathbf{w}_j$ in the xy quadrant, $i, j = 1, 2, 3, i \neq j$, as shown in Figure 6, have the minimum value, say 10º. To avoid collision
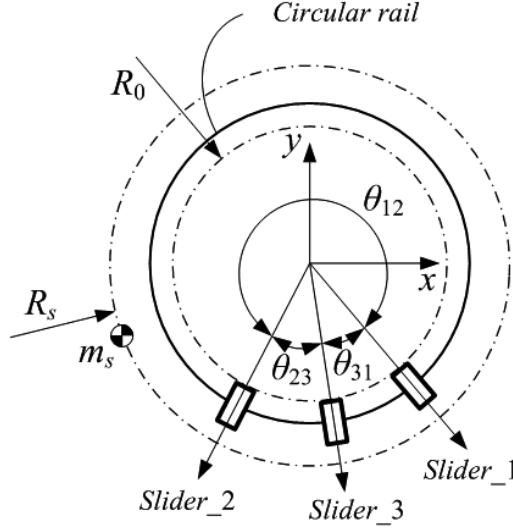
Figure 6: Slide unit configuration of the 3-DOF SPM.

and make the mechanism compact, the following constraints should be satisfied:

$$\theta_{12}, \theta_{23}, \theta_{31} \geq \epsilon_\theta = 10^\circ \tag{38}$$
$$R_0 = 0.120\,\mathrm{m} \leq R\sin\alpha_1 \leq R_s = 0.200\,\mathrm{m}$$

Moreover, the SPM should not reach any singularity in its orientation workspace. Therefore, the following conditions should be satisfied.

$$det(\mathbf{A}) \geq \epsilon, \ b_i = (\mathbf{u}_i \times \mathbf{w}_i) \cdot \mathbf{v}_i \leq -\epsilon \tag{39}$$

where $\mathbf{A}$ is the forward Jacobian matrix of the manipulator defined in Eqn. (9) and $\epsilon > 0$ is a previously specified tolerance set to 0.001.

4.3.2 Conditioning number of the kinematic Jacobian matrix

Maximizing the GCI and constraining the kinematic Jacobian matrix cannot prevent the prescribed workspace away from ill-conditioned configurations. For the design optimization in order to achieve a dexterous workspace, the minimum of the inverse condition number of the kinematic Jacobian matrix $\kappa^{-1}(\mathbf{J})$, based on 2-norm, should be higher than a prescribed value throughout the workspace, say 0.1, namely,

$$min(\kappa^{-1}(\mathbf{J})) \geq 0.1 \tag{40}$$

4.3.3 Accuracy constraints

The accuracy constraints of the optimization problem for the SPM are related to the dimensions of

Table 1: The lower and upper bounds of the design variables $\mathbf{x}$.

	α_1 [deg]	α_2 [deg]	β [deg]	a [m]	R [m]
$\mathbf{x}_{lb}$	45	45	45	0.005	0.120
$\mathbf{x}_{ub}$	135	135	90	0.030	0.300

the curved link and the maximum positional deflection of the rotation center and angular deflection of the moving-platform subject to a given wrench applied on the latter. The control loop stiffness is $K^i_{act} = 10^6\,\mathrm{Nm/rad}$. Let the static wrench capability be specified as the eight possible combinations of moments $\mathbf{m} = [\pm 10, \pm 10, \pm 10]\,\mathrm{Nm}$, while the allowable maximum positional and rotational errors for the workspace points are $1\,\mathrm{mm}$ and $2^\circ = 0.0349\,\mathrm{rad}$, respectively, thus, the accuracy constraints can be written as:

$$\|\Delta\mathbf{p}\|_n = \sqrt{\Delta x_n^2 + \Delta y_n^2 + \Delta z_n^2} \leq \epsilon_p \tag{41}$$
$$\|\Delta\boldsymbol{\phi}\|_n = \sqrt{\Delta\phi_{x,\,n}^2 + \Delta\phi_{y,\,n}^2 + \Delta\phi_{z,\,n}^2} \leq \epsilon_r$$

where the linear and angular displacements are computed from $\$_O = \mathbf{K}^{-1}\mathbf{f}$ with the Cartesian stiffness matrix (23) and $\epsilon_p = 1\,\mathrm{mm}$, $\epsilon_r = 0.0349\,\mathrm{rad}$.

4.4 Formulation of the multiobjective optimization problem

Mathematically, the multi-objective design optimization problem for the spherical parallel manipulator can be formulated as:

$$\begin{aligned}
\text{maximize} \quad & f_1(\mathbf{x}) = GCI \tag{42}\\
\text{maximize} \quad & f_2(\mathbf{x}) = GDI\\
\text{over} \quad & \mathbf{x} = [\alpha_1,\,\alpha_2,\,\beta,\,a,\,R]\\
\text{subject to} \quad & g_1 : \theta \geq 45^\circ\\
& g_2 : R_0 \leq R\sin\alpha_1 \leq R_s\\
& g_3 : \theta_{12}, \theta_{23}, \theta_{31} \geq \epsilon_\theta = 10^\circ\\
& g_4 : det(\mathbf{A}) \geq \epsilon, \ (\mathbf{u}_i \times \mathbf{w}_i) \cdot \mathbf{v}_i \leq -\epsilon\\
& g_5 : min(\kappa^{-1}(\mathbf{J})) \geq 0.1\\
& g_6 : \sqrt{\Delta x_n^2 + \Delta y_n^2 + \Delta z_n^2} \leq \epsilon_p\\
& g_7 : \sqrt{\Delta\phi_{x,\,n}^2 + \Delta\phi_{y,\,n}^2 + \Delta\phi_{z,\,n}^2} \leq \epsilon_r\\
& \mathbf{x}_{lb} \leq \mathbf{x} \leq \mathbf{x}_{ub}\\
& i = 1, 2, 3
\end{aligned}$$

where $\mathbf{x}_{lb}$ and $\mathbf{x}_{ub}$, respectively, are the lower and upper bounds of the variables $\mathbf{x}$ given by Table 1.

Table 2: Algorithm parameters of the implemented NSGA-II

Population size	Generation	Directional crossover probability	Crossover probability	Mutation probability	Distribution index
40	200	0.5	0.9	0.1	20

Table 3: Three Pareto-optimal solutions

Design ID	Variables					Objectives	
	α_1 [deg]	α_2 [deg]	β [deg]	a [m]	R [m]	GCI	GDI
I	56.2	81.0	89.8	0.0128	0.1445	0.366	0.711
II	51.6	84.3	89.9	0.0133	0.1533	0.453	0.665
III	47.2	90.8	89.2	0.0127	0.1641	0.536	0.625

4.5 Pareto-optimal solutions

For the proposed SPM, the actuation transmission mechanism is a combination of actuator of model RE 35 GB and gearhead of model GP 42 C from Maxon (Maxon, 2012) and a set of gear ring-pinion with ratio $n_g = 8$. Moreover, the components are supposed to be made of steel, thus, $E = 210$ Gpa, $\nu = 0.3$. Moreover, the moving platform is supposed to be a regular triangle, thus, the MP and link masses are given by

$$m_p = \frac{3\sqrt{3}}{4}\rho h R^2 \sin^2\beta, \ m_l = \rho a^2 R \alpha_2 \qquad (43)$$

where ρ is the mass density and $h = 0.006$ m is the thickness of the moving platform. The total mass m_s of each slide unit, including the mass of the actuator, gearhead, pinion and the manufactured components, is equal to $m_s = 2.1$ kg.

The previous formulated optimization problem (42) is solved by the genetic algorithm NSGA-II (Deb et al., 2002) with *Matlab*, of which the algorithm parameters are given in Table 2.

The Pareto front of the formulated optimization problem for the SPM is shown in Figure 7 and three optimal solutions, i.e., two extreme and one intermediate, are listed in Table 3.

Figure 8 illustrates the variational trends as well as the inter-dependency between the objective functions and design variables by means of a scatter matrix. The lower triangular part of the matrix represents the correlation coefficients whereas the upper one shows the corresponding scatter plots. The diagonal elements represent the probability density charts of each variable. The correlation coefficients vary from -1 to 1. Two variables are strongly dependent when their correlation coefficient is close to -1 or 1 and independent when the latter is null. Figure 8 shows:

- both objectives functions GCI and GDI are
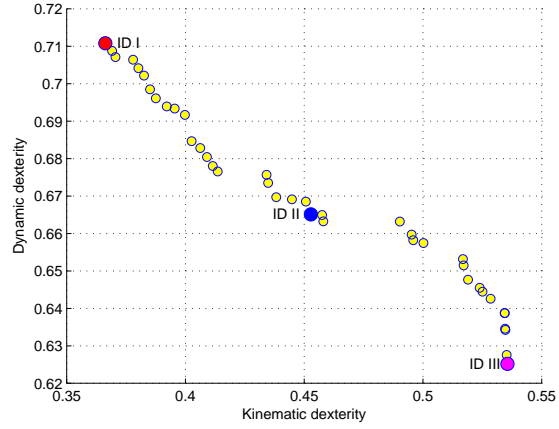
Figure 7: The Pareto front of the multiobjective optimization problem for the SPM.

strongly dependent as their correlation coefficient is equal to -0.975;

- both objectives functions GCI and GDI are strongly dependent on all design variables as all of the corresponding correlation coefficients are greater than 0.6;

- GCI is slightly more dependent than GDI of the design variables as all the corresponding correlation coefficients of former are greater than those of latter;

- GDI is less dependent on the design variables β and a than the other variables although the two former variables influence the SPM mass, this is due to the large portion of the slide unit mass in the total mechanism mass.
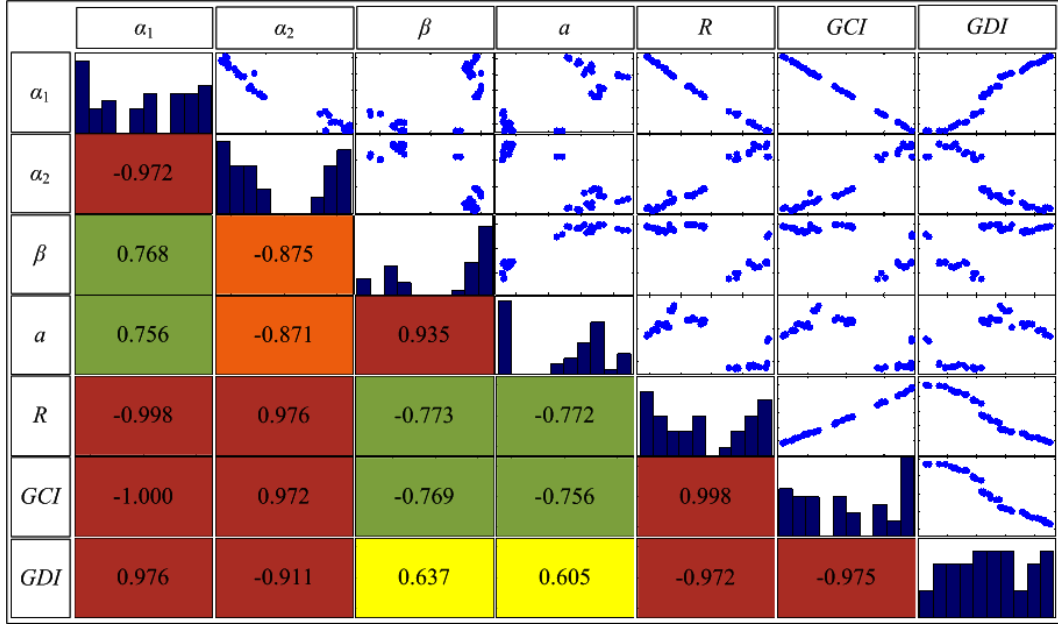
Figure 8: Scatter matrix for the objective functions and the design variables.
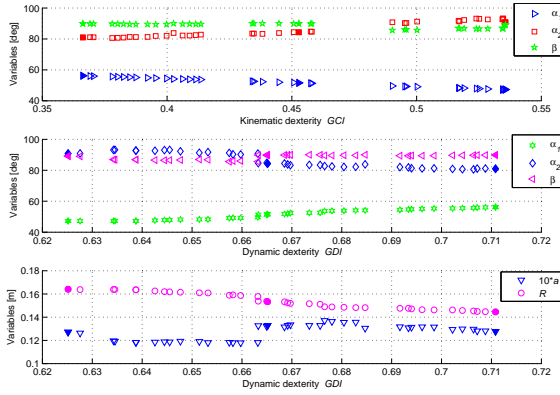
Figure 9: Design variables as functions of objectives for the Pareto-optimal solutions.

Figure 9 displays the design variables as functions of the objectives. It is noteworthy that the higher GCI, the lower α_1, conversely, the higher GDI, the higher α_1. This phenomenon is opposite with respect to variable α_2. The design variable β converges to 90º approximately, which indicates that $\beta = 90$º is the preferred geometric parameter for the SPM under study. The lower link midcurve R and higher a lead to higher GDI. The three sets of of design variables corresponding to the three Pareto-optimal solutions depicted in Table 3 are shown in Figure 9 with solid markers.

5 Conclusions

In this paper, the geometric synthesis of spherical parallel manipulators is discussed. A multiobjective design optimization problem based on the genetic algorithm was formulated in order to determine the mechanism optimum structural and geometric parameters. The objective functions were defined on the basis of the criteria of both kinematic and kinetostatic/dynamic performances. This approach is illustrated with the optimum design of an unlimited-roll spherical parallel manipulator, aiming at maximizing the kinematic and dynamic dexterities to achieve relatively better kinematic and dynamic performances simultaneously. It is found that the parameter β being equal to 90º is a preferred structure for the SPM under study. Finally, the Pareto-front was obtained to show the approximation of the optimal solutions between the various (antagonistic) criteria, subject to the dependency of the performance. The future work will aim to maximize the orientation workspace and optimize the cross-section type of the curved links.

References

Altuzarra, O., Salgado, O., Hernandez, A., and Angeles, J. Multiobjective optimum design of a symmetric parallel schönflies-motion generator.

ASME J. Mechanical Design, 2009. 131(3):031002. doi:10.1115/1.3066659.

Asada, H. A geometrical representation of manipulator dynamics and its application to arm design. *ASME J. Dynamic Systems, Measurement and Control*, 1983. 105(3):131–142. doi:10.1115/1.3140644.

Asada, H. and Granito, J. Kinematic and static characterization of wrist joints and their optimal design. In *IEEE International Conference on Robotics and Automation*. pages 244–250, 1985. doi:10.1109/ROBOT.1985.1087324.

Bai, S. Optimum design of spherical parallel manipulator for a prescribed workspace. *Mechanism and Machine Theory*, 2010. 45(2):200–211. doi:10.1016/j.mechmachtheory.2009.06.007.

Bai, S., Hansen, M. R., and Andersen, T. O. Modelling of a special class of spherical parallel manipulators with Euler parameters. *Robotica*, 2009. 27(2):161–170. doi:10.1017/S0263574708004402.

Bonev, I. A. Direct kinematics of zero-torsion parallel mechanisms. In *IEEE International Conference on Robotics and Automation*. Pasadena, California, USA, pages 3851–3856, 2008. doi:10.1109/ROBOT.2008.4543802.

Bonev, I. A. and Gosselin, C. M. Analytical determination of the workspace of symmetrical spherical parallel mechanisms. *IEEE Transactions on Robotics*, 2006. 22(5):1011–1017. doi:10.1109/TRO.2006.878983.

Caro, S., Chablat, D., Ur-Rehman, R., and Wenger, P. Multiobjective design optimization of 3-PRR planar parallel manipulators. In *Global Product Development*, pages 373–383. Springer-Verlag Berlin Heidelberg, 2011. doi:10.1007/978-3-642-15973-2_37.

Cavallo, E. and Michelini, R. C. A robotic equipment for the guidance of a vectored thrustor. In *35th International Symposium on Robotics*. Paris, France, 2004.

Ceccarelli, M., Carbone, G., and Ottaviano, E. Multi criteria optimum design of manipulators. *In Bulletin of the Polish Academy of Technical Sciences*, 2005. 53(1):9–18.

Chaker, A., Mlika, A., Laribi, M. A., Romdhane, L., and Zeghloul, S. Synthesis of spherical parallel manipulator for dexterous medical task. *Frontiers of Mechanical Engineering*, 2012. 7(2):150–162. doi:10.1007/s11465-012-0325-4.

Deb, K., Pratap, A., Agarwal, S., and Meyarivan, T. A fast and elitist multiobjective genetic algorithm: NSGA-II. *IEEE Trans. Evolutionary Computation*, 2002. 6(2):182–197. doi:10.1109/4235.996017.

Durand, S. L. and Reboulet, C. Optimal design of a redundant spherical parallel manipulator. *Robotica*, 1997. 15(4):399–405. doi:10.1017/S0263574797000490.

Gosselin, C. M. and Angeles, J. The optimum kinematic design of a spherical three-degree-of-freedom parallel manipulator. *ASME J. Mechanisms, Transmissions, and Automation in Design*, 1989. 111:202–207. doi:10.1115/1.3258984.

Gosselin, C. M. and Angeles, J. A global performance index for the kinematic optimization of robotic manipulators. *ASME J. Mechanical Design*, 1991. 113(3):220–226. doi:10.1115/1.2912772.

Gosselin, C. M. and Hamel, J. F. The Agile Eye: a high-performance three-degree-of-freedom camera-orienting device. In *IEEE International Conference on Robotics and Automation*. San Diego, CA, pages 781–786, 1994. doi:10.1109/ROBOT.1994.351393.

Hao, F. and Merlet, J.-P. Multi-criteria optimal design of parallel manipulators based on interval analysis. *Mechanism and Machine Theory*, 2005. 40(2):157–171. doi:10.1016/j.mechmachtheory.2004.07.002.

Hay, A. M. and Snyman, J. A. Methodologies for the optimal design of parallel manipulators. *Inter. J. Numerical Methods in Engineering*, 2004. 59(11):131–152. doi:10.1002/nme.871.

Hibbeler, R. C. *Mechanics of Materials*. Prentice Hall, 1997.

Huang, T., Gosselin, C. M., Whitehouse, D. J., and Chetwynd, D. G. Analytic approach for optimal design of a type of spherical parallel manipulators using dexterous performance indices. *IMechE. J. Mechan. Eng. Sci.*, 2003. 217(4):447–455. doi:10.1243/095440603321509720.

Kong, K. and Gosselin, C. M. Type synthesis of three-degree-of-freedom spherical parallel manipulators. *Inter. J. Robotics Research*, 2004. 23(3):237–245. doi:10.1177/0278364904041562.

Krefft, M. and Hesselbach, J. Elastodynamic optimization of parallel kinematics. In *Proceedings of the IEEE International Conference on Automation Science and Engineering*. Edmonton, AB, Canada, pages 357–362, 2005. doi:10.1109/COASE.2005.1506795.

Li, T. and Payandeh, S. Design of spherical parallel mechanisms for application to laparoscopic surgery. *Robotica*, 2002. 20(2):133–138. doi:10.1017/S0263574701003873.

Liu, X. J., Jin, Z. L., and Gao, F. Optimum design of 3-dof spherical parallel manipulators with respect to the conditioning and stiffness indices. *Mechanism and Machine Theory*, 2000. 35(9):1257–1267. doi:10.1016/S0094-114X(99)00072-5.

Lou, Y., Liu, G., Chen, N., and Li, Z. Optimal design of parallel manipulators for maximum effective regular workspace. In *Proceedings of the IEEE/RSJ International Conference on Intelligent Robots and Systems*. Alberta, pages 795–800, 2005. doi:10.1109/IROS.2005.1545144.

Maxon. *Maxon Motor and Gearhead products catalog.* 2012. URL http://www.maxonmotor.com/maxon/view/catalog/.

Merlet, J.-P. Jacobian, manipulability, condition number, and accuracy of parallel robots. *ASME J. Mechanical Design*, 2006a. 128(1):199–206. doi:10.1115/1.2121740.

Merlet, J.-P. *Parallel Robots*. Kluwer, Norwell, 2006b.

Pashkevich, A., Chablat, D., and Wenger, P. Stiffness analysis of overconstrained parallel manipulators. *Mechanism and Machine Theory*, 2009. 44(5):966–982. doi:10.1016/j.mechmachtheory.2008.05.017.

Stamper, R. E., Tsai, L.-W., and Walsh, G. C. Optimization of a three-dof translational platform for well-conditioned workspace. In *Proceedings of the IEEE International Conference on Robotics and Automation*. Albuquerque, NM, pages 3250–3255, 1997. doi:10.1109/ROBOT.1997.606784.

Stock, M. and Miller, K. Optimal kinematic design of spatial parallel manipulators: Application of linear delta robot. *ASME J. Mechanical Design*, 2003. 125(2):292–301. doi:10.1115/1.1563632.

Tsai, L.-W. The Jacobian analysis of parallel manipulators using reciprocal screws. In J. Lenarčič and M. L. Husty, editors, *Advances in Robot Kinematics: Analysis and Control*, pages 327–336. Kluwer Academic Publishers, 1998.

Appendix A

The elements of the compliance matrix (21) for the curved beam

$$C_{11} = \frac{R}{2}\left(\frac{s_1}{GI_x} + \frac{s_2}{EI_y}\right) \tag{A-1a}$$

$$C_{12} = \frac{s_8 R}{2}\left(\frac{1}{GI_x} - \frac{1}{EI_y}\right) \tag{A-1b}$$

$$C_{16} = \frac{R^2}{2}\left(\frac{s_2}{EI_y} - \frac{s_7}{GI_x}\right) \tag{A-1c}$$

$$C_{22} = \frac{R}{2}\left(\frac{s_2}{GI_x} + \frac{s_1}{EI_y}\right) \tag{A-1d}$$

$$C_{26} = \frac{R^2}{2}\left(\frac{s_4}{GI_x} - \frac{s_2}{EI_y}\right) \tag{A-1e}$$

$$C_{33} = \frac{R\alpha_2}{EI_z} \tag{A-1f}$$

$$C_{34} = \frac{s_5 R^2}{EI_z} \tag{A-1g}$$

$$C_{35} = \frac{s_6 R^2}{EI_z} \tag{A-1h}$$

$$C_{44} = \frac{R}{2A}\left(\frac{s_1}{E} + \frac{s_2}{G}\right) + \frac{s_3 R^3}{2EI_z} \tag{A-1i}$$

$$C_{45} = \frac{s_8 R}{2A}\left(\frac{1}{E} - \frac{1}{G}\right) + \frac{s_4 R^3}{2EI_z} \tag{A-1j}$$

$$C_{55} = \frac{R}{2A}\left(\frac{s_1}{G} + \frac{s_2}{E}\right) + \frac{s_2 R^3}{2EI_z} \tag{A-1k}$$

$$C_{66} = \frac{R\alpha_2}{GA} + \frac{R^3}{2}\left(\frac{s_3}{GI_x} + \frac{s_2}{EI_y}\right) \tag{A-1l}$$

with

$$s_1 = \alpha_2 + \sin\alpha_2\cos\alpha_2 \tag{A-2a}$$

$$s_2 = \alpha_2 - \sin\alpha_2\cos\alpha_2 \tag{A-2b}$$

$$s_3 = 3\alpha_2 + \sin\alpha_2\cos\alpha_2/2 - 4\sin\alpha_2 \tag{A-2c}$$

$$s_4 = 1 - \cos\alpha_2 - \sin^2\alpha_2/2 \tag{A-2d}$$

$$s_5 = \sin\alpha_2 - \alpha_2 \tag{A-2e}$$

$$s_6 = \cos\alpha_2 - 1 \tag{A-2f}$$

$$s_7 = 2\sin\alpha_2 - \alpha_2 - \sin\alpha_2\cos\alpha_2 \tag{A-2g}$$

$$s_8 = -\sin^2\alpha_2 \tag{A-2h}$$

where E is the Young's modulus and $G = E/2(1 + \nu)$ is the shear modulus with the Poisson's ratio ν. I_x, I_y and I_z are the moments of inertia, respectively. A is the area of the cross-section.

<div align="right">

8

</div>

Conclusions

The main scope of the research work in this thesis includes error modeling, stiffness modeling and design optimization for parallel manipulators. An error prediction model and a general kinetostatic model were developed. The developed kinetostatic model was used in the optimal design stage and the proposed optimization approach covers kinematics, statics and dynamics to offer flexibility for different requirements and applications of manipulator design.

8.1   Summary of Results

Error analysis, Article I

Article I presents the error modeling and analysis of a planar parallel manipulator with joint clearances. Apart from joint clearances, the developed error model also includes the error sources of actuation error/backlash, manufacturing and assembly errors, which is derived from the first-order kinematic closure equation. Compared to the developed error models in [91, 93], this model clearly represents the sources of errors from the articular joints to evaluate the influence of these variations of errors to the pose errors of the manipulator end-effector efficiently. The developed model can also be applied to serial manipulators.

The error prediction problem for the manipulator is transformed into the optimization problem, of which the constraints are formulated from the joint clearance models. The maximal pose errors of the end-effector subject to the given joint clearances can be evaluated by solving these optimization problems with the commercial softwares at hand such as Matlab$^{\text{TM}}$ or Maple$^{\text{TM}}$.

Using the developed model, the upper bounds and distributions of the pose errors throughout the constant-orientation Cartesian workspaces for the studied manipulator are mapped. The results show that the pose errors are configuration-dependent and the clearances in the passive prismatic joints have much more influence on the pose errors than those in the revolute joints for the manipulator under study.

A vision system is built to measure the pose errors of the uniformly distributed workspace points, the results being compared with the estimations from the analytical model. The root-mean-square based difference for the positional errors evaluated from these two approach is 0.030–0.080 mm, while the difference for the orientational errors is 0.050–0.100 deg. Moreover, a regression analysis is conducted to describe their differences graphically. With the statistical elaboration, the comparison reveals a good correlation between the results from these two approaches, which verified the correctness of the developed model.

Kinetostatic analysis, Article II

Article II describes the establishment of a kinetostatic model and its application to a spherical parallel manipulator. The model is developed on the basis of the concept of the virtual spring, which inherits its advantages of high computation accuracy, i.e., the difference is less than 5% in the comparison to the FEA approach. It is capable to compute the stiffness at both nonsingular and singular configurations and the problem of the deformation calculation is also investigated with the singular value decomposition when the matrix is invertible. Moreover, the influence of the passive joints are taken into account during the modeling.

An improvement is that the screw theory is introduced to derive the Jacobian in which the deformations are considered as infinitesimal displacements. This eases the complicated kinematic problem of the spherical parallel manipulators due to the high-order trigonometric functions associated with orientation angles, as the inverse kinematic solutions of all the joints need to be obtained in advance during the implementation of D-H parameters to derive the Jacobian in Pashkevich's approach [109].

The developed stiffness model is able to evaluate not only the rotational stiffness of the mobile platform, but also the translational stiffness of the rotation center. The results from the comparison among several spherical parallel manipulators with alternative structures shows that the displacements of the center of rotation or center shift cannot be neglected where high positional accuracy is needed.

It should be noted that the stiffness matrix formulation of the curved link in this paper is based on the circular cross-section that cannot be applied to the curved beams with all kinds of cross-sections, i.e., rectangular. Whereas, this matrix can be applied to the beams with polygonal cross-section, such as square, hexagonal and octagonal, for rough computation. Among them, the beam of square cross-sections gives relatively larger difference but below 9% compared with the FEA based evaluation, which is acceptable. In article III, this type of curved beam is adopted in the optimization procedure as it can reduce the manufacturing cost in prototyping a manipulator.

Multiobjective optimum design, Article III & IV

Articles III and IV deal with the architecture optimization of a spherical parallel manipulator, in which two multiobjective optimization problem are formulated to optimize the manipulator's structural and geometric parameters, respectively. The evaluation criteria in these two optimization problems are based on the previously established kinematic, kinetostatic and dynamic models. The difference between them is the different objective functions for different performances improvement.

In article III, the optimization problem aims to minimize the mechanism mass and to maximize the global conditioning index to enhance both kinematic and dynamic performances. The Pareto-front is obtained to give an image of parameters selection subject to the design requirements. Three selected optimal solutions are used to illustrate this optimization procedure by building their CAD design models and numerical dynamic simulations. It is found that the proposed spherical parallel manipulator can have relatively better kinematic and dynamic performance simultaneously. Article IV aims to achieve both kinematic and dynamic isotropy as well as the improved positional and orientational accuracies due to elastic deformation.

Additionally, the scatter matrices for the objectives and variables of the two given optimization problems are plotted to represent variational trends and the inter-dependency among them. The results show that the performances of the proposed manipulator strongly depend on its geometric parameters, mainly the arc angles α_1 and α_2 of the proximal and distal curved links and the angle β of the pyramidal mobile platform. It is found that the proposed manipulator can have relatively better kinematic and dynamic performances with parameters of smaller α_1 and $\alpha_2 = 90º$, $\beta = 90º$ approximately.

The proposed approach covers different kinds of performances ranging from kinematics, statics to dynamics, which offers flexibility to select any criterion as an objective function based on requirements and can be used for other optimal design tasks.

8.2 Contributions

The presented work in this thesis focuses on developing models to characterize the properties of the manipulators and applying optimization technique in the mechanism design. The following contributions from this project study are made:

- *The error model with joint clearances for the parallel manipulators was first experimentally validated.* The validation for the developed analytical error model is of importance as the error model is the basis for the error compensation in order to improve the mechanism accuracy efficiently. In Article I, the validation at the representative points covering the workspace is implemented to verify the correctness of the developed model effectively.

- *The elastic deformation of the center of rotation for the spherical parallel manipulators was first considered.* Very few publications dealt with the stiffness modeling and analysis for this type of mechanisms and in those works only the rotational compliance of the mobile platform was investigated since the most SPMs are used as orientating devices. With the consideration of the positional error of the center of rotation, it is found that this term cannot be ignored as it influences the positional accuracy of the end-effector even under pure external moments.

- *An optimization approach was formulated for the initial design of parallel manipulators, in which kinetostatic and dynamic performances were first considered for the optimal design of spherical parallel manipulators.* All major performances, including kinematic, kinetostatic and dynamic performances, are considered in the formulated design procedure. For the spherical parallel manipulators, as most of them find their applications with the light-load requirements like orientating devices in medical applications, the analysis and design for this type of mechanisms focus on their kinematic aspects while the statics and dynamics have received relatively less attention. With the proposed approach, selected performance criteria can be emphasized for the design requirement of specified application.

8.3 Concluding Remarks

An error prediction model for parallel manipulators was developed and experimentally validated. The developed model implies that the manipulator accuracy can be improved by calibration after preloading the clearance-affected joints.

A general kinetostatic model is developed for the spherical parallel manipulators to evaluate the positional accuracy when this class of mechanisms are used as robotic manipulator. This model can also be generalized to the other types of manipulators.

A systematic optimization approach is formulated for design optimization and performance improvement of spherical parallel manipulators, in which all major performances, including kinematic, kinetostatic and dynamic performances, are considered. The proposed optimization method offers flexibility with selected design objectives to meet different design requirements.

8.4   Future Work

The work presented in this thesis was primarily concerned with error/stiffness modeling and optimization in the early design stage. No consideration was given to the improvement of accuracy for the mechanisms. Whereas, this is crucial issue of the manipulator applications. The following future work is recommended:

- Based on the developed error model, Article I suggests to preload the joint to improve the manipulator accuracy. The preloaded forces need to be determined without highly increasing energy consumption. Torsional springs will be arranged on the corresponding joints to increase the manipulator accuracy.

- In article III and IV, the curved beam of square cross-section is adopted to evaluated the kinetostatic performance. As a matter of fact, different shaped cross-sections of the curved beam will influence the stiffness matrix formulation. A more general approach of the stiffness matrix formulation for the curved beam is to be developed for more accurate stiffness analysis.

- An optimization approach has been proposed for the design of spherical parallel manipulator. This approach can be applied in the early design stage. The dynamic performance will be addressed in the following optimization procedure for its application as an active joint. According to the optimal results, the manipulator and its control system will be built to validate the proposed approach.

Appendix A

Mass Center and Moments of Inertia of Curved Link

A regular curved link is shown in Figure A.1.
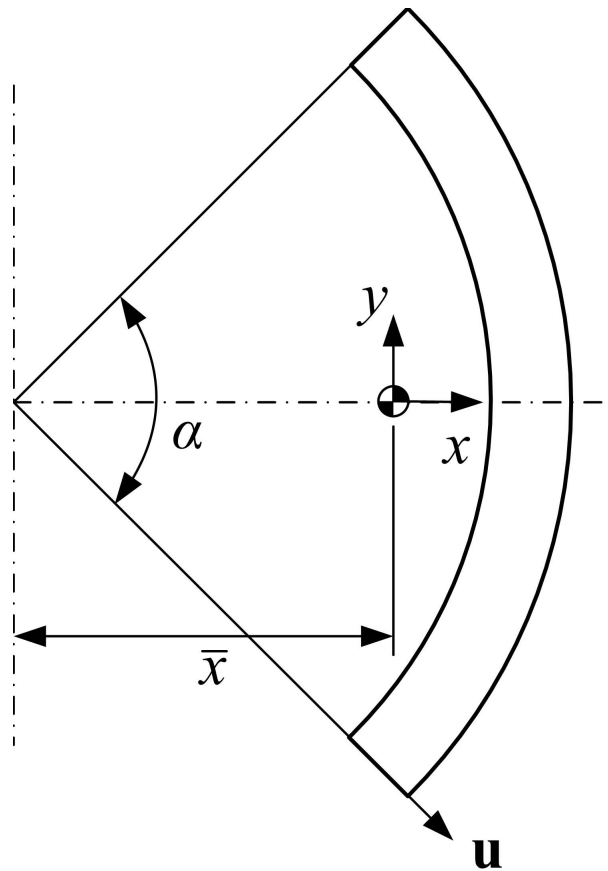
Figure A.1: A regular curved link.

Its mass center is denoted by

$$R\alpha\bar{x} = R^2 \int \cos\varphi \mathrm{d}\varphi \rightarrow \bar{x} = \frac{2R\sin(\alpha/2)}{\alpha} \tag{A.1}$$

The mass moments of inertia are expressed as:

$$L_{xx} = \int_{-\frac{\alpha}{2}}^{\frac{\alpha}{2}} (R\sin\varphi)^2 \cdot \frac{m_l}{R\alpha} \cdot R\mathrm{d}\varphi = \frac{1}{2}m_l R^2 \left(1 - \frac{\sin\alpha}{\alpha}\right) \tag{A.2a}$$

$$L_{yy} = \int_{-\frac{\alpha}{2}}^{\frac{\alpha}{2}} (R\sin\varphi - \bar{x})^2 \cdot \frac{m_l}{R\alpha} \cdot R\mathrm{d}\varphi = \frac{1}{2}m_l \left(\frac{R^2\sin\alpha - 8R\bar{x}\sin\frac{\alpha}{2}}{\alpha} + R^2 + 2\bar{x}^2\right) \tag{A.2b}$$

$$L_{zz} = \int_{-\frac{\alpha}{2}}^{\frac{\alpha}{2}} \left[(R\sin\varphi)^2 + (R\cos\varphi - \bar{x})^2\right] \cdot \frac{m_l}{R\alpha} \cdot R\mathrm{d}\varphi = \frac{1}{2}m_l \left(R^2 + \bar{x}^2 - \frac{4R\bar{x}\sin\frac{\alpha}{2}}{\alpha}\right) \tag{A.2c}$$

Mass moment of inertia about **u**:

$$I_{l1} = \int_{0}^{\alpha} (R\sin\varphi)^2 \cdot \frac{m_l}{R\alpha} \cdot R\mathrm{d}\varphi = \frac{1}{2}m_{l1}R^2 \left(1 - \frac{\sin\alpha\cos\alpha}{\alpha}\right) \tag{A.3}$$

Appendix B

Partial–differential terms of the SPM Lagrange equation

Time-derived differential terms are given as:

$$\dot{L}_{\theta i} = \frac{1}{2} m_l \bar{x}_l^2 \csc^2 \frac{\alpha_2}{2} \mathbf{n}_i^T \dot{\mathbf{n}}_i + \mathbf{u}_i^T \dot{\mathbf{I}}_{li} \mathbf{u}_i \tag{B.1a}$$

$$\dot{\mathbf{M}}_2 = m_p R^2 \cos^2 \beta [\dot{\mathbf{p}}]_\times^T [\mathbf{p}]_\times + m_p R^2 \cos^2 \beta [\mathbf{p}]_\times^T [\dot{\mathbf{p}}]_\times + \sum_{i=1}^{3} \left(\frac{1}{4} m_l \bar{x}_l^2 \csc^2 \frac{\alpha_2}{2} \dot{\mathbf{L}}_{li} + \dot{\mathbf{R}}_{li} \right) \tag{B.1b}$$

$$\dot{\mathbf{L}}_{li} = [\dot{\mathbf{v}}_i]_\times \mathbf{n}_i \mathbf{j}_i^T + [\mathbf{v}_i]_\times \left([\dot{\mathbf{v}}_i]_\times^T + \dot{\mathbf{n}}_i \mathbf{j}_i^T + \mathbf{n}_i \dot{\mathbf{j}}_i^T \right)$$
$$+ \left([\dot{\mathbf{v}}_i]_\times + \dot{\mathbf{j}}_i \mathbf{n}_i^T + \mathbf{j}_i \dot{\mathbf{n}}_i^T \right) [\mathbf{v}_i]_\times^T + \mathbf{j}_i \mathbf{n}_i^T [\dot{\mathbf{v}}_i]_\times^T \tag{B.1c}$$

$$\dot{\mathbf{R}}_{li} = \left(\dot{\mathbf{j}}_i \mathbf{u}_i^T \mathbf{I}_{li} + \mathbf{j}_i \mathbf{u}_i^T \dot{\mathbf{I}}_{li} + \dot{\mathbf{j}}_{\psi i} \mathbf{w}_i^T \mathbf{I}_{li} + \mathbf{j}_{\psi i} \dot{\mathbf{w}}_i^T \mathbf{I}_{li} + \mathbf{j}_{\psi i} \mathbf{w}_i^T \dot{\mathbf{I}}_{li} \right) \mathbf{w}_i \mathbf{j}_{\psi i}^T$$
$$+ \mathbf{j}_i \mathbf{u}_i^T \mathbf{I}_{li} \left(\dot{\mathbf{w}}_i \mathbf{j}_{\psi i}^T + \mathbf{w}_i \dot{\mathbf{j}}_{\psi i}^T \right) + \left(\dot{\mathbf{j}}_{\psi i} \mathbf{w}_i^T + \mathbf{j}_{\psi i} \dot{\mathbf{w}}_i^T \right) \mathbf{I}_{li} \mathbf{u}_i \mathbf{j}_i^T$$
$$+ \mathbf{j}_{\psi i} \mathbf{w}_i^T \left(\dot{\mathbf{I}}_{li} \mathbf{u}_i \mathbf{j}_i^T + \mathbf{I}_{li} \mathbf{u}_i \dot{\mathbf{j}}_i^T + \mathbf{I}_{li} \dot{\mathbf{w}}_i \mathbf{j}_{\psi i}^T + \mathbf{I}_{li} \mathbf{w}_i \dot{\mathbf{j}}_{\psi i}^T \right) \tag{B.1d}$$

with

$$\dot{\mathbf{n}}_i = \mathbf{u}_i \times \dot{\mathbf{w}}_i \tag{B.2a}$$

$$\dot{\mathbf{I}}_{li} = \dot{\mathbf{E}}_i \mathbf{I}_l \mathbf{E}_i^T + \mathbf{E}_i \mathbf{I}_l \dot{\mathbf{E}}_i^T \tag{B.2b}$$

$$\dot{\mathbf{E}}_i = \left[\begin{array}{ccc} \frac{\dot{\mathbf{w}}_i + \dot{\mathbf{v}}_i}{\|\mathbf{x}_i\|} & \frac{\dot{\mathbf{v}}_i - \dot{\mathbf{w}}_i}{\|\mathbf{y}_i\|} & \frac{\dot{\mathbf{w}}_i \times \mathbf{v}_i + \mathbf{w}_i \times \dot{\mathbf{v}}_i}{\|\mathbf{z}_i\|} \end{array} \right] \tag{B.2c}$$

$$\dot{\mathbf{j}}_i = \frac{\dot{\mathbf{w}}_i \times \mathbf{v}_i + \mathbf{w}_i \times \dot{\mathbf{v}}_i}{(\mathbf{u}_i \times \mathbf{w}_i) \cdot \mathbf{v}_i} - \frac{\mathbf{u}_i \times \dot{\mathbf{w}}_i \cdot \mathbf{v}_i + (\mathbf{u}_i \times \mathbf{w}_i) \cdot \dot{\mathbf{v}}_i}{(\mathbf{u}_i \times \mathbf{w}_i) \cdot \mathbf{v}_i} \mathbf{j}_i \tag{B.2d}$$

$$\dot{\mathbf{j}}_{\psi i} = \frac{\mathbf{u}_i \times \dot{\mathbf{v}}_i}{(\mathbf{u}_i \times \mathbf{v}_i) \cdot \mathbf{w}_i} - \frac{\mathbf{u}_i \times \dot{\mathbf{v}}_i \cdot \mathbf{w}_i + (\mathbf{u}_i \times \mathbf{v}_i) \cdot \dot{\mathbf{w}}_i}{(\mathbf{u}_i \times \mathbf{v}_i) \cdot \mathbf{w}_i} \mathbf{j}_{\psi i} \tag{B.2e}$$

Partial-differential terms with respect to θ_i, $i = 1, 2, 3$, are given by:

$$\frac{\partial \mathbf{n}_i}{\partial \theta_i} = \mathbf{u}_i \times \frac{\partial \mathbf{w}_i}{\partial \theta_i}, \; \frac{\partial \mathbf{w}_i}{\partial \theta_i} = \begin{bmatrix} (c\eta_i c\theta_i + s\eta_i c\gamma s\theta_i)s\alpha_1 \\ (s\eta_i c\theta_i - c\eta_i c\gamma s\theta_i)s\alpha_1 \\ -s\gamma s\theta_i s\alpha_1 \end{bmatrix} \tag{B.3a}$$

$$\frac{\partial \mathbf{I}_{li}}{\partial \theta_i} = \frac{\partial \mathbf{E}_i^T}{\partial \theta_i}\mathbf{I}_l\mathbf{E}_i + \mathbf{E}_i^T\mathbf{I}_l\frac{\partial \mathbf{E}_i}{\partial \theta_i}, \; \frac{\partial \mathbf{E}_i}{\partial \theta_i} = \begin{bmatrix} \frac{\frac{\partial \mathbf{w}_i}{\partial \theta_i}}{\|\mathbf{x}_i\|} & -\frac{\frac{\partial \mathbf{w}_i}{\partial \theta_i}}{\|\mathbf{y}_i\|} & \frac{\frac{\partial \mathbf{w}_i}{\partial \theta_i} \times \mathbf{v}_i}{\|\mathbf{z}_i\|} \end{bmatrix} \tag{B.3b}$$

$$\frac{\partial \mathbf{L}_{li}}{\partial \theta_i} = [\mathbf{v}_i]_\times \left(\frac{\partial \mathbf{n}_i}{\partial \theta_i}\mathbf{j}_i^T + \mathbf{n}_i\frac{\partial \mathbf{j}_i^T}{\partial \theta_i} \right) + \left(\frac{\partial \mathbf{j}_i}{\partial \theta_i}\mathbf{n}_i^T + \mathbf{j}_i\frac{\partial \mathbf{n}_i^T}{\partial \theta_i} \right)[\mathbf{v}_i]_\times^T \tag{B.3c}$$

$$\begin{aligned}\frac{\partial \mathbf{R}_{li}}{\partial \theta_i} &= \left(\frac{\partial \mathbf{j}_i}{\partial \theta_i}\mathbf{u}_i^T\mathbf{I}_{li} + \mathbf{j}_i\mathbf{u}_i^T\frac{\partial \mathbf{I}_{li}}{\partial \theta_i} + \frac{\partial \mathbf{j}_{\psi i}}{\partial \theta_i}\mathbf{w}_i^T\mathbf{I}_{li} + \mathbf{j}_{\psi i}\frac{\partial \mathbf{w}_i^T}{\partial \theta_i}\mathbf{I}_{li} + \mathbf{j}_{\psi i}\mathbf{w}_i^T\frac{\partial \mathbf{I}_{li}}{\partial \theta_i} \right)\mathbf{w}_i\mathbf{j}_{\psi i}^T \\ &\quad + \mathbf{j}_i\mathbf{u}_i^T\mathbf{I}_{li}\left(\frac{\partial \mathbf{w}_i}{\partial \theta_i}\mathbf{j}_{\psi i}^T + \frac{\partial \mathbf{j}_{\psi i}^T}{\partial \theta_i} \right) + \left(\frac{\partial \mathbf{j}_{\psi i}}{\partial \theta_i}\mathbf{w}_i^T + \mathbf{j}_{\psi i}\frac{\partial \mathbf{w}_i^T}{\partial \theta_i} \right)\mathbf{I}_{li}\mathbf{u}_i\mathbf{j}_i^T \\ &\quad + \mathbf{j}_{\psi i}\mathbf{w}_i^T\left(\frac{\partial \mathbf{I}_{li}}{\partial \theta_i}\mathbf{u}_i\mathbf{j}_i^T + \mathbf{I}_{li}\mathbf{u}_i\frac{\partial \mathbf{j}_i^T}{\partial \theta_i} + \mathbf{I}_{li}\frac{\partial \mathbf{w}_i}{\partial \theta_i}\mathbf{j}_{\psi i}^T + \mathbf{I}_{li}\mathbf{w}_i\frac{\partial \mathbf{j}_{\psi i}^T}{\partial \theta_i} \right)\end{aligned} \tag{B.3d}$$

$$\frac{\partial \mathbf{j}_i}{\partial \theta_i} = \frac{\frac{\partial \mathbf{w}_i}{\partial \theta_i} \times \mathbf{u}_i}{\mathbf{u}_i \times \mathbf{w}_i \cdot \mathbf{v}_i} - \frac{\mathbf{u}_i \times \frac{\partial \mathbf{w}_i}{\partial \theta_i} \cdot \mathbf{v}_i}{\mathbf{u}_i \times \mathbf{w}_i \cdot \mathbf{v}_i}\mathbf{j}_i \tag{B.3e}$$

$$\frac{\partial \mathbf{j}_{\psi i}}{\partial \theta_i} = -\frac{\mathbf{u}_i \times \mathbf{v}_i \cdot \frac{\partial \mathbf{w}_i}{\partial \theta_i}}{\mathbf{u}_i \times \mathbf{v}_i \cdot \mathbf{w}_i} \tag{B.3f}$$

Partial-differential terms with respect to μ, $\mu \in \{\phi, \theta, \sigma\}$, are expressed as:

$$\frac{\partial \mathbf{p}}{\partial \mu} = \frac{\partial \mathbf{Q}}{\partial \mu}\mathbf{k}, \; \frac{\partial \mathbf{v}_i}{\partial \mu} = \frac{\partial \mathbf{Q}}{\partial \mu}\mathbf{v}_i^* \tag{B.4a}$$

$$\frac{\partial \mathbf{I}_{li}}{\partial \mu} = \frac{\partial \mathbf{E}_i^T}{\partial \mu}\mathbf{I}_l\mathbf{E}_i + \mathbf{E}_i^T\mathbf{I}_l\frac{\partial \mathbf{E}_i}{\partial \mu}, \; \frac{\partial \mathbf{E}_i}{\partial \mu} = \begin{bmatrix} \frac{\frac{\partial \mathbf{v}_i}{\partial \mu}}{\|\mathbf{x}_i\|} & \frac{\frac{\partial \mathbf{v}_i}{\partial \mu}}{\|\mathbf{y}_i\|} & \frac{\mathbf{w}_i \times \frac{\partial \mathbf{v}_i}{\partial \mu}}{\|\mathbf{z}_i\|} \end{bmatrix} \tag{B.4b}$$

$$\frac{\partial \mathbf{M}_2}{\partial \mu} = m_p R^2 \cos^2\beta \left(\left[\frac{\partial \mathbf{p}}{\partial \mu}\right]_\times^T [\mathbf{p}]_\times + [\mathbf{p}]_\times^T \left[\frac{\partial \mathbf{p}}{\partial \mu}\right]_\times \right) + \sum_{i=1}^3 \left(\frac{1}{4}\csc^2\frac{\alpha_2}{2}m_l\bar{x}_l^2\frac{\mathbf{L}_{li}}{\partial \mu} + \frac{\mathbf{R}_{li}}{\partial \mu} \right) \tag{B.4c}$$

$$\frac{\partial \mathbf{L}_{li}}{\partial \mu} = \left[\frac{\partial \mathbf{v}_i}{\partial \mu}\right]_\times ([\mathbf{v}_i]_\times^T + \mathbf{n}_i\mathbf{j}_i^T) + ([\mathbf{v}_i]_\times + \mathbf{j}_i\mathbf{n}_i^T)\left[\frac{\partial \mathbf{v}_i}{\partial \mu}\right]_\times^T + [\mathbf{v}_i]_\times \mathbf{n}_i\frac{\partial \mathbf{j}_i^T}{\partial \mu} + \frac{\partial \mathbf{j}_i}{\partial \mu}\mathbf{n}_i^T[\mathbf{v}_i]_\times^T \tag{B.4d}$$

$$\begin{aligned}\frac{\partial \mathbf{R}_{li}}{\partial \mu} &= \left(\frac{\partial \mathbf{j}_i}{\partial \mu}\mathbf{u}_i^T\mathbf{I}_{li} + \mathbf{j}_i\mathbf{u}_i^T\frac{\mathbf{I}_{li}}{\partial \mu} + \frac{\partial \mathbf{j}_{\psi i}}{\partial \mu}\mathbf{w}_i^T\mathbf{I}_{li} + \mathbf{j}_{\psi i}\mathbf{w}_i^T\frac{\mathbf{I}_{li}}{\partial \mu} \right)\mathbf{w}_i\mathbf{j}_{\psi i}^T + \mathbf{j}_i\mathbf{u}_i^T\mathbf{I}_{li}\mathbf{w}_i\frac{\partial \mathbf{j}_{\psi i}^T}{\partial \mu} \\ &\quad + \left(\frac{\partial \mathbf{j}_{\psi i}}{\partial \mu}\mathbf{w}_i^T\mathbf{I}_{li} + \mathbf{j}_{\psi i}\mathbf{w}_i^T\frac{\mathbf{I}_{li}}{\partial \mu} \right)\mathbf{u}_i\mathbf{j}_i^T + \mathbf{j}_{\psi i}\mathbf{w}_i^T\mathbf{I}_{li}\left(\mathbf{u}_i\frac{\partial \mathbf{j}_i^T}{\partial \mu} + \mathbf{w}_i\frac{\partial \mathbf{j}_{\psi i}^T}{\partial \mu} \right)\end{aligned} \tag{B.4e}$$

$$\frac{\partial \mathbf{j}_i}{\partial \mu} = \frac{\mathbf{w}_i \times \frac{\partial \mathbf{v}_i}{\partial \mu}}{\mathbf{u}_i \times \mathbf{w}_i \cdot \mathbf{v}_i} - \frac{\mathbf{u}_i \times \mathbf{w}_i \cdot \frac{\partial \mathbf{v}_i}{\partial \mu}}{\mathbf{u}_i \times \mathbf{w}_i \cdot \mathbf{v}_i}\mathbf{j}_i \tag{B.4f}$$

$$\frac{\partial \mathbf{j}_{\psi i}}{\partial \mu} = \frac{\mathbf{u}_i \times \frac{\partial \mathbf{v}_i}{\partial \mu}}{\mathbf{u}_i \times \mathbf{v}_i \cdot \mathbf{w}_i} - \frac{\mathbf{u}_i \times \frac{\partial \mathbf{v}_i}{\partial \mu} \cdot \mathbf{w}_i}{\mathbf{u}_i \times \mathbf{v}_i \cdot \mathbf{w}_i}\mathbf{j}_{\psi i} \tag{B.4g}$$

Bibliography

[1] Epson SCARA G10. URL `http://www.directindustry.com/prod/epson-factory-automation/scara-robots-13733-431849.html`.

[2] ABB Co. ABB FlexPicker. URL `http://www.abb.com/product/seitp327`.

[3] J.-P. Merlet. *Parallel Robots*. Kluwer, Norwell, 2006.

[4] J. Angeles. *Fundamentals of Robotic Mechanical Systems: Theory, Methods, and Algorithms*. Springer, NY, USA, 2007.

[5] V.E. Gough. Contribution to discussion to papers on research in automobile stability and control and in tyre performance. *Proc. Auto. Div. Instn. Mech. Eng.*, pages 392–394, 1956–1957.

[6] D. Stewart. A platform with six degrees of freedom. *Proc. Ins. Mech. Eng.*, 180: 371–378, 1965.

[7] C.C. Nguyen, S.S. Antrazi, Z.-L. Zhou, and C.E. Campbell. Adaptive control of a stewart platform-based manipulator. *J. Robotic Syst.*, 10(5):657–687, 1993.

[8] T. Akima, S. Tarao, and M. Uchiyama. Hybrid micro-gravity simulator consisting of a high-speed parallel robot. In *IEEE International Conference on Robotics and Automation*, pages 901–906, 1999.

[9] J. Ares, A. Brazales, and J.M. Busturia. Tuning and validation of the motion platform washout filter parameters for a driving simulator. In *Driving simulation conference*, pages 295–304, Sophia-Antipolis, Sept. 2001.

[10] M.K. Park, M.C. Lee, K.S. Yoo, K. Son, W.S. Yoo, and M.C. Han. Development of the PNU vehicle driving simulator and its performance evaluation. In *Proceedings of the IEEE International Conference on Robotics and Automation*, pages 2325–2330, 2001.

[11] J.Y. Huang and C.Y. Gau. A PC cluster high-fidelity mobile crane simulator. *Tamkang J. Sci. Eng.*, 5(1):7–20, 2002.

[12] I. Hostens, J. Anthonis, and H. Ramon. New design for a 6 dof vibration simulator with improved reliability and performance. *Mech. Syst. Signal Pr.*, 19(1):105–122, 2005.

[13] D. Wu and H. Gu. Adaptive sliding control of six-DOF flight simulator motion platform. *Chinese Journal of Aeronautics*, 20(5):425–433, 2007.

[14] H. Kondo, Y. Tanaka, Y. Shiga, and H. Goto. Prototype model of tripod parallel mechanism with planar actuators for flight simulator. In *International Conference on Fluid Power and Mechatronics*, pages 528–533, Aug. 2011.

[15] W. Dong, Z. Du, Y. Xiao, and X. Chen. Development of a parallel kinematic motion simulator platform. *Mechatronics*, 23(1):154–161, 2013.

[16] T. Li and S. Payandeh. Design of spherical parallel mechanisms for application to laparoscopic surgery. *Robotica*, 20(2):133–138, 2002.

[17] L.E. Bruzzone and R. Molfino. Special-purpose parallel robot for active suspension of ambulance stretchers. *Int. J. Robot. Autom.*, 18(3):121–129, 2003.

[18] M. Shoham, M. Burman, E. Zehavi, L. Joskowicz, E. Batkilin, and Y. Kunicher. Bone-mounted miniature robot for surgical procedures: concept and clinical applications. *IEEE T. Robotic. Autom.*, 19(5):893–901, 2003.

[19] M. Wapler, V. Urban, T. Weisener, J. Stallkamp, M. Dürr, and A. Hiller. A stewart platform for precision surgery. *T. I. Meas. Control*, 25(4):329–334, 2003.

[20] G. Carbone and M. Ceccarelli. A serial-parallel robotic architecture for surgical tasks. *Robotica*, 23(3):345–354, 2005.

[21] G. Rosati, P. Gallina, and S. Masiero. Design, implementation and clinical test of a wirebased robot for neuro rehabilitation. *IEEE T. Neural Syst. Rehabil. Eng.*, 15(4):560–569, 2007.

[22] Mitchell J. H. Lum, Diana C.W. Friedman, G. Sankaranarayanan, H. King, K. Fodero, R. Leuschke, B. Hannaford, J. Rosen, and M.N. Sinanan. The RAVEN: Design and validation of a telesurgery system. *Int. J. Robotic. Res.*, 28(9):1183–1197, 2009.

[23] J.-P. Merlet and D. Daney. A portable, modular parallel wire crane for rescue operations. In *IEEE International Conference on Robotics and Automation*, pages 2834–2839, may 2010.

[24] S. Khan, K. Andersson, and J. Wikander. Optimal design of a 6-Dof haptic device. In *IEEE International Conference on Mechatronics*, pages 713–718, April 2011.

[25] C. Chen, T. Gayral, S. Caro, D. Chablat, G. Moroz, and S. Abeywardena. A six degree of freedom epicyclic-parallel manipulator. *ASME J. Mech. Rob.*, 4(4): 041011(1–8), 2012.

[26] G.S. Chirikjian. Hyper-redundant manipulator dynamics: a continuum approximation. *Adv. Robotics*, 9(3):217–243, 1995.

[27] G.J. Hamlin and A.C. Sanderson. TETROBOT: a modular approach to parallel robotics. *IEEE Rob. Auto. Mag.*, 4(1):42–50, 1997.

[28] L.J. Xu, S.W. Fan, and H. Li. Analytical model method for dynamics of n-celled tetrahedron variable geometry truss manipulators. *Mech. Mach. Theory*, 36, 2001.

[29] M. Hafez, M.D. Lichter, and S. Dubowsky. Optimized binary modular reconfigurable robotic devices. *IEEE/ASME T. Mech.*, 8(1):18–25, 2003.

[30] V.A. Sujan and S. Dubowsky. Design of lightweight hyper-redundant deployable binary manipulator. *ASME J. Mech. Des.*, 126(1):29–39, 2004.

[31] A. Romiti and M. Sorli. Force and moment measurement on a robotic assembly hand. *Sensor. Actuat. A-Phys*, 32(1-3):531–538, 1992.

[32] M. Sorli and S. Pastorelli. Six-axis reticulated structure force/torque sensor with adaptable performances. *Mechatronics*, 5(6):585–601, 1995.

[33] T.A. Dwarakanath, B. Dasgupta, and T.S. Mruthyunjaya. Design and development of a stewart platform based force–torque sensor. *Mechatronics*, 11(7): 793–809, 2001.

[34] Z. Jin, F. Gao, and X. Zhang. Design and analysis of a novel isotropic six-component force/torque sensor. *Sensor. Actuat. A-Phys*, 109(1–2):17–20, 2003.

[35] R. Ranganath, P.S. Nair, T.S. Mruthyunjaya, and A. Ghosal. A force-torque sensor based on a stewart platform in a near-singular configuration. *Mech. Mach. Theory*, 39(9):971–998, 2004.

[36] T.A. Dwarakanath and D. Venkatesh. Simply supported, 'joint less' parallel mechanism based force-torque sensor. *Mechatronics*, 16(9):565–575, 2006.

[37] Y.-J. Li, B.-Y. Sun, J. Zhang, M. Qian, and Z.-Y. Jia. A novel parallel piezoelectric six-axis heavy force/torque sensor. *Measurement*, 42(5):730–736, 2009.

[38] Z. Gao and D. Zhang. Design, analysis and fabrication of a multidimensional acceleration sensor based on fully decoupled compliant parallel mechanism. *Sensor. Actuat. A-Phys*, 163(1):418–427, 2010.

[39] V.T. Portman, B.Z. Sandler, and E. Zahavi. Rigid 6×6 parallel platform for precision 3-D micromanipulation: theory and design application. *IEEE T. Robotic. Autom.*, 16(6):629–643, 2000.

[40] B.-J. Yi, G.B. Chung, H.Y. Na, W.K. Kim, and I.H. Suh. Design and experiment of a 3-dof parallel micromechanism utilizing flexure hinges. *IEEE T. Robotic. Autom.*, 19(4):604–612, 2003.

[41] M.L. Culpepper and G. Anderson. Design of a low-cost nano-manipulator which utilizes a monolithic, spatial compliant mechanism. *J. Precis. Eng.*, 28(4):469–482, 2004.

[42] M.L. Culpepper, M.V. Kartik, and C. DiBiasio. Design of integrated mechanisms and exact constraint fixtures for micron-level repeatability and accuracy. *J. Precis. Eng.*, 29(1):65–80, 2005.

[43] K.A. Jensen, C.P. Lusk, and L.L. Howell. An XYZ micromanipulator with three translational degrees of freedom. *Robotica*, 24(3):305–314, 2006.

[44] Q.S. Xu and Y.M. Li. A novel design of a 3-PRC compliant parallel micromanipulator for nanomanipulation. *Robotica*, 24(4):521–528, 2006.

[45] H.D. Taghirad and M. Nahon. Kinematic analysis of a macrocmicro redundantly actuated parallel manipulator. *Adv. Robotics*, 22(6-7):657–687, 2008.

[46] C. Flynn, A. Taberner, and P. Nielsen. Mechanical characterisation of in vivo human skin using a 3D force-sensitive micro-robot and finite element analysis. *Biomechanics and Modeling in Mechanobiology*, 10:27–38, 2011.

[47] P. Bailey. The merits of hexapods for robotics applications. In *Conference on Next Steps for Industrial Robotics*, pages 11–16, 1994.

[48] R.B. Aronson. Hexapods: Hot or ho hum? *Manuf. Eng.*, 10:60–67, 1997.

[49] J. Hollingum. Features: Hexapods to take over? *Ind. Robot*, 24:428–431, 1997.

[50] G. Matar. Hexapod: application-led technology. *Prototyping Technology International*, pages 70–72, 1997.

[51] G. Pritschow and K.H. Wurst. Systematic design of hexapods and other parallel link systems. *CIRP Ann. Manuf. Tech.*, 46(1):291–295, 1997.

[52] I. Bonev. Delta parallel robot–the story of success. 2001. URL `http://www.parallemic.org/Reviews/Review002`.

[53] Adept quattro parallel robot. URL `http://www.adept.com/products/robots/parallel/quattro-s650h/general`.

[54] E. Ozgur, N. Bouton, N. Andreff, and P. Martinet. Dynamic control of the quattro robot by the leg edges. In *Proceedings of the IEEE International Conference on Robotics and Automation*, pages 2731–2736, Shanghai, China, 2011.

[55] ABB IRB 940 Tricept. URL `http://www.wood-unlimited.com/doc/DatenRoboter/Datenblatt%20IRB%20940%2003.pdf`.

[56] A. Joubair, M. Slamani, and I.A. Bonev. A novel XY-Theta precision table and a geometric procedure for its kinematic calibration. *Robot. CIM-Manuf.*, 28(1): 57–65, 2012.

[57] C.M. Gosselin and J.F. Hamel. The Agile Eye: a high-performance three-degree-of-freedom camera-orienting device. In *IEEE International Conference on Robotics and Automation*, pages 781–786, 1994.

[58] P. Wenger and D. Chablat. Kinematic analysis of a new parallel machine-tool: the Orthoglide. In J. Lenarčič and M.M. Stanišić, editors, *Advances in Robot Kinematics*, pages 305–314. Kluwer Academic Publishers, 2000.

[59] M.K. Lee. Design of a high stiffness machining robot arm using double parallel mechanisms. In *IEEE International Conference on Robotics and Automation*, volume 1, pages 234–240, Nagoya, Japan, may 1995.

[60] H. Asada and J. Granito. Kinematic and static characterization of wrist joints and their optimal design. In *IEEE International Conference on Robotics and Automation*, pages 244–250, 1985.

[61] Agile Wrist by McGill University. URL `http://www.cim.mcgill.ca/~rmsl/Index/M3.htm`.

[62] Z. Kadivar, J.L. Sullivan, D.P. Eng, A.U. Pehlivan, M.K. O'Malley, N. Yozbatiran, and G.E. Francisco. RiceWrist robotic device for upper limb training: Feasibility study and case report of two tetraplegic persons with spinal cord injury. *Inter. J. Biolo. Eng.*, 2(4):27–38, 2012.

[63] Goniometer Micro-Positioner, PI, US. URL `http://www.micropositioning.net/linear_precision_positioning_stages.php`.

[64] M. Ceccarelli. A new 3 D.O.F. spatial parallel mechanism. *Mech. Mach. Theory*, 32(8):895–902, 1997.

[65] J.-P. Merlet. Optimal design for the micro parallel robot MIPS. In *IEEE International Conference on Robotics and Automation*, volume 2, pages 1149–1154, 2002.

[66] K.H. Hunt. Structural kinematics of in-parallel-actuated robot-arms. *J. Mech., Transmiss., Automat. Des.*, 105(4):705–712, 1983.

[67] Project *Dockwelder*. URL `http://www.maritimetransportresearch.com/site/project/5`.

[68] P.D. Lin and J.F. Chen. Accuracy analysis of planar linkages by the matrix method. *Mech. Mach. Theory*, 35(5):507–516, 1992.

[69] J. Carusone and G.M. D'Eleuterio. Tracking control for end-effector position and orientation of structurally flexible manipulators. *J. Robotic. Syst.*, 10(6):847–870, 1993.

[70] H. Zhuang. Self-calibration of parallel mechanisms with a case study on stewart platforms. *IEEE T. Robotic. Autom.*, 13(3):387–397, 1997.

[71] K. Ting, J. Zhu, and D. Watkins. The effects of joint clearance on position and orientation deviation of linkages and manipulators. *Mech. Mach. Theory*, 35(3): 391–401, 2000.

[72] P. Voglewede and I. Uphoff. Application of workspace generation techniques to determine the unconstrained motion of parallel manipulators. *ASME J. Mech. Des.*, 126(2):283–290, 2004.

[73] S. Venanzi and V.P. Castelli. A new technique for clearance influence analysis in spatial mechanisims. *ASME J. Mech. Des.*, 127(3):446–455, 2005.

[74] URL `http://www.machinerylubrication.com/Read/754/oil-whirl-whip`.

[75] URL `http://www.thk.com/?q=eng/node/237`.

[76] URL `http://www.uspto.gov/web/patents/classification/uspc901/defs901.htm`.

[77] T. Jinriki and F. Kozawa. Wrist mechanism for industrial robot. In *EUROPEAN PATENT EP 0 200 202 A2*.

[78] R.E. Garrett and Jr. A.S. Hall. Effect of tolerance and clearance in linkage design. *ASME J. Eng. Ind.*, 91(2):198–202, 1969.

[79] S.G. Dhande and J. Chakraborty. Analysis and synthesis of mechanical error in linkages-a stochastic approach. *ASME J. Eng. Ind.*, 95(8):672–676, 1973.

[80] J. Chakraborty. Synthesis of mechanical error in linkages. *Mech. Mach. Theory*, 10(2-3):155–165, 1975.

[81] S. Dhande and J. Chackraborty. Mechanical error analysis of spatial linkages. *ASME J. Mech. Des.*, 100(4):732–738, 1978.

[82] J.H. Rhyu and B.M. Kwak. Optimal stochastic design of four-bar mechanisms for tolerance and clearance. *ASME J. Mech. Transm.*, 110(3):255–262, 1988.

[83] W. Xu and Q. Zhang. Probabilistic analysis and Monte Carlo simulation of the kinematic error in a spatial linkage. *Mech. Mach. Theory*, 24(1):19–27, 1989.

[84] S.J. Lee and B.J. Gilmore. The determination of the probabilistic properties of velocities and accelerations in kinematic chains with uncertainty. *ASME J. Mech. Des.*, 113(3):84–90, 1991.

[85] J. Zhu and K.-L. Ting. Uncertainty analysis of planar and spatial robots with joint clearances. *Mech. Mach. Theory*, 35(9):1239–1256, 2000.

[86] R. Hartenberg and J. Denavit. *Kinematic Synthesis of Linkages*. McGraw-Hill, New York, 1964.

[87] A. Fogarasy and M. Smith. The influence of manufacturing tolerance on the kinematic performance of mechanisms. *Proc. Inst. Mech. Eng. Part C: Mech. Eng. Sci.*, 212(1):35–47, 1998.

[88] S. Venanzi. Methods for clearance influence analysis in planar and spatial mechanisms. Ph.D. dissertation, University of Bologna, 2004.

[89] V.P. Castelli and S. Venanzi. Clearance influence analysis on mechanisms. *Mech. Mach. Theory*, 40(12):1316–1329, 2005.

[90] H. Bamberger, M. Shoham, and A. Wolf. Kinematics of micro planar parallel robot comprising large joint clearances. In Jadran Lennarčič and B. Roth, editors, *Advances in Robot Kinematics*, pages 75–84. Springer Netherlands, 2006.

[91] J. Meng, D. Zhang, and Z. Li. Accuracy analysis of parallel manipulators with joint clearance. *ASME J. Mech. Des.*, 131(1):011013(1–9), 2009.

[92] N. Binaud, P. Cardou, S. Caro, and P. Wenger. The kinematic sensitivity of robotic manipulators to joint clearance. In *Proceedings of ASME Design Engineering Technical Conferences*, pages 1371–1380, Montreal, QC., Canada, 2010.

[93] N. Binaud, S. Caro, S. Bai, and P. Wenger. Comparison of 3-PPR parallel planar manipulators based on their sensitivity to joint clearances. In *Proceedings of*

IEEE/RSJ International Conference on Intelligent Robots and Systems (IROS), pages 2778–2783, Taipei, Taiwan, 2010.

[94] A. Chaker, A. Mlika, M.A. Laribi, L. Romdhane, and S. Zeghloul. Clearance, manufacturing errors effects on the accuracy of the 3-RCC spherical parallel manipulators. In V. Padois, P. Bidaud, and O. Khatib, editors, *Romansy 19–Robot Design, Dynamics and Control*, volume 544 of *CISM International Centre for Mechanical Sciences*, pages 27–34. Springer Vienna, 2013.

[95] S.R. Lim, K.W. Kang, S.C. Park, W.C. Choi, J.B. Song, D.H. Hong, and J.K. Shim. Error analysis of a parallel mechanism considering link stiffness and joint clearances. *J. Mech. Sci. Tech.*, 16(6):799–809, 2002.

[96] J. Aginaga, O. Altuzarra, E. Macho, and J. Olza. Accuracy analysis considering clearances and elastic deformations in parallel manipulators. In *ASME 2011 International Design Engineering Technical Conferences and Computers and Information in Engineering Conference (IDETC/CIE2011)*, pages 387–394, Washington, DC, USA, August 2011.

[97] W. Wei and N. Simaan. Design of planar parallel robots with preloaded flexures for guaranteed backlash prevention. *ASME J. Mech. Rob.*, 2(1):011012(1–10), 2010.

[98] J. Kotlarski, H. Abdellatif, and B. Heimann. Improving the pose accuracy of a planar 3RRR parallel manipulator using kinematic redundancy and optimized switching patterns. In *IEEE International Conference on Robotics and Automation*, pages 3863–3868, May 2008.

[99] H. Asada and J.-J.E. Slotine. *Robot Analysis and Control*. John Wiley & Sons, 1986.

[100] J. Kenneth Salisbury. Active stiffness control of a manipulator in Cartesian coordinates. In *19th IEEE Conference on Decision and Control including the Symposium on Adaptive Processes*, volume 19, pages 95–100, 1980.

[101] C. Gosselin. Stiffness mapping for parallel manipulators. *IEEE T. Robotic. Autom.*, 6(3):377–382, 1990.

[102] B.S. El-Khasawneh and P.M. Ferreira. Computation of stiffness and stiffness bounds for parallel link manipulators. *Int. J. Mach. Tool. Manu.*, 39(6):321–342, 1999.

[103] S.F. Chen and I. Kao. Conservative congruence transformation for joint and cartesian stiffness matrices of robotic hands and fingers. *Int. J. Robtic. Res.*, 19(9): 835–847, 2000.

[104] M. Ceccarelli and G. Carbone. A stiffness analysis for CaPaMan (Cassino Parallel Manipulator). *Mech. Mach. Theory*, 37(5):427–439, 2002.

[105] G. Alici and B. Shirinzadeh. Enhanced stiffness modeling, identification and characterization for robot manipulators. *IEEE T. Robotic.*, 21(4):554–564.

[106] F. Majou, C. Gosselin, P. Wenger, and D. Chablat. Parametric stiffness analysis of the orthoglide. *Mech. Mach. Theory*, 42(3):296–311, 2007.

[107] J. Kövecses and J. Angeles. The stiffness matrix in elastically articulated rigid-body systems. *Multibody Syst. Dyn.*, 18:169–184, 2007.

[108] C. Quennouelle and C.M. Gosselin. Stiffness matrix of compliant parallel mechanisms. In J. Lenarčič and P. Wenger, editors, *Advances in Robot Kinematics: Analysis and Design*, pages 331–341. Springer Netherlands, 2008.

[109] A. Pashkevich, D. Chablat, and P. Wenger. Stiffness analysis of overconstrained parallel manipulators. *Mech. Mach. Theory*, 44(5):966–982, 2009.

[110] J. Angeles. On the nature of the cartesian stiffness matrix. *Revista de la Sociedad Mexicana de Ingenieria Mecáica*, pages 163–170, 2010.

[111] D. Zhang. Kinetostatic analysis and optimization of parallel and hybrid architectures for machine tools. Ph.D. dissertation, Laval University, 2000.

[112] C.M. Gosselin and D. Zhang. Stiffness analysis of parallel mechanisms using a lumped model. *Int. J. Robot. Autom.*, 17(1):17–27, 2010.

[113] H.K. Arumugam, R.M. Voyles, and S. Bapat. Stiffness analysis of a class of parallel mechanisms for micro-positioning applications. In *Proceedings of 2004 IEEE/RSJ International Conference on Intelligent Robots and Systems (IROS 2004).*, volume 2, pages 1826–1831, 2004.

[114] D. Zhang, F. Xi, C.M. Mechefske, and S. Y.T Lang. Analysis of parallel kinematic machine with kinetostatic modelling method. *Robot. Cim-Int. Manuf.*, 20(2):151–165, 2004.

[115] R. Vertechy and V. Parenti-Castelli. Static and stiffness analyses of a class of over-constrained parallel manipulators with legs of type US and UPS. In *2007 IEEE International Conference on Robotics and Automation*, april 2007.

[116] D. Zhang. *Parallel Robotic Machine Tools*. Springer, New York, NY, 2009.

[117] J.K. Davidson and K.H. Hunt. *Robots and Screw Theory: Applications of Kinematics and Statics to Robotics*. Oxford University Press, 2004.

[118] X. Kong and C.M. Gosselin. *Type Synthesis of Parallel Mechanisms*. Springer-Verlag Berlin Heidelberg, 2007.

[119] S. Caro, D. Chablat, R. Ur-Rehman, and P. Wenger. Multiobjective design optimization of 3-PRR planar parallel manipulators. In A. Bernard, editor, *Global Product Development*, pages 373–383. Springer-Verlag Berlin Heidelberg, 2011.

[120] X.J. Liu, Z.L. Jin, and F. Gao. Optimum design of 3-dof spherical parallel manipulators with respect to the conditioning and stiffness indices. *Mech. Mach. Theory*, 35(9):1257–1267, 2000.

[121] A. Pashkevich, D. Chablat, and P. Wenger. Design optimization of parallel manipulators for high-speed precision machining applications. In *13th IFAC Symposium on Information Control Problems in Manufacturing*, Moscow, Russia, June 2009.

[122] L.-W. Tsai and S. Joshi. Kinematics and optimization of a spatial 3-UPU parallel manipulator. *ASME J. Mech. Des.*, 122(4):439–446, 2000.

[123] J.A. Carretero, R.P. Podhorodeski, M.A. Nahon, and C.M. Gosselin. Kinematic analysis and optimization of a new three degree-of-freedom spatial parallel manipulator. *ASME J. Mech. Des.*, 122(1):17–24, 2000.

[124] D. Chablat and P. Wenger. Architecture optimization of a 3-dof translational parallel mechanism for machining applications, the orthoglide. *IEEE T. Robotic. Autom.*, 19(3):403–410, 2003.

[125] J.-P. Merlet. Designing a parallel manipulator for a specific workspace. *Int. J. Robotic. Res.*, 16:545–556, 1997.

[126] V. Parenti-Castelli, R.Di Gregorio, and F. Bubani. Workspace and optimal design of a pure translation parallel manipulator. *Meccanica*, 35:203–214, 2000.

[127] M. Stock and K. Miller. Optimal kinematic design of spatial parallel manipulators: Application of linear delta robot. *ASME J. Mech. Des.*, 125(2):292–301, 2003.

[128] A.M. Hay and J.A. Snyman. Methodologies for the optimal design of parallel manipulators. *Int. J. Numer. Meth. Eng.*, 59(11):131–152, 2004.

[129] K. Miller. Optimal design and modeling of spatial parallel manipulators. *Int. J. Robotic. Res.*, 23:127–140, 2004.

[130] Y. Lou, G. Liu, N. Chen, and Z. Li. Optimal design of parallel manipulators for maximum effective regular workspace. In *Proceedings of the IEEE/RSJ International Conference on Intelligent Robots and Systems*, pages 795–800, Alberta, 2005.

[131] O. Altuzarra, O. Salgado, A. Hernandez, and J. Angeles. Multiobjective optimum design of a symmetric parallel schönflies-motion generator. *ASME J. Mech. Des.*, 131(3):031002(1–11), 2009.

[132] J.S. Hemmerle and F.B. Prinz. Optimal path placement for kinematically redundant manipulators. In *IEEE International Conference on Robotics and Automation*, volume 2, pages 1234–1244, Apr. 1991.

[133] J. Ryu and J. Cha. Volumetric error analysis and architecture optimization for accuracy of hexaslide type parallel manipulators. *Mech. Mach. Theory*, 38(3): 227–240, 2003.

[134] G. Alici and B. Shirinzadeh. Topology optimisation and singularity analysis of a 3-SPS parallel manipulator with a passive constraining spherical joint. *Mech. Mach. Theory*, 39(2):215–235, 2004.

[135] C.M. Gosselin and J. Angeles. The optimum kinematic design of a spherical three-degree-of-freedom parallel manipulator. *ASME J. Mech., Trans., and Auto. in Des.*, 111, 1989.

[136] C.M. Gosselin and J. Angeles. A global performance index for the kinematic optimization of robotic manipulators. *ASME J. Mech. Des.*, 113(3):220–226, 1991.

[137] F. Ranjbaran, J. Angeles, M.A. González-Palacios, and R.V. Patel. The mechanical design of a seven-axes manipulator with kinematic isotropy. *J. Inte. Rob. Syst.*, 14:21–41, 1995.

[138] K.E. Zanganeh and J. Angeles. Kinematic isotropy and the optimum design of parallel manipulators. *Int. J. Robotic. Res.*, 16:185–197, 1997.

[139] T. Huang, M. Li, Z. Li, D.G. Chetwynd, and D.J. Whitehouse. Optimal kinematic design of 2-dof parallel manipulators with well-shaped workspace bounded by a specified conditioning index. *IEEE T. Robot. Autom.*, 20(3):538–543, 2004.

[140] S. Bai. Optimum design of spherical parallel manipulator for a prescribed workspace. *Mech. Mach. Theory*, 45(2):200–211, 2010.

[141] N.A. Aspragathos and S. Foussias. Optimal location of a robot path when considering velocity performance. *Robotica*, 20:139–147, 2002.

[142] S.B. Nokleby, R. Fisher, R.P. Podhorodeski, and F. Firmani. Force capabilities of redundantly-actuated parallel manipulators. *Mech. Mach. Theory*, 40(5):578–599, 2005.

[143] H.S. Kim and L.-W. Tsai. Design optimization of a Cartesian parallel manipulator. *ASME J. Mech. Des.*, 125(1):43–51, 2003.

[144] Z. Gao, D. Zhang, X. Hu, and Y. Ge. Design, analysis, and stiffness optimization of a three degree of freedom parallel manipulator. *Robotica*, 28:349–357, 2010.

[145] Z. Chi and D. Zhang. Stiffness optimization of a novel reconfigurable parallel kinematic manipulator. *Robotica*, 30:433–447, 2012.

[146] D. Chablat, S. Caro, R. Ur-Rehman, and P. Wenger. Comparison of planar parallel manipulator architectures based on a multi-objective design optimization approach. In *Proceedings of the ASME International Design Engineering Technical Conferences & Computers and Information in Engineering Conference*, Montreal, QC., Canada, Aug. 2010.

[147] R. Ur-Rehman, S. Caro, D. Chablat, and P. Wenger. Multiobjective path placement optimization of parallel kinematics machines based on energy consumption, shaking forces and maximum actuators torques: Application to the orthoglide. *Mech. Mach. Theory*, 45(8):1125–1141, 2010.

[148] M. Hassan and A. Khajepour. Optimization of actuator forces in cable-based parallel manipulators using convex analysis. *IEEE T. Robotic.*, 24(3):736–740, 2008.

[149] Z. Gao, D. Zhang, and Y.J. Ge. Design optimization of a spatial six degree-of-freedom parallel manipulator based on artificial intelligence approaches. *Robot. Cim-Int. Manuf.*, 26(2):180–189, 2010.

[150] K. Deb, A. Pratap, S. Agarwal, and T. Meyarivan. A fast and elitist multiobjective genetic algorithm: NSGA-II. *IEEE T. Evolut. Comput.*, 6(2):182–197, 2002.

[151] J.-P. Merlet. Direct kinematics of planar parallel manipulators. In *IEEE International Conference on Robotics and Automation*, volume 4, pages 3744–3749, 1996.

[152] M.J.D. Hayes. Kinematics of general planar stewart-gough platforms. Ph.D. Thesis, McGill University, 1999.

[153] S. Bai and S. Caro. Design and analysis of a 3-PPR planar robot with U-shape base. In *IEEE International Conference on Advanced Robotics*, Munich, Germany, June 2009.

[154] G. Wu, S. Bai, and J.A. Kepler. Error modelling and experimental validation for a planar 3-P̲PR parallel manipulator. In *15th IEEE International Conference on Advanced Robotics (ICAR)*, pages 259–264, Tallinn, Estonia, june 2011.

[155] I.A. Bonev. Direct kinematics of zero-torsion parallel mechanisms. In *IEEE International Conference on Robotics and Automation*, pages 3851–3856, Pasadena, California, USA, 2008.

[156] I.A. Bonev. Geometric analysis of parallel mechanisms. PhD Thesis, Laval University, Canada, 2002.

[157] L.-W. Tsai. The Jacobian analysis of parallel manipulators using reciprocal screws. pages 327–336. Kluwer, 1998.

[158] J. G. de Jalón and E. Bayo. *Kinematic and Dynamic Simulation of Multibody Systems: The Real-Time Challenge*. Springer-Verlag, New-York, 1994.

[159] J. Diebel. Representing attitude: Euler angles, unit quaternions, and rotation vectors. In *Stanford University Technical Report*, Stanford University, Stanford, CA, 2006.

[160] J.F. Gardner. *Simulations of machines using MATLAB and Simulink*. Brooks/-Cole, 2001.